



Ghent University
Faculty of Engineering and Architecture
Department of Applied Physics

Universidad de Complutense de Madrid
Facultad de Ciencias Físicas
Departamento de Física Atómica Molecular y
Nuclear

Assessment of retention of plasma components in tungsten under high flux plasma exposure: multiscale modelling approach

Studie van de retentie van plasmacomponenten in wolfraam
bij blootstelling aan hoge plasmaflux: de
multischaalmodelleringsaanpak

Petr Grigorev

Doctoral thesis submitted in order to obtain the academic
degrees of:
Doctor of Engineering Physics (Ghent University)
Doctor Erasmus Mundus en Ciencia e Ingeniería de la
Fusión (Universidad Complutense de Madrid)
Academic year 2016-2017



Ghent University
Faculty of Engineering and Architecture
Department of Applied Physics

Promoters: Prof. Dr.h.c Ir. Jean-Marie Noterdaeme
Prof. Dr. Guido Van Oost



Universidad Complutense de Madrid
Facultad de Ciencias Físicas
Departamento de Física Atómica Molecular y
Nuclear

Promoters: Prof. Dr. Paloma Fernández Sánchez
Dr. Christophe Ortiz

Doctoral thesis submitted in order to obtain the academic
degrees of:
Doctor of Engineering Physics (Ghent University)
Doctor Erasmus Mundus en Ciencia e Ingeniería de la
Fusión (Universidad Complutense de Madrid)
Academic year 2016-2017

Members of the examination board

Chairman:

Prof. Dr. ir. Rik Van de Walle
Ghent University

Reading committee:

Prof. Dr. ir. Kim Verbeken
Ghent University
Dr. Andree de Backer
Culham Centre for Fusion Energy
Prof. Dr. Francisco Javier del Río Esteban
Universidad de Complutense de Madrid
Prof. Dr. Luis Mario Fraile
Universidad de Complutense de Madrid
Dr. Dmitry Terentyev
SCK•CEN, Institute for Nuclear Materials Science
Dr. ir. Giovanni Bonny
SCK•CEN, Institute for Nuclear Materials Science

Further members of the
examination board:

Prof. Dr.h.c. ir. Jean-Marie Noterdaeme
Ghent University
Prof. Dr. ir. Guido Van Oost
Ghent University
Dr. Christophe Ortiz
*Laboratorio Nacional de Fusión
por Confinamiento Magnético, CIEMAT*
Prof. Dr. Paloma Fernández Sánchez
Universidad de Complutense de Madrid

Doctoral guidance committee

Supervisors:

Dr. Dmitry Terentyev
SCK•CEN, Institute for Nuclear Materials Science
Dr. Christophe Ortiz
*Laboratorio Nacional de Fusión
por Confinamiento Magnético, CIEMAT*

Promoters:

Prof. Dr.h.c. ir. Jean-Marie Noterdaeme
Ghent University
Prof. Dr. ir. Guido Van Oost
Ghent University
Prof. Dr. Paloma Fernández Sánchez
Universidad de Complutense de Madrid

The research was performed at:



Belgian Nuclear Research Center SCK•CEN
Institute for Nuclear Materials Science
Boeretang 200
2400 Mol, België



Centro de Investigaciones Energéticas,
Medioambientales y Tecnológicas Ciemat
Complutense, 40
28040 Madrid, Spain

The work was supported by:



This work was supported by the European Commission and carried out within the framework of the Erasmus Mundus International Doctoral College in Fusion Science and Engineering (FUSION-DC)



SCK•CEN Academy for Nuclear Science and Technology

Table of Contents

List of publications	XVII
Nederlandse samenvatting	XXI
Resumen en Español	XXV
English summary	XXIX
1. Introduction	1-1
1.1. Magnetic confinement fusion	1-2
1.2. Modern tokamaks	1-3
1.3. Plasma facing materials and divertor	1-4
1.4. Tritium retention problem and this thesis	1-7
1.5. Multiscale modelling approach	1-8
References	1-11
2. Hydrogen in tungsten as plasma facing material	2-1
2.1. Hydrogen in bulk tungsten	2-1
2.2. Interaction of hydrogen with defects in tungsten	2-4
2.3. Experimental studies of hydrogen retention in tungsten	2-6
2.4. Modelling and interpretation of the experiments	2-9
2.5. Conclusion	2-12
References	2-13
3. New model based on dislocation-mediated H retention	3-1
3.1. DFT study of H interaction with screw dislocation	3-1
3.2. Migration barrier along the SD core for H attached to the dislocation	3-3
3.3. Interaction of H_N clusters with screw dislocation studied by DFT	3-4
3.4. Jog-punching bubble formation mechanism	3-5
3.5. Model for describing H plasma exposure	3-7
3.6. Model for describing H trapping and bubble formation along dislocations	3-8
3.7. Conclusion	3-11
References	3-13

4. Mechanisms of retention characterized by Molecular Dynamics simulations	4-1
4.1. Selection of the W-W interatomic potential to study the interaction of H with dislocations	4-2
4.2. Development and validation of W-H-He potential	4-4
4.3. Interaction of H and H_N clusters with dislocations	4-7
4.4. Diffusion of H in the bulk crystal and attached to a dislocation	4-11
4.5. Effect of He on H retention: He assisted Frenkel pair formation and $He_M\text{-}H_N$ cluster bonding	4-13
4.6. Diffusion and thermal stability of $He_M\text{-}H_N$ clusters	4-15
4.7. H bubble formation in W in presence of He_M clusters	4-19
4.8. Conclusion	4-21
References	4-22
5. Macroscopic retention assessed by mean field rate theory	5-1
5.1. Numerical model of bubble nucleation on dislocations	5-1
5.2. Parametrization of binding energy of H atom to a vacancy type dislocation jog and threshold for loop punching mechanism	5-3
5.3. Defining the parameters of the model with experimental results	5-5
5.4. Prediction of flux-temperature conditions for the jog-punching mechanism to function	5-6
5.5. Modelling TDS release: universal binding energy fit depending on the bubble size	5-7
5.6. Modelling TDS release: linking bubble size with release stage and mechanism of bubble formation	5-10
5.7. Hybrid model of H retention after high flux high temperature exposure	5-12
5.8. Conclusion	5-14
References	5-16
6. Conclusions and outlook	6-1
6.1. Conclusions	6-1
6.1.1. <i>Ab initio</i> calculations	6-2
6.1.2. Model of dislocation mediated H retention in tungsten	6-2
6.1.3. Molecular static and molecular dynamics simulations	6-3
6.1.4. Continuum scale numerical simulations	6-4
6.2. Outlook	6-4
A. Modelling deuterium release from tungsten after high flux high temperature deuterium plasma exposure	A-1
B. Mobility of hydrogen-helium clusters in tungsten studied by molecular dynamics	B-1

C. Numerical analysis of TDS spectra under high and low flux plasma exposure conditions	C-1
D. Nucleation and growth of hydrogen bubbles on dislocations in tungsten under high flux low energy plasma exposure	D-1
E. Interaction of hydrogen with dislocations in tungsten: An atomistic study	E-1
F. On the binding of nanometric hydrogen-helium clusters in tungsten	F-1
G. Many-body central force potentials for tungsten	G-1
H. Dislocations mediate hydrogen retention in tungsten	H-1
I. Dislocation mechanism of deuterium retention in tungsten under plasma implantation	I-1

List of Figures

- 1.1. Magnetic fields in tokamak from left to right: toroidal component, poloidal component and resulting helical magnetic lines. 1-3
- 1.2. Internal view of JET chamber combined with image of plasma taken with visible spectrum video camera (left). Comparison of the cross sections of vacuum vessels of different tokamaks (right). 1-4
- 1.3. The configuration of ITER inside the cryostat. The purple image in the center of the picture represents plasma inside the vacuum chamber. 1-5
- 1.4. The schematic picture of the ITER's vacuum chamber from [4] (a). Beryllium is shown with green colour and tungsten is shown with red colour. Black lines represent an example of magnetic field lines in the core plasma and a separatrix. The light pink region between the separatrix and the walls of the chamber represents the divertor plasma layer. An image of a divertor cassette (b) and an image of the W monoblock and flat tile configurations (c) from [6]. The tungsten monoblock geometry will be used for inner and outer vertical targets, while the flat tile geometry will be used for the dome umbrellas and the particle reflector plates. 1-6
- 1.5. Summary of simulation techniques used at different length and time scales within the multiscale modelling approach. Quantum mechanical methods of calculation of electronic structure are presented with the picture of electron density distribution for H atoms in tungsten lattice obtained with Density Functional Theory in [15] (a). Molecular Dynamics method is presented with a binding energy map of a hydrogen atom to an edge dislocation from [16] (b) and a snapshot of a simulation of H accumulation at a screw dislocation at a finite temperature (c). Rate Theory method is presented with results of simulation of evolution of H concentration in tungsten sample during isochronal annealing (d). Finite Element methods are presented with a finite element model of tungsten monoblock from [17]. 1-9

-
- 2.1. Schematic energy diagram for H in W. ΔE_{S-B} is the energy barrier for moving of H from the surface to the bulk, ΔE_{Rec} is the recombination barrier for two H atoms adsorbed at the surface to form H₂ molecule and leave the surface, ΔE_D is the diffusion barrier for H in the bulk, ΔE_{Bin} is the binding energy of a H atom to a defect in the material, ΔE_{Trap} is the trapping energy of H to a defect $\Delta E_{Trap} = \Delta E_{Bin} + \Delta E_D$ 2-2
 - 2.2. Comparison of values of H diffusion coefficient obtained by means of Gas Driven Permeation (GDP) [4–8], Plasma Driven Permeation (PDP) [7, 8] and Ion Driven Penetration (IDP) [9, 10] techniques. 2-3
 - 2.3. Schematic representation of the defects in tungsten with strong trapping properties: vacancies and their clusters, voids, dislocation and grain boundaries. Red circles represent trapped H atoms and grey circles represent W lattice atoms. Schematic pictures of positive edge dislocation formed by inserting an extra half plane of atoms ABCD and right-handed screw dislocation formed by displacing faces ABCD in perfect crystal relative to each other in direction BA from [16]. Black lines represent bonds between atoms. 2-4
 - 2.4. Incremental hydrogen binding energy with defects in tungsten. Values for vacancy clusters obtained with empirical model in [17] are shown as yellow stars. Black square represents the value for voids obtained with *ab initio* in [13]. *Ab initio* values for vacancies from [13, 18, 19] are shown with triangles, values for grain boundaries [20] are represented with blue diamond and dislocations [21, 22] are represented with circles. The right hand side Y axis shows the estimation of temperature of release peaks during thermal desorption measurements corresponding to binding energy reported on the left hand side Y axis. 2-5
 - 2.5. Surface and sub-surface modifications of W after irradiation up to fluence of $10^{27} D/m^2$ and flux of $10^{22} 1/m^2 s$ at 480 K (a) and 600 K (a) [23]. The arrow (b) indicates the direction of material transport from the cavity to the surface structure. 2-6
 - 2.6. Blister formation domain in terms of exposure temperature and flux as obtained in [24–27, 30]. The number next to the symbols show the blister size in μm 2-7
 - 2.7. Schematic representations of the results of TDS measurements in two regimes (a) the released gas is extracted from the chamber during the measurement giving instantiations H release and (b) released gas is not extracted during the measurement giving the cumulative H release from the sample. 2-8
 - 2.8. Total retention of H in tungsten as measured by NRA and TDS techniques [27]. Red arrows indicate the discrepancy between values obtained by NRA and TDS. 2-9

2.9. Schematic representation of TMAP7 model of a material containing H from [36]	2-11
3.1. H-SD binding energy map. The colour convention presented in a form of a histogram on the right hand side of the figure denotes the binding energy value in eV as well as the binding energy distribution of H positions presented on the map. Filled triangles display all metastable H positions, black circles display W atoms. Three dashed arrows represent displacement of the atoms along $\langle 111 \rangle$ direction indicating the $\frac{1}{2}\langle 111 \rangle$ SD core. Positions with the highest values of binding energy are numbered from 1 to 9 in the figure.	3-2
3.2. Migration energy paths between the metastable positions indicated in figure 3.1. The legend denotes the path between positions in the notation used in figure 3.1.	3-3
3.3. Incremental binding energy of H to H_{N-1} cluster attached to the dislocation core. Reference states were taken to be either an H atom in a tetrahedral position in the bulk ('Bulk'), or an H atom attached to the dislocation core ('Core').	3-4
3.4. Excess energy needed for jog-punching mechanism to occur on a screw dislocation core in the presence of a H_N cluster, depending on the cluster size.	3-5
3.5. Incremental binding energy of H to a screw dislocation core (magenta triangles), vacancy jog at dislocation (green stars) and vacancy in bulk tungsten from literature (blue circles [6], black squares [7] and red triangles [8]).	3-6
3.6. Concentration profiles during plasma implantation for different values of dislocation density (ρ).	3-9
3.7. Reaction rates for H_N -SD cluster formation versus depth calculated using equations 3.8-3.10 at 460 K, varying dislocation density in the range $10^{11}-10^{13} (m^{-2})$. Horizontal dashed lines reveal dissociation rates, ω_H^- , of H from H_N -SD clusters with $N = 1-3$ ($\Delta E_{Bin} = 0.55$ eV), $N = 4-6$ ($\Delta E_{Bin} = 0.45$ eV), $N = 7-9$ ($\Delta E_{Bin} = 0.35$ eV) obtained using equation 3.11. The orange area specifies the depth threshold until which the nucleation of supercritical H_8 -SD clusters takes place given the dislocation density and exposure temperature. The right hand side Y axis displays the concentration of H isotope, deuterium, as a function of depth measured using nuclear reaction analysis techniques applied to the samples exposed to high flux plasma at 460 K as described in [9, 10].	3-10
3.8. Dark field TEM image of screw dislocations decorated by H clusters. Two examples are indicated by the white circles.	3-11
4.1. Comparison of Vitek differential displacement maps as predicted by DFT. [2] (a), DND [3] (b) and MVG1 [4] (c) potentials.	4-2

4.2.	Comparison of H-H (a) and H-He (b) pairs binding energy as a function of distance as calculated by DFT [31] and the potentials.	4-5
4.3.	Comparison of H-Vacancy binding energy as a function of number of H atoms as calculated by DFT [31, 33] and the potentials.	4-6
4.4.	Distribution of the binding energy of H with the core of the edge dislocation obtained using the EAM2 potential. The geometric position of the dislocation core (i.e. the end of the extra atomic plane) is shown by the symbol ' \perp '. Red area in the figure represents positive values of the binding energy i.e. area with attractive interaction, blue areas represent repulsive interaction.	4-8
4.5.	Incremental binding energy of H_B to a H_{N-1} cluster placed on the SD core ('Bulk') (a). Incremental binding energy of H_{SD} to a H_{N-1} cluster placed on the SD core ('Core') (b). Inset figures schematically demonstrate the partition of H_b , H_{SD} and H_{N-1}	4-10
4.6.	1-D diffusion coefficient of H in the core of the edge dislocation and 3-D bulk diffusion coefficient as calculated using the EAM2 potential and drawn according to the experimental measurements [35]	4-12
4.7.	Incremental binding energy of He atoms to a He_M cluster in bulk tungsten (a) and incremental binding energy of H atom to $H-He_M$ cluster in vacancy (b) as predicted by DFT, BOP and EAM potentials.	4-13
4.8.	Frenkel pair formation energies in presence of He as predicted by BOP and EAM potentials and DFT method in [41]	4-14
4.9.	Incremental binding energy of a H atom to He_M-H_N clusters in the bulk W as predicted by the EAM2 potential.	4-16
4.10.	Arrhenius plot of the decay frequency of He_M-H_N clusters with one to four He atoms in the cluster obtained from MD simulations. The error bars represent 95 % confidence interval around the mean.	4-17
4.11.	Migration energies for He_M-H_N clusters extracted form MD simulations. The error bars represent the 95 % confidence interval.	4-18
4.12.	The critical atomic H concentration variation with the number of He atoms in the W crystal for three values of HIP	4-20
5.1.	Schematic picture of the model	5-2
5.2.	H binding energy to a vacancy (H-Vac) and to a vacancy type dislocation jog H-VJog complexes and approximations	5-3
5.3.	Estimation of the threshold value for the loop punching mechanism	5-4
5.4.	Sensitivity of the system on the loop punching parameters	5-6
5.5.	Exposure temperature vs. flux required for the bubble growth	5-7
5.6.	Illustration of binding energy master curve used in simulations. R is the defect open volume radius, K is the corresponding number of vacancies that defect occupies.	5-9

5.7. Comparison of normalized TDS spectra from work [17] with results of simulation for high flux ($5 \times 10^{23} D/m^2 s$ at 530 K and 870 K) (a) and low flux ($9 \times 10^{21} D/m^2 s$ at 530 K and 630 K)(b) exposures.	5-10
5.8. Comparison of modelling of H release during TDS with experimental results. The sample was exposed to plasma for 70 s with a particle flux in the centre of the sample in the range (0.8 – 1.0) $\times 10^{24} m^{-2}s^{-1}$. The sample temperature was monitored by infra-red camera and was kept at 1000 K. The heating rate during TDS measurements was 0.5 K/s.	5-14

List of Tables

4.1.	Summary of the performance of the potentials for different physical properties. The following nomenclature is used in the header of the table: FS – Finnis and Sinclair [6]; JO – Johnson and Oh [9]; FOI – Foiles [10]; ZWJ – Zhou <i>et al.</i>) [12]; KLL – Kong <i>et al.</i> [13]; ZSG – Zhang <i>et al.</i> [16]; DLK – Dai <i>et al.</i> [18]; DND – Derlet <i>et al.</i> [3]; MVG1, MVG2, MVG3 – 'EAM-2', 'EAM-3', 'EAM-4' by Marinica <i>et al.</i> [4] respectively.	4-3
4.2.	Point defect properties of H and He in BCC W calculated by DFT and the potentials	4-4
4.3.	Binding energy of H atom to a screw dislocation core as predicted by the EAM, BOP and DFT methods.	4-7
4.4.	Migration barriers and dissolution energies for He and mixed He_M - H_N clusters.	4-18

List of Acronyms

B

BCC	Body-Centered Cubic
BOP	Bond Order Potential

C

CRDS	Reaction Diffusion System Code
------	--------------------------------

D

DEMO	DEMOnstration Power Station
DFT	Density Functional Theory

E

EAM	Embedded Atom Method
ED	Edge Dislocation

F

FIB	Focused Ion Beam
-----	------------------

G

GB	Grain Boundaries
GDP	Gas Driven Permeation

H

HIP	Hydrogen Income Periodicity
-----	-----------------------------

I

IAP	Interatomic Potentials
IDP	Ion Driven Penetration
ITER	International Thermonuclear Experimental Reactor
IQR	Interquartile Range

J

JET	Joint European Torus
-----	----------------------

L

LAGB	Low Angle Grain Boundaries
LAMMPS	Large-scale Atomic/Molecular Massively Parallel Simulator
LTD	Liquid-Tear Drop

M

MD	Molecular Dynamics
MS	Molecular Static

N

NRA Nuclear Reaction Analysis

P

PDP Plasma Driven Permeation

S

SD	Screw Dislocation
SEM	Scanning Electron Microscopy
SIA	Self-interstitial Atom
SIMS	Secondary Ion Mass Spectrometry

T

TDS	Thermal Desorption Spectroscopy
TEM	Transmission Electron Microscopy
TMAP7	Tritium Migration Analysis Program
TTT	Tritium Tracer Technique

V

VASP Vienna *Ab initio* Simulation Package

List of publications

- [1] **Grigorev, P.**, A. Bakaev, D. Terentyev, G Van Oost, Noterdaeme, and E. E. Zhurkin. *Interaction of hydrogen and helium with nanometric dislocation loops in tungsten assessed by atomistic calculations.* Nuclear Instruments and Methods in Physics Research Section B: Beam Interactions with Materials and Atoms, 393:164 – 168, 2017.
- [2] **Grigorev, P.**, L. Buzi, A. Bakaeva, D. Terentyev, G. De Temmerman, G. Van Oost, and J. M. Noterdaeme. *Numerical analysis of TDS spectra under high and low flux plasma exposure conditions.* Physica Scripta, 2016(T167):014039, 2016.
- [3] **Grigorev, P.**, D. Matveev, A. Bakaeva, D. Terentyev, E. E. Zhurkin, G. Van Oost, and J.-M. Noterdaeme. *Modelling deuterium release from tungsten after high flux high temperature deuterium plasma exposure.* Journal of Nuclear Materials, 481:181–189, 2016.
- [4] **Grigorev, P.**, D. Terentyev, G. Bonny, E. E. Zhurkin, G. Van Oost, and J.-M. Noterdaeme. *Interaction of hydrogen with dislocations in tungsten: An atomistic study.* Journal of Nuclear Materials, 465:364–372, 2015.
- [5] **Grigorev, P.**, D. Terentyev, G. Bonny, E. E. Zhurkin, G. van Oost, and J.-M. Noterdaeme. *Mobility of hydrogen-helium clusters in tungsten studied by molecular dynamics.* Journal of Nuclear Materials, 474:143–149, 2016.
- [6] **Grigorev, P.**, D. Terentyev, V. Dubinko, G. Bonny, G. Van Oost, J.-M. Noterdaeme, and E. E. Zhurkin. *Nucleation and growth of hydrogen bubbles on dislocations in tungsten under high flux low energy plasma exposure.* Nuclear Instruments and Methods in Physics Research Section B: Beam Interactions with Materials and Atoms, 352(0):96–99, 2015.
- [7] G. Bonny, **Grigorev, P.**, and D. Terentyev. *On the binding of nanometric hydrogen–helium clusters in tungsten.* Journal of Physics: Condensed Matter, 26(48):485001, 2014.
- [8] G Bonny, D Terentyev, A Bakaev, **Grigorev, P.**, and D Van Neck. *Many-body central force potentials for tungsten.* Modelling and Simulation in Materials Science and Engineering, 22(5):053001, 2014.

- [9] V. I. Dubinko, **Grigorev, P.**, A. Bakaev, D. Terentyev, G. van Oost, F. Gao, D. Van Neck, and E. E. Zhurkin. *Dislocation mechanism of deuterium retention in tungsten under plasma implantation*. Journal of Physics: Condensed Matter, 26(39):395001, 2014.
- [10] D. Terentyev, V. Dubinko, A. Bakaev, Y. Zayachuk, W. Van Renterghem, and **Grigorev, P.** *Dislocations mediate hydrogen retention in tungsten*. Nuclear Fusion, 54(4):042004, 2014.
- [11] D. Terentyev, G. Monnet, and **Grigorev, P.** *Transfer of molecular dynamics data to dislocation dynamics to assess dislocation–dislocation loop interaction in iron*. Scripta Materialia, 69(8):578–581, 2013.
- [12] E. E. Zhurkin and **Grigorev, P.** *Sputtering of Al nanoclusters by 1–13 keV monatomic or polyatomic ions studied by Molecular Dynamics simulations*. Nuclear Instruments and Methods in Physics Research Section B: Beam Interactions with Materials and Atoms, 303(0):136–141, 2013.

Nederlandse samenvatting

–Summary in Dutch–

Kernfusie wordt gezien als een potentieel schone, veilige en quasi onuitputbare bron van energie voor de toekomst. Momenteel is het meest belovende reactorconcept de zogenaamde "tokamak", waarbij magnetische velden gebruikt worden voor de opsluiting van het fusieplasma. Op heden is een van de meest ambitieuze energie gerelateerde projecten de bouw van 's werelds grootste tokamak, beter gekend als ITER, wat "de weg" betekent in het Latijn. De geplande experimenten in ITER beogen het testen van de geïntegreerde technologieën, de materialen en de fysische regimes die nodig zijn voor de commerciële uitbating van fusie gebaseerde elektriciteitscentrales. Met andere woorden, ITER vormt de brug tussen de huidige kleinere fusiemachines en de grotere toekomstige DEMO-reactor.

Een van de belangrijkste doelstellingen van de uitbating van ITER is om aan te tonen dat gecontroleerde fusie geen negatieve gevolgen voor het milieu heeft. Daarom wordt extra aandacht besteed aan tritium (T), dat intrinsiek giftig en radioactief is. Door de autoriteiten is de geaccumuleerde T-limiet vastgelegd op 700 g voor het volledige vacuümvat om zo het milieu te beschermen bij een eventueel verlies van T. Een gedetailleerde kennis van de mechanismen die verantwoordelijk zijn voor de penetratie, accumulatie en retentie van T in de materialen die in contact komen met het plasma is dus essentieel.

In het huidige ITER-design is wolfram (W) weerhouden als pantser materiaal voor de divertor – het uitlaatsysteem voor ITER – dat onderhevig is aan moeilijke omstandigheden inzake warmte en deeltjes flux. De keuze voor W is voornamelijk gemotiveerd door zijn superieure fysische eigenschappen, zoals bijvoorbeeld, hoge smeltemperatuur, thermische geleidbaarheid en weerstand tegen sputteren. Deze thesis concentreert zich op de studie van de mechanismen die verantwoordelijk zijn voor de retentie en ontsnapping van T in W.

Het bereiken van ITER relevante omstandigheden met de huidige experimentele opstellingen met betrekking tot deeltjes flux, cyclische thermische belastingen en neutron bestraling is moeilijk te bereiken. Tot nog toe worden lineaire deuterium plasma opstellingen gebruikt om de effecten van T onder ITER relevante omstandigheden te bestuderen. Dus, veel experimentele studies in de wetenschappelijke literatuur volgen deze werkwijze. Na de blootstelling aan het plasma worden de monsters typisch met drie technieken onderzocht. Ten eerste is er de Nucleaire Reactie Analyse (NRA) die informatie verschaft over het diepteprofiel van de deuterium concentratie in het materiaal. Ten tweede, Thermisch Desorptie

Spectroscopie (TDS) volgt de ontsnapping van deuterium van het monster tijdens lineaire verhitting. De analyse van de vorm van de ontsnappingsspectra geven een idee over de mogelijke types van vallen in het materiaal, op het microscopisch niveau. Ten derde, elektron microscopie wordt gebruikt om de oppervlaktegradiatie van het materiaal door het plasma te bestuderen. Echter, geen van de drie vermelde technieken levert directe of eenduidige informatie over de mechanismen die verantwoordelijk zijn voor de deuterium retentie in wolfaam. Daarom wordt multi-schaal modellering beschouwd als een complementaire aanpak, die een diepgaande kennis van alle betrokken interagerende mechanismen op het atomaire niveau bevordert.

Het startpunt van deze doelstelling is een model voor de waterstof retentie dat gedomineerd wordt door de accumulatie van H-dislocaties en gebaseerd is op *ab initio* berekeningen. Kort samengevat wordt de interactie van H met dislocaties berekend door middel van dichtheidsfunctionaaltheorie (DFT), welke een benadering is van de oplossing van de Schrödinger vergelijking voor het veel deeltjes probleem. Na een grondige analyse van de DFT resultaten werd een mechanisme voorgesteld voor de nucleatie en groei van waterstof bellen op dislocaties onder hoge flux plasma blootstelling in wolfaam. Het mechanisme wordt gekarakteriseerd door de volgende drie stappen: (1) interstiële H-atomen worden gevangen op dislocaties door de gunstige energetische omstandigheden; (2) ze migreren snel in één dimensie langs de dislocatiekern door de lage migratie energieën; (3) de groei van vele H-clusters, die uiteindelijk resulteren in de creatie van een jog van vacatures op de dislocatie. Deze mechanismen werden geïmplementeerd in een eenvoudig "Rate Theory Model" dat toelaat de relevante experimentele trends te reproduceren. Dit deel van het onderzoek wordt beschreven in hoofdstuk 3 van deze thesis.

Vervolgens werd dit model verbeterd door middel van klassieke moleculaire dynamica (MD) simulaties, waarin Newtons vergelijkingen geïntegreerd worden over langere tijds en lengte schalen. Op deze manier worden de atomaire interacties geparametriserd door empirische potentiaLEN voor het W-H-He systeem volgens het "embedded atom model". De potentiaAL werd uitgebreid getest door te vergelijken met DFT data en voorspellingen van een Bindings Ordering PotentiaAL (BOP) uit de literatuur. Moleculaire Statica (MS) en MD-simulaties werden uitgevoerd om de stabiliteit van vacature-H-He clusters te parametrizeren, de diffusie en thermische stabiliteit van geïsoleerde H en He atomen en hun clusters in zowel bulk W als in de buurt van dislocaties te bestuderen. Voor schroefdislocaties werd geen 1-D migratie geobserveerd wat toegeschreven wordt aan het feit dat de potentiaAL niet alle aantrekende posities van H in en nabij de schroefdislocatiekern reproduceert. De resultaten van de atomaire simulaties worden beschreven in hoofdstuk 4 en geven een gedetailleerd inzicht in de mechanismen die verantwoordelijk zijn voor de retentie van H in W.

Echter, om het werkelijke effect van de verschillende mechanismen op de H retentie onder experimentele omstandigheden te begrijpen is er nood aan groot-schalige "mean field theory" simulaties gebaseerd op de resultaten van atomaire simulaties. Hoofdstuk 5 beschrijft de implementatie van zo een model voor dis-

locatie gedreven H retentie in W gebaseerd is op de resultaten van atomaire simulaties. Het model werd gebruikt om de nucleatie van stabiele bellen, hun groei en vervolgens blaarvorming te voorspellen onder werkelijke experimentele omstandigheden. Het model werd uitgebreid met een universele functionaal voor de bindingsenergie van H tot een bel, die afhankelijk is van de groeifase van de bel en laat toe de experimentele ontsnappingsfases van hoge temperatuur TDS-spectra te analyseren. De vorm van de beschouwde spectra werd gerelateerd aan het mechanisme dat verantwoordelijk is voor de vorming van de H-bel en de grootte van de bel. Uiteindelijk werd een twee-zones dieptemodel van H-retentie in W met een dynamische val nucleatie net onder de oppervlakte. Het model werd gecombineerd met een klassiek diffusie-vallen programma om TDS-spectra te simuleren en analyseren zoals verkregen na hoge temperatuur-hoge flux blootstellingen. Uit de computeranalyse werd besloten dat de hoge temperatuur-hoge flux blootstellingen ($T = 1000$ K, flux = 10^{24} D/m²s en fluence van 10^{26} D/m²) resulteren in de creatie van plasma geïnduceerde defecten net onder het oppervlak en hun bulk diffusie, zodat de retentie bepaald wordt door plasma geïnduceerde defecten (bellen) net onder de oppervlakte en natuurlijke vallen (zoals bijvoorbeeld holtes en korrelgrenzen). Mogelijke experimentele omstandigheden en procedures voor de verdere validatie van de voorspellingen van de simulaties worden voorgesteld.

Resumen en Español –Summary in Spanish–

La fusión nuclear puede ser considerada como potencialmente limpia, segura y virtualmente una fuente ilimitada de energía para el futuro. Actualmente, el concepto mas prometedor – el llamado “tokamak” utiliza el confinamiento magnético del plasma de fusión. Uno de los proyectos mas ambiciosos relacionados con la energía es hoy en día la construcción del tokamak mas grande del mundo, también conocido como ITER, El Camino en Latin. La campaña experimental planeada en ITER tiene como objetivo probar las tecnologías, los materiales y los regímenes físicos necesarios para la producción comercial de electricidad basada en la fusión nuclear. En otras palabras, el objetivo de ITER es de tender un puente entre el dispositivo de fusión mas pequeño que existe hoy y la planta de fusión nuclear del futuro, el reactor DEMO.

Uno de los principales objetivos para el funcionamiento de ITER es de demostrar el control del plasma de fusión con consecuencias insignificantes para el medioambiente. Por lo tanto, una atención especial ha sido puesta sobre el tritio (T) respecto a su toxicidad y radiactividad intrínsecas. El límite de 700 g de T acumulado en la cámara de ITER fue determinada por las autoridades de seguridad para limitar posibles daños medioambientales en el caso improbable de una fuga de T . Por lo tanto, un conocimiento de los mecanismos que gobernan la penetración, acumulación y retención de T en materiales que están en contacto con el plasma es crucial.

En el diseño actual de ITER, el tungsteno (W) fue retenido como material blindaje para el divertor – el sistema de escape de ITER – y estará sujeto to condiciones extremas en términos de flujo de calor y de bombardeo por partículas. La elección del W es principalmente motivada por sus increíbles propiedades, como un punto de fusión muy alto, una conductividad térmica alta y una buena resistencia a la erosión. Esta tesis doctoral se centra en el estudio de los mecanismos de retención y desorción del T en W .

Sin embargo, alcanzar condiciones relevantes para ITER con configuraciones existentes en términos de bombardeo de partículas, ciclos de cargas térmicas e irradiación por neutrones es, desgraciadamente, difícil de conseguir. Hasta ahora, dispositivos lineares de plasma de deuterio han sido utilizados para reproducir los efectos del tritio bajo condiciones relevantes para ITER. Así, muchos estudios experimentales encontrados en la literatura científica se basan en esta técnica. Despues de exposición al plasma, las muestras son típicamente examinadas utili-

zando las tres técnicas siguientes. Primero, el análisis de reacción nuclear (NRA) aporta información sobre el perfil en profundidad de la concentración de deuterio en el material, después de su implantación durante la exposición. Segundo, la Espectroscopia de Desorción Térmica (TDS) sigue la desorción de deuterio de la muestra durante un calentamiento lineal. El análisis de la forma de los espectros de desorción aporta una idea sobre los posibles sitios de atrapamiento en el material, a nivel microscópico. Finalmente, técnicas de microscopía por electrones son utilizadas para evaluar la degradación de la superficie del material por el plasma. Sin embargo, ninguna de las técnicas mencionadas aporta una información directa o concluyente sobre los mecanismos responsables para la retención del deuterio en el tungsteno. Por consiguiente, enfoques basados en una modelización computacional multi-escalas pueden considerarse como herramientas de apoyo, aportando un conocimiento en profundidad de todos los mecanismos implicados y que interactúan a nivel atómico.

Como punto de partida hacia este objetivo, un modelo para la retención del hidrógeno gobernada por la acumulación en dislocaciones fue propuesto, basado en cálculos de primeros principios. En resumen, la interacción del H con líneas de dislocación fue calculada utilizando la Teoría de la Densidad Funcional (DFT), que consiste en una aproximación para resolver la ecuación de Schrödinger a varios cuerpos. En base a estos cálculos de DFT, se propuso un mecanismo de nucleación y de crecimiento para la burbujas de hidrógeno sobre las líneas de dislocación bajo exposición del tungsteno a un plasma con alto flujo. El mecanismo comprende las siguientes etapas: (1) los átomos de H intersticial se atrapan en las líneas de dislocación debido a una variación energética favorable; (2) una migración unidimensional muy rápida a lo largo del núcleo de la dislocación debido a una energía de migración muy baja; (3) crecimiento de clusters con varios átomos de H, finalmente resultando en la creación de un salto de una vacante sobre el núcleo de la dislocación. La implementación de estos mecanismos en un simple modelo de “Rate Theory” nos permitió encontrar tendencias relevantes en acuerdo con observaciones experimentales. Esta parte de la investigación está descrita en el capítulo 3 de esta tesis.

Después, nuestro modelo fue mejorado utilizando simulaciones de Dinámica Molecular (DM), donde las ecuaciones clásicas del movimiento de Newton son integradas para tiempos y distancias más largos. En este enfoque, las interacciones atómicas son parametrizadas por un potencial interatómico empírico para el sistema W-H-He en el marco de un Modelo de Atomo Embebido (EAM). El potencial fue probado por comparación con datos obtenidos por DFT y predicciones Potencial de Orden de Enlace (BOP) encontradas en la literatura. Numerosas simulaciones de Estática Molecular (SM) y DM fueron necesarias para parametrizar la estabilidad de los clusters de vacante-H-He, la difusión y la estabilidad térmica de los átomos de H y He y sus clusters en el volumen del tungsteno así como en la proximidad de dislocaciones. En el caso de dislocaciones hélice no se observó migración unidimensional, lo cual fue correlacionado con el hecho que el potencial no predice las posiciones de atracción del H dentro y cerca del núcleo de una dislocación hélice. El resultado de nuestras simulaciones atomísticas ha sido re-

sumido en el capítulo 4, aportando un conocimiento profundo de los mecanismos que gobernan la retención del H en W.

Sin embargo, para investigar adecuadamente el efecto de todos estos mecanismos sobre la retención del H en W durante experimentos reales, hay que utilizar simulaciones de “mean field theory” utilizando los parámetros obtenidos por simulaciones atomísticas. El capítulo 5 describe la implementación del modelo incluyendo la retención de H en dislocaciones en tungsteno en una herramienta de simulación numérica utilizando los parámetros obtenidos con simulaciones atomísticas. Este modelo fue utilizado para predecir la nucleación de burbujas estables, su crecimiento y la formación de blíster, bajo condiciones de exposición de plasma en función del flujo y la temperatura. La extensión de este modelo con una función universal para la energía de ligadura describiendo el enlace del H a una burbuja nos permitió analizar etapas de desorción obtenidas a partir de espectros de TDS. La forma de los espectros fue relacionada con los mecanismos de formación de burbujas de H y con su tamaño. Finalmente, proponemos un modelo incluyendo dos zonas de penetración para la desorción del H en W con nucleación por atrapamiento fuera de equilibrio en la zona bajo la superficie. El modelo fue combinado con un código clásico de atrapamiento-difusión para simular y analizar espectros de TDS obtenidos después de una exposición a alto flujo y alta temperatura. A partir del análisis computacional, concluimos que una exposición a alta temperatura y alto flujo ($T = 1000$ K, flujo = 10^{24} D/m²s anddosis of 10^{26} D/m²) resulta en la generación de difusión en el volumen y daño bajo la superficie, de tal manera que la retención es gobernada por defectos creados bajo la superficie (burbujas) y el atrapamiento en defecto naturales (como cavidades y bordes de grano) Condiciones experimentales para una validación futura de las predicciones han sido propuestas.

English summary

Nuclear fusion can be regarded as a potentially clean, secure and virtually unlimited source of energy for the future. Currently, the most promising reactor concept – the so-called "tokamak" device employs magnetic confinement of fusion plasma. One of the most ambitious energy-related projects today is the construction of the world's largest tokamak, also known as ITER, "The Way" in Latin. The experimental campaigns planned at ITER aim at testing integrated technologies, materials and physical regimes necessary for commercial production of fusion-based electricity. In other words, ITER aims at bridging the gap between today's smaller fusion devices and the demonstrational power plant of the future, the DEMO reactor.

One of the main goals for the operation of ITER is to demonstrate the control of fusion plasma with negligible consequences for the environment. Hence, special attention is drawn to tritium (T) regarding its intrinsic toxicity and radioactivity. The limit of 700 g of T accumulated in the ITER chamber was set by the safety authorities in order to limit possible environmental hazards in the unlikely event of T release. A full understanding of the mechanisms governing T penetration, accumulation and retention in the materials that are in contact with plasma is thus important.

In the current ITER design, tungsten (W) is retained as armour material for the divertor – the exhaust system of ITER – that is subjected to harsh conditions in terms of heat flux and particle bombardment. The choice of W is mainly motivated by its outstanding properties, such as high melting point, high thermal conductivity and resistivity to sputtering. This thesis focuses on studying the mechanisms of retention and release of T from W.

Reaching ITER-relevant conditions with existing set-ups in terms of particle bombardments, cyclic thermal loads and neutron irradiation is, unfortunately, rather hard to achieve. Up to now, linear deuterium plasma devices are used to mimic the effects of tritium under ITER relevant conditions. Thus, many experimental studies reported in the scientific literature are based on this technique. After exposure to plasma, the samples are typically examined using the following three techniques. Firstly, Nuclear Reaction Analysis (NRA) provides information about the depth profile of the deuterium concentration found in the material, as implanted during the exposure. Secondly, Thermal Desorption Spectroscopy (TDS) follows the release of deuterium from the sample during linear heating. The analysis of the shape of the release spectra gives an idea about the possible trapping sites in the material, at the microscopic level. Thirdly, electron microscopy tech-

niques are used to assess the surface degradation of the material by the plasma. However, none of the mentioned techniques provide direct or conclusive information about the mechanisms responsible for deuterium retention in tungsten. Hence, computer-based multiscale modelling approaches can be regarded as companion tools, providing a full-depth understanding of all involved mechanisms interplaying at the atomic level.

As a starting point towards this objective, a model for hydrogen retention governed by accumulation at dislocations was proposed, based on first principles calculations. In a nutshell, the interaction of H with dislocation lines was computed using Density Functional Theory (DFT), which is an approximate scheme to solve the Schrödinger's equation for the many body problem. A mechanism for the nucleation and growth of hydrogen bubbles on dislocation lines under high flux plasma exposure of tungsten was put forward after analysis of the DFT results. The mechanism comprises of the following stages: (1) interstitial H atoms getting trapped at dislocation lines due to favourable energetics; (2) their very fast one dimensional migration along the dislocation core because of low migration energies; (3) the growth of multiple H atoms clusters, eventually resulting in the creation of a vacancy jog on the dislocation core. Implementation of these mechanisms in simple Rate Theory model allowed reaching relevant trends in agreement with experimental evidence. This part of the research is described in chapter 3 of this thesis.

Next, the model was further improved using Molecular Dynamics (MD) simulations, where the Newton's classical equations of motion are integrated over much longer time and length scales. In this approach the atomic interactions are parametrized by an empirical interatomic potential for W-H-He system in the framework of Embedded Atom Model. The potential was benchmarked by comparison with DFT data and predictions of a Bond Order Potential (BOP) from the literature. A number of Molecular Static (MS) and MD simulations were performed in order to parametrize the stability of Vacancy-H-He clusters, diffusion and thermal stability of H and He single atoms and their clusters in the bulk tungsten as well as in the vicinity of dislocations. In the case of screw dislocations one dimensional migration was not observed which was related to the fact that the potential does not predict all the attractive positions of H in and near the screw dislocation core. The result of atomistic simulations are reported in chapter 4 and provide a thorough insight into the mechanisms that determine H retention in W.

However, in order to properly investigate the effect of all the considered mechanisms on the H retention during real experiments one has to perform a full scale mean field theory simulation using the parametrizations obtained by atomistic simulations. Chapter 5 describes the implementation of the model of dislocation driven H retention in tungsten in a numerical simulation tool using the parametrization obtained from atomistic simulations. The model was used to predict plasma exposure conditions in terms of flux and temperature for the nucleation of stable bubbles, their growth and subsequent blister formation. The extension of the model with a universal binding energy function describing binding of H to a bubble depending on the growth stage of the bubble, allowed one to analyse high tem-

perature release stages of TDS spectra. The shape of the considered spectra was related to the mechanism of H bubble formation and the size of the bubble. Finally a two-zoned depth distribution model of H retention in W with non-equilibrium trap nucleation in the subsurface region was proposed. The model was combined with classical diffusion-trapping code in order to simulate and analyse TDS spectra obtained after high flux high temperature exposures. From the performed computational analysis, it was concluded that high flux high temperature exposures ($T = 1000$ K, flux = 10^{24} D/m²s and fluence of 10^{26} D/m²) result in the generation of sub-surface damage and bulk diffusion, so that the retention is driven by both sub-surface plasma-induced defects (bubbles) and trapping at natural defects (such as cavities and grain boundaries). Experimental conditions and procedures for further validation of the predictions of the simulations were proposed.

“When mankind needs it – maybe a short time before the first thermonuclear reactor would start its work.”

Lev Artsimovich (1909 – 1973)

1

Introduction

In 2014 estimated global final energy consumption was provided by three main energy sources: fossil fuels (78.3 %), renewables (19.2 %) and nuclear energy (2.5 %) [1]. The fossil fuels: oil, gas and coal are finite resource. It is possible that cheap oil and gas will run out in our lifetime. Moreover burning fossil fuels strongly affects climate due to the vast CO₂ production and subsequent greenhouse effect. The distribution of the sources of fossil fuels is not uniform around the globe with different nations having different access to the resources. Fossil fuels based economy is vulnerable to decisions of the supplier leading to political instabilities and conflicts around the world. In other words, fossil fuels are limited and are far from being a clean and secure energy source. Thus there is a need for alternatives.

Two main currently used alternatives are renewable energy and nuclear power. Renewables include biomass, hydro, geothermal, solar and wind power sources. However most of them have the caveat of intermittency: the source is not continuously available and cannot be dispatched (i.e. cannot be turned on and off or adjust their power according to an order). Nuclear power based on nuclear fission does not have this disadvantage. However, it has the potential for very dangerous accidents and produces radioactive waste and spent fuel, which, in addition, can be used as a material for nuclear weaponry. Another type of nuclear energy – nuclear fusion can be a clean, secure and virtually unlimited alternative energy source of the future.

1.1. Magnetic confinement fusion

In a nuclear fusion reaction, energy is produced when two light nuclei are fused together to form a heavier nucleus. This is the same process that provides the energy in the sun and other stars. In order to make nuclear fusion reaction happen, one has to bring two nuclei as close as $10^{-14} - 10^{-15}$ m. However, to do this it is necessary to overcome electrostatic or Coulomb's repulsion between the positively charged protons in the nuclei. This fact is the main reason of the colossal obstacles standing on the way towards controlled nuclear fusion.

The Coulomb's interaction increases with the charge of a particle. Theoretically it is possible to fuse any particles lighter than iron. However, the difficulty in overcoming the electric repulsion limits the selection of practically possible fusion reactions to reactions between light particles: isotopes of hydrogen, lithium and helium. Fusion reactions involving these isotopes provide an energy gain in order of few MeV and have low value of the Coulomb's barrier in the range of 0.1 – 0.5 MeV. However reaction between two hydrogen isotopes: deuterium (D) and tritium (T) has the highest cross section. In nuclear physics value of cross section is used to characterize the probability of a nuclear reaction: the higher the cross section, the higher the probability of the reaction. Thus the following reaction between hydrogen isotopes was chosen as the most favourable for controlled nuclear fusion:



For hydrogen isotopes the energy of the Coulomb's repulsion is around 0.15 MeV. This is a very large value. Hydrogen atoms in gas heated up to $\sim 1.6 \times 10^9$ degrees of Kelvin will have comparable value of the average kinetic energy. It is not easy to achieve such temperatures. Historically it was achieved first in a hydrogen bomb where a fission based nuclear explosion was used as a sort of a match to ignite the fusion reaction. On top of that there is no material on Earth that can sustain such a high temperature without being destroyed. The best known refractory metals are not able to sustain even ten thousands of degrees. This brings the problem of confinement – the way to hold fusing matter together. On sun and other stars this problem is solved by the enormous size. The particles are confined by means of gravity. For obvious reasons this way of confinement is not achievable on Earth.

At fusion relevant temperatures matter transforms in the state of plasma. In this state, the atoms are fully ionized, meaning that all electrons are separated from the nuclei. The difference with gas state is that plasma fully consists of charged particles. Charged particles can be controlled by electric and magnetic fields. Thus it is possible to confine hot fusion plasma by strong magnetic fields. The implementation of this idea is called magnetic confinement. There are several

types of devices that utilize magnetic confinement: magnetic mirrors, stellarators and tokamaks. The most promising one is the tokamak where powerful magnetic fields in the shape of torus are used.

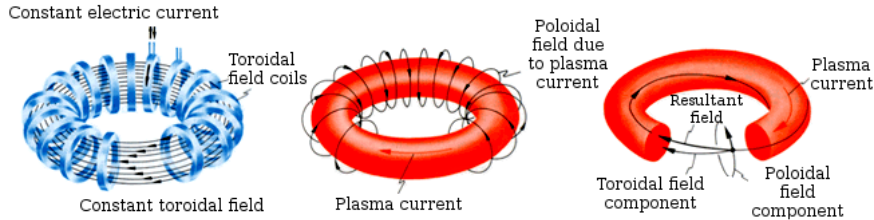


Figure 1.1: Magnetic fields in tokamak from left to right: toroidal component, poloidal component and resulting helical magnetic lines.

The name tokamak comes from Russian acronym that stands for "toroidal chamber with magnetic coils". The magnetic coils are used to create a toroidal magnetic field around the torus. A poloidal magnetic field (orthogonal to the toroidal direction) is created by inducing toroidal electric current that flows inside the plasma. The resulting magnetic field lines travel around the torus in a helical way, required for achieving plasma equilibrium. Toroidal, poloidal and resulting magnetic fields in tokamak are schematically shown in figure 1.1.

1.2. Modern tokamaks

First experiments with toroidal configuration started in 1956 in USSR with a device called "TMP". First tokamaks were very small with a main radius of around 40 cm. However already at that time theoretical estimations of the design of a thermonuclear reactor predicted a device with main radius of 12 meters and 1000 m^3 of plasma volume [2, 3]. The increase of the size of the device is necessary for the improvement of three components needed for effective energy production: plasma temperature, plasma density and confinement time. Currently the biggest tokamak in operation is Joint European Torus (JET) located in Culham Centre for Fusion Energy in Oxfordshire, UK. It has a major radius of 2.96 meters and holds the record of fusion power of 16 MW achieved in 1997. The image of the internal of the JET vacuum chamber is shown in figure 1.2 together with a comparison of the cross sections of the plasma volumes of different tokamaks.

One of the most ambitious energy projects in the world today is the construction of the world's largest tokamak called ITER (the acronym for International Thermonuclear Experimental Reactor and also "The Way" in Latin). The experimental campaign planned at ITER aims at testing the integrated technologies,

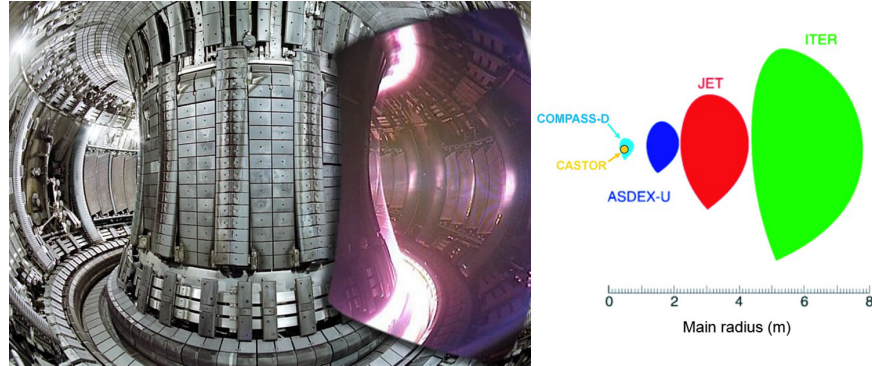


Figure 1.2: Internal view of JET chamber combined with image of plasma taken with visible spectrum video camera (left). Comparison of the cross sections of vacuum vessels of different tokamaks (right).

materials and physical regimes necessary for the commercial production of fusion based electricity. The size of the cross section of ITER's vacuum chamber is compared with JET and other tokamaks in the right part of figure 1.2. ITER aims to be the first device to produce tenfold return in energy, i.e. the ratio between total input power to the fusion power (Q) will be ten. For the current record of 15 MW of fusion power achieved at JET, the value of Q was only 0.67. Superconductive magnets cooled to 4° K will be used in ITER for producing the magnetic field. The whole magnetic system will be surrounded by a cryostat for thermal insulation. The ITER's tokamak configuration surrounded by the cryostat is shown in figure 1.3. The purpose of the device is to bridge the gap between today's smaller fusion devices to the demonstrational power station of the future or DEMO project. The final goal of the long term strategy is the PROTO project – prototype fusion based power plant.

1.3. Plasma facing materials and divertor

The choice of the plasma facing materials is extremely important for the performance of a fusion device. It was hardly possible to obtain a plasma discharge in the first toroidal configuration device "TMP" due to the poor choice of the plasma facing material. The vacuum chamber was made of porcelain. The evaporation of porcelain during the operation of the device polluted the plasma with silicon. Due to excitation, ionization and recombination with plasma electrons, atoms of impurities emit electromagnetic radiation which carries away the energy from the plasma and can be a serious problem for plasma heating. This effect is more pronounced for heavy impurities and thus light elements are usually chosen as plasma

facing materials. In figure 1.4(a) a schematic image of ITER's vacuum chamber from [4] is shown. As can be seen from the picture, in ITER beryllium (Be) will be used as a first wall material and tungsten (W) will be used for the divertor armour material.

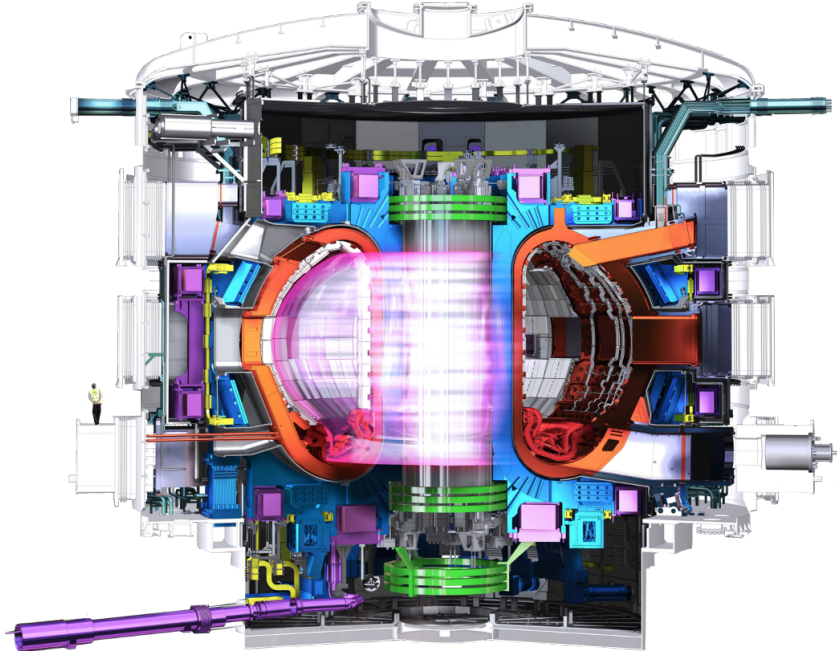


Figure 1.3: The configuration of ITER inside the cryostat. The purple image in the center of the picture represents plasma inside the vacuum chamber.

Since impurities enter the plasma from the exterior, they first appear in the outer layer of the plasma. Thus it is possible to fight plasma pollution if one could continuously extract impurities from the outer layer of the plasma. This was the idea behind the device proposed by the inventor of the stellarator concept – Lyman Spitzer [5]. He named the device “divertor”. In ITER, the divertor is located at the bottom of the vacuum chamber. Additional magnetic coils are used in the divertor to modify the magnetic field in order to extract the outer part of the magnetic field lines from the vacuum chamber. As can be seen from figure 1.4(a), closed magnetic field lines form D shape in the middle of the chamber where the core plasma is located. The outer magnetic field lines closer to the wall are not closed and intersect the divertor plates. The first non-closed magnetic field line is called separatrix and marks the border between the divertor plasma layer (marked with pink colour in figure 1.4(a)) and the rest of the plasma. Plasma particles in the

divertor layer follow the magnetic lines and reach the divertor plates. After cooling down the plasma particles are pumped out of the chamber. The use of the divertor allows reducing plasma contamination with impurities, extracting heat and helium ash produced in fusion reaction together with protecting the surrounding walls of the vacuum chamber.

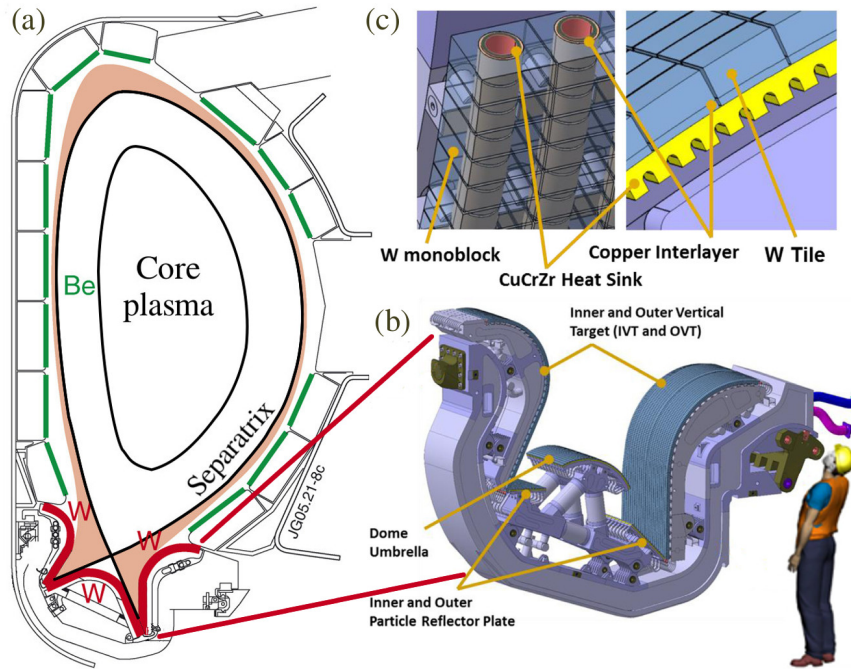


Figure 1.4: The schematic picture of the ITER's vacuum chamber from [4] (a). Beryllium is shown with green colour and tungsten is shown with red colour. Black lines represent an example of magnetic field lines in the core plasma and a separatrix. The light pink region between the separatrix and the walls of the chamber represents the divertor plasma layer.

An image of a divertor cassette (b) and an image of the W monoblock and flat tile configurations (c) from [6]. The tungsten monoblock geometry will be used for inner and outer vertical targets, while the flat tile geometry will be used for the dome umbrellas and the particle reflector plates.

The ITER divertor will be composed out of 54 "cassette assemblies" shown in figure 1.4(b). Each cassette has three plasma facing components: the inner and the outer vertical target and the dome. Current design of the divertor uses tungsten monoblock geometry for inner and outer vertical targets and flat tile geometry for the dome umbrellas and the particle reflector plates [6]. Both configurations are shown in figure 1.4(c). The inner and outer vertical targets are positioned at the intersection of the magnetic field lines and particle bombardment will be

particularly high in ITER. The tungsten monoblock is required to be able to sustain heat loads of 10 MW/m^2 in steady state and 20 MW/m^2 during transients (less than ten seconds). The number of stationary loads on the tungsten monoblock surface is 5000 cycles for 10 MW/m^2 and 300 cycles for 20 MW/m^2 [7, 8]. Currently the biggest challenge in terms of materials for ITER is the risk of melting of tungsten in the divertor that may occur in case of unmitigated plasma disruptions [8]. Since the choice of materials has been fixed it will be necessary to develop disruption detection and mitigation techniques in order to exclude such events.

1.4. Tritium retention problem and this thesis

Together with the demonstration and testing the technologies for the fusion power plant, ITER was designed to demonstrate the safety characteristics of a fusion device. In 2012, the ITER Organization was licensed as a nuclear operator in France. One of the main goals of operation of ITER is to demonstrate the control of fusion plasma with negligible consequences for the environment. From this point of view special attention is drawn to tritium (T).

Tritium is toxic and radioactive material. Thus a limit of 700 g of tritium accumulated in the ITER's chamber was set by the safety authorities [9] in order to limit possible environmental consequences in case of the unlikely event of T release. It is thus important to understand physical mechanisms governing T penetration, accumulation and retention in the materials that are in direct contact with plasma. In this thesis, the behaviour of hydrogen isotopes in tungsten is studied. The focus on tungsten is made because tungsten will be used in ITER divertor where the most harsh conditions are expected and also because tungsten is the main candidate for the divertor and the first wall material for DEMO reactor [10].

Unfortunately, until ITER itself starts operating it is very difficult to achieve exposure conditions close to the expected one in ITER in terms of particle loads, cyclic thermal loads and neutron irradiation. Up to now, linear deuterium plasma devices are used to mimic the effects of tritium under ITER relevant conditions. Thus, many experimental studies reported in the scientific literature are based on this technique [11–13]. Computational methods of materials science can be very useful as a complementary technique. Commonly used approach in computational material science is to create physical models based on and validated with available experimental results and then use these models to predict the behaviour of materials under unexplored conditions.

The aim of this thesis was to create a physical model of hydrogen isotopes retention in tungsten under ITER relevant exposure conditions, specifically addressing very high flux of plasma particles, and implement it in a numerical simulation tool. The results of the numerical simulations were tested and validated by comparison with available experimental results. In this thesis the so-called multiscale

modelling approach described in detail in the next section was used.

1.5. Multiscale modelling approach

The modelling and simulation of materials can be very challenging due to the extreme range of length and timescales of the physical mechanisms that govern the behaviour of the material. Length scales may span from nanometers and atoms to meters of physical constructions. Similarly, time scales can range from femtoseconds of atomic vibrations to the decades of the material's exploitation. Given the range of the length- and time-scales, it is natural that no single technique will work for all scales. Many methods have been developed with the focus on a specific set of physical phenomena appropriate for a given range of length and time-scales. Figure 1.5 summarizes the multi-scale paradigm with respect to the problem of hydrogen retention in tungsten. The bottom left corner of the figure represents the smallest scale while the top right corner represents the largest scale. Introduction to computational material science describing the techniques used in this thesis can be found in [14].

In the ranges of length scales of 1 Ångström (0.1 nm) to 100 nm, the bonding between atoms dominates the behaviour of the material. A description of the bonding requires the use of quantum mechanics in order to calculate the distribution of electrons. These methods are often called first principles or *ab initio* calculations meaning that there is no empirical approximations in the simulation. One of the most popular *ab initio* methods is based on Density Functional Theory (DFT) formulation of quantum mechanics. In DFT, the energy is written as a function of the electronic density, which is a function of a position, thus the energy is a functional of the electronic density. This method allows calculating the energies of the ground states of different atomic systems. Therefore, this method is extremely efficient in extracting local energy barriers/bonds such as migration energy of an atom or interaction energy of a foreign atom with a lattice defect. The method itself is computationally costly and its applicability is typically limited to systems of few hundreds of atoms (a few nm). An image of an electronic density distribution for two hydrogen atoms in tetrahedral positions in tungsten lattice from [15] is used as an illustration of the technique in figure 1.5(a).

To consider large scale atomic systems one has to approximate, due to the complexity of DFT methods for the description of atomic bonding, the atomic bonding by introducing empirical functions that are called Interatomic Potentials (IAP). One of the methods that employ interatomic potentials is called Molecular Dynamics (MD). It can be described as a simulation of the behavior of a large atomic system by numerical integration of Newton's equations of motion for the atoms where forces on the atoms are defined by their relative positions via applied interatomic potentials. Nowadays MD is used to study systems of up to billions of

atoms (hundreds of nm) at finite temperatures for times of few nanoseconds. As an illustration of the method, a binding energy map of a hydrogen atom to an edge dislocation from [16] is shown in figure 1.5(b) and a snapshot of a simulation of H accumulation at a screw dislocation at a finite temperature is shown in figure 1.5(c).

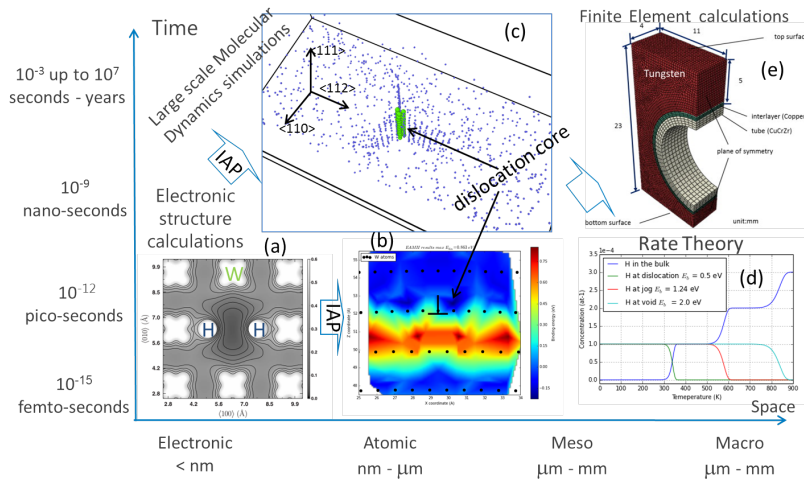


Figure 1.5: Summary of simulation techniques used at different length and time scales within the multiscale modelling approach. Quantum mechanical methods of calculation of electronic structure are presented with the picture of electron density distribution for H atoms in tungsten lattice obtained with Density Functional Theory in [15] (a). Molecular Dynamics method is presented with a binding energy map of a hydrogen atom to an edge dislocation from [16] (b) and a snapshot of a simulation of H accumulation at a screw dislocation at a finite temperature (c). Rate Theory method is presented with results of simulation of evolution of H concentration in tungsten sample during isochronal annealing (d). Finite Element methods are presented with a finite element model of tungsten monoblock from [17].

At larger length scales where there are too many atoms to consider, one has to move to continuum scale techniques. One of the continuum scale techniques, usually applied to study the microstructural evolution, is called a kinetic Rate Theory approach, which allows simulating evolution of concentrations on the timescale of days and years. As an illustration of the technique an evolution of H concentration in tungsten sample during isochronal annealing is shown in figure 1.5(d). An example of a method that can simulate a real space and time scale is the finite element method. As an illustration of the method a finite element model of a tungsten monoblock from [17] is shown in figure 1.5(e).

One of the most challenging parts of any modelling task is the identification of the physical mechanisms that govern the phenomenon of interest. A complete picture of the fundamental phenomenology of the problem may not be available. At this point, modelling at small scale may be very helpful for identifying the basic underlying physical processes, which are then to be transferred to a large-scale approach. For instance, DFT calculations provide the database for fitting the interatomic potentials for larger scale MD simulations. Such stepwise development of the model going from a small scale to larger scale is called multiscale modelling approach. It is important to note that close examination of experimental data and trends also leads to clearer understanding of physical mechanisms. Thus the feedback from larger scale to smaller scale is also an important part of the multiscale modelling. In this thesis the development of the model of hydrogen retention in tungsten started with DFT calculations (chapter 3). After identifying the key mechanisms for the model, an interatomic potential was developed. A number of MD simulations at finite temperatures were performed in order to obtain parameterizations for upper scale models (chapter 4). Finally, the model was implemented in the Rate Theory-based approach to simulate hydrogen retention at full-scale and validate the method by comparison with available experimental data (chapter 5).

The author of the thesis did not perform the DFT calculations himself, his main contribution at this part was processing the data and the development of the physical model based on the DFT results. The author's contribution to the development of the interatomic potential was mainly testing the multiple versions of the potential and providing the feedback to achieve the required accuracy. All Molecular Dynamics and Rate Theory simulations reported in the thesis were developed and performed by the author together with the subsequent analysis of the results.

References

- [1] G. Wetstone, K. Thornton, R. Hinrichs-rahlwes, S. Sawyer, M. Sander, R. Taylor, D. Rodgers, M. Alers, H. Lehmann, M. Eckhart, and D. Hales. *Renewables 2016 global status report 2016*. Paris: REN21 Secretariat, 2016.
- [2] I. E. Tamm. *Theory of a magnetic thermonuclear reactor (Part I)*. In Plasma Physics and the Problem of Controlled Thermonuclear Reactions, Volume 1, volume 1, page 1, 1960.
- [3] A. D. Sakharov. *Theory of the magnet thermonuclear reactor*, volume 1, page 20. USSR Academy of Science, 1958.
- [4] J. Paméla, F. Romanelli, M. L. Watkins, A. Lioure, G. Matthews, V. Philipps, T. Jones, A. Murari, A. Géraud, F. Crisanti, and R. Kamendje. *The JET programme in support of ITER*. Fusion Engineering and Design, 82(5-14):590–602, 2007.
- [5] J. Lyman Spitzer. *The Stellarator Concept*. Physics of Fluids, 1(1958):253–264, 1958.
- [6] T. Hirai, S. Panayotis, V. Barabash, C. Amzallag, F. Escourbiac, A. Durocher, M. Merola, J. Linke, T. Loewenhoff, G. Pintsuk, M. Wirtz, and I. Uytdenhouwen. *Use of tungsten material for the ITER divertor*. Nuclear Materials and Energy –, 2016.
- [7] S. Carpentier-Chouchana, T. Hirai, F. Escourbiac, a. Durocher, a. Fedosov, L. Ferrand, M. Firdaouss, M. Kocan, a. S. Kukushkin, T. Jokinen, V. Komarov, M. Lehnens, M. Merola, R. Mitteau, R. a. Pitts, P. C. Stangeby, and M. Sugihara. *Status of the ITER full-tungsten divertor shaping and heat load distribution analysis*. Physica Scripta, T159(T159):014002, 2014.
- [8] R. A. Pitts, S. Carpentier, F. Escourbiac, T. Hirai, V. Komarov, S. Lisgo, A. S. Kukushkin, A. Loarte, M. Merola, A. Sashala Naik, R. Mitteau, M. Sugihara, B. Bazylev, and P. C. Stangeby. *A full tungsten divertor for ITER: Physics issues and design status*. Journal of Nuclear Materials, 438(SUPPL):S48–S56, 2013.
- [9] J. Roth, E. Tsitrone, T. Loarer, V. Philipps, S. Brezinsek, A. Loarte, G. F. Counsell, R. P. Doerner, K. Schmid, O. V. Ogorodnikova, and R. a. Causey. *Tritium inventory in ITER plasma-facing materials and tritium removal procedures*. Plasma Physics and Controlled Fusion, 50(10):103001, 2008.
- [10] R. E. H. Clark and D. Reiter. *Nuclear fusion research: understanding plasma-surface interactions*, volume 78. Springer, 2005.

- [11] Y. Zayachuk. *Deuterium Retention in Tungsten and Tungsten-Tantalum Alloys under High Flux Plasma Exposure ('Deuteriumretentie in wolfraam en wolfraam-tantaallegeringen onder blootstelling aan een hoge plasmaflux')*. Thesis, 2013.
- [12] Y. Zayachuk, M. 't Hoen, P. Zeijlmans van Emmichoven, I. Uytdehouwen, and G. van Oost. *Deuterium retention in tungsten and tungsten–tantalum alloys exposed to high-flux deuterium plasmas*. Nuclear Fusion, 52(10):103021, 2012.
- [13] L. Buzi, G. De Temmerman, B. Unterberg, M. Reinhart, T. Dittmar, D. Matveev, C. Linsmeier, U. Breuer, A. Kreter, and G. Van Oost. *Influence of tungsten microstructure and ion flux on deuterium plasma-induced surface modifications and deuterium retention*. Journal of Nuclear Materials, 463(1–3):320–324, 2015.
- [14] R. LeSar. *Introduction to computational materials science: fundamentals to applications*. Cambridge University Press, 2013.
- [15] K. Heinola, T. Ahlgren, K. Nordlund, and J. Keinonen. *Hydrogen interaction with point defects in tungsten*. Physical Review B - Condensed Matter and Materials Physics, 82(9):94102, 2010.
- [16] P. Grigorev, D. Terentyev, G. Bonny, E. E. Zhurkin, G. Van Oost, and J. M. Noterdaeme. *Interaction of hydrogen with dislocations in tungsten: An atomistic study*. Journal of Nuclear Materials, 465:364–372, oct 2015.
- [17] M. Li, E. Werner, and J. H. You. *Fracture mechanical analysis of tungsten armor failure of a water-cooled divertor target*. Fusion Engineering and Design, 89(11):2716–2725, 2014.

2

Hydrogen in tungsten as plasma facing material

This chapter gives an overview about the behavior of H in W as a plasma facing material. Prior to considering fusion relevant experiments, a review of basic properties of H in tungsten such as diffusivity, solubility and trapping properties obtained by both experimental and simulations techniques is given. This is followed by a short overview of effects of fusion relevant plasma exposure on tungsten and description of experimental techniques typically used to study the phenomenon of concern. Finally, a summary of different modelling techniques conventionally applied to interpret experimental data is presented.

2.1. Hydrogen in bulk tungsten

Before consideration of the mechanisms of hydrogen retention in tungsten, it is important to understand the basic properties of H in the material. Figure 2.1 shows schematic energy diagram of H in W. The uptake of H in W is endothermal process meaning that there is an energy barrier for the absorption. Molecular H must dissociate prior being adsorbed by the surface. After that, atomic H on the surface has to overcome the barrier from surface to bulk (S-B) ΔE_{S-B} in order to enter the lattice. At the same time, there is an alternative for recombination with another adsorbed H atom by overcoming the energy barrier ΔE_{Rec} to form H₂ molecule and leave the surface. Diffusion of H in W lattice is thermally activated

and is characterized by the energy barrier ΔE_D . H can also be trapped by different defects in the bulk material characterized by the energy barrier ΔE_{Trap} . The values of these barriers define the behavior of H in the material.

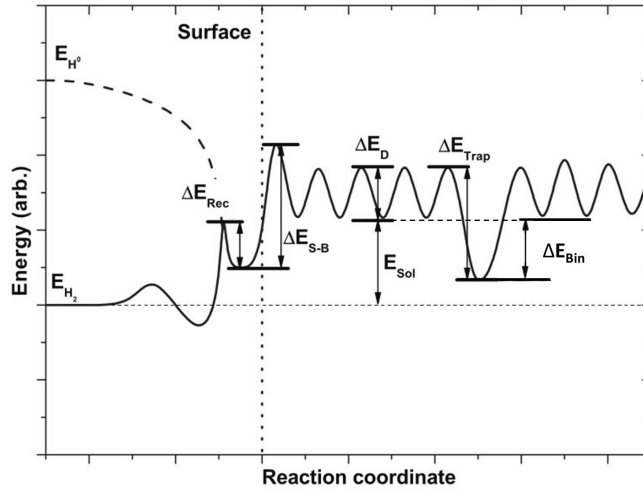


Figure 2.1: Schematic energy diagram for H in W. ΔE_{S-B} is the energy barrier for moving of H from the surface to the bulk, ΔE_{Rec} is the recombination barrier for two H atoms adsorbed at the surface to form H_2 molecule and leave the surface, ΔE_D is the diffusion barrier for H in the bulk, ΔE_{Bin} is the binding energy of a H atom to a defect in the material, ΔE_{Trap} is the trapping energy of H to a defect $\Delta E_{Trap} = \Delta E_{Bin} + \Delta E_D$

The status of the data for these parameters was reviewed by Causey and Venhaus [1] and more recently in works of Roth and Schmid [2] and Tanabe [3]. Several papers report H diffusion coefficient in tungsten obtained by means of Gas Driven Permeation (GDP) [4–8], Plasma Driven Permeation (PDP) [7, 8] and Ion Driven Penetration (IDP) [9, 10] techniques. However there is a large discrepancy in the data as shown in figure 2.2 adapted from [3]. The data points obtained at low temperatures are influenced by both surface and trapping effects. The Frauenfelder's data obtained at elevated temperatures is usually considered as the most reliable [2, 3]. The Arrhenius fit to the data gives the following expression for H diffusion coefficient in W:

$$D = (3.8 \pm 0.4) \times 10^{-7} \times \exp\left(-\frac{(0.39 \pm 0.02)}{kT}\right) \quad (2.1)$$

Moreover the data for lower temperatures recently obtained by Tritium Tracer Technique (TTT) [7, 8] is in agreement with extrapolation of the Frauenfelder's data. A number of first principles studies reported a significantly lower value of

the diffusion barrier ΔE_D of 0.2 eV [11, 12] while in [13] a value of 0.4 eV was declared. A recent summary of modelling activities on H in tungsten [14] reported that the reason for these discrepancies is not known, however speculation about possible influence of slight difference in methods of reaction coordinate detection was made. The discrepancy between experimental and computational results was related to the effect of trapping on defects in the experiments especially at lower temperatures. In addition, in [12, 15] it was demonstrated that removing two lower temperature points out of ten point Frauenfelder's dataset from the Arrhenius fitting gives the value of the migration barrier of 0.25 eV. Thus the authors suggested using the barrier of 0.25 eV instead of 0.39 eV. In this thesis, both values were tested and it was found out that in the temperature range of interest, both values give similar results. In order to be able to compare the simulation results with other continuum scale models where Frauenfelder's values are more commonly used, the equation 2.1 was used.

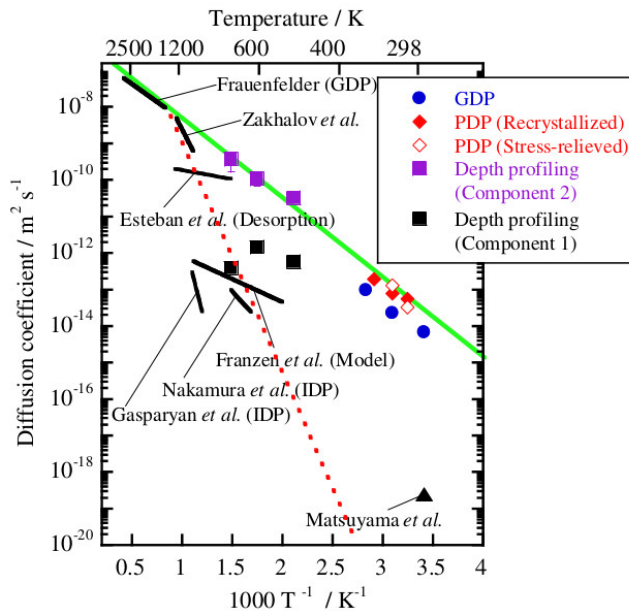


Figure 2.2: Comparison of values of H diffusion coefficient obtained by means of Gas Driven Permeation (GDP) [4–8], Plasma Driven Permeation (PDP) [7, 8] and Ion Driven Penetration (IDP) [9, 10] techniques.

Another important parameter that should be considered is surface recombination rates. Causey [1] and more recently Tanabe [3] reported that there is very limited amount of reliable data for this parameter predicting very low value of the recombination energy barrier (fast recombination). In addition, recombina-

tion rates may be strongly affected by the impurities on the surface. Nevertheless Roth [2] stated that at fusion relevant exposure conditions recombination happens instantaneously and assumption of the boundary condition on the surface $C_S = 0$ will not underestimate the retention. It is possible to conclude that at a fusion relevant temperature range H diffuses very fast with low solubility and instantaneous surface recombination. Therefore, retention of H in W must be significantly influenced by trapping on the defects in the material.

2.2. Interaction of hydrogen with defects in tungsten

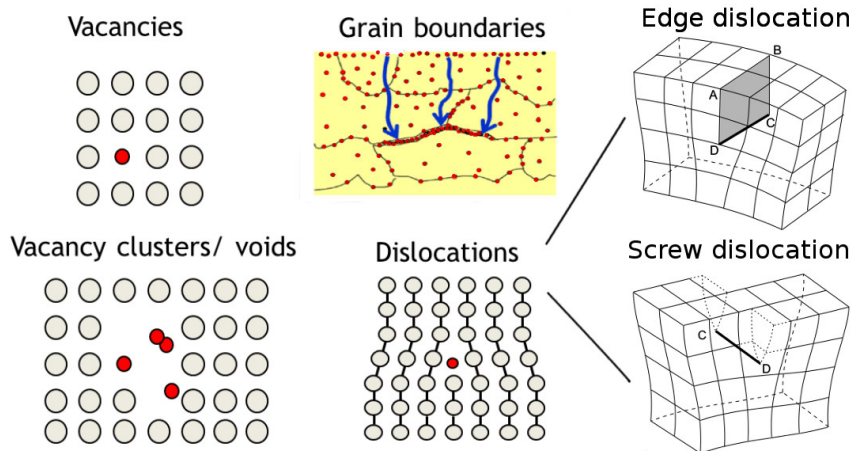
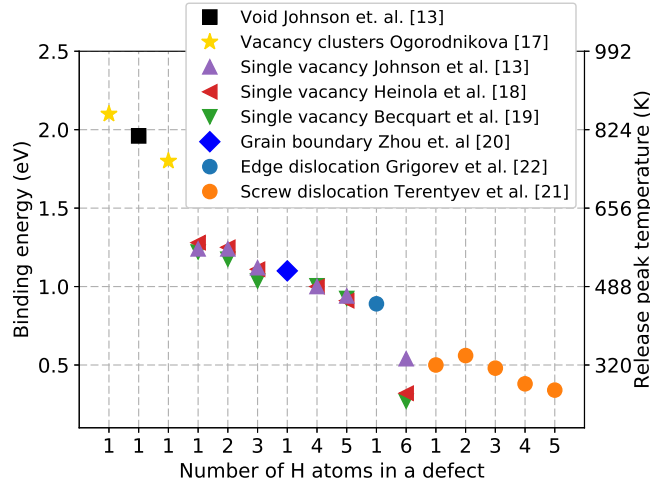


Figure 2.3: Schematic representation of the defects in tungsten with strong trapping properties: vacancies and their clusters, voids, dislocation and grain boundaries. Red circles represent trapped H atoms and grey circles represent W lattice atoms. Schematic pictures of positive edge dislocation formed by inserting an extra half plane of atoms ABCD and right-handed screw dislocation formed by displacing faces ABCD in perfect crystal relative to each other in direction BA from [16]. Black lines represent bonds between atoms.

As was mentioned before, H can be immobilized by various defects in the material. These defects can be intrinsic, i.e. naturally present in the material or extrinsic, i.e. introduced by interaction of energetic particles with the material. Point defects (interstitial and vacancies), their clusters, voids and dislocation loops work as trapping sites for solute H in the bulk. However open volume defects such as vacancies, vacancy clusters and voids provide the strongest trapping and can trap multiple H atoms. Grain boundaries and dislocations can act either as trapping sites or enhanced diffusion paths for H. The most important defects in terms of

H trapping are schematically presented in figure 2.3. Due to the importance of dislocations for the model of H retention in tungsten developed in the thesis, a schematic picture explaining the core structure of a screw and edge dislocation is also shown in figure 2.3.



*Figure 2.4: Incremental hydrogen binding energy with defects in tungsten. Values for vacancy clusters obtained with empirical model in [17] are shown as yellow stars. Black square represents the value for voids obtained with *ab initio* in [13]. *Ab initio* values for vacancies from [13, 18, 19] are shown with triangles, values for grain boundaries [20] are represented with blue diamond and dislocations [21, 22] are represented with circles. The right hand side Y axis shows the estimation of temperature of release peaks during thermal desorption measurements corresponding to binding energy reported on the left hand side Y axis.*

Trapping of H in W has been extensively studied by atomistic simulations, a thorough review of recent modelling activities can be found in [14]. The values of incremental binding energy for different defects in tungsten are summarized in figure 2.4 where the data on the X axis is arranged from left to right going from the strongest to weakest trapping. Number on X axis represents the number of H atoms trapped at a certain defect. The mechanism of H trapping at large vacancy clusters and voids is similar to chemisorption on a surface giving 2.0 eV as a value of binding energy as was first predicted by *ab initio* calculations in [13] and later confirmed by semi-empirical "adsorption model" in [17]. Thus vacancy clusters (yellow stars) and voids (black square) are the strongest H traps in tungsten and are shown on the left part of the graph in figure 2.4. *Ab initio* calculations for H interaction with single vacancy predict multiple trapping of up to 6 H atoms with a binding energy in a range of 1.24 – 0.5 eV [13, 18, 19] shown with triangles in

figure 2.4. A value of binding energy of 1.1 eV for Grain Boundaries (GB) was calculated in [20] where the interaction of H with $[100]\{013\}\Sigma 5$ symmetric tilt GB was studied by means of DFT calculations (data is shown with blue diamonds). At the same time, edge and screw dislocations exhibit weakest trapping with the binding energy in a range of 0.45 – 0.9 eV [21, 22], shown by circles. As can be seen from the figure 2.4, there is a large number of possible H trapping sites in W giving a wide range of possible binding energies.

2.3. Experimental studies of hydrogen retention in tungsten

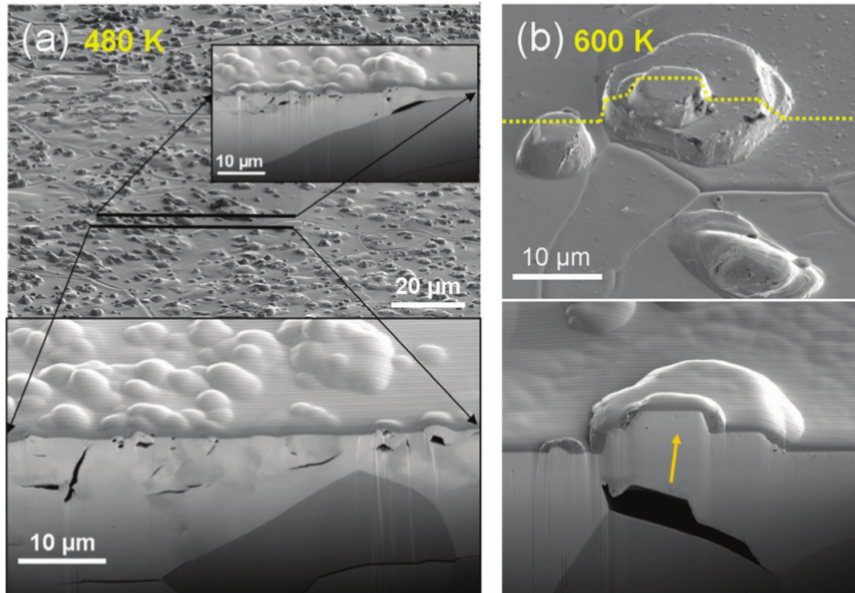


Figure 2.5: Surface and sub-surface modifications of W after irradiation up to fluence of 10^{27} D/m^2 and flux of $10^{22} \text{ 1/m}^2 \text{s}$ at 480 K (a) and 600 K (a) [23]. The arrow (b) indicates the direction of material transport from the cavity to the surface structure.

The effect of plasma exposure on W has been extensively studied [24–32]. During high flux plasma exposure H concentration can easily exceed solubility limits in the subsurface area. Plastic deformation of W matrix caused by H supersaturation is assumed to result in H bubble and void formation. For experiments at low fluxes direct observation of the bubbles was not possible, however, at higher fluxes ($10^{22} \text{ 1/m}^2 \text{s}$) and fluence (10^{27} 1/m^2) surface and subsurface structures can

be resolved. Observed surface morphology showing blister like structures varies with flux and exposure temperature and depends on grain orientation. Figure 2.5 shows an example of Scanning Electron Microscopy (SEM) images combined with sputter cross sectioning by Focused Ion Beam (FIB) from [23]. It can be seen that at 480 K small cracks within the grain are observed with a length of few μm while at 600 K large cavity on the grain boundary corresponding to a large surface blister is formed.

To summarize the visual observation available in literature [24–27, 30], blister formation domain and size distribution depending on exposure flux and temperature from [29] is shown in figure 2.6. In all considered cases, the total fluence was in order of $\sim 10^{26} \text{ J/m}^2$ while the exposure temperature varied in range 350–870 K and ion energy varied from 30 to 70 eV. The number next to the symbols shows the blister size in μm . The graph is split in two regions of blister size distribution: blue squared region represents exposures performed at low fluxes and temperatures where a significant variation of blister diameters was observed. No blisters were observed at temperatures higher than 700 K [2] for low flux exposures, however for high fluxes blisters were observed at higher temperatures. These findings demonstrate the strong variation (and even principal observation) of W surface blistering depending on the exposure temperature and flux.

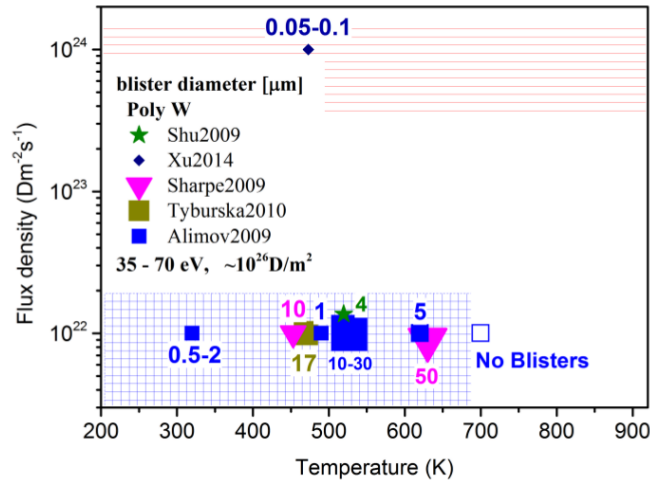
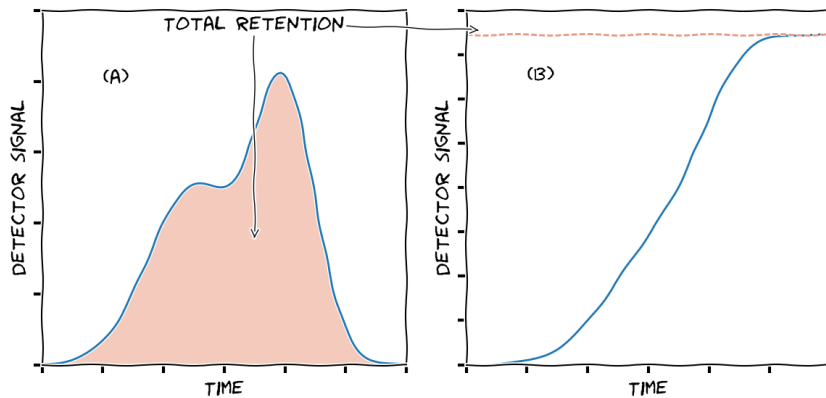


Figure 2.6: Blister formation domain in terms of exposure temperature and flux as obtained in [24–27, 30]. The number next to the symbols show the blister size in μm .

However systematic studies are scarce and large scattering of the data is usually attributed to different material preparation procedures, material microstructure and impurity levels in different studies [29]. A number of mechanisms of bubble

growth were proposed in [3, 33] including shift of the whole grains due to the H accumulation on the grain boundaries or punching out interstitial loops by pressurized bubble (loop punching mechanism). However all of these mechanisms assume localized H pressure build up in the material. Given the high H diffusivity at exposure temperatures, the mechanism implying accumulation of H into clusters growing to bubbles with the high localized pressure is not clear.

Two main experimental techniques used to study H retention in tungsten are Thermal Desorption Spectroscopy (TDS) and depth profiling by Nuclear Reaction Analysis (NRA). During TDS measurement an exposed sample is heated linearly and the released gas is detected by a mass-spectrometer giving a desorption spectrum. There are two possible regimes of TDS measurements schematically shown in figure 2.7: when the gas is pumped out of the chamber during the measurement giving the instantaneous release (a) and when the cumulative H release is detected (b). The first regime is reported more often where the integral over the spectra gives the information about the total amount of retained H and the peaks on the spectra can be interpreted as the release of H from different trapping sites in the material. NRA allows one to obtain depth profile of retained H up to depth of 10 μm and give the information about the total amount of retained H in the sample.



*Figure 2.7: Schematic representations of the results of TDS measurements in two regimes
(a) the released gas is extracted from the chamber during the measurement giving instantiations H release and (b) released gas is not extracted during the measurement giving the cumulative H release from the sample.*

The graph of the total retention as measured by NRA and TDS in [27] with its dependence on the exposure temperature is presented in figure 2.8. As can be seen from the picture, there is a significant difference in total retention measured by TDS and NRA marked by the red arrows. Thus it can be concluded that a

significant amount of retained H is located deeper than $\sim 10 \mu\text{m}$ i.e. beyond the NRA resolution. Another important trend is a significant decrease of H retention with an increase of exposure temperature starting from 700 K. Together with the absence of blisters at temperatures above 700 K (see figure 2.6), it is a strong indication of the influence of increased H diffusivity together with increased H detrapping from defects on H retention and H bubble formation.

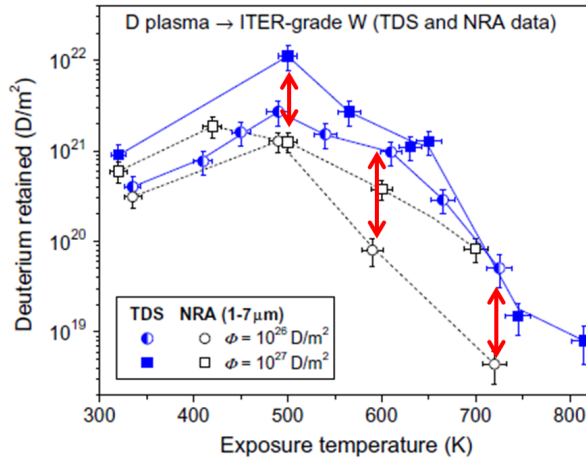


Figure 2.8: Total retention of H in tungsten as measured by NRA and TDS techniques [27]. Red arrows indicate the discrepancy between values obtained by NRA and TDS.

As has been recently summarized by Tanabe [3], H depth profiles under high flux exposures typically consist of three components, namely: (1) top-most layer: several nanometers; (2) saturated sub-surface layer: several micrometers and (3) bulk: from several micrometers to millimeters depths, basically across the whole sample. Due to small thickness of the top-most layer, the fraction of trapped H is usually rather low as compared to the total retention. Therefore upon high flux/fluence and high temperature exposures, the retention is defined by the partition of H trapped at plasma-induced microstructural defects (e.g. cavities, bubbles), established in the saturated sub-surface layer and in the bulk. The bulk retention, in turn, is defined by the initial microstructure of the material and by the H flux coming through the subsurface layer.

2.4. Modelling and interpretation of the experiments

TDS measurements are used to obtain information the total amount of retained H in the sample but also about the trapping sites in the material since one can at-

tribute the release stage in TDS profile to certain trapping energies. However, the number of the peaks, their positions and intensities in a TDS spectrum is a result of an interplay of detrapping, diffusion with possible re-trapping and surface desorption. Hence, the assignment of the peak to a certain trap can be rarely done based solely on the knowledge of the dominant process.

Detrapping of H is a thermally activated process and is usually described by an Arrhenius type equation:

$$R^- = C_H \nu \exp \left(-\frac{\Delta E_{Trap}}{kT} \right) \quad (2.2)$$

where C_H is concentration of trapped H, ν is an attempt frequency usually assumed to be equal to Debye frequency ($10^{13}/\text{s}$), k is the Boltzmann constant, T is temperature and ΔE_{Trap} is trapping energy. Trapping energy ΔE_{Trap} is usually calculated as a sum of binding energy ΔE_{Bin} and H migration barrier ΔE_D as can be seen from the H energy diagram presented in figure 2.1. The easiest estimation of the release of H from a trap during TDS can be done by integrating the equation $\frac{\partial C_H}{\partial t} = -R^-$ with a proper heating rate where R^- is defined by equation 2.2. This method was used to estimate release peak temperatures for different defects presented in figure 2.4 on right hand side Y axis. However this approach does not take into account diffusion and re-trapping and cannot be used for the interpretation of TDS profiles especially for low temperature release stages.

In order to take into account diffusion and trapping process, H behaviour during plasma exposure and TDS measurements should be described by a set of 1-D rate equations following classical reaction-diffusion approach [34]. The evolution of solute H in the bulk is described by:

$$\frac{\partial C_H^b}{\partial t} = \frac{\partial}{\partial x} \left(D_H \frac{\partial C_H^b}{\partial x} \right) + S_H^b + \sum_{i=1}^N R_i^- - \sum_{i=1}^N R_i^+ \quad (2.3)$$

The first term on the right hand part of the equation describes the diffusion of mobile hydrogen in the bulk, C_H^b is the concentration of mobile H in the bulk and D_H is the diffusion coefficient usually described by equation 2.1. S_H^b is the source term describing the increase of H concentration in the bulk due to the implantation. Implantation profiles obtained by binary collision approximation codes such as SDTrimSP [35] can be used to determine S_H^b . Term $\sum_{i=1}^N R_i^-$ describes the release of H from traps. The summation is done over N type of traps in the material. H release rate R_i^- for a certain is defined by equation 2.2. Term $\sum_{i=1}^N R_i^+$ describes trapping of mobile hydrogen on defects in the material. Trapping rate R_i^+ for a certain trap is defined by $R_i^+ = k_i^2 C_H^b D_H^b$, where k^2 is so called sink strength used to describe the tendency of a reaction to occur. With units of [m^{-2}] sink strength reflects the strength or affinity of the defect to capture mobile H [34].

Physically means mean distance that mobile H travels before becoming trapped by the defect of type i .

One of the most widely used implementation of reaction-diffusion model is a computational tool called Tritium Migration Analysis Program (TMAP7) [36]. Schematic representation of TMAP7 model of the material containing H is shown in figure 2.9. TMAP7 features three different traps and up to ten diffusing elements, which are reduced to three H isotopes for fusion applications. The main difficulty of modelling H implantation is related to the fact that the spatial distributions of trapping sites should be defined prior simulations and is fixed during simulation. At the same time, even at incident energies lower than displacement damage threshold, plasma exposure leads to creation of defects with subsequent H bubble formation. These effects imply dynamic creation of defects in the material during plasma exposure and these kind of phenomenon cannot be modelled by TMAP7. Similar reaction-diffusion model is implemented in a Coupled Reaction Diffusion System Code (CRDS) [37] which has a potential for taking into account the dynamics of defect formation, their migration and evolution [29]. Another implementation of reaction-diffusion model is a computational code created by Dr. Tommy Ahglren [38] which features a dynamic vacancy creation by displacement damage together with their migration and clustering. The code was successfully used to interpret the results of ion beam experiments with energies 5 – 30 keV. However, the mechanism of defect creation by displacement damage is not applicable for fusion relevant plasma exposure where the ion energy is by far too low (~ 50 eV vs 1 keV) for creation of displacement damage.

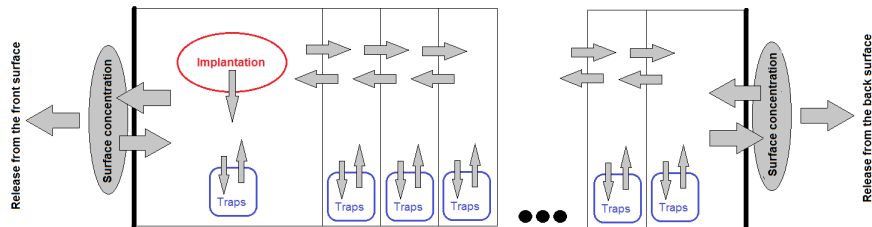


Figure 2.9: Schematic representation of TMAP7 model of a material containing H from [36]

Computational assessment of H retention by reaction-diffusion codes like TMAP7 [36, 38, 39] allows one to fit the TDS spectra by assigning three trapping site energies of 0.45 eV, 1.05 eV and 1.44 eV to dislocations, vacancies and pores, respectively [39–41], however the amount of traps used in these models is limited. A thorough theoretical study highlighting how characteristic temperatures of TDS spectra depend on hydrogen retention parameters, such as trap concentration depth distribution or activation energy of detrapping processes was reported in [42]. Fol-

lowing *ab initio* studies [18, 43], trapping of multiple H atoms in one vacancy is possible and the binding energy of subsequent H atoms decreases from 1.28 eV for one trapped atom down to 0.32 eV for six atoms. In order to utilize these results, a number of works aiming on extension of the reaction diffusion models for higher amount of traps treating a vacancy filled with different number of trapped H atoms as a separate traps were done in [17, 44–46], as well as an introduction of traps with continuum binding energy distribution [17, 47, 48]. Using the multiple trap model with an NRA profile as trap concentration depth distribution allowed accurate fit of TDS spectra at different fluencies in [44] with a possible attribution of the traps to vacancies located near material surface. Special attention to the role of voids and blisters in the molecular H release during TDS and was drawn in [49]. However the mechanism of the formation of such voids remains unclear.

2.5. Conclusion

From the above listed experimental data and current status of computational tools describing H trapping and release, it is possible to conclude that H retention in tungsten under high flux fusion relevant exposure conditions is a complex physical phenomenon. Despite many studies available in literature, the experimental data have significant scattering and there is a lack of complete understanding of the basic physical mechanisms governing H retention under high flux exposure conditions. On top of that, conventional modelling tools used to interpret the experiments, where strong modification of the surface microstructure takes place upon exposure, do not provide an adequate physical insight into the problem. Hence, there is a need for alternative models employing physically-justified mechanisms explaining sub-surface trapping of fast diffusing hydrogen and formation of H clusters despite inability of self-trapping (opposite to He). Demonstration of the relevance of the newly discovered mechanisms requires their implementation into the full scale computational methods and their application to simulate the H retention and release by taking currently available well established set of experimental data. In the next chapter a new model of hydrogen retention in tungsten based on the hypotheses of H trapping and bubble formation on dislocations is proposed.

References

- [1] R. A. Causey and T. J. Venhaus. *The use of tungsten in fusion reactors: a review of the hydrogen retention and migration properties.* Physica Scripta, 2001(T94):9, 2001.
- [2] J. Roth and K. Schmid. *Hydrogen in tungsten as plasma-facing material.* Physica Scripta, 2011(T145):014031, 2011.
- [3] T. Tanabe. *Review of hydrogen retention in tungsten.* Physica Scripta, 2014(T159):014044, 2014.
- [4] R. Frauenfelder. *Solution and Diffusion of Hydrogen in Tungsten.* Journal of Vacuum Science & Technology, 6(3):388–397, 1969.
- [5] A. P. Zakharov, V. M. Sharapov, and A. A. Babad-Zakhryapin. *Permeation of hydrogen through molybdenum and tungsten at elevated temperatures.* In International Congress on Hydrogen in Metals. Vols. 1 and 2, pages 217–221. Moscow Inst., 1972.
- [6] G. A. Esteban, A. Perujo, L. A. Sedano, and K. Douglas. *Hydrogen isotope diffusive transport parameters in pure polycrystalline tungsten.* Journal of Nuclear Materials, 295(1):49–56, 2001.
- [7] T. Ikeda, T. Otsuka, and T. Tanabe. *Application of tritium tracer technique to determination of hydrogen diffusion coefficients and permeation rate near room temperature for tungsten.* Fusion Science and Technology, 60(4):1463–1466, 2011.
- [8] T. Otsuka, M. Shimada, R. Kolasinski, P. Calderoni, J. P. Sharpe, Y. Ueda, Y. Hatano, and T. Tanabe. *Application of tritium imaging plate technique to examine tritium behaviors on the surface and in the bulk of plasma-exposed materials.* Journal of Nuclear Materials, 415(1, Supplement):S769–S772, 2011.
- [9] Y. M. Gasparyan, A. V. Golubeva, M. Mayer, A. A. Pisarev, and J. Roth. *Ion-driven deuterium permeation through tungsten at high temperatures.* Journal of Nuclear Materials, 390–391:606–609, 2009.
- [10] H. Nakamura, W. Shu, T. Hayashi, and M. Nishi. *Tritium permeation study through tungsten and nickel using pure tritium ion beam.* Journal of Nuclear Materials, 313–316:679–684, 2003.
- [11] Y.-L. Liu, Y. Zhang, G. N. Luo, and G.-H. Lu. *Structure, stability and diffusion of hydrogen in tungsten: A first-principles study.* Journal of Nuclear Materials, 390–391:1032–1034, 2009.

- [12] K. Heinola and T. Ahlgren. *Diffusion of hydrogen in bcc tungsten studied with first principle calculations.* Journal of Applied Physics, 107(11):113531, 2010.
- [13] D. F. Johnson and E. A. Carter. *Hydrogen in tungsten: Absorption, diffusion, vacancy trapping, and decohesion.* Journal of Materials Research, 25(02):315–327, 2010.
- [14] G.-H. Lu, H.-B. Zhou, and C. S. Becquart. *A review of modelling and simulation of hydrogen behaviour in tungsten at different scales.* Nuclear Fusion, 54(8):086001, 2014.
- [15] T. Ahlgren and L. Bokonte. *Concentration dependent hydrogen diffusion in tungsten.* Journal of Nuclear Materials, 479:195–201, 2016.
- [16] D. Hull and D. J. Bacon. *Introduction to dislocations.* Butterworth-Heinemann, 2001.
- [17] O. V. Ogorodnikova. *Fundamental aspects of deuterium retention in tungsten at high flux plasma exposure.* Journal of Applied Physics, 118(7):074902, 2015.
- [18] K. Heinola, T. Ahlgren, K. Nordlund, and J. Keinonen. *Hydrogen interaction with point defects in tungsten.* Physical Review B: Condensed Matter, 82(9):094102, 2010. PRB.
- [19] C. S. Becquart and C. Domain. *A density functional theory assessment of the clustering behaviour of He and H in tungsten.* Journal of Nuclear Materials, 386–388(0):109–111, 2009.
- [20] Z. Hong-Bo, L. Yue-Lin, J. Shuo, Z. Ying, G. N. Luo, and L. Guang-Hong. *Investigating behaviours of hydrogen in a tungsten grain boundary by first principles: from dissolution and diffusion to a trapping mechanism.* Nuclear Fusion, 50(2):025016, 2010.
- [21] D. Terentyev, V. Dubinko, A. Bakaev, Y. Zayachuk, W. V. Renterghem, and P. Grigorev. *Dislocations mediate hydrogen retention in tungsten.* Nuclear Fusion, 54(4):042004, 2014.
- [22] P. Y. Grigorev, D. A. Terentyev, A. V. Bakaev, and E. E. Zhurkin. *Interaction of hydrogen with dislocations and grain boundaries in Tungsten.* Journal of Surface Investigation, 9(6):1287–1292, 2015.
- [23] S. Lindig, M. Balden, V. K. Alimov, T. Yamanishi, W. M. Shu, and J. Roth. *Subsurface morphology changes due to deuterium bombardment of tungsten.* Physica Scripta, 2009(T138):014040, 2009.

- [24] H. Y. Xu, G. N. Luo, H. Schut, Y. Yuan, B. Q. Fu, A. Godfrey, W. Liu, and G. D. Temmerman. *Enhanced modification of tungsten surface by nanoscale formation during high flux deuterium plasma exposure*. Journal of Nuclear Materials, 447(1–3):22–27, 2014.
- [25] J. P. Sharpe, R. D. Kolasinski, M. Shimada, P. Calderoni, and R. A. Causey. *Retention behavior in tungsten and molybdenum exposed to high fluences of deuterium ions in TPE*. Journal of Nuclear Materials, 390–391:709–712, 2009.
- [26] W. M. Shu, G. N. Luo, and T. Yamanishi. *Mechanisms of retention and blistering in near-surface region of tungsten exposed to high flux deuterium plasmas of tens of eV*. Journal of Nuclear Materials, 367–370, Part B:1463–1467, 2007.
- [27] V. K. Alimov, W. M. Shu, J. Roth, K. Sugiyama, S. Lindig, M. Balden, K. Isobe, and T. Yamanishi. *Surface morphology and deuterium retention in tungsten exposed to low-energy, high flux pure and helium-seeded deuterium plasmas*. Physica Scripta, 2009(T138):014048, 2009.
- [28] K. Tokunaga, M. J. Baldwin, R. P. Doerner, N. Noda, Y. Kubota, N. Yoshida, T. Sogabe, T. Kato, and B. Schedler. *Blister formation and deuterium retention on tungsten exposed to low energy and high flux deuterium plasma*. Journal of Nuclear Materials, 337–339:887–891, 2005.
- [29] L. Buzi. *Influence of the Particle Flux on Surface Modifications of Tungsten*. Thesis, Université de Lorraine, 2015.
- [30] B. Tyburska. *Deuterium Retention in Carbon and Self-Implanted Tungsten*. Report, Max-Planck-Institut für Plasmaphysik, 2010.
- [31] Y. Zayachuk, M. H. J. . t. Hoen, P. A. Z. v. Emmichoven, D. Terentyev, I. Uytdenhouwen, and G. v. Oost. *Surface modification of tungsten and tungsten-tantalum alloys exposed to high-flux deuterium plasma and its impact on deuterium retention*. Nuclear Fusion, 53(1):013013, 2013.
- [32] Y. Zayachuk. *Deuterium Retention in Tungsten and Tungsten-Tantalum Alloys under High Flux Plasma Exposure ('Deuteriumretentie in wolfaam en wolfaam-tantaallegeringen onder blootstelling aan een hoge plasmaflux')*. Thesis, Ghent University, 2013.
- [33] J. B. Condon and T. Schober. *Hydrogen bubbles in metals*. Journal of Nuclear Materials, 207:1–24, 1993.
- [34] G. S. Was. *Fundamentals of radiation materials science: metals and alloys*. Springer Verlag, New York, 2007.

- [35] A. Mutzke, R. Schneider, W. Eckstein, and R. Dohmen. *SDTrimSP Version 5.00*. IPP, Report,(12/8), 2011.
- [36] G. R. Longhurst. *TMAP7 User Manual*. Report INEEL/EXT-04-02352; TRN: US0902408 United States10.2172/952013TRN: US0902408Thu Aug 27 07:27:04 EDT 2009INLEnglish, Idaho National Laboratory (INL), 2008.
- [37] M. Oberkofler, M. Reinelt, and C. Linsmeier. *Retention and release mechanisms of deuterium implanted into beryllium*. Nuclear Instruments and Methods in Physics Research Section B: Beam Interactions with Materials and Atoms, 269(11):1266–1270, 2011.
- [38] T. Ahlgren, K. Heinola, K. Vörtler, and J. Keinonen. *Simulation of irradiation induced deuterium trapping in tungsten*. Journal of Nuclear Materials, 427(1–3):152–161, 2012.
- [39] O. V. Ogorodnikova, B. Tyburska, V. K. Alimov, and K. Ertl. *The influence of radiation damage on the plasma-induced deuterium retention in self-implanted tungsten*. Journal of Nuclear Materials, 415(1, Supplement):S661–S666, 2011.
- [40] K. Schmid, V. Rieger, and A. Manhard. *Comparison of hydrogen retention in W and W/Ta alloys*. Journal of Nuclear Materials, 426(1–3):247–253, 2012.
- [41] M. Poon, A. A. Haasz, and J. W. Davis. *Modelling deuterium release during thermal desorption of D+-irradiated tungsten*. Journal of Nuclear Materials, 374(3):390–402, 2008.
- [42] J. Guterl, R. D. Smirnov, and S. I. Krasheninnikov. *Revisited reaction-diffusion model of thermal desorption spectroscopy experiments on hydrogen retention in material*. Journal of Applied Physics, 118(4):043302, 2015.
- [43] N. Fernandez, Y. Ferro, and D. Kato. *Hydrogen diffusion and vacancies formation in tungsten: Density Functional Theory calculations and statistical models*. Acta Materialia, 94:307–318, 2015.
- [44] J. Guterl, R. D. Smirnov, S. I. Krasheninnikov, M. Zibrov, and A. A. Pisarev. *Theoretical analysis of deuterium retention in tungsten plasma-facing components induced by various traps via thermal desorption spectroscopy*. Nuclear Fusion, 55(9):093017, 2015.
- [45] E. A. Hodille, Y. Ferro, N. Fernandez, C. S. Becquart, T. Angot, J. M. Layet, R. Bisson, and C. Grisolia. *Study of hydrogen isotopes behavior in tungsten by a multi trapping macroscopic rate equation model*. Physica Scripta, 2016(T167):014011, 2016.

- [46] K. Schmid, U. von Toussaint, and T. Schwarz-Selinger. *Transport of hydrogen in metals with occupancy dependent trap energies.* Journal of Applied Physics, 116(13):134901, 2014.
- [47] S. I. Krasheninnikov, E. D. Marenkov, R. D. Smirnov, and A. A. Pisarev. *Hydrogen transport in solids with traps in the case of continuum distribution of detrapping energies.* Physica Scripta, 2014(T159):014060, 2014.
- [48] P. Grigorev, L. Buzi, A. Bakaeva, D. Terentyev, G. D. Temmerman, G. V. Oost, and J. M. Noterdaeme. *Numerical analysis of TDS spectra under high and low flux plasma exposure conditions.* Physica Scripta, 2016(T167):014039, 2016.
- [49] R. A. Causey, R. Doerner, H. Fraser, R. D. Kolasinski, J. Smugeresky, K. Umstadter, and R. Williams. *Defects in tungsten responsible for molecular hydrogen isotope retention after exposure to low energy plasmas.* Journal of Nuclear Materials, 390–391:717–720, 2009.

"Thermonuclear fortress is surrounded on all sides by equally tall wall. If for the supporters of a new path it seems to be that from their side the wall is lower, or there is a gap in the wall, it indicates the immaturity of the path."

Igor Golovin (1913 – 1997)

3

New model based on dislocation-mediated H retention

As was already explained in the introduction section, there is a lack of understanding for the mechanisms of H retention and bubble formation (blistering) in tungsten (W) under ITER relevant plasma exposure conditions. However, experimental trends suggest that dislocations may be an important microstructural feature of the material defining the behaviour of H isotopes. H interaction with Screw Dislocations (SD) in W was studied by means of *ab initio* calculations using Density Functional Theory (DFT) in order to test this hypothesis. In this chapter the results of this study are presented and analysed. On the basis of the analysis of the DFT results a so-called "jog-punching" mechanism of H bubble nucleation on dislocations is proposed. A Rate Theory model of H retention in W based on the proposed mechanism is developed. The model is then tested by comparing the trends predicted by the model with experimental results available in the literature.

3.1. DFT study of H interaction with screw dislocation

To assess H-SD interaction the Vienna *Ab initio* Simulation Package (VASP) [1] was used. The projected augmentation wave [2] and the generalized gradient approximation [3] were used for the pseudopotential and the exchange-correlation potential, respectively. The 1s state for H and 5d6s states for W were treated as va-

lence states. The atomic relaxation was carried out using the conjugate-gradient algorithm with the force convergence criterion of $0.03 \text{ eV}/\text{\AA}$. The dislocation dipole approach [4] was applied to model a $\frac{1}{2}\langle 111 \rangle$ SD in a periodic crystal. A principal unit cell consisted of three non-equivalent (111) atomic layers and has dimensions of $41.01 \times 38.82 \times 2.75 \text{ \AA}^3$ in the [11–2] (x), [1–10] (y) and [111] (z) directions, which amounts to 135 W atoms in total. The binding energy (i.e. the difference between total energies of two stable configurations of the system as schematically shown in figure 2.1) of H with dislocation was defined as:

$$\Delta E_{Bin}^{HD} = E_H + E_D - E_{HD} - N_{at}E_{coh} \quad (3.1)$$

where E_{HD} is the total energy of the relaxed system when H is attached to the defect, E_H and E_D are the total energies of the relaxed system (i.e. a vacancy, another interstitial H atom or dislocation) respectively. $N_{at}E_{coh}$ is introduced to respect the particle number balance and to compensate for the difference in number of matrix W atoms present in the configurations corresponding to E_{HD} , E_H and E_D energies. Thus, N_{at} is the number of atoms, E_{coh} is the energy per atom in pure BCC W. In this notation, a positive value of the binding energy corresponds to attraction between defects.

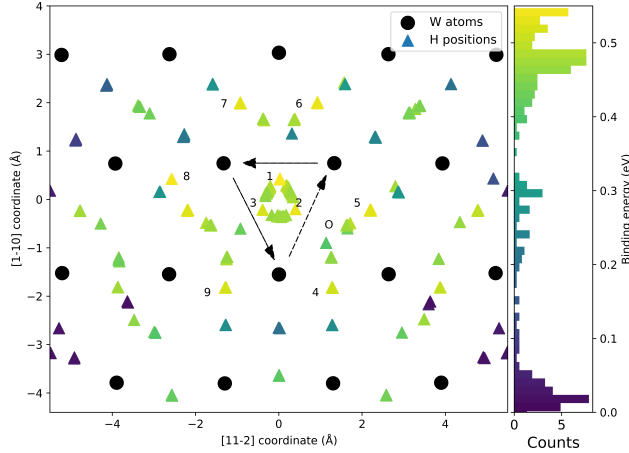


Figure 3.1: H-SD binding energy map. The colour convention presented in a form of a histogram on the right hand side of the figure denotes the binding energy value in eV as well as the binding energy distribution of H positions presented on the map. Filled triangles display all metastable H positions, black circles display W atoms. Three dashed arrows represent displacement of the atoms along $\langle 111 \rangle$ direction indicating the $\frac{1}{2}\langle 111 \rangle$ SD core. Positions with the highest values of binding energy are numbered from 1 to 9 in the figure.

The binding energy map shown in figure 3.1 reveals three deep (equivalent) energy minima configurations for H atom inside the core and six particularly favourable (and again equivalent) positions adjacent to the core, numbered 1 to 9 in the figure. An H atom occupying these positions is bound to the core with the energy of ~ 0.55 eV as compared to a reference H tetrahedral interstitial position in the bulk W. Analysis of the charge distribution reveals that these positions coincide with the regions depleted of charge density.

3.2. Migration barrier along the SD core for H attached to the dislocation

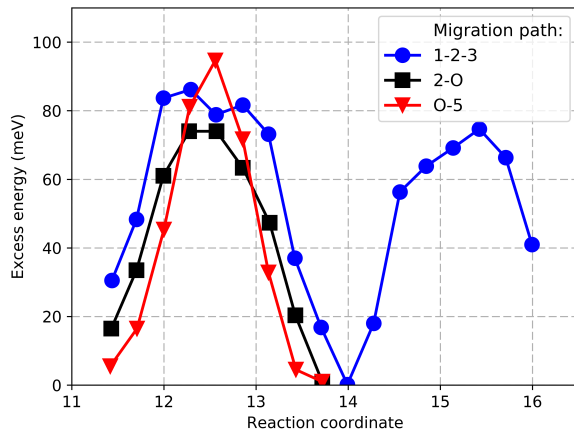


Figure 3.2: Migration energy paths between the metastable positions indicated in figure 3.1. The legend denotes the path between positions in the notation used in figure 3.1.

A possibility of migration of H atom trapped on the SD core by jumping between the positions with strong attraction was explored. Two migration trajectories were studied, namely: 'in-core' and 'out-core' paths taking into account the site preference near the SD core, shown in figure 3.1. The 'in-core' migration mode involves jumps between positions '1-2-3'. The 'out-core' migration from the inner to outer part of the core requires a jump from '2' to 'O' positions (a group of positions also seen as a peak in binding energy distribution histogram near 0.47 eV in figure 3.1) and from 'O' to '5'. By performing a sequence of 'O-5-O' jumps H atom may migrate along the dislocation line adjacent to its core. According to the estimations, shown in figure 3.2, the migration barrier does not exceed 0.1 eV,

proving a possibility for fast 1-D migration of H along the SD line at room temperature and above. In addition, H can occupy any of the nine trapping positions (see figure 3.1), as the transition barriers are also extremely low.

3.3. Interaction of H_N clusters with screw dislocation studied by DFT

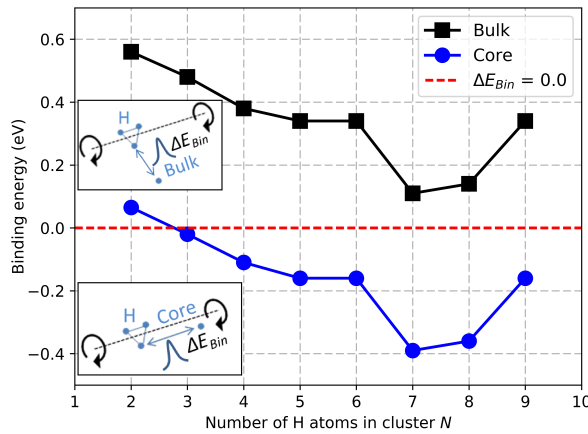


Figure 3.3: Incremental binding energy of H to H_{N-1} cluster attached to the dislocation core. Reference states were taken to be either an H atom in a tetrahedral position in the bulk ('Bulk'), or an H atom attached to the dislocation core ('Core').

It is important to investigate the behaviour of H_N clusters attached to the dislocation core in order to understand the mechanism of H accumulation on SD. Therefore the binding energy and site preference for multiple H_N clusters when forming on a SD line was explored. It was found out that cluster of nine H atoms on the dislocation core exhibits a local minima i.e. forming a (111) platelet (henceforth denoted H_N -SD cluster). For each relaxed H_N -SD configuration, the incremental binding energy for a H atom to a H_{N-1} cluster on the SD core, taking the case of a tetrahedral H in bulk W as reference state, was computed. The results are presented in figure 3.3. A progressive removal of the electron density depleted zone begins once the size of H cluster added to the core is $N > 3$. The most energetically favourable sequence to add H atoms can be appreciated in figure 3.1. It is more favourable to continue growing the cluster along the dislocation line starting from the seventh H atom (i.e. place H in the next in-core position) rather than to build a (111) platelet.

Due to the low migration energy for H between the attraction sites along the SD core, it is interesting to consider the stability of H_N clusters on the SD core taking an H atom attached to the SD core as a reference state. The resulting binding energy is shown with blue circles noted as 'Core' in the figure 3.3, together with schematic explanation of the considered processes. It can be seen that starting from three H atoms, the binding energy becomes negative, meaning a repulsive interaction. This means that on a perfect dislocation line, the accumulation of H clusters into a compact 3-D structure is not a favourable process, and H atoms would prefer to form chains attached to the dislocation core. (Note that H chains also remain trapped by the dislocation). Therefore the formation and growth of compact larger H_N clusters requires the presence of nucleation sites, such as jogs or dislocation intersections, in which H atoms become immobilized.

3.4. Jog-punching bubble formation mechanism

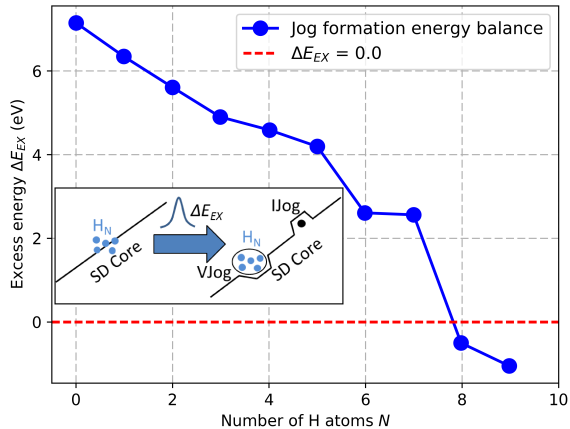


Figure 3.4: Excess energy needed for jog-punching mechanism to occur on a screw dislocation core in the presence of a H_N cluster, depending on the cluster size.

An analysis of the atomic configuration of H_N clusters at SD core after relaxation showed that after adding the 8th H atom a considerable reconstruction of the H_N -D cluster, accompanied by a shift of the W atoms, occurs. This effect was attributed to the formation of a pair of jogs, namely: a vacancy jog (VJog) occupied by H_N cluster and an interstitial jog (IJog) pushed aside. This process is analogous to the interstitial punching mechanism in the case of He self-trapping in bulk Fe [5]. To validate this hypothesis, the energy excess of the process (ΔE_{EX}) was

computed as:

$$\Delta E_{EX} = [E_{HN-SD} + E_{SD}] - [E_{HN-VJog} + E_{IJog}] \quad (3.2)$$

here, E_{SD} and E_{HN-SD} are the total energies of the crystals containing, respectively, SD dipole and H_N cluster attached to SD core, while, $E_{HN-VJog}$ and E_{IJog} are the energy of crystals with H_N cluster attached to a vacancy jog and SD dipole containing an interstitial jog. The process is schematically shown in figure 3.4. A positive value of implies that the jog-punching is not favourable, while a negative value points to an exothermic reaction expected to occur spontaneously.

The vacancy (VJog) and interstitial jogs (IJog) were constructed, respectively, by removing and adding one W atom from/to the core of the SD. The formation energies for IJog and VJog were computed to be 7.2 eV and 2.23 eV, respectively. Their sum (9.43 eV) is 3.8 eV lower than the Frenkel pair formation energy in W bulk (13.23 eV) which is the sum of formation energy for a vacancy (3.5 eV) and a self-interstitial atom (9.73), computed in a 128 atomic supercell. As the creation of a pair of anti-jogs requires less energy than the Frenkel pair formation, a threshold for jog-punching on SD core may occur for a relatively low number of H atoms (H_N) still affordable for DFT techniques. ΔE_{EX} as a function of H_N is shown in figure 3.4, which proves that the spontaneous jog-punching occurs once $N = 8$.

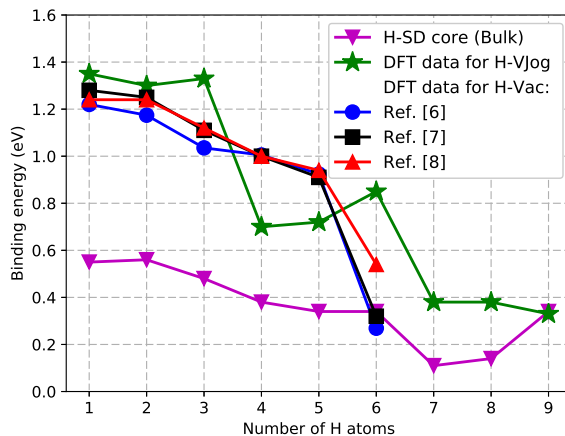


Figure 3.5: Incremental binding energy of H to a screw dislocation core (magenta triangles), vacancy jog at dislocation (green stars) and vacancy in bulk tungsten from literature (blue circles [6], black squares [7] and red triangles [8]).

In addition, the incremental binding energy of H to a H_N cluster in a vacancy jog was calculated. The comparison of the incremental binding energy of H atom

to VJog with incremental binding energy of H to vacancy from literature [6–8] is shown in figure 3.5. As can be seen from the graph, the trapping of H atom for a pre-existing jog is much stronger than for a undisturbed dislocation and is comparable to the binding energy for a single vacancy. Therefore, jogs on dislocation lines, formed due to e.g. cyclic deformation under transient heat loads, or via jog-punching mechanism during plasma exposure, will act as additional trapping sites for hydrogen and its isotopes.

3.5. Model for describing H plasma exposure

The experiments from [9, 10] were considered as a set of studies performed with ITER relevant plasma exposure conditions. In these experiments, the W samples were exposed to plasma with a flux 10^{24} H/m²s, the pulse duration was 70 s, and the sample surface temperature was maintained at 460 K. In these experiments, the average ion energy coming from the plasma was about 50 eV. Particles with this energy have an implantation depth (R) of several nm in W [11]. After implantation, the particles start to diffuse deep into the material as well as towards the surface of the material. At a certain point, the diffusion flux out of the material will counterbalance the particle flux coming from plasma thereby establishing a steady state (see schematic image in figure 3.6). This condition can be expressed as:

$$F = D \frac{\partial C}{\partial x} \quad (3.3)$$

where F is the plasma flux on the surface, D is diffusion coefficient and C is the H concentration at a depth x . It is assumed that all the implanted atoms are thermalized after they reach the implantation range R . Thus, the diffusion flux of H from the material is determined by the value of H concentration at implantation depth C_R . Approximating the derivative in equation 3.3 by finite differences, we write:

$$F = D \frac{(C_S - C_R)}{R} \quad (3.4)$$

Common assumption is that as soon as H atoms reach the surface, they immediately form H₂ molecule and leave the surface, i.e. the process of desorption is not limited by surface recombination. The surface concentration is therefore assumed to be $C_S = 0$. We thus write:

$$C_R = \frac{FR}{D} \quad (3.5)$$

Time evolution of H concentration in the material for the case of H diffusion, given the sink strength k^2 associated to traps, writes (see Ref. [12]):

$$\frac{\partial C_H}{\partial t} = D \frac{\partial^2 C_H}{\partial x^2} - k^2 D C_H \quad (3.6)$$

Here, C_H is the distribution of the hydrogen concentration over depth x . Regarding the previous discussion, based on DFT calculations predicting the importance of dislocations for the bubble formation mechanism, dislocations were considered as uniformly distributed traps. In this case the sink strength is $k^2 = \rho$ [12], where ρ is the dislocation density. Because the particle implantation range is of the order of a few nm and the typical depth at which H is detected after plasma exposure is of the order of a few μm , the boundary condition for the solution of equation 3.6 was taken as $C(0) = C_R = \frac{F_R}{D}$. For the second boundary condition, $C(\infty) = 0$ was taken. For the steady state solution, i.e. times long enough to ensure H atoms reach depth x , $\frac{\partial C}{\partial t} = 0$ was taken. Given the duration of plasma exposure (70 s), H migration energy (0.4 eV) and sample temperature (460 K), a steady-state profile is established after H atoms diffuse through the region of interest (H covers 10 μm per second). The assumption of $\frac{\partial C}{\partial t} = 0$ is thus appropriate. Taking all elements mentioned above into account, the solution of equation 3.6 describing the H concentration during plasma exposure of a sample with dislocations writes:

$$C_H(x) = C_R \exp(-x\sqrt{\rho}) \quad (3.7)$$

One can use this equation in order to estimate a steady state depth profile of H in the material during plasma exposure. For instance, the concentration profiles defined by equation 3.7 for three typical values of dislocation density are shown in figure 3.6. It can be seen that H concentration decreases rapidly with the depth and ceases at depth few tens of μm depending on dislocation density.

3.6. Model for describing H trapping and bubble formation along dislocations

A model for describing H trapping and bubble formation along dislocations was proposed on the basis of the results described in the previous sections. The mean free path λ_d^0 , that H travels along the dislocation core before release, can be estimated given the binding energy ΔE_{Bin} , the migration energy ΔE_D^d along the core and the migration energy ΔE_D^b in the bulk [13]:

$$\lambda_d^0 = b \exp\left(\frac{\Delta E_D^b - \Delta E_D^d + \Delta E_{Bin}}{2kT}\right) \quad (3.8)$$

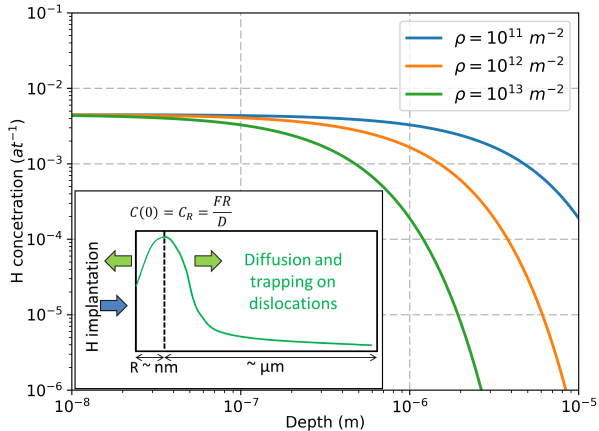


Figure 3.6: Concentration profiles during plasma implantation for different values of dislocation density (ρ).

Here, b is the length of the dislocation burgers vector $\sim 2.8 \text{ \AA}$, and k is Boltzmann's constant. At 460 K, λ_d^0 exceeds $10 \mu\text{m}$, indicating that trapped H atoms practically do not dissociate from the dislocation core prior to reaching a grain boundary or a free surface. While migrating along the core, H atoms in fact form H_N-SD clusters.

The rate of formation of H_N-SD clusters in a dislocation segment of length λ_d^0 located at a depth x is given by product of the H flux from bulk to the dislocation unit length J_H^d (in units of particles per m and per second), and λ_d^0 :

$$\omega_{H_N}^+ = J_H^d \lambda_d^0 \quad (3.9)$$

$$J_H^d = \frac{Z_d}{\omega} D C_H(x) \quad (3.10)$$

where Z_d is the dimensionless dislocation capture efficiency for H atoms diffusion from the bulk, D is the H diffusion coefficient in the bulk W and ω is the atomic volume $\sim 15 \text{ \AA}^3$. $\omega_{H_N}^+$ depends on the depth via the bulk H concentration $C_H(x)$ defined by equation 3.7.

The balance of trapping and release of H atoms to/from H_N-SD clusters define the condition for the formation of critical H₈-SD clusters and the condition for the jog-punching. The release rate, ω_H^- is independent of depth and is defined as:

$$\omega_H^- = \nu \exp \left(- \frac{\Delta E_{Bin} + \Delta E_D^d}{kT} \right) \quad (3.11)$$

here, E_{bin} is the incremental binding energy of H_N cluster to the dislocation core, ν is an attempt frequency factor taken as 10^{13} m^{-2} and E_m^d is a migration energy along the dislocation core. The rates, ω_H^- , obtained for the relevant exposure conditions [10] are plotted in figure 3.7. For medium dislocation density (i.e. typical for annealed BCC metals 10^{12} m^{-2}) H permeation extends to a several μm thick layer, in which and therefore the supercritical clusters are expected to form there, which is in a good agreement with the NRA profiles reported in [14].

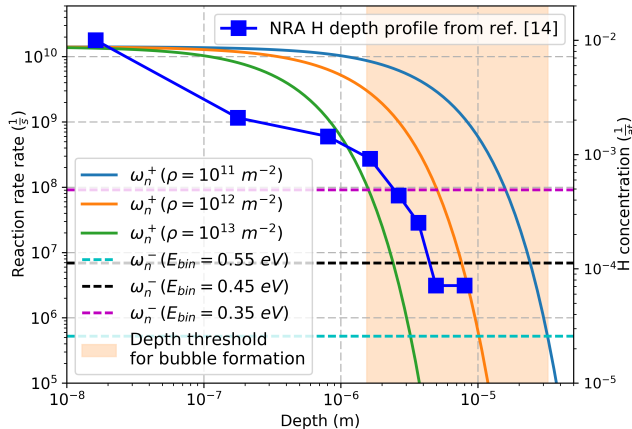


Figure 3.7: Reaction rates for H_N -SD cluster formation versus depth calculated using equations 3.8-3.10 at 460 K, varying dislocation density in the range $10^{11} - 10^{13} (\text{m}^{-2})$. Horizontal dashed lines reveal dissociation rates, ω_H^- , of H from H_N -SD clusters with $N = 1 - 3 (\Delta E_{Bin} = 0.55 \text{ eV}), N = 4 - 6 (\Delta E_{Bin} = 0.45 \text{ eV}), N = 7 - 9 (\Delta E_{Bin} = 0.35 \text{ eV})$ obtained using equation 3.11. The orange area specifies the depth threshold until which the nucleation of supercritical H_N -SD clusters takes place given the dislocation density and exposure temperature. The right hand side Y axis displays the concentration of H isotope, deuterium, as a function of depth measured using nuclear reaction analysis techniques applied to the samples exposed to high flux plasma at 460 K as described in [9, 10].

When the clustering process starts, the actual linear number density of H_N -SD clusters ($N_C [\text{m}^{-1}]$) will define λ_d as soon as N_C exceeds $\rho \lambda_d^0$. Accordingly, the trapping rate will decrease inversely proportional to N_C , which will limit the number density of H_N -SD clusters. The maximum value of N_C was estimated to be $N_C^{max} \approx 10^{19} - 10^{20} \text{ m}^{-3}$, corresponding to the mean cluster density spacing $\lambda_d \approx 100 - 10 \text{ nm}$ using the DFT results on H_N -SD binding described above. This estimations are in agreement with Transmission Electron Microscopy (TEM) study of plasma exosed samples in [15]. As an example, a typical dark field image

showing SD lines decorated by cavities is given in figure 3.8. The amount of visible hydrogen clusters was rather low for an accurate statistical determination, but based on the inspection of dozens of images, a mean linear spacing of 100 ± 20 nm was obtained, which is in the range estimated using the rate theory analysis.

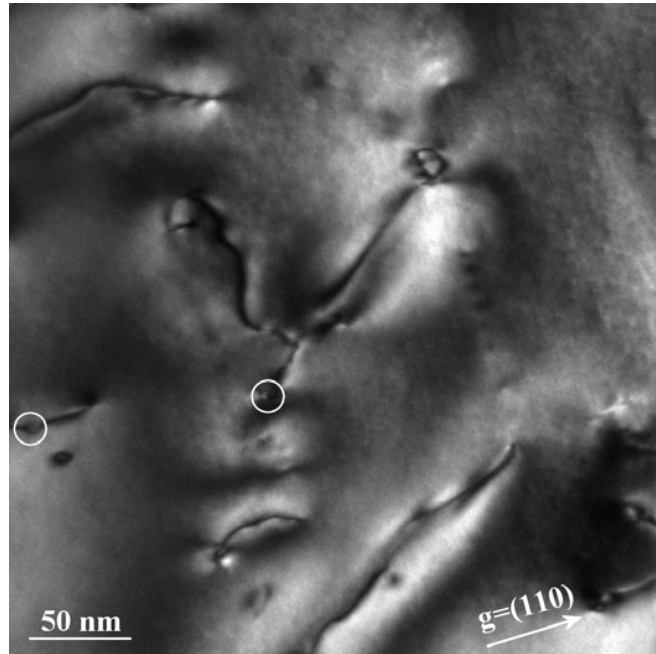


Figure 3.8: Dark field TEM image of screw dislocations decorated by H clusters. Two examples are indicated by the white circles.

3.7. Conclusion

A comprehensive mechanism for the nucleation and growth of hydrogen bubbles on dislocation lines under high flux plasma exposure of tungsten was proposed. The mechanism comprises the following stages: (1) interstitial H atoms getting trapped at dislocation lines thanks to extremely favourable energetics; (2) their very fast 1-D migration along the dislocation core thanks to low migration energies; (3) the growth of multiple H_N clusters, eventually resulting in the creation of a vacancy jog on the dislocation core. DFT calculations suggest that the jog-punching operates spontaneously once at least eight atoms have clustered. This information, coupled with a continuum rate theory model, provides an adequate description of the depth profile typically observed after high flux plasma exposure

in W. The density of supercritical hydrogen bubbles, predicted by the proposed model, was also confirmed by the TEM study. Hence, the proposed mechanism reconciles long-standing experimental observations of hydrogen isotopes retention and debates about its dependence on W microstructure. Moreover, further extension of the model allows one to explain the saturation of the retention with implantation together with the interpretation of experimental TDS spectra. The description of further details goes beyond the scope of the thesis and can be found in appendixes [H](#) and [I](#).

References

- [1] G. Kresse and J. Hafner. *Ab initio molecular dynamics for liquid metals*. Physical Review B, 47(1):558–561, 1993. PRB.
- [2] P. E. Blöchl. *Projector augmented-wave method*. Physical Review B, 50(24):17953–17979, 1994. PRB.
- [3] J. P. Perdew, Y. Wang, and E. Engel. *Liquid-drop model for crystalline metals: Vacancy-formation, cohesive, and face-dependent surface energies*. Physical Review Letters, 66(4):508–511, 1991. PRL.
- [4] W. Cai, V. V. Bulatob, J. Chang, J. Li, and S. Yip. *Periodic image effects in dislocation modelling*. Philosophical Magazine, 83(5):539–567, 2003.
- [5] C.-C. Fu and F. Willaime. *Interaction between helium and self-defects in α -iron from first principles*. Journal of Nuclear Materials, 367–370, Part A:244–250, 2007.
- [6] C. S. Becquart and C. Domain. *A density functional theory assessment of the clustering behaviour of He and H in tungsten*. Journal of Nuclear Materials, 386–388(0):109–111, 2009.
- [7] K. Heinola, T. Ahlgren, K. Nordlund, and J. Keinonen. *Hydrogen interaction with point defects in tungsten*. Physical Review B: Condensed Matter, 82(9):094102, 2010. PRB.
- [8] D. F. Johnson and E. A. Carter. *Hydrogen in tungsten: Absorption, diffusion, vacancy trapping, and decohesion*. Journal of Materials Research, 25(02):315–327, 2010.
- [9] Y. Zayachuk, M. H. J. . t. Hoen, P. A. Z. v. Emmichoven, D. Terentyev, I. Uytdenhouwen, and G. v. Oost. *Surface modification of tungsten and tungsten–tantalum alloys exposed to high-flux deuterium plasma and its impact on deuterium retention*. Nuclear Fusion, 53(1):013013, 2013.
- [10] Y. Zayachuk, M. t. Hoen, P. Z. v. Emmichoven, I. Uytdenhouwen, and G. v. Oost. *Deuterium retention in tungsten and tungsten–tantalum alloys exposed to high-flux deuterium plasmas*. Nuclear Fusion, 52(10):103021, 2012.
- [11] G. Pintsuk. *4.17 - Tungsten as a Plasma-Facing Material*. Comprehensive Nuclear Materials, 4:551–581, 2012.
- [12] G. S. Was. *Fundamentals of radiation materials science: metals and alloys*. Springer Verlag, New York, 2007.

- [13] A. I. Ryazanov, G. A. Arutyunova, V. M. Manichev, Y. N. Sokursky, and V. I. Chuev. *Kinetics of the growth of helium bubbles at the grain boundaries. formation of the spatially inhomogeneous distribution of helium bubbles near the grain boundaries.* Journal of Nuclear Materials, 135(2):232–245, 1985.
- [14] Y. Zayachuk. *Deuterium Retention in Tungsten and Tungsten-Tantalum Alloys under High Flux Plasma Exposure ('Deuteriumretentie in wolfraam en wolraam-tantaallegeringen onder blootstelling aan een hoge plasmaflux')*. Thesis, 2013.
- [15] D. Terentyev, V. Dubinko, A. Bakaev, Y. Zayachuk, W. V. Renterghem, and P. Grigorev. *Dislocations mediate hydrogen retention in tungsten.* Nuclear Fusion, 54(4):042004, 2014.

“Product of optimism and knowledge is a constant.”

Lev Landau (1908 – 1968)

4

Mechanisms of retention characterized by Molecular Dynamics simulations

According to the multi-scale modelling approach and in order to provide temperature dependent parameterisations for upper scale models, the mechanisms of H retention predicted by Density Functional Theory (DFT) should be investigated for larger model systems at finite temperatures. Among different modelling tools, large-scale atomistic simulations such as Molecular Dynamics (MD) are suitable for this. At the core of MD simulations lies the interatomic potential, which enables computation of the forces between interacting atoms. In order to study fusion relevant conditions one has to consider W-H-He system.

In this chapter, the process of the development of the interatomic potential together with a number of MD simulations employing the potential are reported. It starts with the selection of base W-W potential from the literature and its extension to the W-H-He system. The developed potential is carefully benchmarked by comparison with DFT values and predictions of W-H-He potential in the framework of Bond Order Potentials (BOP) prior the application of the potential for simulations. Finally the developed potential is applied to perform a number of simulations studying H and He interaction with defects in W, H and He diffusion properties in the bulk material and attached to the dislocation core and Frenkel pair formation initiated by H and He in the material.

4.1. Selection of the W-W interatomic potential to study the interaction of H with dislocations

Presently, for W-H-He system only a potential in the framework of bond order model is available in literature [1]. Bond Order Potentials (BOP) are significantly computationally slower than potentials created in the framework of Embedded Atom Method (EAM). Moreover, it is always a good practice to test the performance of the potentials by comparison with other types of the potentials. Thus there is a need for a new interatomic EAM potential for W-H-He system. Prior to considering the properties of H and He in tungsten the first step is a choice of the base W-W potential. Currently more than 30 potentials for W are available in the literature in different forms. Each potential comes with its strength and weaknesses and since all results depend on quality of the interatomic potential, it is important that its properties are well understood.

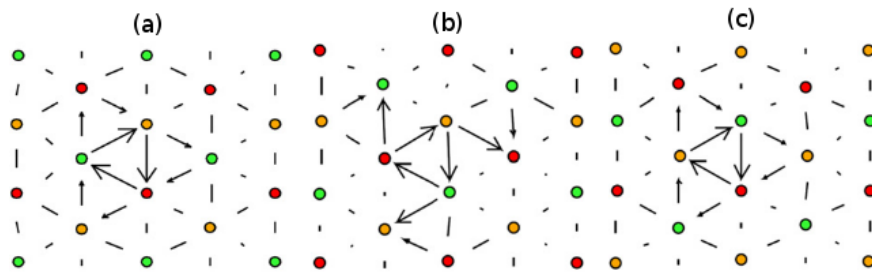


Figure 4.1: Comparison of Vitek differential displacement maps as predicted by DFT. [2] (a), DND [3] (b) and MVG1 [4] (c) potentials.

Here the focus was made on the many-body central force formalism, which offers a good compromise between transferability/predictability and computational speed, especially when it comes to large-scale finite-temperature simulations. The many-body central force framework was developed independently under the forms: ‘embedded atom method’ [5], ‘Finnis-Sinclair formalism’ [6] and ‘glue model’ [7]. Properties of 19 such potentials for W found in the literature [3, 4, 6, 8–21] were reviewed. As basic features relative lattice stability, elastic constants and point-defect properties were considered and benchmarked against experimental data and density functional theory (DFT) calculations. In addition, extended lattice defects, namely: free surfaces, symmetric tilt grain boundaries, the $\frac{1}{2}\langle 111 \rangle\{110\}$ and $\frac{1}{2}\langle 111 \rangle\{112\}$ stacking fault energy profiles were investigated. A special attention was drawn to the performance of the potentials with regard to the $\frac{1}{2}\langle 111 \rangle$ Screw Dislocation (SD) core due to the importance of dislocations in the proposed model of H retention in W.

For all Body-centered Cubic (BCC) transition metals and W in particular, DFT predicts a compact isotropic dislocation core [2, 22–25]. The dislocation core structures were analysed using Vitek differential displacement maps [26]. The examples of the maps predicted by DFT [2], MVG1 [4] and DND [3] potentials are shown in figure 4.1. On the maps, different colours of atoms represent non-equivalent atomic planes along $\langle 111 \rangle$ direction and arrows represent a displacement of atoms along $\langle 111 \rangle$ direction with respect to ideal BCC structure. As can be seen from the figure, MVG1 potential predicts the compact core structure consistent with DFT, while DND potential predict three fold core structure.

Property	FS	JO	FOI	ZWJ	KLL	ZSG	DLK	DND	MVG1	MVG2	MVG3	WZL
Elastic constants	C	C	C	C	IC	C	C	C	C	C	C	C
E_f (Vac)	C	C	C	C	C	C	C	C	C	C	C	C
E_m (Vac)	UE	C	IC	C	C	IC	C	C	C	UE	C	UE
E_b (Vac)	IC	UE	UE	IC	UE	UE						
E_f (SIA)	UE*	IC	IC	IC	IC	IC	IC	C	C	C	C	C
$\langle 111 \rangle$ row potential	C	OE	IC	OE	OE	IC	OE	IC	OE	C	OE	C
Screw dislocation core	IC	IC	C	C	IC	C	C	IC	C	C	C	IC
Screw dislocation glide	IC	IC	IC	C	IC	IC	IC	IC	C	C	C	IC
Edge dislocation glide	C	C	IC	C	C	IC	C	IC	C	C	C	C
Free surface	UE	C	UE	UE								
Grain boundary	UE	C	C	C	C	C	C	UE	C	UE	C	UE
Gamma surface cuts	UE	C	IC	C	C	IC	UE	IC	C	UE	C	UE
R_{cut}	2nn	2nn	2nn	2nn	2nn	2nn	6nn	2nn	5nn	4nn	5nn	2nn

- IC - Inconsistent with experimental or DFT data
- C - Consistent with experimental or DFT data
- OE - Overestimation compared to experimental or DFT data
- UE - Underestimation compared to experimental or DFT data

Table 4.1: Summary of the performance of the potentials for different physical properties.

The following nomenclature is used in the header of the table: FS – Finnis and Sinclair [6]; JO – Johnson and Oh [9]; FOI – Foiles [10]; ZWJ – Zhou et al.) [12]; KLL – Kong et al. [13]; ZSG – Zhang et al. [16]; DLK – Dai et al. [18]; DND – Derlet et al. [3]; MVG1, MVG2, MVG3 – ‘EAM-2’, ‘EAM-3’, ‘EAM-4’ by Marinica et al. [4] respectively.

The W-W potential, which gives the best ‘global performance’, i.e. ‘EAM2’ from the work of Marinica et al. [4] noted as MVG1 in table 4.1 was selected for the base of the new W-H-He potential. As key features, this potential provides

elastic constants, point-defect, edge and screw dislocation properties as well as grain boundary energies consistent with DFT calculations and experiments.

4.2. Development and validation of W-H-He potential

In the literature three semi-empirical potentials exist for W-He [20, 27, 28] and two for W-H [1, 29]. From those potentials, the ones by Wilson *et al.* [28] and Henriksson *et al.* [27] predict opposite stability for He in an octahedral and tetrahedral position. The one by Juslin and Wirth [20] provides a He migration barrier of 0.21 eV, which overestimates the DFT value (0.06 eV) by more than a factor three. The W-H potential by Juslin *et al.* [29], on the other hand, predicts the $\langle 110 \rangle$ dumbbell self-interstitial to be more stable than the $\langle 111 \rangle$ one in BCC W, which is in contradiction with DFT data. The one by Li *et al.* [30] is a part of the ternary W-H-He BOP that is used as a benchmark throughout this work. At this point it should be noted that none of the potentials for pure W used in the above works reproduce the key features as good as 'EAM2' by Marinica *et al.* [4]. In addition, a $\frac{1}{2}\langle 111 \rangle$ screw dislocation in BCC W relaxed by BOP provides a threefold degenerate core structure, which is contradictory to DFT results [2] and 'EAM2' by Marinica *et al.* [4].

The H-H interaction in bulk W is essentially different from its description in vacuum. In vacuum, two H atoms form the strongly bonded H_2 molecule ($H_b = 4.75$ eV) [29]. In bulk W, on the other hand, two H atoms exhibit repulsion or weak binding [31] as they cannot form the strongly bonded H_2 molecule due to interactions with the surrounding W atoms. The modulation of such behaviour within the EAM framework is difficult to achieve. Therefore, it was decided to focus on the effective interaction of H (and He) in bulk W. As a consequence, the here derived potentials for H and He should not be used in vacuum.

Property	Hydrogen				Helium			
	DFT	EAM1	EAM2	BOP	DFT	EAM1	EAM2	BOP
$\Delta E(\text{Octa-Tetra})$ (eV)	0.38	0.35	0.38	0.32	0.22	0.19	0.23	0.17
$\Delta E(\langle 100 \rangle\text{-Tetra})$ (eV)	0.39	0.35	0.38	0.32	0.23	0.19	0.23	0.17
$\Delta E(\langle 110 \rangle\text{-Tetra})$ (eV)	0.21	0.22	0.21	0.22	0.07	0.09	0.06	0.02
$\Delta E(\langle 111 \rangle\text{-Tetra})$ (eV)	1.51	2.1	2.7	2.29	0.51	1.4	0.98	0.75
$\Delta E_{\text{Bin}}(X\text{-Vac})$ (eV)	1.19	1.24	1.33	2.03	4.55	4.55	4.54	5.04
$\Delta E_D(X)$ (eV)	0.2	0.22	0.21	0.22	0.06	0.09	0.06	0.02

Table 4.2: Point defect properties of H and He in BCC W calculated by DFT and the potentials

Two sets of W-H-He potentials were created, namely, EAM1 and EAM2. Both potentials were fitted to reproduce the relative stability between tetrahedral (T) and octahedral (O) sites as well as between tetrahedral and $\langle 110 \rangle$ dumbbell position, with the latter serving as saddle for T-T migration. In addition, the binding between H-H, He-He and H-He pairs in bulk W and the binding between vacancy-H and vacancy-He pairs were fitted. For EAM1, emphasis was put on a quantitative reproduction of DFT data of the binding between H-H, He-He and H-He pairs. The off-centre position of a H atom in a vacancy as predicted by DFT [32] was not considered, and therefore both H and He are described by pair potentials only. For EAM2 the focus was made on stabilizing H in an off-centre position in the vacancy and therefore an embedding function was added for H. For both H and He no density function is defined, i.e. only W adds to the electron density at a given site and there is no contribution to it by H or He.

In table 4.2 the point defects properties of H and He in bcc W calculated with the potentials are compared to DFT [31] and BOP [30]. Clearly, DFT predicts the tetrahedral position to be the most favourable for both H and He, which is reproduced by all considered potentials. In addition, all potentials predict the correct ordering in interstitial formation energies, although EAM1 and EAM2 show the best quantitative agreement with DFT. With respect to the binding energy between a H or He to a vacancy, both EAM1 and EAM2 closely reproduce the DFT values, while BOP underestimates and overestimates the binding for H and He, respectively. The migration energy for H is well reproduced by all potentials, but the one for He is only reproduced by EAM1 and EAM2, and underestimated by BOP by a factor three.

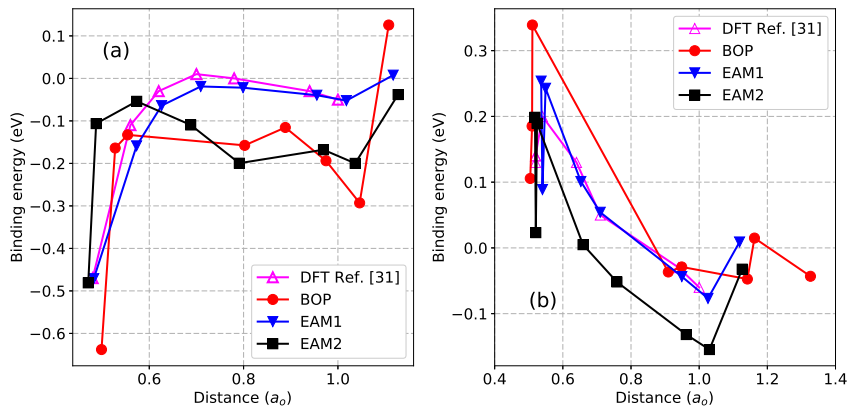


Figure 4.2: Comparison of H-H (a) and H-He (b) pairs binding energy as a function of distance as calculated by DFT [31] and the potentials.

In figure 4.2 the binding energy between H-H (a) and H-He (b) pairs as a function of separation distance is plotted as calculated by DFT and the potentials. The considered configurations were taken from [31] and only the final distance between the pairs was considered. As with both DFT and the potentials the distance between H and He pairs changed considerably during atomic relaxation, a comparison of binding energy with distance was more sensible than a one-to-one comparison between the specific configurations. According to DFT He-H attract with maximum value of binding energy of 0.20 eV, while H-H pairs repel with a maximum of -0.47 eV. This behaviour is qualitatively reproduced by all potentials and also quantitatively by EAM1. Both BOP and EAM2 have a too long interaction range for H-H pairs and overestimate (BOP) the H-He binding or underestimate (EAM2) the H-He interaction range.

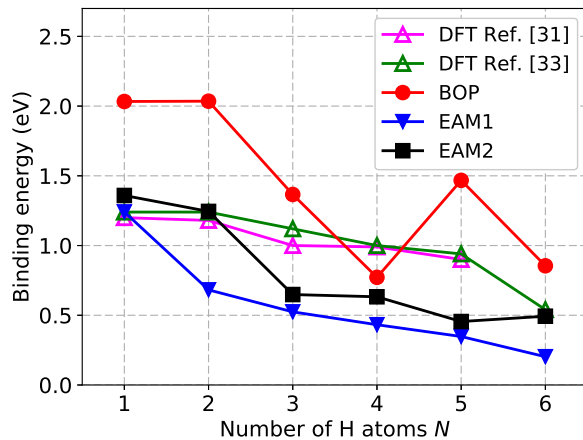


Figure 4.3: Comparison of H-Vacancy binding energy as a function of number of H atoms as calculated by DFT [31, 33] and the potentials.

In figure 4.3 the binding energy of a H atom to H-Vacancy clusters calculated by the potentials is compared with DFT values from [31, 33]. The binding energy slightly decreases with increasing cluster size. For EAM1, the values for the binding energy are within the DFT range. For EAM2, the values for the binding energy are also within the DFT range, and qualitatively, also the binding energy decreases with cluster size. For BOP, the binding energy for H is overestimated by about a factor two. Qualitatively, BOP reproduces the decrease in binding energy with cluster size.

From the validation results presented above, EAM2 potential was chosen for further calculations regarding Vac-H-He clusters. Vac_K-H_L-He_M (K, L, M are

number of vacancies, H atoms and He atoms in the the clusters respectively) clusters containing up to $K = 12$ vacancies with a H to Vac ratio, $X_H = N/K$, and He to Vac ration, $X_{He} = M/K$, in the range of 0.1 – 6 were considered. The sequential binding energy was calculated for 2087 clusters in total. Based on the dissociation energy of various Vac-H-He clusters of nano-metric size, a parameterization for a simple Liquid-Tear Drop (LTD) model applicable to up-scale mean field or kinetic Monte Carlo simulations was suggested. The obtained results show that the dissociation of mixed Vac-H-He clusters primarily takes place by emission of H, whose trapping energy is not essentially changed by the presence He in the clusters. Hence, the H-He interaction does not affect the thermal stability of H in the vacancy-stabilized H-He clusters. Therefore it was concluded that the origin of the H-He synergy expressed by the enhanced H uptake should be investigated at the stage of the nucleation of H-He defects. The details of parametrizations for LTD model as well of the both versions of EAM potentials can be found in the attached paper in appendix F.

4.3. Interaction of H and H_N clusters with dislocations

In order to study interaction of H with screw and edge dislocations the model systems described below were used. For calculations involving a $\frac{1}{2}\langle 111 \rangle$ screw dislocation model box with size $152.9 \times 78.1 \times 32.6$ containing 25920 atoms with axis orientations [1 – 10], [11 – 2], [111], respectively for X, Y, Z principal axes was used. Free surfaces along the X and Y were introduced, while periodic boundary conditions were applied along the Z direction, coinciding with the orientation of the dislocation line and dislocation Burgers vector. For the calculations involving a $\frac{1}{2}\langle 111 \rangle\{110\}$ edge dislocation, the box size was $80.9 \times 38.8 \times 111.7$ (22155 atoms). The X, Y, Z axes orientations were [111], [11 – 2], [–110] with periodic conditions imposed along the X and Y directions and free surfaces perpendicular to the Z direction. The dislocation line was oriented along [11 – 2] direction. The calculations were done using Large-scale Atomic/Molecular Massively Parallel Simulator (LAMMPS) [34].

Position type	Binding energy (eV)			
	EAM1	EAM2	BOP	DFT
A	0.0	0.0	0.41	0.55
B	0.42	0.66	1.03	0.54

Table 4.3: Binding energy of H atom to a screw dislocation core as predicted by the EAM, BOP and DFT methods.

As was reported in chapter 3, DFT calculations revealed two types of energy minimum configurations for the H atom: inside the core and adjacent to the core. Inside the core positions are numbered from 1 to 3 in figure 3.1 and will be referred as A type in this chapter. Adjacent to the core positions are numbered from 4 to 9 on the figure 3.1 and will be referred as B type positions. According to the DFT results, the binding energy in the two configurations amounts to 0.55 eV and 0.54 eV, i.e., practically the same. Neither the BOP, nor the EAM potentials could completely reproduce the DFT data, see table 4.3. While the BOP model predicts reasonable agreement for the binding energy in position A, it overestimates the binding energy by a factor of two in position B. Both versions of the EAM potential do not predict the binding in position A, instead the interaction is practically neutral. The binding energy in the position B was calculated to be 0.42 eV and 0.66 eV for the two versions of the EAM potential, which bounds the DFT result. Note that the BOP potential predicts the three-fold split structure for the dislocation core, which contradicts the DFT result (see figure 4.1). Both versions of the EAM potential return the isotropic non-degenerate core structure, which complies with the DFT data.

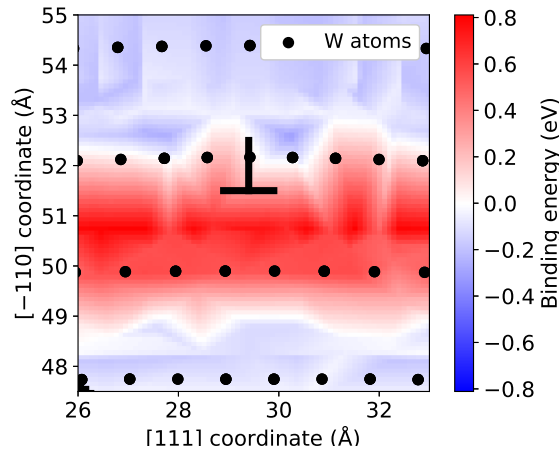


Figure 4.4: Distribution of the binding energy of H with the core of the edge dislocation obtained using the EAM2 potential. The geometric position of the dislocation core (i.e. the end of the extra atomic plane) is shown by the symbol '⊥'. Red area in the figure represents positive values of the binding energy i.e. area with attractive interaction, blue areas represent repulsive interaction.

The relaxed structures for edge dislocation were found to be symmetric and extended in the {110} glide plane. It was similar with all the applied potentials. An example of the distribution of the binding energy is provided in figure 4.4, which

was obtained using the EAM2 potential. The binding energy maps calculated using the other potentials are essentially similar. From figure 4.4 it follows that the maximum binding energy is realized if H is placed in between the two planes forming the imaginary dislocation glide plane. The attractive interaction (red area) sharply vanishes as the H atom is moved above or below the glide plane. While inside the glide plane, the range of the strong interaction is spread over ~ 10 Å, which can be expected given the rather extended structure of the dislocation core. The maximum binding energy is found to be 0.63, 0.81 and 1.64 eV for the EAM1, EAM2 and BOP, respectively. As in the case of the interaction with the SD (in position B) and H-Vacancy, the BOP predicts a binding energy of a factor two higher than the EAM potentials. Even there is no reference DFT data available, it was considered that the BOP model overestimates the binding energy following the previous trends.

The next step was to characterize the formation of H_N clusters on dislocations and deduce the incremental binding energy as a function of cluster size depending on the character of the dislocation. First, the results for the SD is presented since it was also studied by DFT calculations reported in chapter 3 providing an important reference data to judge on the quality of the interatomic potentials (see figure 3.3). The incremental binding energy as a binding energy of H atom to H_{N-1} cluster on the SD core (H_{N-1} -SD) with respect to a tetrahedral H in bulk W (H_b) as a reference state was computed for each relaxed H_N -SD configuration. The methodology used in the chapter is essentially the same as one described in section 3.3 of chapter 3, which allows direct comparison of the results with the DFT data.

The incremental binding energy of H_B to H_{N-1} -SD complex (referred as "Bulk" on the figure 4.5) i.e. binding of an interstitial H added from the bulk to the H_{N-1} cluster placed on the SD is presented in figure 4.5(a). As can be seen from the figure, the BOP potential predicts much stronger binding for the second H atom as compared with DFT, while the binding energy for the larger clusters is adequately described up to size $N = 6$. The EAM1 also provides a reasonable description but does not capture the reduction of the binding energy at $N > 6$. The EAM2 predicts a flat curve for the binding energy function, as is the case of the EAM1, but overestimates the result by about 0.1 – 0.2 eV as compared to the DFT data.

The incremental binding energy of a H_{SD} to a H_{N-1} -SD complex, i.e. binding of an interstitial H attached to the SD core with the H_{N-1} cluster placed on the SD (referred as 'Core' in the figure), is presented in figure 4.5(b). DFT data suggest that only two H atoms may form a stable compact complex. Adding more H atoms should result in the formation of the H_N clusters 'stretched' along the dislocation line. Both BOP and EAM potentials correctly predict this trend, however, the strength of the interaction differs. The BOP potential provides much lower values for the binding energy, in absolute terms, as compared to the both EAM potentials.

It can be concluded that both types of the potentials predict correctly qualitative trends obtained from the DFT calculations, while none of the potentials provides a good quantitative agreement.

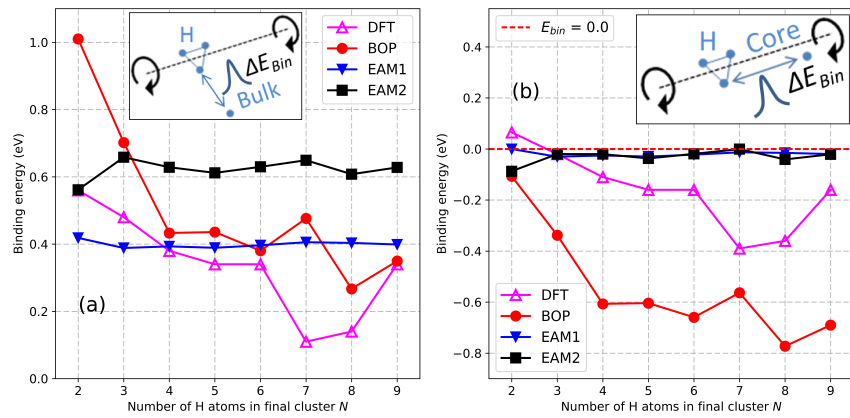


Figure 4.5: Incremental binding energy of H_B to a H_{N-1} cluster placed on the SD core ('Bulk') (a). Incremental binding energy of H_{SD} to a H_{N-1} cluster placed on the SD core ('Core') (b). Inset figures schematically demonstrate the partition of H_b , H_{SD} and H_{N-1} .

The results for edge dislocation showed that the incremental binding energy of H_N clusters is of the order of the H-ED binding energy, which implies that H atoms inside the H_N cluster can accommodate inside the Edge Dislocation (ED) core practically not disturbing each other. This was not the case of the screw dislocation, for which the reduction of the attractive interaction of H_B to the H_{N-1} -SD was seen already starting from $N = 2$. This result reflects that the space available for the formation of the energetically stable H_N cluster is essentially larger in the core of the ED as compared to that in the SD core. The incremental binding energy of a H_{ED} to a H_{N-1} -ED complex suggests the absence of attractive interaction between H atoms moving along the ED core. Just as in the case of the screw dislocation, H_N clusters are expected to grow preferentially forming configurations 'stretched' along the dislocation line. All three interatomic models predict the same trend, but according to the EAM1 the interaction of a H_{ED} with a H_{N-1} -ED cluster is practically neutral.

4.4. Diffusion of H in the bulk crystal and attached to a dislocation

MD simulations studying the diffusion of H in a crystal containing an ED were done only using the EAM2 potential. Since these calculations were computationally heavy (due to large crystal and a relatively long MD run necessary to achieve satisfactory statistic), the BOP potential was excluded because of larger computational demand comparing to EAM potentials and also due to the poor performance regarding the properties of dislocations.

In order to estimate the diffusion parameters of H atoms and validate DFT predictions regarding the preferential one dimensional H migration along the dislocation core, a number of MD calculations were performed at finite temperature, T . The main goal was to obtain the diffusion coefficient as a function of temperature, which would allow one to extract the pre-exponential factor D_0 and activation energy ΔE_D using the Arrhenius type equation:

$$D = D_0 \exp\left(\frac{-\Delta E_D}{kT}\right) \quad (4.1)$$

In each MD run that lasted for a time τ , the trajectory of the H atom was followed and visualized to quantify the dimensionality of the H motion, which depends on the ambient temperature and type of defect present in the system. Then, the mean square displacement of the position of the H atom was calculated to obtain the diffusion coefficient using the well-known Einstein equation:

$$D_n(T) = \frac{R_n^2}{2n\tau}(T) \quad (4.2)$$

where n is dimensionality of the motion (i.e., $n = 1$ for one dimensional migration along a dislocation core, and $n = 3$ for three dimensional bulk diffusion), τ is the simulation time.

By following and visualizing the movement of H atom it was found that it exhibits one dimensional migration along the dislocation core moving by jumping between the planes bounding to the imaginary dislocation glide plane. At temperatures below 1300 K, H was attached to the ED core for the whole time span of the MD run. This behavior is consistent with the strong attractive interaction of a H to a ED ($\Delta E_{Bin} = 0.63/0.89$ eV depending on the potential). Above 1300 K, a detachment of the H atom was regularly registered. The trajectory of the H atom whilst migrating along the dislocation core was therefore reconstructed to obtain the diffusion coefficient from high temperature MD simulations. The resulting diffusion coefficient for 1D-migration along the ED core is drawn in figure 4.6 as a function of temperature. The extracted prefactor D_0 and migration barrier ΔE_D are, respectively, 8.1×10^{-9} m²/s and 0.17 eV. Note that this value is significantly

smaller than the migration energy of a H in W bulk, estimated experimentally to be 0.4 eV [35] and obtained by MD: 0.23 eV. The experimentally measured [35] and calculated here with the same potential 3-D bulk diffusion coefficient is also drawn in figure 4.6 for comparison. Due to the scale of the graph the error bars are not seen, however, the relative error is in range of 5 – 10 % of the absolute values. The calculated value of ΔE_D is 0.23 eV and is lower than the experimentally obtained value, but is consistent with the values of the migration barrier between tetrahedral positions, which is 0.21 eV as predicted by the potential, and 0.2 eV as obtained by DFT in [31]. Clearly, the diffusivity of H attached to the dislocation line is much higher than the bulk diffusivity, especially at low temperatures as can be seen in figure 4.6.

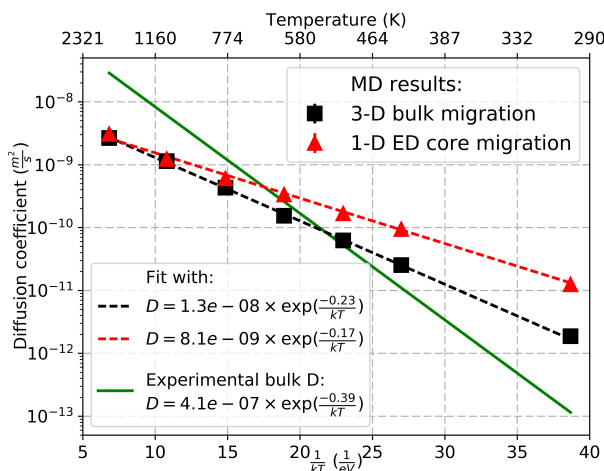


Figure 4.6: 1-D diffusion coefficient of H in the core of the edge dislocation and 3-D bulk diffusion coefficient as calculated using the EAM2 potential and drawn according to the experimental measurements [35]

Unfortunately simulations with screw dislocations did not reveal one dimensional migration of H atom along the core. This is related to the fact that interatomic potentials used do not fully reproduce all attraction positions of H at a screw dislocation core as was reported in the previous section. Thus the potentials do not reproduce the migration passes studied by DFT and reported in section 3.2.

4.5. Effect of He on H retention: He assisted Frenkel pair formation and $\text{He}_M\text{-H}_N$ cluster bonding

DFT studies of He-H interaction [31, 36, 37] showed that there is an attractive interaction between He clusters and H atoms suggesting synergetic effects under mixed He-H plasma implantation. Suppressing of blistering, confirmed by experimental studies [38, 39], is one of the effects seen under simultaneous H and He exposures. The suppression of blistering was attributed to a decrease of H permeability through the subsurface region due to He bubble formation. Another remarkable effect was a detection of nanometric He bubbles at a depth significantly larger than the He implantation range [38], not seen in pure He exposures. However, comprehensive physical mechanisms leading to these synergetic effects are so far not clear.

The interaction of $\text{He}_M\text{-H}_N$ clusters of different sizes and chemical morphology was assessed by means of Molecular Static (MS) and MD simulations in order to contribute to the understanding of the He-H interaction in a W lattice. The obtained MS results were compared with available DFT data to validate and substantiate the application of central-force interatomic potentials for the studied problem. The diffusion and thermal stability of mixed $\text{He}_M\text{-H}_N$ clusters were studied by means of MD simulations in order to gain an understanding of the mechanisms causing the above mentioned synergetic effects under mixed He-H implantation conditions.

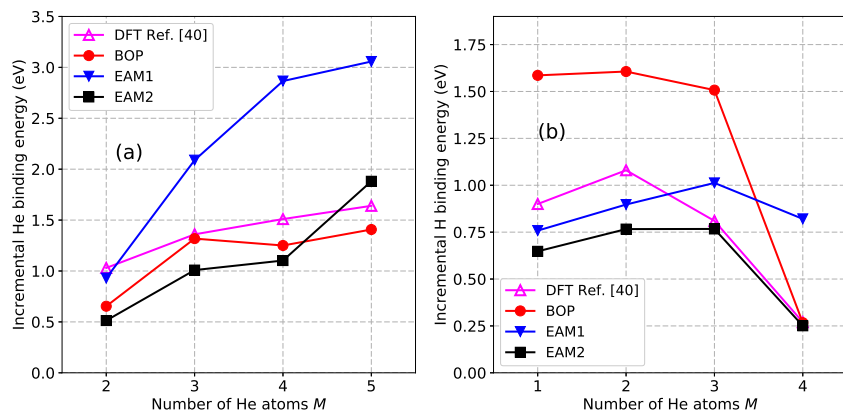


Figure 4.7: Incremental binding energy of He atoms to a He_M cluster in bulk tungsten (a) and incremental binding energy of H atom to H-He_M cluster in vacancy (b) as predicted by DFT, BOP and EAM potentials.

In figure 4.7(a) the results for incremental binding energy of a He atom to a

cluster of He atoms (He_M) in bulk tungsten, predicted by the potentials and DFT values from [40] are compared. As was shown before, EAM1 gives better agreement for the He-He pair interaction and EAM2 underestimates the corresponding binding energy. However, as can be seen from figure 4.7(a), EAM1 shows a rapid increase of the binding energy with increasing cluster size, which is not in agreement with the trend coming from DFT data. At the same time EAM2 and BOP potentials give reasonable agreement for the binding energy function. In figure 4.7(b) the results for incremental binding energy of a H atom to a H-He_M cluster in vacancy are compared. As can be seen from the figure, BOP potential overestimates the binding energy almost by factor of two for clusters containing from one to three He atoms. EAM1 potential gave reasonable agreement for clusters with one and two He atoms with overestimation of the binding energy for bigger clusters failing to reproduce the DFT trend of the binding energy drop for cluster with four atoms. At the same time EAM2 potential reproduces the DFT trend well with some underestimations for small clusters. The adequate reproduction of the binding He and mixed $\text{He}_M\text{-H}_N$ clusters is important for the correct description the thermal stability of the clusters during MD simulations. Since the focus was made on the modelling of mixed $\text{He}_M\text{-H}_N$ clusters, it was concluded that EAM2 is the most suitable potential for this purpose.

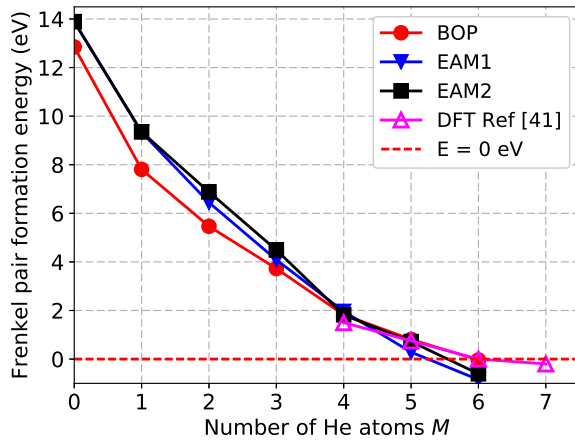


Figure 4.8: Frenkel pair formation energies in presence of He as predicted by BOP and EAM potentials and DFT method in [41]

An important process that affects the diffusivity of He_M clusters is the so called self-trapping mechanism. After a cluster of He_M atoms of a certain size (number atom in cluster M) is created, it becomes energetically more favourable to create a

Frenkel pair in order to release the stress created by the interstitial He atoms. After the Frenkel pair is created, He atoms occupy the vacancy and become immobile. Thus it is important to test the ability of the potentials to reproduce this mechanism for reliable simulations of $\text{He}_M\text{-H}_N$ clusters mobility. MS calculations were used to assess the energy balance of a system containing a He_M cluster in an ideal W matrix and a system where the same He_M cluster is placed in a vacancy close to a W self-interstitial atom (SIA). The same energy balance calculations were also performed by DFT techniques in [41]. The results from this work are compared with MS calculations in figure 4.8. It can be seen that all considered versions of the interatomic potential are in good agreement with the DFT values. Regarding the threshold size of the He_M cluster at which the formation of a Frenkel pair becomes more favorable the potentials predict a value for M between five and six atoms. Despite the significant difference in description of bonding of He_M clusters in bulk tungsten and H- He_M cluster in vacancy (see figure. 4.8), both versions of the EAM potentials together with BOP potential give very similar values for the formation energy of Frenkel pairs. Since there is no difference between both EAM and BOP potentials with respect to the He self-trapping mechanism, but the EAM2 potential describes the energetics of He_M clusters in the bulk W and H- He_M clusters in vacancy better, the EAM2 potential was chosen for the finite temperature simulations.

4.6. Diffusion and thermal stability of $\text{He}_M\text{-H}_N$ clusters

Prior to studying the mobility of $\text{He}_M\text{-H}_N$ clusters, it is important to first assess the binding energy of He and H atoms in these clusters by MS calculations. In figure 4.9, the results for the incremental binding energy of a H atom to $\text{He}_M\text{-H}_N$ clusters are presented. It is important to note that the He binding energy is higher than for a H atom because of the strong He-He bonding (1.03 eV), while the He-H bond strength is only 0.2 eV. Thus, the stability of the mixed $\text{He}_M\text{-H}_N$ clusters is determined by the binding energy of a H atom as it has the lowest binding energy. It can be seen from figure 4.9 that there is a rapid decrease of the binding energy as the number of H atoms in the cluster increases. Starting from three H atoms in the cluster, the binding energy becomes negligible, indicating that the cluster becomes unstable. This result is in agreement with DFT data from [37] where low stability of clusters containing more than three H atoms was demonstrated. These static calculations defined the configurations that should be studied by MD simulations. The energy needed for He-induced Frenkel pair formation becomes quite low (~ 2 eV) if the cluster contains four He atoms (see figure. 4.8). When the fifth He atom is added to the system, spontaneous generation of a Frenkel pair occurs. This

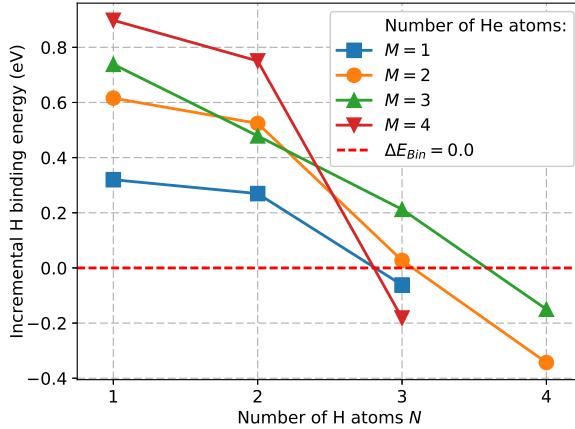


Figure 4.9: Incremental binding energy of a H atom to $\text{He}_M\text{-H}_N$ clusters in the bulk W as predicted by the EAM2 potential.

means that the punching of a tungsten self-interstitial is also possible for $\text{He}_M\text{-H}_N$ clusters containing four He atoms at sufficiently high temperature, as was actually demonstrated in [41]. Thus, it was decided to study only clusters containing at most four He atoms to avoid the transformation caused by self-trapping. Figure 4.9 shows that starting from three H atoms in the cluster it becomes unstable which means that it will decay during MD runs at finite temperatures. Thus for further MD studies, the pure and mixed clusters containing from one to four He atoms and up to two H atoms were considered.

A set of MD simulations was performed in order to obtain information on the diffusivity and thermal stability (i.e. lifetime) of the $\text{He}_M\text{-H}_N$ clusters. Only the time and trajectories where the atoms were clustered together was taken into account. Some weakly bound clusters have limited stability at finite temperature and therefore they frequently decay and bond back during the simulation. Only a set of separate segments where the cluster was stable and moved as a whole object was considered by applying a post-processing algorithm. If the number of such independent segments was higher than ten, an average value of the diffusion coefficient calculated over these segments was used. If the number of these segments was lower than ten, the method described in section 4.4 was applied to the longest time segment. The average time length of the segments when the cluster remains stable \bar{t} allows one to calculate a decay frequency as $\nu = \frac{1}{\bar{t}}$. An Arrhenius expression $\nu = \nu_0 \exp(-\frac{\Delta E_{Diss}}{k_B T})$ was fitted to the dataset for decay frequency as a function of temperature in order to deduce the dissociation energy,

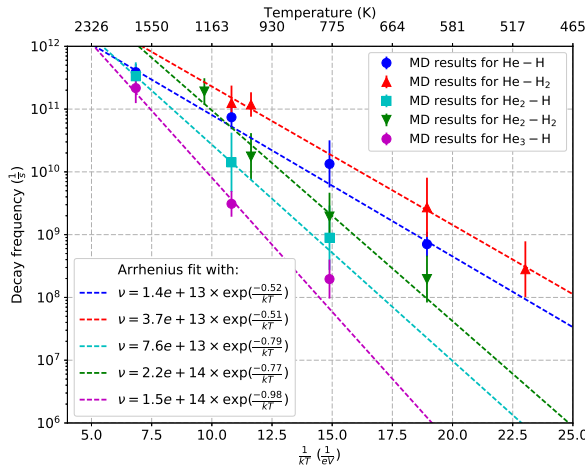


Figure 4.10: Arrhenius plot of the decay frequency of $\text{He}_M\text{-H}_N$ clusters with one to four He atoms in the cluster obtained from MD simulations. The error bars represent 95 % confidence interval around the mean.

ΔE_{Diss} and pre-exponential factor v_0 . The decay frequency together with Arrhenius fits for the $\text{He}_M\text{-H}_N$ clusters are presented in figure 4.10. The slope of the plot corresponds to the dissociation energy ΔE_{Diss} . The error bars correspond to 1.96 times the standard error around the average, which corresponds to the 95 % confidence interval of the mean value. Following the standard assumption, the dissociation energy ΔE_{Diss} is a sum of binding energy and migration barrier ($\Delta E_{Diss} = \Delta E_{Bin} + \Delta E_D$). The average discrepancy between the values of the dissociation energy ΔE_D obtained by fitting the MD data and the results of the static calculations for binding energies ΔE_{Bin} (see figure 4.9) is 0.21 ± 0.03 eV. This is in excellent agreement with the H migration barrier (0.21 eV) in bulk W both predicted by the potential and obtained with DFT calculations (0.2 eV) [31].

The migration energies of different $\text{He}_M\text{-H}_N$ clusters as well as of pure He clusters obtained by applying the above described techniques are summarized in figure 4.11. It can be seen that the migration energy of He clusters increases with the size of the cluster (black curve). It is important to note that for the He_4 cluster an event of self-trapping was detected during the MD run at 1700 K, which is in agreement with the MS predictions as well as with the MD results from [31]. If H atoms are added to a He cluster, the migration energy increases almost by a factor of two and gets close to the value of the migration energy of a single H atom, denoted by the green area in the graph. The increase of the migration energy of the mixed clusters compared to pure He clusters is consistent with the fact that it

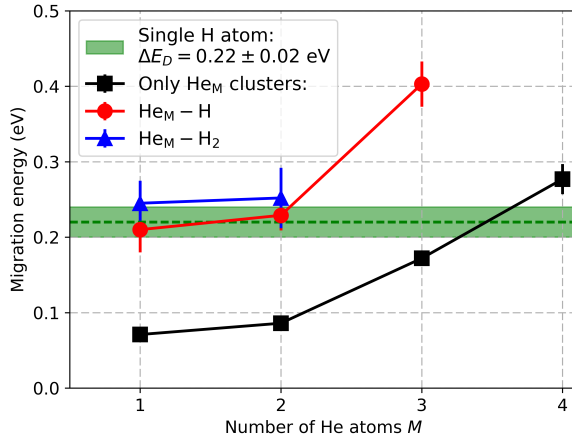


Figure 4.11: Migration energies for $\text{He}_M\text{-H}_N$ clusters extracted from MD simulations.
The error bars represent the 95 % confidence interval.

is defined by the slowest constituent of the cluster, which is a H atom. Hence, the formation of mixed clusters will have a strong impact on the diffusivity of pure He clusters, which migrate extremely fast in a H-free tungsten lattice. On the other hand, pure He_M and mixed $\text{He}_M\text{-H}_N$ clusters would act as trapping sites for freely migrating H atoms, which do not feature self-clustering in bulk W. The obtained values for the migration barriers and dissolution energies are summarized in table 4.4.

Cluster type	Migration barrier (eV)	Dissolution energy (eV)
He	0.07 ± 0.07	–
He_2	0.09 ± 0.01	–
He_3	0.17 ± 0.01	–
He_4	0.28 ± 0.02	–
He-H	0.21 ± 0.03	0.52 ± 0.02
$\text{He}-\text{H}_2$	0.25 ± 0.03	0.51 ± 0.04
$\text{He}_2\text{-H}$	0.23 ± 0.02	0.79 ± 0.01
$\text{He}_2\text{-H}_2$	0.25 ± 0.04	0.77 ± 0.08
$\text{He}_3\text{-H}$	0.40 ± 0.03	0.98 ± 0.09

Table 4.4: Migration barriers and dissolution energies for He and mixed $\text{He}_M\text{-H}_N$ clusters.

4.7. H bubble formation in W in presence of He_M clusters

As it was demonstrated in the previous sections of this chapter, He atoms exhibit strong attraction in the bulk tungsten leading to so-called self-trapping i.e. He assisted Frenkel pair formation (see figure 4.8). This means that a cluster of He atoms can push out a lattice W atom creating a vacancy and a self-interstitial atom. On the other hand, H atoms exhibit weak interaction between each other in the bulk tungsten (see figure 4.2(a)) and require high concentration in order to be able to generate defects in W [42]. The synergetic effects of these two different mechanisms of defect creation in tungsten during simultaneous presence of H and He in the material was studied at finite temperature by means of MD simulations.

The computational cell was a cube with size of $10 \times 10 \times 10$ lattice units in which the crystal's $\langle 100 \rangle$ directions were aligned with the coordinate axes. Periodic boundary conditions were applied in all three directions. The needed number of He atoms was assigned random positions in the crystal at the beginning of the simulation, and H atoms were added to the computation cell in random positions with a certain periodicity. The temperature was kept constant in all the simulations and was equal to 800 K. The interatomic potential EAM2 and NVT ensemble were used. The initial number of He atoms varied from zero to six, the Hydrogen In-compare Periodicity (HIP) was varied in 30 – 90 ps/atom range in all the simulations. A lattice site was considered empty if no W atoms were detected inside the sphere of radius equal to $0.2 \times a_0$, encircled around the site, where a_0 is the lattice parameter. The value of 0.2 was chosen so as the sphere radius was larger than the thermal oscillation amplitude. Only a persistently empty lattice site corresponds to a vacancy, which is why the W atom ejection is detected only if an empty lattice site was detected repeatedly in 80 % of the 300 ps timespan.

The simulation series results regarding H concertation at the moment of detection of vacancy formation are shown in figure 4.12. For every considered combination of the initial number of He atoms and HIP a number of successful simulation runs varied from eight to 14 with an exception of simulations with six He atoms with low and middle values of HIP, where the number of successful runs was two. Due to the small number of the data points, the best way to represent such dataset is so-called box-and-whiskers plot [43]. The bottom and the top of the box indicate H-spread or Interquartile Range (IQR), i.e. the area containing 50 % of the data. The band inside the box represents the median of the data and “whiskers” indicate the extremes of the dataset. The plus symbols on the graph show outliers, i.e. the data points that lie further than a border value of $1.5 \times \text{IQR}$ from the median. The box-and-whiskers plot gives an opportunity to visually represent the properties of the distribution of the data such us spread and symmetry. For the two cases where number of data points in dataset was two, the raw data was plotted (coloured stars)

since boxplot for such datasets is misleading. For better visualization of the trend of critical H concentration evolution, a red dashed line connecting median values for HIP = 50 ps/atom was added.

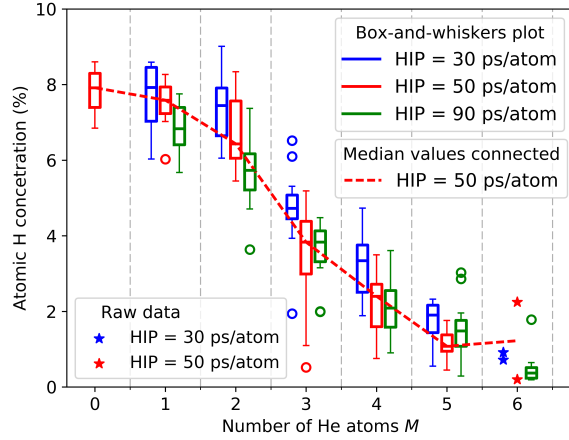


Figure 4.12: The critical atomic H concentration variation with the number of He atoms in the W crystal for three values of HIP

The results presented on the figure 4.12 show decrease of the critical H concentration with an increase of the number of helium atoms present in the simulation box. The spread of the data allows to estimate the decrease of the critical H concentration approximately by the factor of eight, thus showing the clear evidence of the synergy between hydrogen and helium atoms when they eject a tungsten atom. At the same time the hydrogen income periodicity presented by different colours on the figure has a small effect on the critical H concentration with a tendency to higher values for low HIP and lower values for high values of HIP. The helium atoms were found to bond together at the very beginning of the simulation, thus causing lattice distortion and facilitating the tungsten atom ejection. It was concluded that if more than four He atoms were present in the computation cell, then the vacancy formation process was not primarily driven by hydrogen concentration anymore, but by the helium atoms themselves. Thus the presence of small clusters of He atoms in the material during H implantation enhances the H bubble formation. Clusters containing more than four He atoms act as additional traps for H atoms. Both of these effects would increase the overall H retention in the material. However to give a qualitative estimations of the effect a full scale mean field theory simulations of mixed He-H implantation in the material is needed. MS and MD simulations presented in this chapter provide the necessary input for this

type of simulations such as diffusion parameters of He_N and $\text{He}_M\text{-H}_N$ clusters and parametrization of Frenkel pair formation mechanisms.

4.8. Conclusion

Two versions of a new interatomic potential for W-H-He system in the framework of EAM model were developed. On the basis of the benchmarking of the potentials by comparison with DFT data and predictions of BOP potential it was concluded that version EAM2 of the potential is the most suitable for further MS and MD simulations. Based on MS calculations regarding the stability of Vacancy-H-He clusters, LTD parameterisation for binding energy of the constituents of large Vacancy-H-He clusters (bubbles) was proposed. Results of MD simulations at finite temperature allowed to parametrize diffusion of H atom in the bulk tungsten as well as in the vicinity of ED core confirming fast one-dimensional migration along the dislocation core. In the case of SD one dimensional migration was not observed which was related to the fact that the potential does not predict all the attraction position of H at the SD core. Thermal stability and diffusion properties of He_N and $\text{He}_M\text{-H}_N$ clusters were also studied and parametrized. The dissociation energies were found to be in an excellent agreement with MS and DFT predictions of binding and migration energies. The obtained migration barriers of mixed $\text{He}_M\text{-H}_N$ clusters were higher than for pure He_N clusters, being close to the values of H migration barrier. Finally, an effect of He atoms on H bubble formation mechanism in bulk W was investigated. It was found that the presence of He atoms in the material facilitate defect formation by decreasing the critical H concentration needed for Frenkel pair formation. On top of that, due to the self-trapping mechanism He atoms can create vacancies are thus additional source of traps for H. The results reported in this chapter provide a thorough insight into the mechanisms that determine H retention in W. However, in order to properly investigate the effect of all the considered mechanisms on the H retention during real experiments one has to perform a full scale mean field theory simulation using the obtained parametrizations. The next chapter focuses on such simulations.

References

- [1] X.-C. Li, X. Shu, Y.-N. Liu, F. Gao, and G.-H. Lu. *Modified analytical interatomic potential for a W–H system with defects*. Journal of Nuclear Materials, 408(1):12–17, 2011.
- [2] G. D. Samolyuk, Y. N. Osetsky, and R. E. Stoller. *The influence of transition metal solutes on the dislocation core structure and values of the Peierls stress and barrier in tungsten*. Journal of Physics: Condensed Matter, 25(2):025403, 2013.
- [3] P. M. Derlet, D. Nguyen-Manh, and S. L. Dudarev. *Multiscale modeling of crowdion and vacancy defects in body-centered-cubic transition metals*. Physical Review B, 76(5):054107, 2007. PRB.
- [4] M. C. Marinica, V. Lisa, M. R. Gilbert, L. Proville, S. L. Dudarev, J. Marian, G. Bencteux, and F. Willaime. *Interatomic potentials for modelling radiation defects and dislocations in tungsten*. Journal of Physics: Condensed Matter, 25(39):395502, 2013.
- [5] M. S. Daw and M. I. Baskes. *Embedded-atom method: Derivation and application to impurities, surfaces, and other defects in metals*. Physical Review B, 29(12):6443–6453, 1984. PRB.
- [6] M. W. Finnis and J. E. Sinclair. *A simple empirical N-body potential for transition metals*. Philosophical Magazine A, 50(1):45–55, 1984.
- [7] F. Ercolessi, E. Tosatti, and M. Parrinello. *Au (100) Surface Reconstruction*. Physical Review Letters, 57(6):719–722, 1986. PRL.
- [8] G. J. Ackland and R. Thetford. *An improved N-body semi-empirical model for body-centred cubic transition metals*. Philosophical Magazine A, 56(1):15–30, 1987.
- [9] R. A. Johnson and D. J. Oh. *Analytic embedded atom method model for bcc metals*. Journal of Materials Research, 4(05):1195–1201, 1989.
- [10] S. M. Foiles. *Interatomic interactions for Mo and W based on the low-order moments of the density of states*. Physical Review B, 48(7):4287–4298, 1993. PRB.
- [11] Y. R. Wang and D. B. Boercker. *Effective interatomic potential for body centered cubic metals*. Journal of Applied Physics, 78(1):122–126, 1995.
- [12] X. W. Zhou, H. N. G. Wadley, R. A. Johnson, D. J. Larson, N. Tabat, A. Cerezo, A. K. Petford-Long, G. D. W. Smith, P. H. Clifton, R. L. Martens,

- and T. F. Kelly. *Atomic scale structure of sputtered metal multilayers*. Acta Materialia, 49(19):4005–4015, 2001.
- [13] K. Ling Ti, L. Xin Yu, L. Wen Sheng, L. Jian Bo, and L. Bai Xin. *Interfacial Reaction of W/Cu Examined by an n-body Potential through Molecular Dynamics Simulations*. Japanese Journal of Applied Physics, 41(7R):4503, 2002.
- [14] H. R. Gong, L. T. Kong, W. S. Lai, and B. X. Liu. *Glass-forming ability determined by an n -body potential in a highly immiscible Cu-W system through molecular dynamics simulations*. Physical Review B, 68(14):144201, 2003. PRB.
- [15] R. F. Zhang, L. T. Kong, H. R. Gong, and B. X. Liu. *Comparative study of metastable phase formation in the immiscible Cu-W system by ab initio calculation and n -body potential*. Journal of Physics: Condensed Matter, 16(29):5251, 2004.
- [16] R. F. Zhang, Y. X. Shen, H. R. Gong, L. T. Kong, and B. X. Liu. *Atomistic Modeling of Metastable Phase Selection of a Highly Immiscible Ag–W System*. Journal of the Physical Society of Japan, 73(7):2023–2027, 2004.
- [17] R. F. Zhang, Y. X. Shen, H. F. Yan, and B. X. Liu. *Formation of Amorphous Alloys by Ion Beam Mixing and Its Multiscale Theoretical Modeling in the Equilibrium Immiscible Sc-cW System*. The Journal of Physical Chemistry B, 109(10):4391–4397, 2005.
- [18] X. D. Dai, J. H. Li, and Y. Kong. *Long-range empirical potential for the bcc structured transition metals*. Physical Review B, 75(5):052102, 2007. PRB.
- [19] C. Björkas, K. Nordlund, and S. Dudarev. *Modelling radiation effects using the ab-initio based tungsten and vanadium potentials*. Nuclear Instruments and Methods in Physics Research Section B: Beam Interactions with Materials and Atoms, 267(18):3204–3208, 2009.
- [20] N. Juslin and B. D. Wirth. *Interatomic potentials for simulation of He bubble formation in W*. Journal of Nuclear Materials, 432(1–3):61–66, 2013.
- [21] J. Wang, Y. L. Zhou, M. Li, and Q. Hou. *A modified W–W interatomic potential based on ab initio calculations*. Modelling and Simulation in Materials Science and Engineering, 22(1):015004, 2014.
- [22] L. Romaner, C. Ambrosch-Draxl, and R. Pippan. *Effect of Rhenium on the Dislocation Core Structure in Tungsten*. Physical Review Letters, 104(19):195503, 2010. PRL.

- [23] H. Li, S. Wurster, C. Motz, L. Romaner, C. Ambrosch-Draxl, and R. Pippan. *Dislocation-core symmetry and slip planes in tungsten alloys: Ab initio calculations and microcantilever bending experiments.* Acta Materialia, 60(2):748–758, 2012.
- [24] S. L. Frederiksen and K. W. Jacobsen. *Density functional theory studies of screw dislocation core structures in bcc metals.* Philosophical Magazine, 83(3):365–375, 2003.
- [25] S. Ismail-Beigi and T. A. Arias. *Ab Initio Study of Screw Dislocations in Mo and Ta: A New Picture of Plasticity in bcc Transition Metals.* Physical Review Letters, 84(7):1499–1502, 2000. PRL.
- [26] V. Vitek, R. Perrin, and D. Bowen. *The core structure of $\frac{1}{2} (111)$ screw dislocations in bcc crystals.* Philosophical Magazine, 21(173):1049–1073, 1970.
- [27] K. O. E. Henriksson, K. Nordlund, J. Keinonen, D. Sundholm, and M. Patzschke. *Simulations of the Initial Stages of Blistering in Helium Implanted Tungsten.* Physica Scripta, 2004(T108):95, 2004.
- [28] R. Johnson, W. Wilson, P. C. Gehlen, J. Beeler, and R. I. Jaffee. *Interatomic potentials and simulation of lattice defects.* In Battelle Institute Materials Science Colloquia, Plenum, New York, 1972.
- [29] N. Juslin, P. Erhart, P. Träskelin, J. Nord, K. O. E. Henriksson, K. Nordlund, E. Salonen, and K. Albe. *Analytical interatomic potential for modeling nonequilibrium processes in the W-C-H system.* Journal of Applied Physics, 98(12):123520, 2005.
- [30] X.-C. Li, X. Shu, Y.-N. Liu, Y. Yu, F. Gao, and G.-H. Lu. *Analytical W–He and H–He interatomic potentials for a W–H–He system.* Journal of Nuclear Materials, 426(1–3):31–37, 2012.
- [31] C. S. Becquart and C. Domain. *A density functional theory assessment of the clustering behaviour of He and H in tungsten.* Journal of Nuclear Materials, 386–388(0):109–111, 2009.
- [32] K. Heinola, T. Ahlgren, K. Nordlund, and J. Keinonen. *Hydrogen interaction with point defects in tungsten.* Physical Review B: Condensed Matter, 82(9):094102, 2010. PRB.
- [33] D. F. Johnson and E. A. Carter. *Hydrogen in tungsten: Absorption, diffusion, vacancy trapping, and decohesion.* Journal of Materials Research, 25(02):315–327, 2010.

- [34] S. Plimpton. *Fast Parallel Algorithms for Short-Range Molecular Dynamics*. Journal of Computational Physics, 117(1):1 – 19, 1995.
- [35] R. Frauenfelder. *Solution and Diffusion of Hydrogen in Tungsten*. Journal of Vacuum Science & Technology, 6(3):388–397, 1969.
- [36] H.-B. Zhou, Y.-L. Liu, S. Jin, Y. Zhang, G.-N. Luo, and G.-H. Lu. *Towards suppressing H blistering by investigating the physical origin of the H-He interaction in W*. Nuclear Fusion, 50(11):115010, 2010.
- [37] A. Takayama, A. M. Ito, Y. Oda, and H. Nakamura. *First principles investigation of cluster consisting of hydrogen–helium atoms interstitially-trapped in tungsten*. Journal of Nuclear Materials, 463:355–358, 2015.
- [38] Y. Ueda, M. Fukumoto, J. Yoshida, Y. Ohtsuka, R. Akiyoshi, H. Iwakiri, and N. Yoshida. *Simultaneous irradiation effects of hydrogen and helium ions on tungsten*. Journal of Nuclear Materials, 386–388:725–728, 2009.
- [39] M. Miyamoto, D. Nishijima, M. J. Baldwin, R. P. Doerner, Y. Ueda, K. Yasunaga, N. Yoshida, and K. Ono. *Microscopic damage of tungsten exposed to deuterium–helium mixture plasma in PISCES and its impacts on retention property*. Journal of Nuclear Materials, 415(1, Supplement):S657–S660, 2011.
- [40] C. S. Becquart and C. Domain. *Migration Energy of He in W Revisited by Ab Initio Calculations*. Physical Review Letters, 97(19):196402, 2006. PRL.
- [41] J. Boisse, C. Domain, and C. S. Becquart. *Modelling self trapping and trap mutation in tungsten using DFT and Molecular Dynamics with an empirical potential based on DFT*. Journal of Nuclear Materials, 455(1–3):10–15, 2014.
- [42] Y. N. Liu, T. Ahlgren, L. Bokonte, K. Nordlund, X. Shu, Y. Yu, X. C. Li, and G. H. Lu. *Mechanism of vacancy formation induced by hydrogen in tungsten*. AIP Advances, 3(12), 2013. Cited By :12 Export Date: 4 October 2016.
- [43] J. W. Tukey. *Exploratory data analysis*. Adisson-Wesley, New York, 1977.

5

Macroscopic retention assessed by mean field rate theory

In the chapters 3 and 4 the results of atomistic simulations of H behaviour in W were reported. Unfortunately due to computational limitations, atomistic techniques do not allow to perform full scale simulations of experiments involving plasma exposure of W. However these techniques provide parametrizations of the key processes guiding H retention in tungsten. After careful selection of these parametrizations, they can be used in the core of mean field theory techniques for full scale simulations. In this chapter a numerical Rate Theory [1] simulation in the framework of dislocation driven H retention in W is described. The parametrizations of the key processes for the model were taken from atomistic simulations and benchmarked prior the application of the tool for full scale simulations. Finally the simulation tool was used to analyse the experimental results in terms of prediction of H bubble and blister formation and H release during Thermal Desorption Spectroscopy (TDS).

5.1. Numerical model of bubble nucleation on dislocations

The rate theory model previously formulated in chapter 3 was implemented in a numerical simulation tool in order to investigate the exposure conditions (i.e. flux and temperature) resulting in the bubble growth and blister formation. A schematic

picture of the numerical system used in the simulations is shown in figure 5.1. The system is one-dimensional where material is divided into slabs of equal width λ_d . Each slab corresponds to a single nucleation site and is fed with H by a source term $S(x)$ defined from the steady state solution for the bulk concentration of H atoms discussed in section 3.5 (see equation 3.7). H atoms accumulate into H_N clusters at dislocation trapping sites following a binding energy function, and H atom can be dissolved from a H_N clusters at a rate defined by the equation:

$$R^-(i) = \nu C(i) \exp\left(-\frac{\Delta E_{Bin}(N) + \Delta E_D}{kT}\right) \quad (5.1)$$

where ν is the attempt frequency, $C(i)$ is the trap (or trapped cluster) concentration at slab number i , $\Delta E_{Bin}(N)$ is the binding energy of a H atom to the trapped H_N cluster, ΔE_D is H migration barrier in bulk tungsten, k is Boltzmann constant. The amount of H atoms that escapes from the traps is redistributed between neighbouring slabs. Thus, the amount of trapped H at a certain slab i is defined by the balance of a source term $S(x)$, dissolution rate (R^-) and exchange between neighbouring slabs (numbers $i-1$ and $i+1$):

$$\frac{\partial C_H(i)}{\partial t} = S(x) + \frac{1}{2}[R^-(i-1) + R^-(i+1)] - R^-(i) \quad (5.2)$$

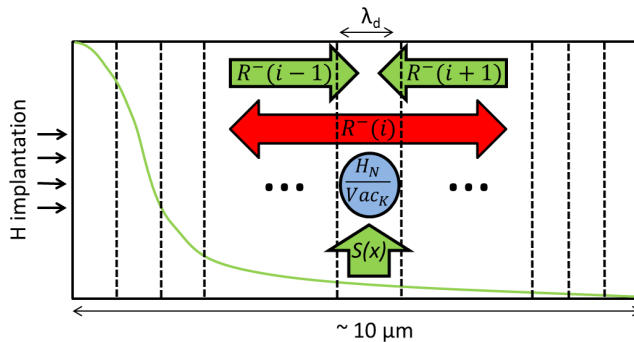


Figure 5.1: Schematic picture of the model

The size of H_N clusters growing during the exposure is determined by a simulation that follows the number of vacant sites generated by the jog punching mechanism. To introduce the jog punching mechanism that allows a bubble to grow, one has to introduce a threshold value for the number of trapped H atoms per vacancy (N/K) in a $Vac_K H_N$ complex beyond which the jog punching mechanism starts to operate. The main parameters of the model, which define the conditions for the bubble growth, is the binding energy of a H atom to a trapped $Vac_K H_N$

complex, and the threshold size for a H_N cluster beyond which it is converted into H_{N+1} -VJog configuration (see figure 3.4 for the schematic picture of the process).

5.2. Parametrization of binding energy of H atom to a vacancy type dislocation jog and threshold for loop punching mechanism

Firstly, the binding energy of H_N cluster to a screw dislocation and to a vacancy jog (VJog) on a screw dislocation was considered. Figure 5.2 compares the binding energy of a H atom to a H_{N-1} cluster trapped at a vacancy (Vac) [2–4] and trapped at the dislocation vacancy jog, obtained by *ab initio* and reported in chapter 3 [5]. As can be seen from the figure, there is no significant difference between the evolution of the binding energy at a vacancy and at the dislocation jog. The red dashed line represents a function numerically fitted to these *ab initio* results, which are valid for small H_N clusters forming as nuclei for H bubbles. For the well-developed H bubbles, one cannot apply the *ab initio* fitted function. The formula obtained within the so-called Liquid-Tear Drop (LTD) model [6] reported in section 4.2 was used as a limiting case for large bubbles. The model is based on the balance of volume and surface energies and is shown with the blue dashed line in figure 5.2.

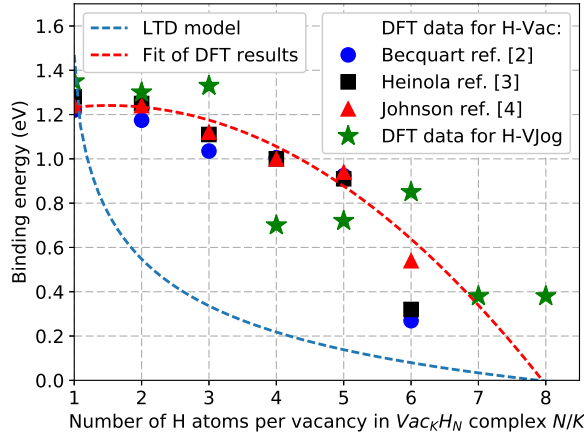


Figure 5.2: H binding energy to a vacancy (H-Vac) and to a vacancy type dislocation jog H-VJog complexes and approximations

To define the threshold number of H atom per vacancy (N/K) that would allow

a H bubble to grow, the loop punching mechanism when a pressurized gas bubble increases its volume by pushing out dislocation loops was considered. Pressure is exerted on the bubble surface and the critical one needed to create a dislocation loop was defined as [7]:

$$P_{lp} = \frac{2\gamma + \mu b}{R_b} \quad (5.3)$$

where $\gamma = 2.65 \text{ N/m}$ is the surface tension, $\mu = 158.6 \text{ GPa}$ is the shear modulus, $b = 2.7$ is the Burgers vector of the $\frac{1}{2}\langle 111 \rangle$ loop, and R_b is the bubble radius. The values for the surface tension (γ) and shear modulus (μ) were taken from [8, 9]. The variation of the critical pressure as a function of the bubble size (expressed as a number of vacant sites K) is plotted in figure 5.3 on the right-hand side Y axis. To estimate the critical concentration of hydrogen contained in the bubble needed to induce the dislocation loop emission, the following equation of state for hydrogen from [10] was used:

$$N_b = \frac{4\pi R_b^3 N_a}{3\nu(p, T)} \quad (5.4)$$

where R_b is the bubble radius, N_a is the Avogadro constant, and $\nu(p, T)$ is the molar volume from the equation of state.

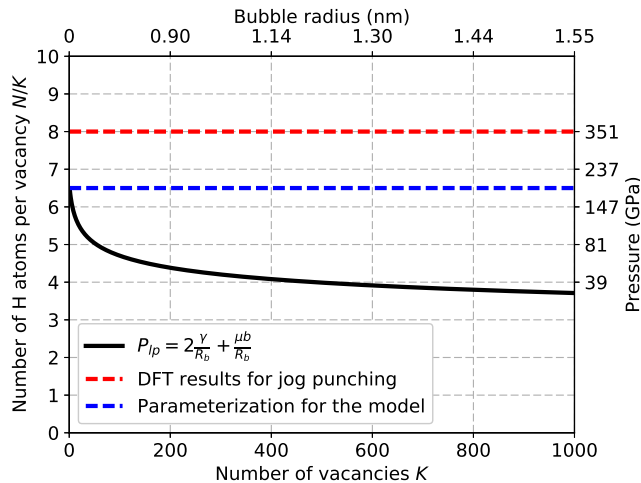


Figure 5.3: Estimation of the threshold value for the loop punching mechanism

The resulting number of H atoms per vacancy N/K corresponding to the loop punching pressure is shown in figure 5.3 on the left Y axis. As one can see, the ratio obtained using elasticity theory and equation of state goes from six to four

with increasing of the bubble size up to ~ 4 nm (1000 vacancies). On the other hand, the critical ratio obtained from *ab initio* calculations is eight. Here, the sensitivity of the results by varying the N/K value within these two limits should be explored.

5.3. Defining the parameters of the model with experimental results

Prior to performing the simulations, it is important to understand the influence of the choice of the binding energy function on the nucleation of a H bubble (i.e. punching out the first lattice atoms and creating a vacancy jog on the dislocation). As it was said in the previous section, there is an uncertainty associated with the binding energy and N/K ratio for the jog punching. The first uncertainty comes from the two models for the binding energy function, namely: LTD model from [6] and the fit to *ab initio* results from [5], shown in figure 5.2. These two models were applied in order to investigate the evolution of the growth of H_N clusters and see whether the condition for the jog-punching is met. To define the simulation system, the experimental conditions were considered. The intensive blistering (presumably originating as a result of loop punching) was reported in [11] after the exposure at 450 K with an ion flux of $10^{24} \text{ m}^{-2}\text{s}^{-1}$. It was found that using the LTD model the average size reached by the clusters is 3.6 H atoms per trapping site, while using the *ab initio* fit it is 7. Clearly, the LTD model does not satisfy the condition for the jog-punching in the nucleation regime when H clusters are still very small. That was expected because the extrapolation of the linear elasticity theory to describe atomic-size bubbles is inappropriate. The *ab initio* parametrized model allows for the jog punching mechanism to take place. However, the *ab initio* data are available only for the punching of the first jog. Thus, the information about the binding energy function for the transition from atomic-scale bubbles to classical bubbles should be filled using empirical interatomic potentials.

A parametric study varying threshold for jog punching hydrogen to vacancy ratio N/K from five to seven was performed in order to provide a physical choice for the critical pressure. The depth distribution of H deposited in the material for the experimental conditions applied in [11] was computed. In the original experiment the H depth profile was measured by means of Nuclear Reaction Analysis (NRA) technique. In particular, the plasma exposure of 50 eV ions at 450 K with a flux of $10^{24} \text{ m}^{-2}\text{s}^{-1}$ was considered. In these calculations, the critical nucleation depth was the primary result of interest. Experimental profiles practically ceased at a depth around $4 - 5 \mu\text{m}$. Three different profiles for threshold N/K values of 5.0, 6.5, and 7.0 are shown on the figure 5.4. In case of a low value of the threshold (5.0), the evaporation of H atoms from the trap at 450 K is too low to influence the

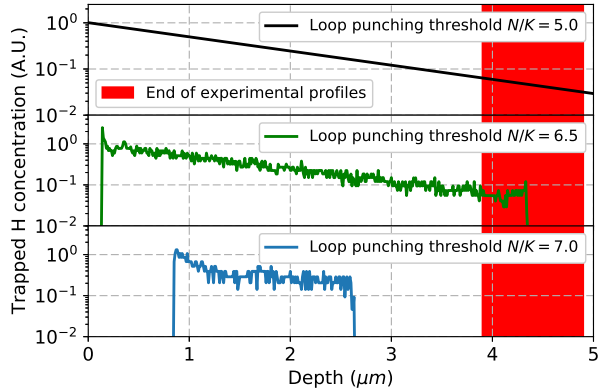


Figure 5.4: Sensitivity of the system on the loop punching parameters

growth of the bubble and the threshold value for jog-punching is reached easily (this also explains the fact that there is almost no fluctuations in this depth profile). The calculations were performed for the system with a depth up to $5 \mu\text{m}$, but it can be stated that in case of $N/K = 5.0$, the growth of the bubble continues at a depth deeper than several tens of μm , which is not in line with the NRA measurements. In the case of the highest value of the threshold (7.0), nucleation of bubbles ceased at a depth around $2.5 \mu\text{m}$ meaning that beyond this level dislocations do not serve any more as nucleation sites for bubbles and act as migration networks for H diffusion. The best fit for the experimental profile is obtained for N/K , at which the nucleation stops at a depth around $4.5 \mu\text{m}$. Therefore, this threshold was used for the calculations addressing the effect of temperature and flux on the nucleation of stable bubbles.

5.4. Prediction of flux-temperature conditions for the jog-punching mechanism to function

A parametric study employing the above formulated kinetic model and here derived binding energy function was performed in order to study the conditions for the bubble formation and growth. The incident flux and ambient temperature were varied to cover the ranges relevant for ITER conditions. The value of the critical temperature was defined for every value of the flux. At a temperature higher than critical value, no bubble formation at dislocation networks by the jog- and then

later by loop-punching is foreseen. Boundaries corresponding to the conditions in which the loop punching is expected to function and in which H clusters do not convert into stable bubbles are provided as a results of these calculations. The boundaries obtained for W with dislocation density of $0.5 \times 10^{12} \text{ m}^{-2}$, which is typical for a stress-relieved BCC metal, is shown in figure 5.5.

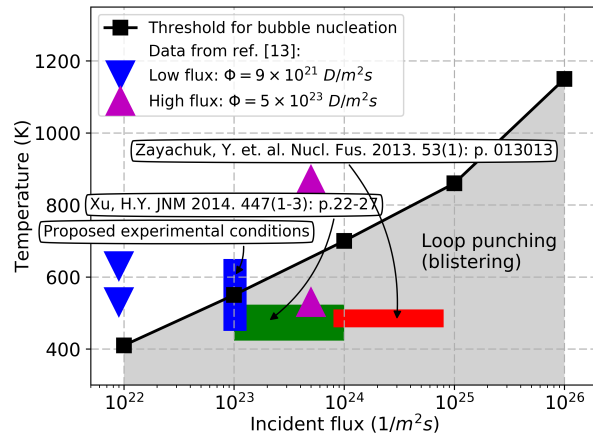


Figure 5.5: Exposure temperature vs. flux required for the bubble growth

Several experiments that addressed the effect of a low energy ion beam or plasma on the surface of tungsten reported blistering [11–13]. The range of doses and temperatures in which blisters were reported is shown in figure 5.5 by coloured boxes. In general, the observation of blisters is registered below 700 K for fluxes up to $10^{24} \text{ m}^{-2}\text{s}^{-1}$, which is in line with the prediction of our model.

5.5. Modelling TDS release: universal binding energy fit depending on the bubble size

In the framework of the above mentioned dislocation-driven model of H trapping, one can distinguish the formation of four types of defects: (I) sub-critical H clusters (up to eight H atoms), which are not yet capable to punch out W matrix atoms; (II) super-critical H clusters, whose transformation into H_NVJog configuration is energetically favourable; (III) large super-critical clusters, which have already released several jogs for itself and grow further; and finally (IV) nanometric bubble attached to a dislocation line, whose properties (in terms of H trapping) are equivalent to the usual bubble in W bulk. Here, the trapping and release from

the defects of type I was not considered, since these clusters are unstable above 450 K, while the latter being the lower bound of the relevant temperature range.

In work [14], a rate theory model of H desorption from tungsten surface and subsurface defects demonstrated that H release at temperatures, higher than 600 K is not affected by surface recombination. Here, high temperature desorption stage (above 600 K) was assessed, and therefore an immediate release of H from the surface after detrapping from the nano-cavities and vacancies was assumed. The main parameter of the model that defines the release rate of H from a certain type of a trapping defect is the binding energy (ΔE_{Bin}). As it was mentioned before, *ab initio* calculations showed that dislocation jogs exhibit trapping properties similar to vacancies (see figure 3.5). The corresponding value of the binding energy is 1.24 eV for one H atom and it decreases with an increase of H atoms trapped at the jog. The dependence of $H_N V J o g$ binding energy on number of H atoms (N) in a cluster is plotted in figure 5.6. These data points were fitted in order to generate a family of ΔE_{Bin} functions for super-critical clusters. Similarly to equation 5.1 for the release rate from such defects was defined as:

$$R_J^- = \nu C_H \exp \left(-\frac{\Delta E_{Bin} + \Delta E_D}{kT} \right) \quad (5.5)$$

where C_H is concentration of trapped H atoms (assuming that each H in a cluster has equal probability for detrapping event), ν is the Debye frequency, ΔE_{Bin} is the binding energy, ΔE_D is the migration energy (0.4 eV is taken from Frauenfelder's data [15]), k is Boltzmann constant, T is temperature.

For large vacancy clusters (i.e. nano-voids, type IV defects in the above notation) it is reasonable to consider that the binding energy is equal to the permeation energy, i.e. ~ 2.0 eV [4]. Under this assumption, one can assign the high temperature TDS peak (usually seen in low flux exposures around 700 – 900 K) to the release from bubbles [16]. However, the TDS spectra obtained after the high flux exposures, at high temperature (above 600 K) and/or high dose (above 10^{26} D/m²), reveal broadening or presence of extra peaks above 900 K [17, 18]. These high temperature release stages cannot be simply explained by detrapping from voids with the binding energy of 2.0 eV, while there are no reasons to assume the presence of any stronger traps than voids/cavities.

To address the issue of high temperature detrapping stage, the information available from atomic scale was analysed. *Ab initio* and Molecular Dynamics simulations showed that H tends to occupy off-centred position in a vacancy, experiencing weak attraction to W atoms [3, 19]. This implies that H atoms, when filling a void, first should occupy the inner surface positions and then fill the centre.

Thus for the binding energy corresponding to the H trapped at nm size bubbles (type IV defects) the results of *ab initio* calculations for the transition of H atom from adsorbed state on W surface into the bulk material [4] were used. These

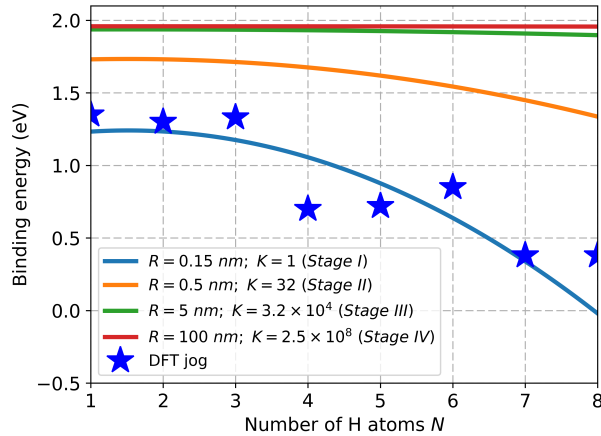


Figure 5.6: Illustration of binding energy master curve used in simulations. R is the defect open volume radius, K is the corresponding number of vacancies that defect occupies.

calculations reported 1.96 eV as a value of the adsorption barrier and attempt frequency of $1.07 \times 10^{13} \text{ s}^{-1}$. However, the expression for the release rate should be different from equation 5.5, since only atoms in adsorbed state on the inner surface of the bubble are available for the detrapping reaction. Thus, the release from nm-scale bubbles was defined by:

$$R_B^- = C_T N_S \nu_{Ads} \exp\left(-\frac{\Delta E_{Ads}}{kT}\right) \quad (5.6)$$

where C_T is the trap concentration, N_S is the number of available sites for the reaction, this was estimated as a ratio between an inner surface area of the bubble and unit surface for the reaction reported in [4] ($\sqrt{2}a_0$, a_0 is the lattice unit), ν_{Ads} , ΔE_{Ads} are the attempt frequency and adsorption barrier from [4] respectively. To create a universal binding energy master curve accounting for a size of the trapping defect (i.e. number of vacancies released), following expression was proposed:

$$R^- = R_B^- + (R_J^- - R_B^-)^3 \sqrt[3]{K} \quad (5.7)$$

here R_B^- and R_J^- are the release rates for bubble (equation 5.6) and jog (equation 5.5) correspondingly, K is the number of vacancies which the trapping defect occupies. The illustration of the binding energy variation as a function of K is presented in figure 5.6. To compute the H release profile from a defect (of a given size and for a given temperature ramp), it was assumed that after the exposure the defect is filled with H up to a critical pressure (6.5 H atoms per W site), following

the analysis reported in section 5.2 based on the jog-punching mechanism. Then, the H release rate from the defect was calculated as a function of increasing temperature. The goal of such calculations was to define the position of the release peak, depending on the size of the defect and concentration of trapped H.

5.6. Modelling TDS release: linking bubble size with release stage and mechanism of bubble formation

The TDS spectra obtained in [17] were analysed using the above formulated equations. In figure 5.7, a comparison of three normalized TDS spectra with the release rate according to the calculations is represented. Normalization of the TDS spectra was done by dividing each one by the maximum release rate value, since the focus was on correspondence of the peak positions, but not the absolute values of H release. As can be seen from figure 5.7, TDS spectra for the low flux (b) and high flux high temperature exposure (a) reveals similar single peak as in the spectrum measured after ~ 870 K exposure. Temperature position of the peak corresponds to the release from 5 – 10 nm bubbles according to our calculations. TDS spectrum for high flux low temperature exposure (blue triangles) shows two peaks at lower temperature, whose positions can be well fit by imposing the release rate from 1.5 nm and 0.5 nm defects (blue and green lines in figure 5.7(a)).

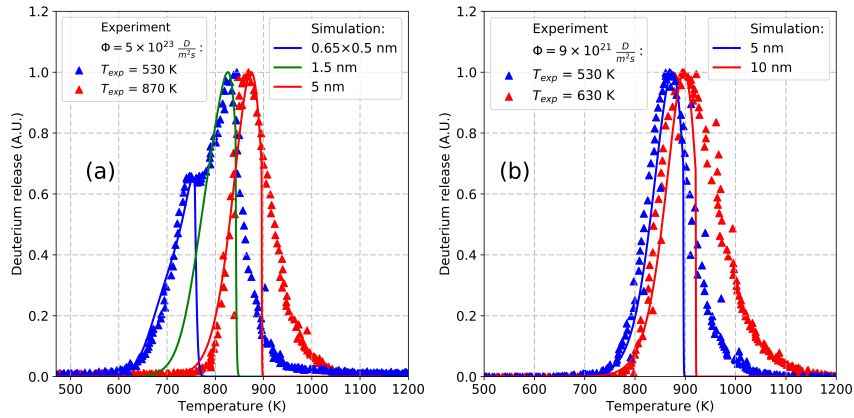


Figure 5.7: Comparison of normalized TDS spectra from work [17] with results of simulation for high flux ($5 \times 10^{23} \frac{D}{m^2 s}$ at 530 K and 870 K) (a) and low flux ($9 \times 10^{21} \frac{D}{m^2 s}$ at 530 K and 630 K)(b) exposures.

The difference in the shape of the peak and peak position of the TDS spec-

tra can be related to a size of releasing defects, and in turn interlinked with the trapping mechanism, governing H retention depending on exposure conditions. In section 5.4, the prediction of experimental flux-temperature combination for the dislocation-driven H trapping leading to the formation of super-critical H clusters (contributing to the TDS release at high temperature) was made. The flux-temperature combination favouring the nucleation of super-critical H bubbles is represented by a grey area in figure 5.5. As one can see, only high flux low temperature exposure is within the range of the dislocation-mediated retention. At the same time, all three other dots are outside the defined area. This is consistent with the fact that only the TDS spectrum after high flux low temperature exposure exhibits two peaks (low temperature peak can be attributed to 1 nm size defects). Whereas, all other spectra show only one peak corresponding to bubbles of 5 – 10 nm size. Small (1 nm scale) defects can be seen as traces of bubble nucleation on dislocation and their subsequent growth. While, if only large defects contribute to the TDS spectra, it is very likely that other mechanisms (such as triple junctions, natural porosity, etc.) but dislocation-driven trapping govern H retention and bubble formation.

The proposed modification for H release rate from nano-metric pressurized bubbles allows one to relate positions of TDS peaks and explain a shift of high-temperature peak up to 200 K under exposure conditions favouring the growth of the bubbles. The occurrence of a single-peak or multiple-peak in TDS spectra can be related to the mechanism of H bubble formation, depending on plasma flux and surface temperature. The proposed here computational analysis was applied to experimental data from [17]. According to it, only a combination of high flux and low temperature exposure ($530\text{ K} - 5 \times 10^{23}\text{ D/m}^2\text{s}$) promotes the nucleation and growth of H bubbles on dislocations, as proposed earlier by jog punching mechanism. In these exposure conditions, the TDS spectra exhibit two well defined peaks attributed to 1 nm size H clusters (presumably, H is trapped in jogs on dislocation lines) and H bubbles (resulting in the high temperature release peak). The three other TDS spectra exhibit only one peak (at high temperature) to be attributed to H bubbles with a size of 5 – 10 nm, nucleated at other "natural" traps such as random grain boundaries and their junctions. Validation of the dislocation-driven mechanism and proposed here H release model can be realized by performing dedicated exposures in $450 - 650\text{ K}$ temperature range at flux of $10^{23}\text{ D/m}^2\text{s}$ (blue rectangle on figure 5.5), which should result in the dislocation-driven trapping below $\sim 500\text{ K}$ to be seen in TDS spectrum as a peak conventionally attributed to vacancy-like defects (i.e. positioned around $600 - 700\text{ K}$).

5.7. Hybrid model of H retention after high flux high temperature exposure

As was demonstrated in section 5.4 (see. figure 5.5), the dislocation-driven trapping mechanism can operate only at a certain plasma flux and material temperature combination: the higher is the temperature - the higher must be the flux to sustain the jog nucleation. According to the estimations, plasma exposure at temperatures above 800 K requires a flux of at least $10^{25} \text{ m}^{-2}\text{s}^{-1}$ for the H clustering to take place. However, recent experiments employing fluxes of about $10^{24} \text{ m}^{-2}\text{s}^{-1}$ at 50 eV biased D plasma exposure of polycrystalline tungsten (non-recrystallized grade with average grain size of $20 \mu\text{m}$ [17]) demonstrated the presence of blisters with high areal density and the high temperature TDS release peak around 800 – 1000 K, suggesting the presence of hydrogen filled bubbles.

Dome-shaped blisters, observed on the exposed surface, also support the assumption of the presence of bubbles growing by plastic deformation. Secondary Ion Mass Spectrometry (SIMS) measurements have confirmed significant trapping of deuterium within first 200 nm under the surface. At the same time, NRA analysis shows that the uptake does not vanish beyond 200 nm and in fact remains constant at a level of 5×10^{-4} atomic fractions through the maximal probing depth of $10 \mu\text{m}$. These experimental facts suggest that non-equilibrium trapping in the sub-surface leading to the formation of bubbles also occurs at high temperature exposures where the trapping on bulk dislocation lines should be ineffective.

The hypothesis of H trapping at Low Angle Grain Boundaries (LAGB) was proposed to explain the high temperature retention. LAGB, in fact, represent a network of edge, screw and mixed dislocations with a relatively small spacing [1]. The network nodes were suggested to act as trapping sites, which attract and emit hydrogen atoms simultaneously. Hydrogen atoms escaping from LAGB trapping sites diffuse along LAGB interfaces either towards the surface or deeper into the bulk and can be captured only by stronger traps such as open volume sites on random (high angle) grain boundaries. Hence, a two-zone model is proposed. The sub-surface trapping (within the first sub-grain) occurs as a non-equilibrium process, i.e. via over-saturation with H leading to the formation of H-filled bubbles. While beyond the first sub-grain H diffuses in a field of static traps and its resulting depth distribution is defined by the concentration and strength of intrinsic traps (e.g. open volume sites on High Angle Grain Boundaries (HAGB)).

In the framework of the above described model, a computational analysis of the H trapping and release by combining the two trapping processes: non-equilibrium and diffusion-based ones. The high flux D plasma exposure at 1000 K of well pre-characterized polycrystalline tungsten of 1 mm thickness was simulated. The exposure was performed at Pilot-PSI [20] plasma generator. The exposure was applied in a single plasma shot of 70 s with the particle flux in the centre of the

sample in the range $(0.8 - 1.0) \times 10^{24} \text{ m}^{-2}\text{s}^{-1}$. The first $10 \mu\text{m}$ (i.e. the first sub-grain) was treated using the non-equilibrium retention model, while the trapping in the rest of the sample was accounted for by the diffusion-based approach.

In particular, the nucleation of bubbles was assumed to take place on the dislocation networks (triple junctions) made of screw, edge and mixed dislocations with frequent nodes, where trapping is expected to be especially strong. The similar set of equations as was reported in section 3.6 was used. The value for the binding energy to dislocation was taken to be 1.0 eV, considering that edge dislocation segments of LAGB will provide the strongest trapping [21, 22]. According to the estimations, the total H concentration stored in LAGB traps lies in the range of $(1.0 - 8.0) \times 10^{-5} \text{ at}^{-1}$ depending on the size of the grain boundary. This amount of trapped H represents 15 to 45 percent of the total H in the material for LAGB sizes from $d = 10 \mu\text{m}$ to $d = 100 \mu\text{m}$. These values for the fraction of H retained in the sub-surface and bulk regions were used as a starting approximation to model H release upon TDS cycle.

An initial depth distribution of trapped H is an important input for the simulation of the release during TDS experiment. As has been discussed above, all trapped H can be subdivided into two fractions corresponding to two regions: sub-surface and bulk, as schematically shown on the right part of the figure 5.8. The sub surface region is characterized by non-equilibrium trapping and bubble formation, while bulk region is described by classical diffusion-trapping model, so that bulk retention is defined by filling natural traps (cavities and open volumes at HAGB). Given the known fraction of H stored in the subsurface region, the concentration of H trapped in the bulk can be defined by the following expression: $C_B = \frac{(1-f)R_T}{d-X_1}$, where R_T – total amount of retained H (as measured experimentally), f is the fraction of trapped H in the subsurface region as estimated here, d is the sample thickness, X_1 is the thickness of the subsurface region. This procedure ensures that the total amount of H released in the simulation will be the same as in the experiment.

For the simulation of H release during the TDS experiment the following set of parameters was used: depth of the subsurface region (i.e. region characterized by non-equilibrium trapping) $X_1 = 10 \mu\text{m}$, fraction of H trapped in the subsurface region $f = 0.23$, subsurface concentration of trapped H $C_S = 1.16 \times 10^{-5} \text{ at}^{-1}$, bulk concentration of trapped H: $C_B = 3.92 \times 10^{-7} \text{ at}^{-1}$. The initial guess for the f parameter was 0.15 on the basis of the estimations given in the previous section. However, a limited variation of the f parameter revealed the best agreement with the experiment by taking $f = 0.23$. The detrapping rate is calculated following the Arrhenius expression. Where, detrapping energy was assumed to be $E_t = 2.0 \text{ eV}$, prefactor (attempt frequency) as assumed to be $\nu = 10^{13} \text{ s}^{-1}$.

The importance of the subsurface plasma-induced defects was demonstrated by analysing different initial depth distributions of trapped H. Subsurface plasma-

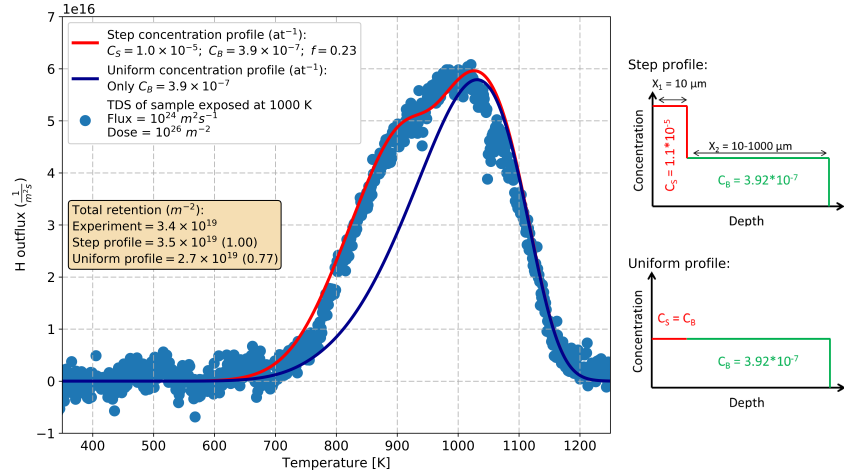


Figure 5.8: Comparison of modelling of H release during TDS with experimental results. The sample was exposed to plasma for 70 s with a particle flux in the centre of the sample in the range $(0.8 - 1.0) \times 10^{24} m^{-2}s^{-1}$. The sample temperature was monitored by infra-red camera and was kept at 1000 K. The heating rate during TDS measurements was 0.5 K/s.

induced defects act as a primary release source and also retrap H diffusing from the bulk towards the surface. The blue curve in figure 5.8 depicts the release of H from a flat H distribution profile over the whole sample depth. Such a profile would correspond to the situation when no plasma-induced defects would be created and natural traps would be filled homogeneously. One can see the classical release peak from a trap with a fixed trapping energy and uniform distribution. The comparison provided in figure 5.8 demonstrates that assigning a two-zone depth distribution of trapped H and assuming only one type of traps (bubbles in the present case), one can reproduce well the TDS spectrum composed of two peaks. Note that the impact of H trapped in the sub-surface region on the appearance of the TDS spectrum can be experimentally revealed by careful polishing the surface (i.e. removing $10 - 20 \mu m$) prior to performing the TDS measurement. The change of the spectra from the red to the blue curve as demonstrated in figure 5.8 is expected after applying such a procedure.

5.8. Conclusion

The model of dislocation driven H retention in tungsten was implemented in a numerical simulation tool using the parametrization obtained from atomistic sim-

ulations. Based on the benchmark calculations a fit to DFT results from [5] was chosen over the LTD model [6] for the description of H binding energy to a bubble. The threshold value for jog punching mechanism of 6.5 H atoms per vacancy was used. The parametrized model was used to predict the exposure conditions for the nucleation of stable bubbles, their growth and subsequent blister formation. Extension of the model with a universal binding energy function describing binding of H to a bubble depending on the growth stage of the bubble allowed one to analyse high temperature release stages of TDS spectra. The shape of the considered spectra was related to the mechanism of H bubble formation and the size of the bubble. Finally a two-zoned depth distribution model of H retention in W with non-equilibrium trap nucleation in the subsurface region was proposed. The model was combined with classical diffusion-trapping code in order to simulate and analyse TDS spectra obtained after high flux high temperature exposures. From the computational analysis performed, it was concluded that high flux high temperature exposures ($T = 1000$ K, flux = 10^{24} D/m²s and fluence of 10^{26} D/m²) result in generation of sub-surface damage and bulk diffusion, so that the retention is driven by both sub-surface plasma-induced defects (bubbles) and trapping at natural defects (such as cavities and HAGB). Experimental conditions and procedures for further validation of the predictions of the simulations were proposed.

References

- [1] G. S. Was. *Fundamentals of radiation materials science: metals and alloys*. Springer, 2016.
- [2] C. S. Becquart and C. Domain. *A density functional theory assessment of the clustering behaviour of He and H in tungsten*. Journal of Nuclear Materials, 386–388(0):109–111, 2009.
- [3] K. Heinola, T. Ahlgren, K. Nordlund, and J. Keinonen. *Hydrogen interaction with point defects in tungsten*. Physical Review B: Condensed Matter, 82(9):094102, 2010. PRB.
- [4] D. F. Johnson and E. A. Carter. *Hydrogen in tungsten: Absorption, diffusion, vacancy trapping, and decohesion*. Journal of Materials Research, 25(02):315–327, 2010.
- [5] D. Terentyev, V. Dubinko, A. Bakaev, Y. Zayachuk, W. V. Renterghem, and P. Grigorev. *Dislocations mediate hydrogen retention in tungsten*. Nuclear Fusion, 54(4):042004, 2014.
- [6] G. Bonny, P. Grigorev, and D. Terentyev. *On the binding of nanometric hydrogen–helium clusters in tungsten*. Journal of Physics: Condensed Matter, 26(48):485001, 2014.
- [7] G. W. Greenwood, A. J. E. Foreman, and D. E. Rimmer. *The role of vacancies and dislocations in the nucleation and growth of gas bubbles in irradiated fissile material*. Journal of Nuclear Materials, 1(4):305–324, 1959.
- [8] K. O. E. Henriksson, K. Nordlund, and J. Keinonen. *Molecular dynamics simulations of helium cluster formation in tungsten*. Nuclear Instruments and Methods in Physics Research Section B: Beam Interactions with Materials and Atoms, 244(2):377–391, 2006.
- [9] R. D. Kolasinski, D. F. Cowgill, and R. A. Causey. *A continuum-scale model of hydrogen precipitate growth in tungsten plasma-facing materials*. Journal of Nuclear Materials, 415(1, Supplement):S676–S679, 2011.
- [10] M. Tkacz and A. Litwiniuk. *Useful equations of state of hydrogen and deuterium*. Journal of Alloys and Compounds, 330–332(0):89–92, 2002.
- [11] Y. Zayachuk, M. t. Hoen, P. Z. v. Emmichoven, I. Uytdenhouwen, and G. v. Oost. *Deuterium retention in tungsten and tungsten–tantalum alloys exposed to high-flux deuterium plasmas*. Nuclear Fusion, 52(10):103021, 2012.

- [12] J. Roth and K. Schmid. *Hydrogen in tungsten as plasma-facing material*. Physica Scripta, 2011(T145):014031, 2011.
- [13] Y. Zayachuk, M. H. J. . t. Hoen, P. A. Z. v. Emmichoven, D. Terentyev, I. Uytdenhouwen, and G. v. Oost. *Surface modification of tungsten and tungsten–tantalum alloys exposed to high-flux deuterium plasma and its impact on deuterium retention*. Nuclear Fusion, 53(1):013013, 2013.
- [14] H. Eleveld and A. van Veen. *Deuterium interaction with impurities in tungsten studied with TDS*. Journal of Nuclear Materials, 191–194, Part A:433–438, 1992.
- [15] R. Frauenfelder. *Solution and Diffusion of Hydrogen in Tungsten*. Journal of Vacuum Science & Technology, 6(3):388–397, 1969.
- [16] O. V. Ogorodnikova, B. Tyburska, V. K. Alimov, and K. Ertl. *The influence of radiation damage on the plasma-induced deuterium retention in self-implanted tungsten*. Journal of Nuclear Materials, 415(1, Supplement):S661–S666, 2011.
- [17] L. Buzi, G. D. Temmerman, B. Unterberg, M. Reinhart, A. Litnovsky, V. Philipps, G. V. Oost, and S. Möller. *Influence of particle flux density and temperature on surface modifications of tungsten and deuterium retention*. Journal of Nuclear Materials, 455(1–3):316–319, 2014.
- [18] Y. Z. Jia, G. De Temmerman, G. N. Luo, H. Y. Xu, C. Li, B. Q. Fu, and W. Liu. *Surface morphology and deuterium retention in tungsten exposed to high flux D plasma at high temperatures*. Journal of Nuclear Materials, 457(0):213–219, 2015.
- [19] L. Sun, S. Jin, X.-C. Li, Y. Zhang, and G.-H. Lu. *Hydrogen behaviors in molybdenum and tungsten and a generic vacancy trapping mechanism for H bubble formation*. Journal of Nuclear Materials, 434(1–3):395–401, 2013.
- [20] G. J. van Rooij, V. P. Veremiyenko, W. J. Goedheer, B. de Groot, A. W. Kleyn, P. H. M. Smeets, T. W. Versloot, D. G. Whyte, R. Engeln, D. C. Schram, and N. J. L. Cardozo. *Extreme hydrogen plasma densities achieved in a linear plasma generator*. Applied Physics Letters, 90(12):121501, 2007.
- [21] W. Xiao and W. T. Geng. *Role of grain boundary and dislocation loop in H blistering in W: A density functional theory assessment*. Journal of Nuclear Materials, 430(1–3):132–136, 2012.
- [22] X.-C. Li, X. Shu, Y.-N. Liu, F. Gao, and G.-H. Lu. *Modified analytical interatomic potential for a W–H system with defects*. Journal of Nuclear Materials, 408(1):12–17, 2011.

“One day I will find the right words, and they will be simple.”

Jack Kerouak (1922 – 1969)

6

Conclusions and outlook

6.1. Conclusions

Main objective of this thesis was to develop a physical model of H retention in tungsten and perform continuum scale simulations in order to analyse and interpret available experimental results recently obtained using European high flux plasma-testing facilities. This allowed one to gain understanding of the physical mechanisms governing H retention under fusion relevant plasma exposure conditions in tungsten with a variety of initial microstructure. The physical model is based on data coming from *ab initio* calculations of H interaction with dislocations, which unravel the complex H-dislocation interaction depending on local atomic arrangement and local hydrogen concentration. Estimations, made using the macroscopic model for retention and release, which was based on the binding and migration energy for the H-dislocation interaction, point to the capability of the model to reproduce experimental trends in a wide temperature range. Further advances of the model were performed to implement the data obtained by large-scale atomistic simulations using semi-empirical interatomic potentials. The interatomic potential for W-H-He system was developed and allowed studying mixed H-He exposures at finite temperature by means of MD simulations. The parameters obtained from MD simulations were used to perform a number of continuum scale simulations and analyse experimental results of tungsten exposed to D plasma.

6.1.1. *Ab initio* calculations

Ab initio results can be summarized as following:

- Interstitial H atom is attracted to the core of the screw dislocation with the binding energy of 0.5 eV;
- The attractive interaction remains when more H atoms are added, slowly decreasing with a number of H atoms added and reaching 0.1 eV for the seventh atom in the cluster;
- When the number of H atoms accumulated on the dislocation core exceeds eight the re-arrangement of lattice W atoms occurs resulting in the formation of the interstitial-vacancy jog pair on the dislocation core and referred here as "jog-punching" mechanism;
- The binding properties of a vacancy jog in the dislocation core appeared to be very similar to a bulk H-Vacancy interaction with the binding of 1.24 eV for a single H atom decreasing to 0.7 for seven H atoms;

All of the above suggests that nucleation of H bubble is possible on screw dislocations by means of "jog-punching" mechanism.

However, binding between H atoms in compact clusters attached to the screw dislocation core is rather weak if calculated for H atoms escaping to dislocation core and even becomes negligible for clusters containing more than three H atoms. Accounting for a low value of the migration energy of H atoms along the dislocation core (~ 0.1 eV), the formation of the cluster elongated along the core rather than the formation of a compact (spherical) cluster needed for "jog-punching" mechanism is more favourable. This fact indicates that homogeneous nucleation of H bubbles on straight dislocation lines is questionable. Thus, the nucleation of the spherical clusters (precursors of bubbles) most likely occurs on some imperfections at the dislocations such us dislocation junctions, kinks and jogs, which always present in the commercially available materials due to fabrication process.

6.1.2. Model of dislocation mediated H retention in tungsten

Motivated by the above-noted results of the *ab initio* calculations a model of H trapping at dislocations in tungsten was developed and numerically implemented. The model is based on the following assumptions:

- Low energy plasma implantation process is equivalent to a diffusion of H in a field of traps (dislocations) with a boundary condition of constant concentration of H on the surface of the sample. This process is described by a differential equation with a steady state solution for H depth distribution;

- Binding of H atoms to the dislocation lines together with low migration barrier along the dislocation core suggests that H quickly migrates along the dislocation core before getting trapped by another microstructural defect;
- Nucleation and growth of H bubbles occurs by means jog-punching mechanism on the dislocation core or on pre-existing imperfections on the dislocation core;

Balance rate theory calculations within the model allow one to reproduce the following experimental qualitative trends:

- Experimental H depth profiles in a range of few micrometres as measured by NRA techniques;
- Mean distance between H bubbles attached to dislocation lines (being 80 – 250 nm) in good agreement with TEM investigations;
- Saturation of the total amount of retained H in the sub-surface with the increase of the dose;
- Profiles of the TDS spectra, revealing the two channels of H release from the bubbles attached to dislocations, namely: release to the bulk from the bubble surface and release via dislocation lines;

6.1.3. Molecular static and molecular dynamics simulations

In order to study mechanisms of H retention on a large scale and at finite temperatures, the EAM interatomic potential for W-H-He system was developed. The base potential for W-W interaction was chosen by assessing 14 already available potentials. Since the main interest was the interaction of H with dislocations, the potential with the best performance regarding stability and symmetry of the screw dislocation core was chosen. The potential was validated by comparison of the results with ab initio and BOP model regarding H-H and H-He pair interaction in bulk tungsten and vacancy/dislocation-H-He interaction.

The results of the MD simulations can be summarised as following:

- Parameters of H and He diffusion in the bulk as well as at the dislocation core were obtained;
- Diffusion parameters of pure He and mixed He-H clusters were obtained in a wide temperature range;
- He and H assisted Frenkel pair formation (self-trapping and punching of self-interstitial) was studied;

- Based on the results of Vacancy-H-He interaction, the parametrisation set (called LTD model) was proposed

Results of the MD and MS simulations confirmed earlier assumptions made on the basis of *ab initio* results. The complete parameterization for the mean-field theory calculations was obtained using the best-fit to the low and high temperature experimental data.

6.1.4. Continuum scale numerical simulations

On the basis of the physical model a number of numerical simulations were performed aiming at understanding and analyzing experimental results. Based on the results of the simulations the following conclusions were made:

- LTD model does not describe binding of H to vacancy clusters well enough to model H bubble nucleation and growth. Numerical fit of *ab initio* results was used instead. The failure of the LTD model can be explained by the fact that it is based on the elasticity theory and does not describe atomic features of the H-dislocation/vacancy interaction in tungsten adequately enough for single and small H clusters;
- "Jog punching" mechanism of bubble nucleation and growth was linked to the loop punching mechanism operating for large bubbles. This parametrization was used in simulations to explore flux-temperature exposure conditions under which the "jog punching" operates leading to bubble formation and blistering;
- The universal H binding energy function, linking the H binding to vacancy clusters and large bubbles, allowed one to simulate H trapping and release in the TDS experiment and link position of the release peaks to the bubble size distribution function;
- Model of H trapping at LAGB (relevant for the high temperature exposures) was proposed and allowed one to investigate the influence of the H depth distribution on the shape of the TDS spectra;

6.2. Outlook

Based on the results presented in this thesis a number of topics for further investigation can be proposed. It can be divided into two parts: atomistic simulations and continuum scale simulations.

Atomistic simulations:

- Further investigation of the interaction of H/He with microstructural defects in W: low angle grain boundaries (dislocation networks), triple junctions and high angle grain boundaries. This involves both *ab initio* and MD simulations in order to validate the available interatomic potentials needed to perform simulations at finite temperature. The primary aim would be the estimation of the influence of microstructure on H and He retention and parameterisation of H trapping and diffusion at natural microstructural defects (i.e. existing in commercially produced tungsten) for upper scale models;
- Another line of investigations is clarification of the synergetic effects between H and He during plasma implantation which can be done by large scale MD simulations with implantation conditions similar to real plasma exposure;
- Large scale MD simulations to directly see bubble and blister formation in the bulk and at different microstructural defects

Continuum scale simulations:

- Not all the parameters derived from the MD simulations were used in current numerical simulations. The extension of the model by including H and He synergy effects as well as defects produced by neutron irradiation is to be implemented;
- The proposed model gives an opportunity to predict the results of experiments involving high flux plasma exposure. The model gives predictions in terms of flux and temperature conditions for blister formation: this can be checked by choosing a set of experimental conditions and investigating blister formation;
- The analysis done for TDS release after exposure was performed for limited number of experiments and can be extended for bigger range of exposure conditions in terms of flux and temperature;
- The significance of H depth distribution for TDS release demonstrated by the model can be validated by polishing the sample after the exposure and before the TDS measurement in order to remove sub surface H and thus extract only the information about H stored in the bulk;

A

Modelling deuterium release from tungsten after high flux high temperature deuterium plasma exposure

**P. Grigorev, D. Matveev, A. Bakaeva, D. Terentyev, E. E. Zhurkin,
G. Van Oost, J.-M. Noterdaeme**

published in Journal of Nuclear Materials, 2016, Vol. 481, pp. 181-189.



Modelling deuterium release from tungsten after high flux high temperature deuterium plasma exposure



Petr Grigorev ^{a,b,c,*}, Dmitry Matveev ^d, Anastasiia Bakaeva ^{a,e}, Dmitry Terentyev ^a, Evgeny E. Zhurkin ^c, Guido Van Oost ^b, Jean-Marie Noterdaeme ^{b,f}

^a SCK•CEN, Nuclear Materials Science Institute, Boeretang 200, Mol, 2400, Belgium

^b Ghent University, Applied Physics EA17 FUSION-DC, St. Pietersnieuwstraat, 41 B4, B-9000, Gent, Belgium

^c Department of Experimental Nuclear Physics K-89, Institute of Physics, Nanotechnologies, and Telecommunications, Peter the Great St. Petersburg Polytechnic University, St. Petersburg, Russia

^d Institute of Energy and Climate Research – Plasma Physics, Forschungszentrum Jülich GmbH, Trilateral Euregio Cluster, 52425, Jülich, Germany

^e Department of Applied Physics, Ghent University, Belgium

^f Max-Planck-Institut für Plasmaphysik, Garching, Germany

ARTICLE INFO

Article history:

Received 4 May 2016

Received in revised form

19 August 2016

Accepted 18 September 2016

Available online 19 September 2016

ABSTRACT

Tungsten is a primary candidate for plasma facing materials for future fusion devices. An important safety concern in the design of plasma facing components is the retention of hydrogen isotopes. Available experimental data is vast and scattered, and a consistent physical model of retention of hydrogen isotopes in tungsten is still missing. In this work we propose a model of non-equilibrium hydrogen isotopes trapping under fusion relevant plasma exposure conditions. The model is coupled to a diffusion-trapping simulation tool and is used to interpret recent experiments involving high plasma flux exposures. From the computational analysis performed, it is concluded that high flux high temperature exposures ($T = 1000$ K, flux = 10^{24} D/m²/s and fluence of 10^{26} D/m²) result in generation of sub-surface damage and bulk diffusion, so that the retention is driven by both sub-surface plasma-induced defects (bubbles) and trapping at natural defects. On the basis of the non-equilibrium trapping model we have estimated the amount of H stored in the sub-surface region to be $\sim 10^{-5}$ at⁻¹, while the bulk retention is about 4×10^{-7} at⁻¹, calculated by assuming the sub-surface layer thickness of about 10 μm and adjusting the trap concentration to comply with the experimental results for the integral retention.

© 2016 Elsevier B.V. All rights reserved.

1. Introduction

The current choice of materials to be used for ITER plasma-facing components (PFCs) includes tungsten (W) [1], which is due to its low sputtering yield, high melting point and high thermal conductivity. One of the issues still to be clarified is the retention of hydrogen (H) isotopes – deuterium (D) and radioactive tritium (T) – in W, as PFCs are supposed to sustain high flux plasma irradiation combined with neutron and heat fluxes. In the ITER divertor, plasma-facing surfaces will be exposed to a very high plasma flux ($\sim 10^{24}$ D/m²s) [2] with ion energies below 100 eV, i.e. well below the atom displacement threshold (the energy needed to generate a

stable Frenkel pair), and the implantation range will be limited to several nanometers. Following the implantation, plasma ions are thermalized and their permeation deeper in the material depends on hydrogen diffusion and solubility properties in W. According to the phase diagram of a W-H system, in the temperature region of 300–1000 K relevant for ITER conditions, an equilibrium concentration of H dissolved in α -W ranges from 10^{-18} to 10^{-6} at.% [3,4]. High flux plasma implantation introduces H concentration in the material significantly higher than the solubility limit. It is known that under such conditions H in W does not form hydrides and rather precipitates in the form of bubbles filled with H₂ molecules. Moreover recent *ab initio* calculations followed by statistical estimations [5] demonstrated that high H concentration in W reduces vacancy formation energy thus increasing the probability of bubble nucleation. However, the thermodynamic diagram does not indicate the mechanism of the bubble formation, which should occur via H diffusion, trapping, bubble nucleation and growth. Trapping

* Corresponding author. SCK•CEN, Nuclear Materials Science Institute, Boeretang 200, Mol, 2400, Belgium.

E-mail address: grigorievpit@gmail.com (P. Grigorev).

of H in W is defined by the implantation conditions and interaction of implanted H with microstructural defects [6]. The critical issue here is the determination of mechanisms leading to the nucleation of initial hydrogen clusters turning into bubbles at a higher fluence.

Commercially available tungsten grades are usually heavily deformed polycrystalline materials with relatively high dislocation densities, low angle grain boundaries (LAGB) of sizes up to several micrometers, high angle grain boundaries (HAGB) of sizes up to tens of micrometers, and minor impurities in amount of up to 0.1–0.4 at%, which are all contributing to trapping of H atoms. However, typical impurities dissolved in W matrix (such as carbon and oxygen) do not bind H strongly and usually affect the uptake of H indirectly, e.g. by precipitation or grain boundaries segregation [7–9]. Dislocations and grain boundaries are usually considered as major traps in the powder metallurgy-produced polycrystalline tungsten grades. Due to the low solubility and low migration energy of H in W (0.25–0.4 eV [3,10,11]), even under room temperature exposure conditions, H promptly occupies different microstructural traps in the material so that there are almost no dissolved interstitial H atoms in W lattice.

As has been recently summarized by Tanabe [6], H depth profiles under high flux exposures typically consist of three components, namely: (1) top-most layer: several nano-meters; (2) saturated sub-surface layer: several micrometers and (3) bulk: from several micrometers to millimeters depths, basically across the whole sample. Due to small thickness of the top-most layer, the fraction of H trapped there is usually rather low as compared to the total retention. Therefore upon high flux/fluence and high temperature exposures, the retention is defined by the partition of H trapped at plasma-induced microstructural defects (e.g. cavities, bubbles), established in the saturated sub-surface layer, and in the bulk. The bulk retention, in turn, is defined by the initial microstructure of the material and the H flux coming through the sub-surface layer.

Experimentally available microstructure and depth distributions of retained H represent important information that is used to establish and verify principal physical models describing retention and release of hydrogen isotopes in fusion materials. Linear plasma accelerators are conventionally used to simulate fusion-relevant high flux plasma conditions utilizing D ions. Thus, while discussing the experimental results we use D notation. However in atomistic simulations H is used. Since chemical properties of these two isotopes are the same, we use H notation while discussing the theoretical model. Nuclear reaction analysis (NRA) and scanning electron microscopy (SEM) are the most conventional tools used to study surface modifications and depth distribution of D after plasma exposure [12–16]. Typical measurements done by NRA show that the concentration of retained D sharply decreases within first several μm of the exposed surface (see e.g. Refs. [6,15,17,18]) after high flux ($>10^{22} \text{ ion/m}^2/\text{s}$) exposures performed at material temperatures in the range of 300–800 K. However, the NRA technique does not allow probing the material deeper than about 10 μm from the surface. Additional information comes from measurements by secondary ion mass spectrometry (SIMS) as well as from the thermal desorption spectroscopy (TDS). A comparison of the integral retention measured with NRA and TDS confirms the above mentioned division of D retention into three zones: top-surface layer, sub-surface layer and the bulk. The bulk retention component depends strongly on the exposure temperature and fluence, and for high temperature exposures (800 K and above) the D permeation can reach mm depth [6,19,20].

The microstructural modification expressed in the formation of cavities at a depth of tens of micrometers and deeper is reported in Ref. [21], which confirms that increasing exposure temperature enhances the permeation of D towards bulk. The initial

microstructure appears to play an important role in hydrogen retention properties of the material. Formation of cavities deeper than several micrometers was observed at 500 K exposure under low flux conditions ($10^{20} \text{ ion/m}^2/\text{s}$) in the case of recrystallized and large-grain materials [22]. Besides SEM-visible cavities, a significant amount of D can be retained in nanoscale bubbles formed as a result of plasma exposure and located within first micrometers, as was recently reported by direct TEM observations [23]. Dislocation networks can offer nucleation sites for the formation of such bubbles at sufficiently high plasma fluxes, as was recently suggested in Ref. [24]. Therefore the initial density of dislocations plays an important role especially at low temperature conditions.

Computational assessment of H retention by diffusion-trapping codes like TMAP7 [25–27] provides the possibility to associate features of experimental TDS spectra with particular trapping sites in the material. Experimental TDS spectra can be rather well fitted by assigning three trapping site energies of 0.45 eV, 1.05 eV and 1.44 eV to dislocations, vacancies and pores, respectively [27–29], however the amount of traps used in these models was limited. A thorough theoretical study highlighting how characteristic temperatures of TDS spectra depend on hydrogen retention parameters, such as trap concentration depth distribution or activation energy of detrapping processes was reported in Ref. [30]. Following the *ab initio* studies [5,31], trapping of multiple H atoms in one vacancy is possible and the binding energy of subsequent H atoms decreases from 1.28 eV for one trapped atom down to 0.32 eV for six atoms. In order to utilize these results, a number of works aiming on extension of the reaction diffusion models for higher amount of traps treating a vacancy filled with different number of trapped H atoms as a separate traps were done in Refs. [32–35], as well as an introduction of traps with continuum binding energy distribution [35–37]. Using the multiple trap model with an NRA profile as trap concentration depth distribution allowed accurate fit of TDS spectra at different fluencies in Ref. [32] with a possible attribution of the traps to vacancies located near material surface. Special attention to the role of voids and blisters in the molecular H release during TDS and was drawn in work [38]. However the mechanism of formation of such voids remains unclear.

Theoretical formulation of the high flux plasma-induced bubble formation at dislocations has been recently performed using *ab initio* atomistic calculations [23]. By exploring the interaction of H atoms with dislocations in W, it was demonstrated that H atoms are bound to the screw dislocation core with the energy of ~0.6 eV and an interstitial H exhibits fast one-dimensional migration along the dislocation line. An elementary dislocation segment accepts up to six H atoms gradually losing its interaction strength. Here elementary segment means a dislocation line with a length of a translation vector in the direction of the dislocation line. For $\frac{1}{2}\langle 111 \rangle$ screw dislocations this length is $\sqrt{3}a_0$ since dislocation line is oriented along the direction of burgers vector $\langle 111 \rangle$ direction. Once the cluster of eight atoms is formed, it spontaneously transforms into an immobile configuration by punching out a jog and thus creating an open volume jog on a dislocation line. *Ab initio* suggests that no more than 6 H atoms can be trapped by perfect dislocation core. However in real material imperfections on the dislocation such as kinks and jogs together with intersection of dislocations exist. Properties of such imperfections are similar to vacancy in tungsten. Thus they can play a role of nucleation sites for clustering enough H atoms to initiate jog formation. In this way, the dislocation network may act not simply as a weak trap, but also as an extended defect for heterogeneous nucleation of stable hydrogen clusters, potentially converting into bubbles by punching the dislocation jogs. We would call such process “non-equilibrium trapping” meaning that it is governed by trapping of H at the defect created during the implantation.

However, the dislocation-driven trapping mechanism can operate only at a certain plasma flux and material temperature combination: the higher is the temperature – the higher must be the flux to sustain the jog nucleation. According to the estimations done in Ref. [39], plasma exposure at temperatures above 800 K requires a flux of at least $10^{25} \text{ m}^{-2} \text{ s}^{-1}$ for the H clustering to take place. However, recent experiments employing fluxes of about $20^{24} \text{ m}^{-2} \text{ s}^{-1}$ at 50 eV-biased D plasma exposure of polycrystalline tungsten (non-recrystallized grade with average grain size of $20 \mu\text{m}$ [16]) demonstrated the presence of blisters with high areal density and the high temperature TDS release peak around 800–1000 K, suggesting the presence of D-filled bubbles. Dome-shaped blisters, observed on the exposed surface, also support the assumption of the presence of bubbles growing by plastic deformation. SIMS measurements have confirmed significant trapping of deuterium within first 200 nm under the surface. At the same time, NRA analysis shows that the uptake does not vanish beyond 200 nm and in fact remains constant at a level of 5×10^{-4} atomic fractions through the maximal probing depth of $10 \mu\text{m}$. These experimental facts suggest that non-equilibrium trapping in the sub-surface leading to the formation of bubbles also occurs at high temperature exposures where the trapping on bulk dislocation lines should be ineffective.

In addition to dislocations and vacancies, *ab initio* calculations addressing the dissolution and segregation of H at high angle grain boundaries in W also provide evidence for strong binding. Zhou et al. [40] have shown that an H interstitial can be bound to a HAGB of S5{013} type with an energy of up to 1.11 eV, which is close to the value for a single vacancy. However, contrary to an isolated vacant site, the capacity of the studied HAGB to accept additional H atoms was found to be limited to a 2-H cluster (not a molecule) only with a weak binding of 0.13 eV [40].

In this work, we perform a theoretical analysis of trapping of hydrogen in polycrystalline W under high temperature high flux plasma exposure. To explain the high temperature retention, we put forward the hypothesis of H trapping at low angle grain boundaries (LAGB), which, in fact, represent a network of edge, screw and mixed dislocations with a relatively small spacing. The network nodes are suggested to act as trapping sites, which attract and emit hydrogen atoms simultaneously. Hydrogen atoms escaping from LAGB trapping sites diffuse along LAGB interfaces either towards the surface or deeper into the bulk and can be captured only by stronger traps such as open volume sites on random (high angle) grain boundaries. Hence, we consider a two-zone model where sub-surface trapping (within the first sub-grain) occurs as a non-equilibrium process, i.e. via over-saturation with H leading to the formation of H-filled bubbles, while beyond the first sub-grain H diffuses in a field of static traps and its resulting depth distribution is defined by the concentration and strength of intrinsic traps (e.g. open volume sites on HAGBs). Following the above described model, we have performed a computational analysis of the H trapping and release by combining the two trapping processes: non-equilibrium and diffusion-based ones. We simulate the high flux D plasma exposure at 1000 K of well pre-characterized polycrystalline tungsten of 1 mm thickness. The exposure was performed at Pilot-PSI [41] plasma generator. The exposure was applied in a single plasma shot of 70 s with the particle flux in the center of the sample in the range $(0.8–1.0) \times 10^{24} \text{ m}^{-2} \text{ s}^{-1}$. The first $10 \mu\text{m}$ (i.e. the first sub-grain) was treated using the non-equilibrium retention model, while the trapping in the rest of the sample was accounted for by the diffusion-based approach. Based on the comparison of computational results with experimentally obtained TDS spectra and TEM microstructure observations, we draw a conclusion on the partition of deuterium retention between the sub-surface region and the

bulk.

2. Computational model for sub-surface trapping

As we have outlined in the introduction, upon high temperature exposure (above 800 K), the flux of $10^{24} \text{ D/m}^2/\text{s}$ is estimated to be not sufficient for the nucleation of bubbles on dislocations by clustering and subsequent punching out of an interstitial atom on a dislocation line [39]. However, a strong gradient of the concentration of the retained D within the first micrometer depth of polycrystalline W is still detected by the SIMS even at temperatures as high as 1000 K [42] also blistering is reported. This observations point out the formation of bubbles driven by microstructural defects spatially distributed within several micrometers beneath the exposed surface. The size of sub-grains in polycrystalline W is typically of about several micrometers [43], meaning that spacing between LAGBs is much smaller than between that for HAGBs. Therefore, the LAGBs are considered in this work as the major source of H trapping sites in the sub-surface region eventually leading to the nucleation of stable defects.

In particular, we consider the nucleation of bubbles to take place on dislocation networks (triple junctions) made of screw, edge and mixed dislocations with frequent nodes, where trapping is expected to be especially strong. In the following, we shall formulate a set of equations defining the growth of bubbles at dislocation nodes of LAGB and evaluate the limiting cases for the concentration of those nodes, given the high flux high temperature exposure conditions.

To apply the mean field rate theory, we consider that a LAGB dislocation network represents an array of traps (associated with dislocation nodes) homogeneously distributed over the sub-surface layer of a width comparable to the sub-grain size ($\sim 10 \mu\text{m}$). Upon implantation, H thermalizes and migrates in the sub-surface region. Diffusion of H in a static field of traps with a sink strength k^2 is described by the equation [24,44]:

$$\frac{\partial C_H}{\partial t} = D \frac{d^2 C_H}{dx^2} - k^2 D C_H; \quad (1)$$

The steady-state solution of the above equation reads [45]:

$$C_H(x) = C_0 \exp(-xk), \quad C_0 = C_R = \frac{F \cdot R}{D}; \quad (2)$$

where F – plasma flux, R – particle penetration range, D – diffusion coefficient. The LAGB sink strength is $k^2 = \frac{24}{d^2}$, for the grain size d , as adopted from Ref. [46].

Accounting for the desired plasma exposure conditions, the steady state solution of Eq. (1) leads to depth profiles of the H concentration plotted in Fig. 1 for LAGB sizes $d = 1, 10$ and $100 \mu\text{m}$. One can see that the steady-state H concentration quickly decreases within 1–10 μm permeation depth, depending on the grain size. Later on we shall apply these H concentration profiles to estimate the rate of nucleation and growth of H clusters on LAGB triple junctions depending on the LAGB size.

At a high temperature exposure (i.e. 1000 K), the diffusion of H in a perfect W bulk is extremely fast and all incoming H atoms are almost immediately trapped at LAGBs, as we can neglect bulk screw dislocations due to high rate of detrapping (i.e. low binding energy). Let us estimate the diffusion range along the LAGB within which an H atom is detrapped. The mean free path along a linear defect is given by Ref. $\lambda_{LAGB} = a_0 \exp\left(\frac{E_m^b - E_m^{LAGB} + E_b}{2kT}\right)$ [21], where E_m^b – migration energy in the bulk, E_m^{LAGB} – migration energy along the grain boundary, E_b – binding energy to the linear defect, a_0 – lattice

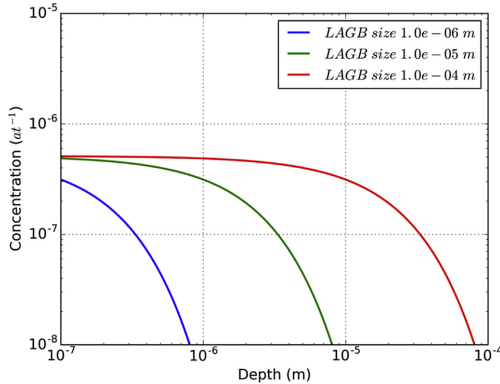


Fig. 1. Steady state solution for H concentration defined by equation (1) for 3 different LAGB sizes.

constant. If we consider the LAGB as an array of straight dislocations, we can use the value of the migration energy along dislocation core (~0.1 eV [47]) to describe the migration along the LAGB. The value for the bulk migration energy is taken to be 0.4 eV [3] and the value for the binding energy to dislocation is taken to be 1.0 eV, considering that edge dislocation segments will provide the strongest trapping [48,49]. At 1000 K, the mean free path along the LAGB will amount to 0.5 μm. Assuming that nucleation of H clusters occurs at dislocation junctions, the H trapping on the junctions will be defined by the flux of H from the bulk to the unit length of LAGB ($J_{LAGB}(x)$) multiplied by the H mean free path along the LAGB (λ_{LAGB}), i.e. the LAGB effective length that gather H atoms contributing to the bubble growth as is written below:

$$R^+ = \lambda_{LAGB} J_{LAGB}(x), \text{ where } J_{LAGB}(x) = \frac{Z_{LAGB}}{\omega} D_H C_H(x); \quad (3)$$

Where $Z_{LAGB} \sim 1$ – geometrical capture efficiency, ω – atomic volume. As can be seen from Eq. (3), the incoming flux depends on the depth, because the flux of free H atoms moving in a trap field reduces with the permeation depth due to the trapping. Therefore a sufficiently high flux of H is needed at a given depth to sustain the growth of H clusters and to initiate their transformation into stable bubbles. If the flux is not sufficient, H clusters dissolve by emitting H atoms. The emission rate depends on the binding capacity of a particular defect, where the binding energy for H atoms depends on the cluster size. That is why the nucleation of the bubbles is favoured close to the surface and assisted by open volume defects such as grain boundaries, edge dislocations and vacancies.

As the nucleation of stable clusters (i.e. bubbles) progresses, at a certain point the distance between them will become shorter than the mean free path λ_{LAGB} (see Fig. 2), and the arrival rate to each stable cluster will be defined by their mean spacing $\lambda_{cl} = \pi d^2/N$, where N is the volumetric concentration of the clusters. In this case the average arrival rate of H atoms to clusters will decrease if their concentration increases. Fig. 3 shows the balance of rates for the arrival (R^+) to and dissolution from the clusters ($R^- = Cr \exp\left(-\frac{E_{bin}}{KT}\right)$), considering different detrapping energies (tentatively attributed to the detrapping from a screw dislocation line, edge dislocation line, vacancy and void). The nucleation of bubbles will occur only if the trapping rate is higher than

dissolution rate ($R^+ > R^-$). As can be seen from the graph, depending on the grain size, the critical cluster density varies from 10^{18} to 10^{21} m^{-3} (10^{-11} – 10^{-8} at^{-1}) and is marked as a green area on the graph.

In Ref. [52], the trapping rate of H at a dislocation segment was derived. It can be modified for LAGB as:

$$R_b^+ = k^2 D_b [C_H(x) - C_{Th}^{LAGB}]; \quad (4)$$

where k is the sink strength of LAGB and $C_{Th}^{LAGB} = \exp\left(-\frac{E_b + E_m}{kT}\right)$ is the equilibrium concentration of H atoms per trapping site determined by the emission rate [24]. Expression (4) predicts a constant increase of the amount of H trapped at the LAGB interface and does not take into account the diffusion along the LAGB interface, which would reduce the H concentration in sub-surface bubbles and promote deeper diffusion of H atoms. Following the same description as it was introduced for bulk dislocations in Refs. [24,52], the effect of diffusion along LAGB (via trapping-detrapping from dislocation nodes) is accounted for by the following expression:

$$\frac{dC_H^{LAGB}}{dt} = R_b^+ - \frac{D_{eff}}{x^2 + d^2} C_H^{LAGB}(x); \quad (5)$$

where d is the LAGB length, and D_{eff} is the effective diffusion coefficient along the LAGB interface taken as $D_{eff} = a_0^2 \nu \exp\left(-\frac{E_{diff}}{kT}\right)$. A steady state solution of Eq. (5) for the concentration of trapped H reads

$$C_H^{LAGB}(x) = \frac{x^2 + d^2}{D_{eff}} R_b^+; \quad (6)$$

The solution of Eq. (6) is drawn in Fig. 4 for two particular values of the effective migration energy and LAGB size. It can be seen that due to diffusion along LAGB the steady-state concentration profile decreases faster as compared to the profiles shown in Fig. 1. Profiles for $d = 10$ and $100 \mu\text{m}$ are in a good agreement with SIMS results [42]. The values of the effective migration energy used are 0.45 eV and 0.55 eV. The total retention predicted by these curves strongly depends on the effective migration energy. By performing a parameter study, we reveal the range of migration energies that can provide a reasonable fraction of the total retention with respect to the total retention as compared to the experimental results (from 0.1 to 0.5).

The total H concentration stored in LAGB traps lies in the range of $(1.0\text{--}8.0) \times 10^{-5} \text{ at}^{-1}$ depending on the size of the grain boundary. This amount of trapped H represents 15 to 45% of the total H in the material for LAGB sizes from $d = 10 \mu\text{m}$ to $d = 100 \mu\text{m}$. These estimates for the fraction of H retained in the sub-surface and bulk regions are used as a starting approximation to model H release upon TDS cycle.

3. Construction of the depth profile of trapped H

An initial depth distribution of trapped H is an important input for the simulation of the release during TDS experiment. As has been discussed above, all trapped H can be subdivided into two fractions corresponding to two regions: sub-surface and bulk, as schematically shown in Fig. 5. The sub surface region is characterized by non-equilibrium trapping and bubble formation, while bulk region is described by classical diffusion-trapping model, so that bulk retention is defined by filling natural traps (cavities and open

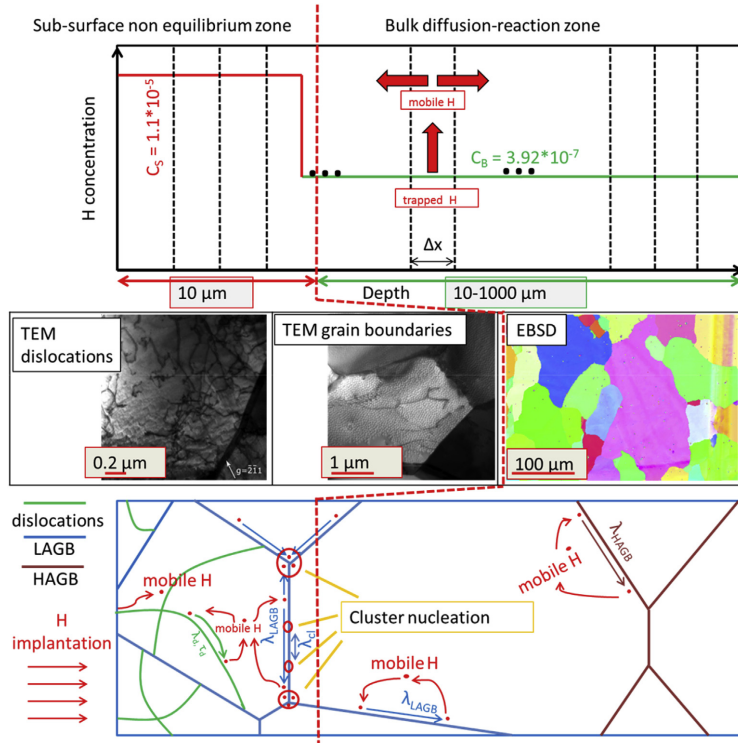


Fig. 2. Schematic picture of the model coupling non-equilibrium trapping and diffusion limited trapping and explanation of the interrelation between the primary microstructural defects and diffusion/trapping processes. Upper bar represents schematically the mesh of the numerical model integrating the differential equations in time and space; Green and red full curves denote the concentration profile of the trapped H in the two regions: sub-surface and bulk. Middle bar demonstrates different elements of the microstructure, experimentally obtained by transmission and scanning electron microscopy, which control the H trapping at different length scales. Namely, dislocation lines – control nucleation of bubbles in the sub-surface region at low temperatures, low-angle grain boundaries (LAGB) control trapping and diffusion towards bulk and nucleation of bubbles at high temperatures; and finally high angle grain boundaries control trapping of H in the bulk. These three types of the microstructural features are shown in the middle bar as TEM micrographs and an EBSD polar map with corresponding spatial scales indicated. The experimental data are coming from Refs. [50,51] where the microstructure of the high flux plasma exposed W was investigated. Bottom bar illustrates physical reactions contributing to the retention process: diffusion, initial trapping, nucleation of bubbles, and growth of cavities. The distances used in the figure are λ_{LAGB} , λ_{HAGB} – mean free paths of H along LAGB and HAGB respectively (see Eq. (3)), λ_d – mean free path of H along dislocations, λ_{cl} – mean distance between H clusters. Vertical red dashed line going through all three bars represents the boundary between sub surface non-equilibrium zone and bulk diffusion-reaction zone. (For interpretation of the references to colour in this figure legend, the reader is referred to the web version of this article.)

volumes at HAGB).

The estimation of the amount of H trapped at the sub-surface region has been made above, and we take the value corresponding to the sub-grain size of 10 \$\mu\text{m}\$. This sub-grain size is an adequate choice for the hot forged W grade relevant to ITER specifications [53], for which TDS experimental data after high flux high temperature plasma exposure are available. These results will be used in the following to validate the proposed model.

Given the known fraction of H stored in the sub-surface region, the concentration of H trapped in the bulk can be defined by the following expression:

$$C_B = \frac{(1-f)R_T}{d - X_1},$$

where \$R_T\$ – total amount of retained H (as measured experimentally), \$f\$ - fraction of trapped H in the sub-surface region as

estimated here, \$d\$ – sample thickness, \$X_1\$ – thickness of subsurface region. This procedure ensures that the total amount of H released in the simulation will be the same as in the experiment.

Another important input parameter for the modelling of TDS spectra is the binding state of trapped H. As was defined before (see Fig. 3), the critical cluster concentration varies from \$10^{18}\$ to \$10^{21} \text{ m}^{-3}\$ or from \$10^{-11}\$ to \$10^{-8} \text{ at}^{-1}\$, depending on the grain size chosen. According to our estimations given above (Fig. 4), the total H concentration stored in LAGB traps lies in the range of \$(1.0\text{--}8.0) \times 10^{-5} \text{ at}^{-1}\$. We use the notation of a vacant site to estimate the size of the bubbles formed. Assuming that after implantation the bubbles formed will be under pressure needed for the bubble growth via jog/loop punching mechanism, we expect, following the calculations made in Ref. [4], that the number of H per one vacant site within a cluster will be of about 6. This allows us to estimate the number of vacant sites per cluster. As a result, we obtain \$10^2\text{--}10^5\$ vacant sites per cluster, which correspond to bubble

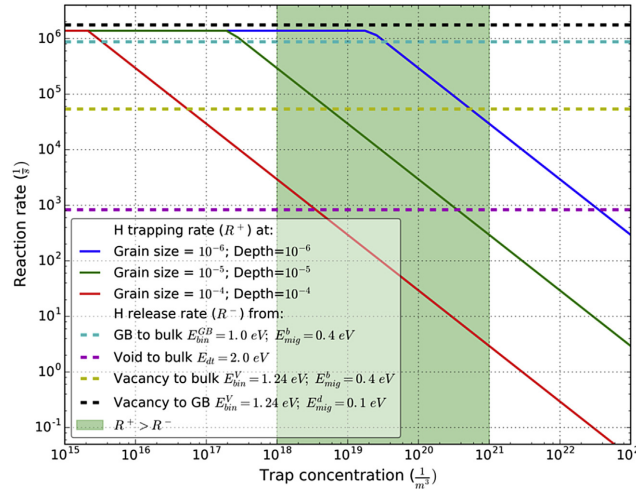


Fig. 3. Trapping and detrapping rate coefficients of H on LAGB calculated for different values of binding energies and effective trap concentrations.

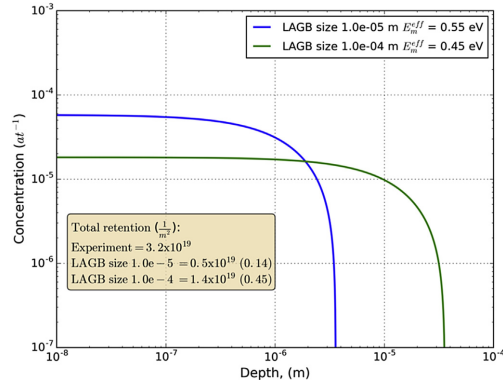


Fig. 4. Depth distribution of trapped H calculated at different LAGB sizes and different values of effective migration energy.

sizes from 2 nm to 20 nm. Given that we address a high temperature exposure, we assume that all trapped H is stored in bubbles (no intra-grain H in vacancies etc.) and the trapping energy is about 2.0 eV [11].

4. Modelling TDS spectra and discussion

For the simulation of H release during the TDS experiment we used the following set of parameters: depth of the sub-surface region (i.e. region characterized by non-equilibrium trapping) $X_1 = 10 \mu\text{m}$, fraction of H trapped in the sub-surface region $f = 0.23$, sub-surface concentration $C_S = 1.16 \times 10^{-5}$, bulk concentration $C_B = 3.92 \times 10^{-7}$. The initial guess for f was 0.15 on the basis of the estimations given in the previous section. However, a limited variation of f revealed the best agreement with the experiment by

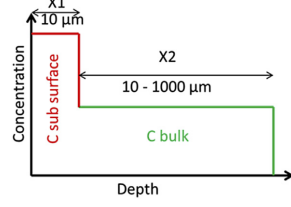


Fig. 5. Schematic picture of a two-zone depth distribution of trapped H proposed in this paper.

taking $f = 0.23$.

The detrapping rate is calculated following the Arrhenius expression: $F_{dt} = v \exp\left(-\frac{E_t}{kT}\right)$. Where, detrapping energy was assumed to be $E_t = 2.0 \text{ eV}$, prefactor (attempt frequency) as assumed to be $v = 10^{13} \text{ s}^{-1}$. As was noted before, we assume that all H is stored in nm sized bubbles. Detrapping of H from such defects is similar to transition of the H atoms from adsorbed state on the surface to the bulk which was studied in Ref. [11] resulting in value of 2.0 eV for the barrier for such transition. The diffusion, detrapping, retrapping and surface release of H was followed by solving a set of differential equations in space and time. Integration of the system was performed using a code based on Coupled Reaction–Diffusion Systems (CRDS) simulation tool [54] and modified for the simulation of H release from tungsten. The spectrum obtained using the above specified parameter set is plotted and compared with the experimental result in Fig. 6. The details of the experimental procedure are briefly specified in the figure caption. The simulated curve is in good agreement with the experimental result in terms of both peak position and shape of the spectrum.

By analyzing different initial depth distributions of trapped H, we have revealed the importance of the sub-surface plasma-induced defects, which act as primary release source and also retrap H diffusing from the bulk towards the surface. The blue curve

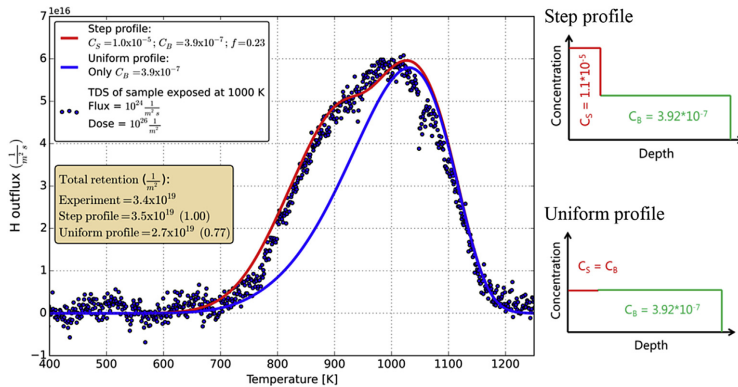


Fig. 6. Comparison of modelling of H release during TDS with experimental results. The sample was exposed to plasma for 70 s with a particle flux in the center of the sample in the range $(0.8\text{--}1.0) \times 10^{24} \text{ m}^{-2} \text{ s}^{-1}$. The sample temperature was monitored by infrared camera and was kept at 1000 K. The heating rate during TDS measurements was 0.5 K/s.

in Fig. 6 depicts the release of H applying a flat distribution profile over the whole sample depth. Such a profile would correspond to the situation when no plasma-induced defects would be created and natural traps would be filled homogeneously. One can see the classical release peak from a trap with a fixed trapping energy and uniform distribution. The comparison provided in Fig. 6 demonstrates that assigning a two-zone depth distribution of trapped H and assuming only one type of traps (bubbles in the present case), one can reproduce well the TDS spectrum composed of two peaks. Note that the impact of H trapped in the sub-surface region on the appearance of the TDS spectrum can be experimentally revealed by careful polishing the surface (i.e. removing 10–20 μm) prior to performing the TDS measurement. By applying such a procedure, we expect the change of the spectra from the red to the blue curve as demonstrated in Fig. 6. We plan to perform such an experiment in near future in order to validate our model.

Another important role played by sub-surface plasma-induced defects is retrapping of H diffusing from larger depths. To demonstrate the effect of retrapping, we performed a simulation with the same parameter set as in Fig. 6, but without retrapping. This means that once an atom is released from a trap it can freely diffuse to the

surface without interaction with other available traps. The simulated TDS spectrum without retrapping is shown by a blue curve in Fig. 7 in comparison to the best fit curve and experimental data. As can be seen from the graph, exclusion of retrapping events shifts the spectrum to lower temperatures by about 200 K, which is well resolved given the accuracy of the TDS technique. This comparison demonstrates that the introduction of the two-zone depth distribution and retrapping process in the sub-surface region are reasonable physical assumptions for computational models, which can successfully explain experimentally observed TDS results.

5. Conclusions

From the computational analysis performed, we conclude that high flux high temperature exposures ($T = 1000 \text{ K}$, $\text{flux} = 10^{24} \text{ D/m}^2 \text{ s}$ and fluence of 10^{20} D/m^2) result in generation of sub-surface damage and bulk diffusion, so that the retention is driven by both sub-surface plasma-induced defects (bubbles) and trapping at natural defects (such as cavities and HAGB). On the basis of the non-equilibrium trapping model we have estimated the amount of H stored in the sub-surface region to be $\sim 10^{-5} \text{ at}^{-1}$, while the bulk

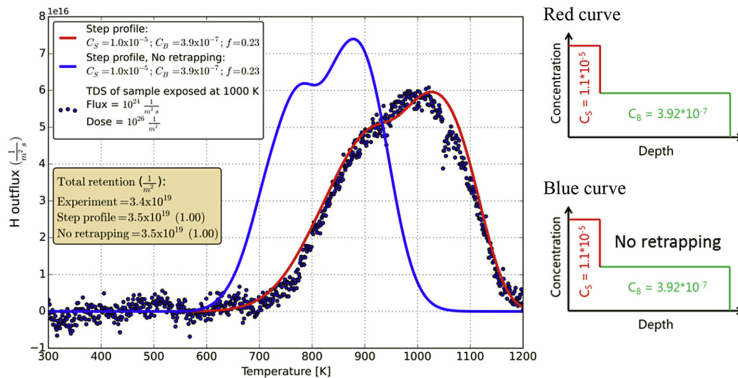


Fig. 7. Comparison of modelling of H release during TDS with experimental results.

retention is about 4×10^{-7} at⁻¹, calculated by assuming the sub-surface layer thickness of about 10 μm and adjusting the trap concentration to comply with the experimental result for the integral retention. The sub-surface to bulk trapping ratio obtained this way agrees with the fact that NRA measurements usually provide lower integral retention compared to TDS, especially at high temperature exposures.

By applying thereby obtained H spatial distribution, we have performed simulations of a TDS cycle assuming that all retained H is stored in bubbles heterogeneously distributed in sub-surface and bulk regions. By applying the rate theory calculations, we have found a good agreement with the double-peak experimental TDS spectrum. The reason for the two peaks and non-Gaussian shape originates from the delayed release from the front surface of the sample due to retrapping of bulk H at numerous sub-surface defects, and possible H release at the back surface of the sample.

Combination of the non-equilibrium and diffusion-limited trapping model has proven to be effective in the estimation of the retention under high flux high temperature exposure conditions and rationalization of the release process under thermal annealing.

Acknowledgements

This work was supported by the European Commission and carried out within the framework of the Erasmus Mundus International Doctoral College in Fusion Science and Engineering (FUSION-DC).

This work has been carried out within the framework of the EUROfusion Consortium and has received funding from the Euratom research and training programme 2014–2018 under grant agreement No 633053. The views and opinions expressed herein do not necessarily reflect those of the European Commission.

Dmitry Terentyev acknowledges the support of Federal Belgium Government.

References

- [1] R.E. Clark, D. Reiter, *Nuclear Fusion Research: Understanding Plasma-surface Interactions*, Springer, 2005.
- [2] R.A. Pitts, S. Carpenter, F. Escourbiac, T. Hirai, V. Komarov, S. Lisog, A.S. Kukushkin, A. Loarte, M. Merola, A. Sashala Naik, R. Mitteau, M. Sugihara, B. Bazylev, P.C. Stangeby, A full tungsten divertor for ITER: physics issues and design status, *J. Nucl. Mater.* 438 (2013) S48–S56. Supplement.
- [3] R. Frauenfelder, Solution and diffusion of hydrogen in tungsten, *J. Vac. Sci. Technol. B* 6 (3) (1969) 388–397.
- [4] J.B. Condon, T. Schober, Hydrogen bubbles in metals, *J. Nucl. Mater.* 207 (1993) 1–24.
- [5] N. Fernandez, Y. Ferro, D. Kato, Hydrogen diffusion and vacancies formation in tungsten: density functional theory calculations and statistical models, *Acta Mater.* 94 (2015) 307–318.
- [6] T. Tanabe, Review of hydrogen retention in tungsten, *Phys. Scr.* 2014 (T159) (2014) 014044.
- [7] T.N.M. Fukumoto, K. Masaki, K. Itami, Y. Ueda, T. Tanabe, Deuterium retention in tungsten coating on the CFC tiles exposed to JT-60U divertor plasmas, *J. plasma Fusion Res.* 9 (2010) 369–374.
- [8] M. Fukumoto, T. Nakano, K. Itami, T. Wada, Y. Ueda, T. Tanabe, Effects of carbon impurity on deuterium retention in VPS-tungsten coatings exposed to JT-60U divertor plasmas, *J. Nucl. Mater.* 415 (Suppl. 1) (2011) S705–S708.
- [9] A. Inouye, S. Yamamoto, S. Nagata, M. Yoshikawa, T. Shikama, Hydrogen retention induced by ion implantation in tungsten trioxide films, *Nucl. Instr. Meth. Phys. Res. B* 267 (8–9) (2009) 1480–1483.
- [10] K. Heinola, T. Ahlgren, Diffusion of hydrogen in bcc tungsten studied with first principle calculations, *J. Appl. Phys.* 107 (11) (2010) 113531.
- [11] D.F. Johnson, E.A. Carter, Hydrogen in tungsten: absorption, diffusion, vacancy trapping, and decohesion, *J. Mater. Res.* 25 (02) (2010) 315–327.
- [12] Y. Zayachuk, A. Manhard, M.H.J.t. Hoen, W. Jacob, P.A.Z.v. Emmichoven, G.v. Oost, Depth profiling of the modification induced by high-flux deuterium plasma in tungsten and tungsten–tantalum alloys, *Nucl. Fusion* 54 (12) (2014) 123013.
- [13] Y. Zayachuk, M.H.J.t. Hoen, P.A.Z.v. Emmichoven, D. Terentyev, I. Uytdenhoven, G.v. Oost, Surface modification of tungsten and tungsten–tantalum alloys exposed to high-flux deuterium plasma and its impact on deuterium retention, *Nucl. Fusion* 53 (1) (2013) 013013.
- [14] Y. Zayachuk, M.H.J.t. Hoen, P.A.Z.v. Emmichoven, I. Uytdenhoven, G.v. Oost, Deuterium retention in tungsten and tungsten–tantalum alloys exposed to high-flux deuterium plasmas, *Nucl. Fusion* 52 (10) (2012) 103021.
- [15] V.K. Alimov, J. Roth, M. Mayer, Depth distribution of deuterium in single- and polycrystalline tungsten up to depths of several micrometers, *J. Nucl. Mater.* 337–339 (2005) 619–623.
- [16] L. Buzi, G.D. Temmerman, B. Unterberg, M. Reinhart, A. Litnovsky, V. Philipp, G.V. Oost, S. Möller, Influence of particle flux density and temperature on surface modifications of tungsten and deuterium retention, *J. Nucl. Mater.* 455 (1–3) (2014) 316–319.
- [17] V.K. Alimov, W.M. Shu, J. Roth, K. Sugiyama, S. Lindig, M. Balden, K. Isobe, T. Yamanishi, Surface morphology and deuterium retention in tungsten exposed to low-energy, high flux pure and helium-seeded deuterium plasmas, *Phys. Scr.* 2009 (T138) (2009) 014048.
- [18] M.H.J.t. Hoen, B. Tyburska-Puschel, K. Ertl, M. Mayer, J. Rapp, A.W. Kleyn, P.A.Z.v. Emmichoven, Saturation of deuterium retention in self-damaged tungsten exposed to high-flux plasmas, *Nucl. Fusion* 53 (2) (2012) 023008.
- [19] K. Sugiyama, K. Krieger, M. Mayer, S. Lindig, M. Balden, D. Th, A.U. team, Deuterium retention in bulk tungsten exposed to the outer divertor plasma of ASDEX Upgrade, *Phys. Scr.* 2011 (T145) (2011) 014033.
- [20] K. Sugiyama, M. Mayer, A. Herrmann, K. Krieger, V. Rohde, M. Balden, S. Lindig, R. Neu, H.W. Müller, A.U.T. the, Deuterium retention in tungsten used in ASDEX Upgrade: comparison of tokamak and laboratory studies, *Phys. Scr.* 2014 (T159) (2014) 014043.
- [21] B. Khripunov, V. Gureev, V. Koidan, S. Kornienko, S. Latushkin, V. Petrov, A. Ryazanov, E. Semenov, V. Stolyarova, L. Danelyan, V. Kulikauskas, V. Zatekin, V. Umezhev, Erosion and deuterium retention in ion-irradiated tungsten under plasma exposure, *J. Nucl. Mater.* 463 (2015) 258–262.
- [22] M. Balden, A. Manhard, S. Elgeti, Deuterium retention and morphological modifications of the surface in five grades of tungsten after deuterium plasma exposure, *J. Nucl. Mater.* 452 (1–3) (2014) 248–256.
- [23] D. Terentyev, V. Dubinko, A. Bakaev, Y. Zayachuk, W.V. Renterghem, P. Grigorev, Dislocations mediate hydrogen retention in tungsten, *Nucl. Fusion* 54 (4) (2014) 042004.
- [24] V.I. Dubinko, P. Grigorev, A. Bakaev, D. Terentyev, G. Van Oost, F. Gao, D. Van Neck, E.E. Zhurkin, Dislocation mechanism of deuterium retention in tungsten under plasma implantation, *J. Physics-condensed Matter* 26 (39) (2014).
- [25] G.R. Longhurst, *TMAP7 User Manual*, 2008 p. Medium: ED.
- [26] T. Ahlgren, K. Heinola, K. Vöröslér, J. Keinonen, Simulation of irradiation induced deuterium trapping in tungsten, *J. Nucl. Mater.* 427 (1–3) (2012) 152–161.
- [27] O.V. Ogorodnikova, B. Tyburska, V.K. Alimov, K. Ertl, The influence of radiation damage on the plasma-induced deuterium retention in self-implanted tungsten, *J. Nucl. Mater.* 415 (Suppl. 1) (2011) S661–S666.
- [28] K. Schmid, V. Rieger, A. Manhard, Comparison of hydrogen retention in W and W/Ta alloys, *J. Nucl. Mater.* 426 (1–3) (2012) 247–253.
- [29] M. Poon, A.A. Haasz, J.W. Davis, Modelling deuterium release during thermal desorption of D-irradiated tungsten, *J. Nucl. Mater.* 374 (3) (2008) 390–402.
- [30] J. Guterl, R.D. Smirnov, S.I. Krasheninnikov, Revisited reaction-diffusion model of thermal desorption spectroscopy experiments on hydrogen retention in material, *J. Appl. Phys.* 118 (4) (2015) 043302.
- [31] K. Heinola, T. Ahlgren, K. Nordlund, J. Keinonen, Hydrogen interaction with point defects in tungsten, *Phys. Rev. B* 82 (9) (2010) 094102.
- [32] J. Guterl, R.D. Smirnov, S.I. Krasheninnikov, M. Zibrov, A.A. Pisarev, Theoretical analysis of deuterium retention in tungsten plasma-facing components induced by various traps via thermal desorption spectroscopy, *Nucl. Fusion* 55 (9) (2015) 093017.
- [33] E.A. Hodille, Y. Ferro, N. Fernandez, C.S. Becquart, T. Angot, J.M. Layet, R. Bisson, C. Grisolía, Study of hydrogen isotopes behavior in tungsten by a multi trapping macroscopic rate equation model, *Phys. Scr.* 2016 (T167) (2016) 014011.
- [34] K. Schmid, U. von Toussaint, T. Schwarz-Selinger, Transport of hydrogen in metals with occupancy dependent trap energies, *J. Appl. Phys.* 116 (13) (2014) 134901.
- [35] O.V. Ogorodnikova, Fundamental aspects of deuterium retention in tungsten at high flux plasma exposure, *J. Appl. Phys.* 118 (7) (2015) 074902.
- [36] S.I. Krasheninnikov, E.D. Marenkov, R.D. Smirnov, A.A. Pisarev, Hydrogen transport in solids with traps in the case of continuum distribution of detrapping energies, *Phys. Scr.* 2014 (T159) (2014) 014060.
- [37] P. Grigorev, L. Buzi, A. Bakaeva, D. Terentyev, G.D. Temmerman, G.V. Oost, J.M. Noterdaeme, Numerical analysis of TDS spectra under high and low flux plasma exposure conditions, *Phys. Scr.* 2016 (T167) (2016) 014039.
- [38] R.A. Causey, R. Doerner, H. Fraser, R.D. Kolasinski, J. Smugeresky, K. Ümstädter, R. Williams, Defects in tungsten responsible for molecular hydrogen isotope retention after exposure to low energy plasmas, *J. Nucl. Mater.* 390–391 (2009) 717–720.
- [39] P. Grigorev, D. Terentyev, V. Dubinko, G. Bonny, G. Van Oost, J.-M. Noterdaeme, E.E. Zhurkin, Nucleation and growth of hydrogen bubbles on dislocations in tungsten under high flux low energy plasma exposure, *Nucl. Instr. Meth. Phys. Res. B* 352 (0) (2015) 96–99.
- [40] H.-B. Zhou, Y.-L. Liu, S. Jin, Y. Zhang, G.-N. Luo, G.-H. Lu, Investigating behaviours of hydrogen in a tungsten grain boundary by first principles: from dissolution and diffusion to a trapping mechanism, *Nucl. Fusion* 50 (2010) 025016.

- [41] G.J. van Rooij, V.P. Veremiyenko, W.J. Goedheer, B. de Groot, A.W. Kleyn, P.H.M. Smeets, T.W. Versloot, D.G. Whyte, R. Engeln, D.C. Schram, N.J.L. Cardozo, Extreme hydrogen plasma densities achieved in a linear plasma generator, *Appl. Phys. Lett.* 90 (12) (2007) 121501.
- [42] L. Buzzi, Influence of the Particle Flux on Surface Modifications of Tungsten, Department of Applied Physics, Ghent University, 2015.
- [43] H. Sheng, Z. Sun, I. Uytdehouwen, G. Van Oost, J. Vleugels, Temperature and deformation effect on the low and high angle grain boundary structure of a double forged pure tungsten, *Int. J. Refract. Metals Hard Mater.* 50 (2015) 184–190.
- [44] V.I. Dubinko, S. Hu, Y. Li, C.H. Henager Jr., R.J. Kurtz, Dislocation vs. production bias revisited with account of radiation-induced emission bias. I. Void swelling under electron and light ion irradiation, *Philos. Mag.* 92 (33) (2012) 4113–4150.
- [45] G. Pintsuk, 4.17-Tungsten as a plasma-facing material, *Compr. Nucl. Mater.* 4 (2012) 551–581.
- [46] G.S. Was, Fundamentals of Radiation Materials Science: Metals and Alloys, Springer Verlag, New York, 2007.
- [47] P. Grigorev, D. Terentyev, G. Bonny, E.E. Zhurkin, G. Van Oost, J.-M. Noterdaeme, Interaction of hydrogen with dislocations in tungsten: an atomistic study, *J. Nucl. Mater.* 465 (0) (2015) 364–372.
- [48] W. Xiao, W.T. Geng, Role of grain boundary and dislocation loop in H blistering in W: a density functional theory assessment, *J. Nucl. Mater.* 430 (1–3) (2012) 132–136.
- [49] Z. Hong-Ba, L. Yue-Lin, J. Shuo, Z. Ying, G.N. Luo, L. Guang-Hong, Investigating behaviours of hydrogen in a tungsten grain boundary by first principles: from dissolution and diffusion to a trapping mechanism, *Nucl. Fusion* 50 (2) (2010) 025016.
- [50] A. Dubinko, A. Bakaeva, M. Hernández-Mayoral, D. Terentyev, G.D. Temmerman, J.M. Noterdaeme, Microstructural modifications in tungsten induced by high flux plasma exposure: TEM examination, *Phys. Scr.* 2016 (T167) (2016) 014030.
- [51] D. Terentyev, X. Xiao, A. Dubinko, A. Bakaeva, H. Duan, Dislocation-mediated strain hardening in tungsten: thermo-mechanical plasticity theory and experimental validation, *J. Mech. Phys. Solids* 85 (2015) 1–15.
- [52] V.I. Dubinko, E.E. Zhurkin, P. Grigorev, D. Terentyev, G. Van Oost, A. Dubinko, S.V. Dmitriev, Dislocation mechanism of deuterium trapping and transport in tungsten under sub-threshold plasma implantation, *Lett. Mater.* 3 (2013) 5.
- [53] Material Specification for the Supply of Tungsten Bars for the ITER Divertor, 2010. IDM Number: ITER_D_2X38PN v. 1.0.
- [54] M. Oberkofler, M. Reinelt, C. Linsmeier, Retention and release mechanisms of deuterium implanted into beryllium, *Nucl. Instr. Meth. Phys. Res. B* 269 (11) (2011) 1266–1270.

B

Mobility of hydrogen-helium clusters in tungsten studied by molecular dynamics

P. Grigorev, D. Terentyev, G. Bonny, E. E. Zhurkin, G. van Oost, J.-M. Noterdaeme

published in Journal of Nuclear Materials, 2016, Vol. 474, pp. 143-149.



Mobility of hydrogen-helium clusters in tungsten studied by molecular dynamics



Petr Grigorev ^{a,b,c,*}, Dmitry Terentyev ^a, Giovanni Bonny ^a, Evgeny E. Zhurkin ^c, Guido van Oost ^b, Jean-Marie Noterdaeme ^{b,d}

^a SCK-CEN, Nuclear Materials Science Institute, Boeretang 200, Mol, 2400, Belgium

^b Ghent University, Applied Physics EA17 FUSION-DC, St.Pietersnieuwstraat, 41 B4, B-9000, Gent, Belgium

^c Department of Experimental Nuclear Physics K-89, Institute of Physics, Nanotechnologies, and Telecommunications, Peter the Great St.Petersburg Polytechnic University, St. Petersburg, Russia

^d Max-Planck-Institut für Plasmaphysik, Garching, Germany

ARTICLE INFO

Article history:

Received 6 November 2015

Received in revised form

21 March 2016

Accepted 23 March 2016

Available online 25 March 2016

ABSTRACT

Tungsten is a primary candidate material for plasma facing components in fusion reactors. Interaction of plasma components with the material is unavoidable and will lead to degradation of the performance and the lifetime of the in-vessel components. In order to gain better understanding the mechanisms driving the material degradation at atomic level, atomistic simulations are employed. In this work we study migration, stability and self-trapping properties of pure helium and mixed helium-hydrogen clusters in tungsten by means of molecular dynamics simulations. We test two versions of an embedded atom model interatomic potential by comparing it with *ab initio* data regarding the binding properties of He clusters. By analysing the trajectories of the clusters during molecular dynamics simulations at finite temperatures we obtain the diffusion parameters. The results show that the diffusivity of mixed clusters is significantly lower, than that of pure helium clusters. The latter suggest that the formation of mixed clusters during mixed hydrogen helium plasma exposure will affect the helium diffusivity in the material.

© 2016 Elsevier B.V. All rights reserved.

1. Introduction

Tungsten (W) is chosen as a divertor armour material for the International Thermonuclear Experimental Reactor (ITER) and is a candidate for the first wall material for DEMO reactor [1]. During the operation of a fusion reactor, the plasma facing material will be exposed to hydrogen (H) isotopes (deuterium and tritium) and helium (He) particle fluxes as well as high energy neutron irradiation. Thus, both H and He will be present in the material either coming directly from plasma or from the transmutation reactions induced by the neutrons. Understanding the effect of the presence of these elements on the modification of the material's properties and the physical mechanisms guiding the undergoing processes is of great practical and theoretical interest.

Both experimental and modelling efforts were done to

understand the interaction of H with W under ITER relevant exposure conditions [2–7]. It was demonstrated that exposure to H (deuterium) plasma in doses up to $\sim 10^{26}$ D/m² leads to the formation of blisters on the surface of the material and accumulation of H (retention) accompanied by the bubble formation in the material's subsurface. Bubble formation occurred at a depth of several μm , which exceeds the implantation range by an order of magnitude (~ 10 nm). At the same time, experiments involving He implantation demonstrate the presence of He bubbles and 'fuzz' formation in a subsurface region at a length scale comparable to the implantation depth [8,9]. Atomistic modelling [10–13] revealed a significant difference in the behaviour of H and He atoms in tungsten. The binding energy of two H atoms in tungsten is negative (~ -0.06 eV), meaning that H atoms do not cluster together in a W lattice unlike He atoms. This also means that accumulation of H in W will be governed by diffusion and trapping on lattice defects such as vacancies, dislocations and grain boundaries [14,15]. In contrast, He atoms exhibit strong attraction (~ 1.0 eV) and do cluster together and can even push out a W atom from its equilibrium

* Corresponding author. SCK CEN, Nuclear Materials Science Institute, Boeretang 200, Mol, 2400, Belgium.

E-mail address: grigorievpit@gmail.com (P. Grigorev).

lattice site (to form self-interstitial) once the He cluster reaches a certain critical size. This mechanism is called self-trapping and it is believed to be responsible for the bubble and ‘fuzz’ formation under He implantation.

Ab initio studies of He–H interaction [16–18] showed that there is an attractive interaction between He clusters and H atoms suggesting synergistic effects under mixed He–H plasma implantation. Suppressing of blistering, confirmed by experimental studies [19,20], is one of the effects seen under simultaneous H and He exposures. The suppression of blistering was attributed to a decrease of H permeability through the subsurface region due to He bubble formation. Another remarkable effect was a detection of nanometric He bubbles at a depth significantly larger than the He implantation range [20], not seen in pure He exposures. However, comprehensive physical mechanisms leading to these synergistic effects are so far not clear.

To contribute to the understanding of the He–H interaction in a W lattice, we perform atomistic simulations using molecular static (MS) and molecular dynamics (MD) computational techniques. In this work, we assess the interaction of He–H clusters of different sizes and chemical morphology. The obtained MS results are compared with available *ab initio* data to validate and substantiate the application of central-force interatomic potentials for the studied problem. By means of MD simulations, we study the diffusion and thermal stability of mixed He–H clusters to gain an understanding of the mechanisms causing the above mentioned synergistic effects under mixed He–H implantation conditions.

2. Computational details

In this work, we used the interatomic potential for the W–H–He system created in the framework of the Embedded Atom Model (EAM) and published in Ref. [21]. There are two versions referred to as “EAM1” and “EAM2” in Ref. [21]. Both potentials are based on the interatomic potential for bcc W named “EAM2” from work [22]. The choice of the base W potential was made on the basis of benchmark calculations involving 19 up to date available EAM potentials for W [23]. In the derivation of the EAM1 version, an emphasis was put on a quantitative reproduction of *ab initio* data for the binding between H–H, He–He and H–He pairs [21]. The off-centre position of a H atom in a vacancy as predicted by DFT [24] was not considered, and therefore both H and He are described by pair potentials only. For the EAM2 potential, the focus was made on the stabilizing H in an off-centre position in the vacancy and therefore an embedding function was added for the H–H and H–W interaction terms. Both types of the potentials predict the tetrahedral position for H and He atoms as the most favourable in bulk W.

MS and MD calculations were performed using the LAMMPS simulation package [25], where the above-mentioned interatomic potentials were implemented. Simulations were performed in bcc W. All MD simulations were performed using a classical MD algorithm in the NVE ensemble, where the number of particles N, volume V and total energy E in the system are kept constant. Prior to the NVE run, each sample was thermalized and set to zero pressure using the Berendsen algorithm [26]. A simulation time-step of 0.1–1 fs was taken depending on the simulation temperature and the total simulation time varied from 5 ns for high temperature simulations up to 25 ns for low temperature simulations. MS calculations were performed using a conjugate gradient algorithm embedded in the LAMMPS package with a relative energy change tolerance between iterations of 10^{-10} .

The size of the crystallite used in simulations was $10 \times 10 \times 10 a_0^3$ (a_0 is the lattice constant predicted by the potential: 3.14 Å) and it contained 2000 atoms before any point defect or cluster was introduced. Periodic boundary conditions were applied in all three

directions.

The incremental binding energy of a H or He atom to a cluster is defined as the energy difference between the state where the H or He atom is far away from the cluster and the state where it is part of the cluster. As such, the binding energy between an atom A and a cluster B in W is calculated as,

$$E_b(AB) = E(A) + E(B) - E(AB) - E_{ref} \quad (1)$$

Here $E(X)$ is the total energy of the box containing the defect X and E_{ref} is the total energy of the box containing no defects (bcc W in our case). In this notation, a positive value of the binding energy corresponds to attraction between the defects. Prior to the static relaxation of the considered atomic configuration a short MD run at 300 K for 1 ps was performed after which the system was quenched to 0 K. This procedure allows the possibility for the system to evolve out of local minima and arrange itself into most stable configuration.

In order to obtain the diffusion parameters of H and He clusters a number of MD simulations were performed at finite temperature, T , varied in the range of 200–1700 K. The main goal was to obtain the diffusion coefficient as a function of temperature, which allows one to extract the pre-exponential factor D_0 and activation energy E_m using the Arrhenius type equation:

$$D = D_0 \exp\left(-\frac{E_m}{k_B T}\right) \quad (2)$$

In each MD run that lasted over a timespan of τ (5–25 ns), the trajectory of the H atom was followed and visualized. Then, the mean square displacement \bar{R}_n^2 of the position of the H atom was calculated to obtain the diffusion coefficient using the well-known Einstein equation:

$$D_n(T) = \frac{\bar{R}_n^2}{2n\tau}(T) \quad (3)$$

where n is dimensionality of the motion (i.e., $n = 3$ for three dimensional bulk diffusion) and τ is the simulation time.

To improve the accuracy of the diffusion coefficient estimation, we employed the so-called independent interval method (IIM) [27]. The idea of the method is to decompose the full time of the simulation (τ) into a number of independent segments (k) with time length of τ/k and calculate the diffusion coefficient using Eq. (3) on each segment. After that, the mean value of the diffusion coefficient is taken. This method also allows one to estimate the uncertainty of the calculation by calculating the standard deviation of the mean (σ) since the trajectory is divided into statistically independent intervals. Once the diffusion coefficient as a function of temperature is obtained, the Arrhenius equation (Eq. (2)) is fitted to extract the activation energy and prefactor. Employing a weighted least squares method [28] for fitting and using $1/\sigma^2$ as the weights, the diffusion parameters together with corresponding errors were obtained.

In case of simulations with mixed H–He clusters, only the time and trajectories where the atoms were clustered together was taken into account. Some weakly bound clusters have limited stability at finite temperature and therefore they decay quickly and bind back. By applying a post-processing algorithm, we only consider a set of separate segments where the cluster was stable and moved as a whole object. If the number of such independent segments was higher than 10, we used an average value of the diffusion coefficient calculated over these segments. If the number of these segments was lower than 10, the IIM method was applied to the longest time segment. The average time length of the

segments when the cluster remains stable, \bar{t} , allows one to calculate a decay frequency $\nu = \frac{1}{\bar{t}}$. Having a set of data for decay frequency as a function of temperature, an Arrhenius expression $\nu = \nu_0 \exp\left(-\frac{E_d}{k_B T}\right)$ was fitted to this dataset to deduce the dissociation energy, E_d and pre-exponential factor ν_0 . These values were compared with the predictions from static calculations as well as *ab initio* data.

3. Results and discussion

3.1. Molecular static calculations

As was said before, for our calculations we used both EAM1 and EAM2 potentials from Ref. [21]. In this work both versions of the potentials were tested to reproduce *ab initio* values of the interaction energy of H–He, He–He and H–H pairs, reported in Ref. [18]. It was demonstrated that both potentials give qualitative agreement with *ab initio* data and quantitative agreement is achieved by the EAM1 potential. In Fig. 1 we compare the results for incremental binding energy of a He atom to a cluster of He atoms in bulk tungsten, predicted by both versions of the potential and *ab initio* values from Ref. [11]. As was shown in Refs. [21], EAM1 gives better agreement for the He–He pair interaction and EAM2 underestimates the corresponding binding energy. However, as can be seen from Fig. 1, EAM1 shows a rapid increase of the binding energy with increasing of the cluster size, which is not in agreement with the trend coming from *ab initio* data. At the same time EAM2 gives reasonable agreement regarding for the binding energy function. Since in this work we study the mobility of mixed He–H clusters, the adequate reproduction of the binding energy function is important to correctly describe the thermal stability of the clusters during MD simulations.

An important process that affects the diffusivity of He clusters is the so called self-trapping mechanism. After a cluster of He atoms of a certain size is created, it becomes energetically more favourable to create a Frenkel pair in order to release the stress created by the interstitial He atoms. After the Frenkel pair is created, He atoms occupy the vacancy and become immobile. Thus it is important to test the ability of the potentials to reproduce this mechanism for reliable simulations of H–He clusters mobility. MS calculations were used to assess the energy balance of a system containing a He cluster in an ideal W matrix and a system where the same He

cluster is placed in a vacancy close to a W self-interstitial atom (SIA). The same energy balance calculations were also performed by *ab initio* techniques in Ref. [12]. The results from this work are compared with our MS calculations in Fig. 2. It can be seen that both versions of the potential are in good agreement with the *ab initio* values. Regarding the threshold size of the He cluster at which the formation of a Frenkel pair becomes more favourable the potentials predict a value for N_{He} between 5 and 6 atoms. Despite the significant difference in description of binding of He clusters in bulk tungsten (see Fig. 1), both versions of the potentials give very similar values for the formation energy of Frenkel pairs. This observation is explained by the fact that the bias of EAM1 for the binding of He atoms in bulk is similar to its bias for He atoms in a vacancy. Since there is no difference between both EAM potentials with respect to the He self-trapping mechanism; but the EAM2 potential describes the energetics of He clusters in the bulk W better, we chose the EAM2 potential for the finite temperature simulations.

As we study the mobility of He–H clusters, it is important to first assess the binding energy of He and H atoms in these clusters by MS calculations. In Fig. 3, the results for the incremental binding energy of a H atom to He–H clusters are presented. It is important to note that the He binding energy is higher than that for a H atom because of the strong He–He bonding (1.03 eV), while the He–H bond strength is only 0.2 eV. Thus, the stability of the mixed He–H clusters will be determined by the binding energy of a H atom as it has the lowest binding energy. It can be seen from Fig. 3 that there is a rapid decrease of the binding energy as the number of H atoms in the cluster increases. Starting from three H atoms in the cluster, the binding energy becomes negligible, indicating that the cluster becomes unstable. This result is in agreement with *ab initio* data from Ref. [17] where low stability of clusters containing more than three H atoms was demonstrated. The most stable atomic configurations for the considered clusters are shown in Fig. 4.

These static calculations defined the configurations that should be studied by MD simulations. The energy needed for He-induced Frenkel pair formation becomes quite low (~2 eV) if the cluster contains four He atoms. Adding the fifth He atom results in the spontaneous generation of a Frenkel pair. This means that the punching of a tungsten self-interstitial is also possible for He–H clusters containing four He atoms at sufficiently high temperature, as was actually demonstrated in Ref. [12]. Thus, we decided to study only clusters containing at most four He atoms to avoid the

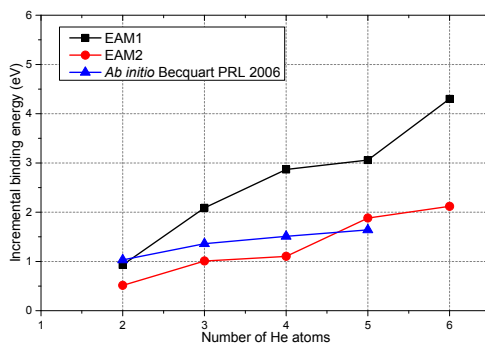


Fig. 1. Comparison of the predictions of the incremental binding energy for He clusters obtained with the EAM1 and EAM2 interatomic potentials and *ab initio* method in Ref. [11].

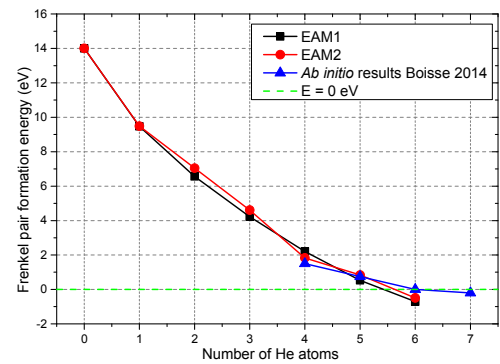


Fig. 2. Comparison of the predictions of the Frenkel pair formation energies in presence of He clusters obtained by EAM1 and EAM2 and *ab initio* method in Ref. [12].

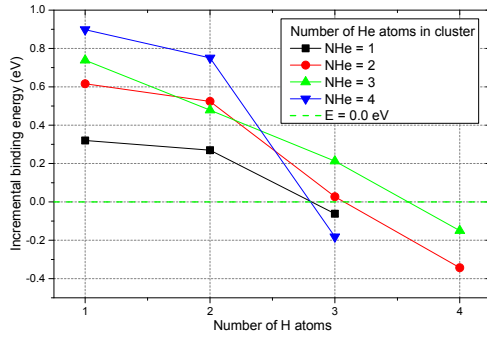


Fig. 3. Incremental binding energy of a H atom to He–H clusters as predicted by the EAM2 potential.

transformation caused by self-interstitial punching. Fig. 3 shows that starting from three H atoms in the cluster, the latter becomes unstable, meaning it will decay during MD runs at finite temperatures. Thus for further MD studies, the pure and mixed clusters containing from one to four He atoms and up to two H atoms were considered.

In this work we did not directly test other types of the available interatomic potentials for W–He–H system regarding He cluster formation energy, He assisted Frenkel pair formation and H and He mobility. However in Ref. [21] a Bond Order Potential (BOP) from Ref. [30] was benchmarked and validated by comparison with *ab initio* data. The results of that comparison allow us to estimate the relevance of the potential for our study. Both types of the potential (BOP and EAM) predict the tetrahedral position as the most favourable for both H and He together with correct ordering of interstitial formation energies, although EAM potentials show the best quantitative agreement with *ab initio*. Both types of the potentials demonstrate good agreement in terms of H–H, H–He and He–He pair interaction. With respect to the binding energy of a H-vacancy or He-vacancy pair, EAM potentials reproduce the *ab initio* values, while BOP underestimates and overestimates the binding for H and He, respectively. BOP predicted binding energy of H atoms

to vacancy–H–He clusters is overestimated by about a factor two, but for He, on the other hand, the values lay within the *ab initio* range. These discrepancies would affect the energetics of the He–H clustering behaviour together with He assisted Frenkel pair, as treated by the BOP potential. The migration energy for H interstitial is well reproduced by all potentials. The migration energy for He interstitial is well reproduced by EAM potentials, but underestimated by BOP by a factor three. Thus, we believe that qualitatively simulations using BOP potential would results similar picture regarding the mobility of He–H clusters. However, numerical discrepancies between BOP and *ab initio* data in He migration energy and H binding energy to vacancy–H–He clusters together with He assisted Frenkel pair formation energy would lead to essential quantitative differences in the results and EAM2 potential remains our choice for dynamic calculations.

3.2. Molecular dynamic simulations

A set of MD simulations was performed to obtain information on the diffusivity and thermal stability (i.e. lifetime) of the He–H clusters. As was described in Section 2, the Arrhenius expression was used to fit the set of diffusion coefficients and decay frequencies obtained at different temperatures from the MD simulations. In Fig. 5, the decay frequency together with Arrhenius fits for the He–H clusters is presented. The slope of the plot corresponds to the dissociation energy E_{diss} . The error bars correspond to 1.96 times the standard error around the average, which corresponds to the 95% confidence interval of the mean value. Following the standard assumption, the dissociation energy E_{diss} is a sum of binding energy and migration barrier ($E_{\text{diss}} = E_b + E_m$). The average discrepancy between the values of the dissociation energy E_{diss} obtained by fitting the MD data and the results of the static calculations for binding energies E_b (see Fig. 3) is 0.21 ± 0.03 eV. This is in excellent agreement with the H migration barrier (0.21 eV) in bulk W both predicted by the potential and obtained with *ab initio* calculations (0.2 eV) [18].

As was said before, for obtaining diffusion parameters of He and He–H clusters we used independent interval method. However, another way to obtain diffusivity from particle trajectory is to calculate the slope of the mean square displacement (MSD) as a function of time. In IIM method the MSD dependence on time is not calculated directly, thus we can validate the results of the method

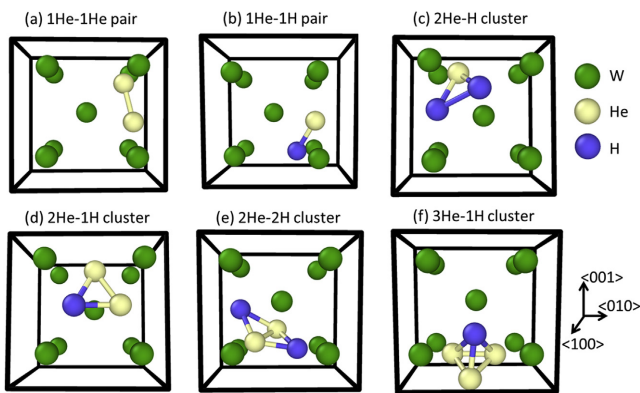


Fig. 4. The atomic configurations of mixed He–H clusters corresponding to binding energy values reported in Fig. 3. The visualization is done using OVITO tool [29].

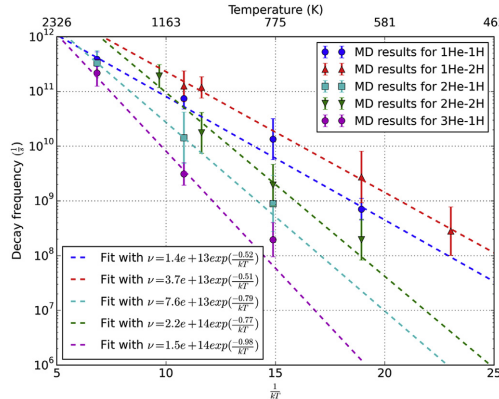


Fig. 5. Arrhenius plot of the decay frequency of He–H clusters with 1–4 He atoms in the cluster obtained from MD simulations. The error bars represent 95% confidence interval around the mean.

by comparison with the theoretical dependence $MSD = 6*t*D$. This comparison is made for He₂-H₁ and He₃ clusters on the Fig. 6. (a) and (b) respectively. It can be seen from the figure that MSD data lies in the area defined by the values of diffusivity the uncertainties obtained by IIM method, which confirms the validity of the method. The similar comparison was made for other clusters showing the same result.

In Fig. 7, the diffusion parameters for He–H clusters (a) and He clusters (b) are shown. From Fig. 7(a) it follows that the slope of the fits for the clusters with 1 and 2 H atoms is almost the same, while the prefactor, D_0 , decreases for the larger cluster. This means that the migration energy is the same for these clusters, but the effective attempt frequency is different. The latter indicates a difference in vibrational entropy between the two clusters. Fig 7(b) demonstrates that the migration energy of a He cluster increases with its size.

It is important to note that for the He₄ cluster an event of self-

trapping was detected during the MD run at 1700 K, which is in agreement with the MS predictions as well as with the MD results from Ref. [12].

The diffusion and lifetime parameters were obtained by fitting Arrhenius equation to the data. Having the uncertainty of the data available from IIM method, we can estimate the validity of the Arrhenius equation for the data. To do this one can use so called reduced Chi squared test, where the following value needs to be

calculated: $\tilde{\chi}^2 = \frac{1}{d} \sum_{i=1}^N \left(\frac{y_i - f(x_i)}{\sigma_i} \right)^2$ [31], where N is number of data points, y_i and x_i is the data set, σ_i – uncertainty of y_i , $f(x)$ is the expected function, in our case it is Arrhenius equation, d – is a number of degrees of freedom of the data distribution. In our case $d = N - c$, where N is number of data points and c – number of constraints. In our study c equals 2 since we define 2 parameters for Arrhenius equation from the data. Values of $\tilde{\chi}^2$ close to 1, or lower indicate high validity of expected function for the data [31]. Using 95% confidence interval for the uncertainty estimation of the data we calculated reduced Chi squared for diffusion and lifetime data. Obtained values are reported in Table 1. As can be seen from the table, most of the values are significantly lower or very close to 1, which confirms the validity of Arrhenius equation for the data.

The migration energy of different He–H clusters as well as of pure He clusters obtained by applying the above described techniques are summarized in Fig. 8. It can be seen that indeed the migration energy of He clusters increases with the size of the cluster (black curve). If H atoms are added to a He cluster, the migration energy increases almost by a factor of two and gets close to the value of the migration energy of a single H atom, denoted by the green area in the graph (in web version). The increase of the migration energy of the mixed clusters compared to pure He clusters is consistent with the fact that it is defined by the slowest constituent of the cluster, which is H atom. Hence, the formation of mixed clusters will have a strong impact on the diffusivity of pure He clusters, which migrate extremely fast in a H-free tungsten lattice. On the other hand, pure He and mixed He–H clusters would act as trapping sites for freely migrating H atoms, which do not feature self-clustering in bulk W. The obtained values for the migration barriers and dissolution energies are summarized in Table 1.

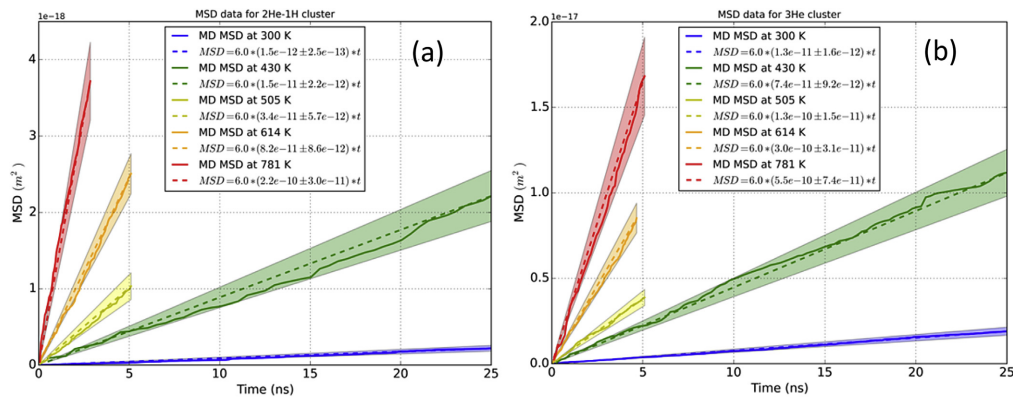


Fig. 6. Mean square displacement as a function of time for 2He-1H (a) and 3He (b) clusters. The dashed lines represent diffusivities obtained with IIM method; the coloured areas represent the error for diffusivity as 95% confidence interval.

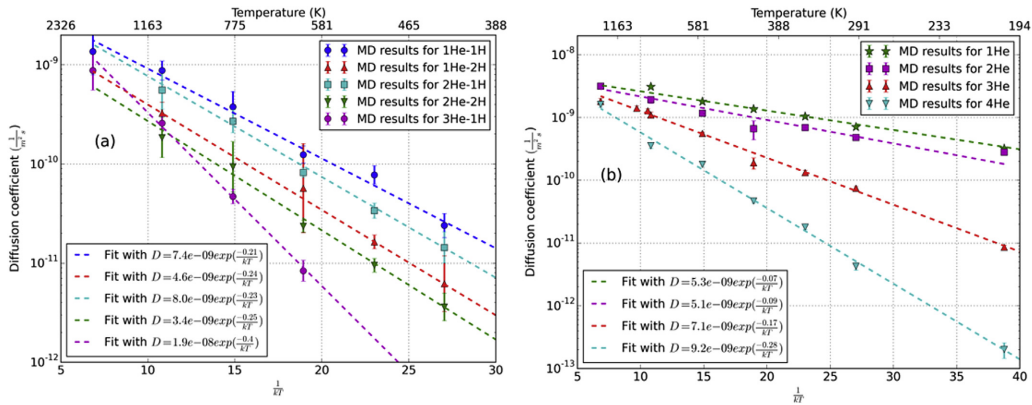


Fig. 7. Arrhenius plot of the diffusion coefficients for He clusters containing 1 to 4 He atoms obtained from MD simulations. The error bars represent 95% confidence interval of the mean.

Table 1
Migration barriers and dissolution energies together with χ^2 values for He and mixed He–H clusters.

Cluster type	Migration barrier (eV)	χ^2 for Diffusion data	Dissolution energy (eV)	χ^2 for Lifetime data
1He	0.071 ± 0.007	0.61	—	—
2He	0.09 ± 0.01	1.23	—	—
3He	0.17 ± 0.01	0.42	—	—
4He	0.28 ± 0.02	1.24	—	—
1He–1H	0.21 ± 0.03	0.08	0.52 ± 0.02	0.50
1He–2H	0.25 ± 0.03	0.02	0.51 ± 0.04	0.13
2He–1H	0.23 ± 0.02	0.12	0.79 ± 0.01	0.23
2He–2H	0.25 ± 0.04	0.07	0.77 ± 0.08	0.11
3He–1H	0.40 ± 0.03	0.67	0.98 ± 0.09	1.17

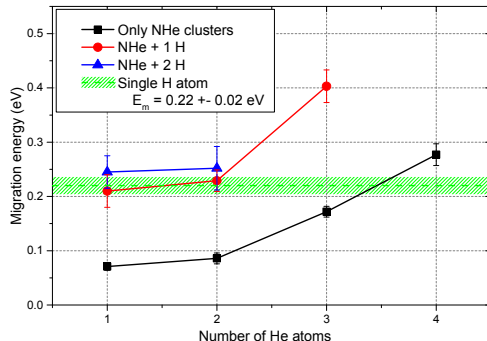


Fig. 8. Migration energies for He–H clusters extracted from MD simulations. The error bars represent the 95% confidence interval.

4. Conclusive remarks

A set of molecular dynamics calculations at finite temperature was performed and diffusion parameters for He–H clusters were obtained. Prior to performing the MD calculations, two versions of EAM potential from Ref. [21] were validated by comparison of the results of static calculations on He–He, He–H and H–H interaction

with *ab initio* data from Refs. [11,12]. The most adequate potential was selected and applied in MD simulations. On the basis of the benchmark MS calculations and results of finite temperature MD simulations, the following conclusions can be drawn:

- The static calculations revealed a significant difference in the binding energy of He in the He clusters as predicted by the EAM1 and EAM2 potentials. The pair interactions of He–He atoms is better reproduced by the EAM1 potential, while EAM2 underestimates the interaction, as compared to the *ab initio* results. However, the EAM1 potential overestimates the increase of the binding energy with cluster size. The EAM2 potential, on the other hand, shows better agreement.
- Comparison of the energy balance for He assisted Frenkel pair formation showed that both versions of the potential demonstrate acceptable agreement with *ab initio* prediction. The inaccuracy of the EAM1 potential with respect to the prediction of the He binding energy in the He clusters should be considered as an important drawback for the modelling of the diffusion process of the small mixed clusters. The EAM2 potential reproduces the binding energy of He in He clusters in close agreement with *ab initio* calculations.
- The binding of a H atom in He–H clusters becomes negligible if the mixed clusters contains three H atoms or more. Thus, stable mixed clusters contain no more than two H atoms.
- On the basis of the diffusion coefficients of pure He and mixed He–H clusters deduced from the MD simulations, we conclude that the migration energy of pure He clusters increases with

increasing cluster size; and for the He_3 cluster it is two times higher than the migration energy of a He interstitial (0.07 eV). • Mixing of H atom(s) with a He cluster leads to the increase of the migration barrier, so that the migration energy of the mixed clusters are comparable to the migration energy of an interstitial H atom (0.2 eV). This implies that the formation of mixed clusters primary leads to the suppression of the He diffusivity.

The conclusions listed above were made based on the analysis of the results of MD simulations using 3D periodic conditions relevant from the bulk material. In order to properly study synergistic effects during mixed He–H implantation one has to perform a full scale simulation of mixed beam exposure conditions taking account surface effects. Unfortunately, experimentally-relevant timescales are not reachable by MD techniques and an upper scale model such as rate theory is needed. Our work provides diffusion and lifetime parameters together with self-trapping energetics for He–H clusters being the necessary input for such simulations.

Acknowledgements

This work was supported by the European Commission and carried out within the framework of the Erasmus Mundus International Doctoral College in Fusion Science and Engineering (FUSION-DC).

This work has been carried out within the framework of the EUROfusion Consortium and has received funding from the Euratom Research And Training Programme 2014–2018 under grant agreement No 633053. The views and opinions expressed herein do not necessarily reflect those of the European Commission.

References

- [1] R.E. Clark, D. Reiter, *Nuclear Fusion Research: Understanding Plasma-surface Interactions*, Springer, 2005.
- [2] Y. Zayachuk, M.H.J. Hoen, P.A.Z.v. Emmichoven, I. Uytdenhouwen, G.v. Oost, *Nucl. Fusion* 52 (2012) 103021.
- [3] O.V. Ogorodnikova, J. Roth, M. Mayer, *J. Nucl. Mater.* 313–316 (2003) 469–477.
- [4] V.K. Alimov, B. Tyburks-Püschel, S. Lindig, Y. Hatano, M. Balden, J. Roth, K. Isobe, M. Matsuyama, T. Yamanishi, *J. Nucl. Mater.* 420 (2012) 519–524.
- [5] T. Ahlgren, K. Heinola, K. Vörtsler, J. Keinonen, *J. Nucl. Mater.* 427 (2012) 152–161.
- [6] A.A. Haasz, J.W. Davis, M. Poon, R.G. Macaulay-Newcombe, Part 1, *J. Nucl. Mater.* 258–263 (1998) 889–895.
- [7] L. Buzzi, G.D. Temmerman, B. Unterberg, M. Reinhart, A. Litovsky, V. Philippis, G.V. Oost, S. Möller, *J. Nucl. Mater.* 455 (2014) 316–319.
- [8] M.J. Baldwin, R.P. Doerner, *J. Nucl. Mater.* 404 (2010) 165–173.
- [9] M. Yamagawa, S. Kajita, N. Ohno, M. Takagi, N. Yoshida, R. Yoshihara, W. Sakaguchi, H. Kurishita, *J. Nucl. Mater.* 417 (2011) 499–503.
- [10] D.F. Johnson, E.A. Carter, *J. Mater. Res.* 25 (2010) 315–327.
- [11] C.S. Becquart, C. Domain, *Phys. Rev. Lett.* 97 (2006) 196402.
- [12] J. Boisse, C. Domain, C.S. Becquart, *J. Nucl. Mater.* 455 (2014) 10–15.
- [13] K.O. Henriksson, K. Nordlund, A. Krasheninnikov, J. Keinonen, *Appl. Phys. Lett.* 87 (2005) 163113–163115.
- [14] V.I. Dubinko, P. Grigorev, A. Bakaev, D. Terentyev, G. Van Oost, F. Gao, D. Van Neck, E.E. Zhurkin, *J. Phys. Condens. Matter* 26 (2014).
- [15] P. Grigorev, D. Terentyev, G. Bonny, E.E. Zhurkin, G. Van Oost, J.-M. Noteerdeame, *J. Nucl. Mater.* 465 (2015) 364–372.
- [16] H.-B. Zhou, Y.-L. Liu, S. Jin, Y. Zhang, G.-N. Luo, G.-H. Lu, *Nucl. Fusion* 50 (2010) 115010.
- [17] A. Takayama, A.M. Ito, Y. Oda, H. Nakamura, *J. Nucl. Mater.* 463 (2015) 355–358.
- [18] C.S. Becquart, C. Domain, *J. Nucl. Mater.* 386–388 (2009) 109–111.
- [19] Y. Ueda, M. Fukumoto, J. Yoshida, Y. Ohtsuka, R. Akiyoshi, H. Iwakiri, N. Yoshida, *J. Nucl. Mater.* 386–388 (2009) 725–728.
- [20] M. Miyamoto, D. Nishijima, M.J. Baldwin, R.P. Doerner, Y. Ueda, K. Yasunaga, N. Yoshida, K. Ono, *J. Nucl. Mater.* 415 (2011) S657–S660.
- [21] G. Bonny, P. Grigorev, D. Terentyev, *J. Phys. Condens. Matter* 26 (2014) 485001.
- [22] M.-C. Marinica, L. Ventelon, M.R. Gilbert, L. Proville, S.L. Dudarev, J. Marian, G. Benteux, F. Willaime, *J. Phys. Condens. Matter* 25 (2013) 395502.
- [23] G. Bonny, D. Terentyev, A. Bakaev, P. Grigorev, D.V. Neck, *Model. Simul. Mater. Sci. Eng.* 22 (2014) 053001.
- [24] K. Heinola, T. Ahlgren, K. Nordlund, J. Keinonen, *Phys. Rev. B* 82 (2010) 094102.
- [25] S. Plimpton, *J. Comput. Phys.* 117 (1995) 1–19.
- [26] H.J.C. Berendsen, J.P.M. Postma, W.F. van Gunsteren, A. DiNola, J.R. Haak, *J. Chem. Phys.* 81 (1984) 3684–3690.
- [27] M.W. Guinan, R.N. Stuart, R.J. Borg, *Phys. Rev. B* 15 (1977) 699–710.
- [28] J.R. Taylor, E. Cohen, *Meas. Sci. Technol.* 9 (1998) 1015.
- [29] A. Stukowski, *Model. Simul. Mater. Sci. Eng.* 18 (2010) 015012.
- [30] X.-C. Li, X. Shu, Y.-N. Liu, Y. Yu, F. Gao, G.-H. Lu, *J. Nucl. Mater.* 426 (2012) 31–37.
- [31] J.R. Taylor, *An Introduction to Error Analysis: the Study of Uncertainties in Physical Measurements*, University Science Books, 1997.

C

Numerical analysis of TDS spectra under high and low flux plasma exposure conditions

P. Grigorev, L. Buzi, A. Bakaeva, D. Terentyev, G. De Temmerman, G. Van Oost and J.-M. Noterdaeme

published in **Physica Scripta**, 2016, Vol. T167 p. 014039 (5 pp.)

Numerical analysis of TDS spectra under high and low flux plasma exposure conditions

P Grigore^{1,4}, L Buzi^{3,4,5,6}, A Bakaeva^{1,4}, D Terentyev¹, G De Temmerman²,
G Van Oost⁴ and J-M Noterdaeme^{4,7}

¹ SCK CEN, Nuclear Materials Science Institute, Boeretang 200, B-2400 Mol, Belgium

² ITER Organisation, Route de Vinon-sur-Verdon—CS 90 046, F-13067 St Paul Lez Durance Cedex, France

³ FOM Institute DIFFER, Edisonbaan 14, 3439 MN Nieuwegein, The Netherlands

⁴ Department of Applied Physics, Ghent University, St. Pietersnieuwstraat 41, B-9000 Ghent, Belgium

⁵ Institut für Energie und Klimaforschung—Plasmaphysik, Forschungszentrum Jülich GmbH, Leo-Brandt-Straße, D-52425 Jülich, Germany

⁶ Université de Lorraine, Institut Jean Lamour, CNRS UMR 7198, Bvd. des Aiguillettes, F-54506 Vandoeuvre, France

⁷ Max-Planck-Institut für Plasmaphysik, Garching, Germany

E-mail: pgrigore@sckcen.be

Received 29 May 2015, revised 3 September 2015

Accepted for publication 18 September 2015

Published 19 January 2016



Abstract

A recently developed numerical model, based on the dislocation-driven nucleation of gas bubbles, is used to analyse experimental results on deuterium retention in tungsten under ITER relevant plasma exposure conditions. Focus is placed on understanding the relation between exposure temperature and flux on primary features of thermal desorption spectra: peak positions and intensities of the desorption flux. The model allows one to relate the peak positions with the size of plasma induced deuterium bubbles and envisage exposure conditions (temperature and flux) for their formation. Based on the performed analysis, dedicated experimental conditions to validate the model are proposed.

Keywords: hydrogen, retention, plasma, blisters, bubbles

(Some figures may appear in colour only in the online journal)

1. Introduction

Development and qualification of plasma facing materials is one of the main challenges in designing large-scale fusion devices (i.e. ITER and DEMO). Due to its favorable physical properties, tungsten (W) is considered to be one of the main candidate materials and is chosen for divertor armour in ITER [1]. The latter should be able to withstand severe conditions in terms of heat and particle loads without considerable degradation of its mechanical and thermal properties within the scheduled operational time. Moreover, the ITER nuclear licensing imposes limits on the amount of tritium making the problem of hydrogen isotope (hereinafter referred to as ‘hydrogen’ or ‘H’) retention an additional technological challenge.

H retention is expressed in surface modification, formation of subsurface blisters and accumulation of H in the bulk material. These effects are attributed to trapping of H atoms on lattice defects such as vacancies, dislocations/grain boundaries and voids [2–4]. Typical kinetic energy of H ions coming from plasma (below 500 eV) is far below the threshold energy needed to create a stable Frenkel-pair defect in W, and the implantation range of H ions is limited to several nanometers [5]. Nevertheless, experiments with ion beams and linear plasma generators show that H penetrates up to a depth of several μm [6–8]. H retention under such conditions cannot be assigned to vacancies since the thermal concentration of vacancies is negligible and no vacancies are created during plasma exposure directly via displacement

damage. However, thermal desorption spectroscopy (TDS) demonstrates three typical release stages, attributed to static traps in the material or also called ‘natural traps’: dislocations, grain boundaries, vacancies and voids [8]. The formation of the vacancy-like trapping defects with subsequent bubble nucleation/growth and blistering under sub-threshold exposure conditions was proposed to originate from the dynamic plasma-induced material modification in the vicinity of a trapping lattice defect, namely: a screw dislocation line.

An alternative model of plasma-induced dislocation-driven bubble formation was proposed recently on the basis of *ab initio* calculations [9]. It was demonstrated that H atoms are attracted to a screw dislocation core and exhibit fast one-dimensional migration along the dislocation line. However, the binding energy of this interaction of 0.5 eV is not high enough to keep H atoms trapped at experimental temperature range (usually above 400 K). According to the calculations, once a cluster of eight H atoms is formed, it should spontaneously transform into a vacancy-like defect (jog) on a dislocation line, and this defect traps H with a considerably higher binding energy. Thus, dislocations (and dislocation junctions) are suggested to act as nucleation sites for stable H bubbles. The interaction strength of H with a newly formed jog on a dislocation is very similar to vacancy-H, as was confirmed by *ab initio* calculations in [9]. Further growth of H-jog clusters and accumulation of vacancy jogs will lead to the formation of a nanometric cavity-like defect. These defects will exhibit extended open volume, and thus, H interaction with such traps will be similar to nano-voids and cavities. The role of dislocations in bubble formation was validated in recent experiments involving the plasma exposure of annealed and plastically deformed W samples [9, 10]. Based on the dislocation-driven nucleation, a numerical simulation tool was developed and used to predict the conditions for the bubble formation depending on exposure temperature and flux [11]. However under the conditions where dislocation-driven mechanism is not active, other microstructural features may act as nucleation sites for bubble nucleation. For example in work [12], the observation of bimodal size distribution of blisters was attributed to an alternative mechanisms—cavity growth and coalescence on grain boundary interfaces.

In [13], the effect of exposure flux–temperature on surface modification and TDS spectra was studied by a set of experiments varying the flux and exposure temperature, respectively, in the range of $9 \times 10^{21} - 5 \times 10^{23} \text{ D m}^{-2} \text{ s}^{-1}$ and 530–870 K. The goal of this work is to estimate H release from H-jog and void-like (multiple vacancy jogs) defects formed during the exposure by successive jog-punching events in support of interpretation of the desorption spectra. We propose a parameterization of the binding energy, defining the H release based on *ab initio* results for H interaction with jogs and cavities as limiting cases. For describing the binding of H to jogs, and jog clusters (in transition state from jogs to bubbles), we use size-dependent fitting. By comparing the release rate, computed following our model, with experimental TDS spectra we establish a relation between positions of release stages and mean size of the defects releasing H.

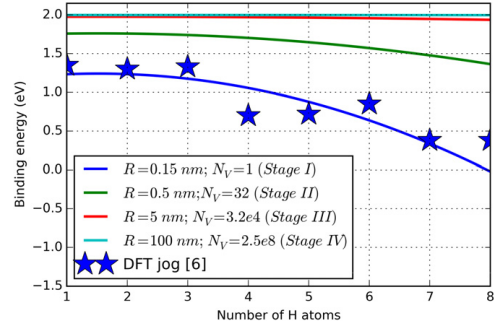


Figure 1. Illustration of binding energy master curve used in simulations. R —defect open volume radius, N_V —corresponding number of W lattice sites that defect occupies.

2. Model description

Following the above mentioned dislocation-driven model of H trapping, one can distinguish the formation of four types of defects: (I) sub-critical H clusters (up to eight H), which are not yet capable to punch out W matrix atoms; (II) super-critical H clusters, whose transformation into jog-H_N configuration is energetically favorable; (III) large super-critical clusters, which already released several jogs for itself and grow further; and finally (IV) nanometric bubble attached to a dislocation line, whose properties (in terms of H trapping) are equivalent to the usual bubble in W bulk. Here, we will not consider the trapping and release from the defects of type I, since these clusters are unstable above 450 K, while the latter being the lower bound of the relevant temperature range.

In work [3], a rate theory model of H desorption from tungsten surface and subsurface defects demonstrated that H release at temperatures, higher than 600 K is not affected by surface recombination. Here, we deal with assessment of high temperature desorption stage (above 600 K), and therefore assume an immediate release of H from the surface after detrapping from the nano-cavities and vacancies. The main parameter of the model that defines the release rate of H from a certain type of a trapping defect is the binding energy (E_b). As mentioned before, *ab initio* calculations showed that dislocation jogs exhibit trapping properties similar to vacancies [9]. The corresponding value of the binding energy is 1.24 eV for one H atom and it decreases with an increase of H atoms trapped at the jog. The dependence of H_N-jog binding energy on N in a cluster is plotted in figure 1. We fitted these data points to generate a family of E_b functions for super-critical clusters. The release rate from such defects is defined as:

$$R_j^- = C_H \nu \exp\left(-\frac{E_b + E_m}{kT}\right), \quad (1)$$

where C_H —concentration of trapped H atoms (assuming that each H in a cluster has equal probability for detrapping event), ν —Debye frequency, E_b —binding energy,

E_m —migration energy (0.4 eV is taken from Frauenfelder's data [14]), k —Boltzmann constant and T —temperature.

For large vacancy clusters (i.e. nano-voids, type IV defects in the above notation) it is reasonable to consider that the binding energy is equal to the permeation energy, i.e. ~2.0 eV [15]. Under this assumption, one can assign the high temperature TDS peak (usually seen in low flux exposures around 700–900 K) to the release from bubbles [16]. However, the TDS spectra obtained after the high flux exposures, at high temperature (above 600 K) and/or high dose (above 10^{26} D m^{-2}), reveal broadening or presence of extra peaks above 900 K [13, 17]. These high temperature release stages cannot be simply explained by detrapping from voids with the binding energy of 2.0 eV, while there are no reasons to assume the presence of any stronger traps than voids/cavities.

To address the issue of high temperature detrapping stage, we analyse the information available from atomic scale. *Ab initio* and molecular dynamics simulations showed that H tends to occupy off-centred position in a vacancy, experiencing weak attraction to W atoms [18, 19]. This implies that H atoms, when filling a void, first should occupy the inner surface positions and then fill the centre.

Thus for the binding energy corresponding to the H trapped at nm size bubbles (type IV defects) we used the results of *ab initio* calculations to account for the transition of H atom from adsorbed state on W surface into the bulk material [15]. These calculations reported 1.96 eV as a value of the binding energy and attempt frequency of $1.07 \times 10^{13} \text{ s}^{-1}$. However, the expression for the release rate should be different from equation (1), since only atoms in adsorbed state on the inner surface of the bubble are available for the detrapping reaction. Thus, the release from nm-scale bubbles is defined by:

$$R_B^- = C_T N_S \nu_{\text{ads}} \exp\left(-\frac{E_b^{\text{ads}} + E_m}{kT}\right), \quad (2)$$

where C_T —trap concentration, N_S —number of available sites for the reaction, we estimate this as a ratio between an inner surface area of the bubble and unit surface for the reaction reported in [15] ($\sqrt{2} a_0^2$, a_0 —lattice unit), ν_{ads} , E_b^{ads} attempt frequency and binding energy from [15]. To create a universal binding energy master curve accounting for a size of the trapping defect (i.e. number of vacancies released), we propose the following expression:

$$R^- = R_B^- + (R_J^- - R_B^-) N_V^{-1/3}. \quad (3)$$

here R_B^- and R_J^- are the release rates for bubble and jog correspondingly, N_V —number of empty lattice sites in tungsten lattice which the trapping defect occupies. The illustration of the binding energy variation as a function of N_V is presented in figure 1. To compute the H release profile from a defect (of a given size and for a given temperature ramp), we assume that after the exposure the defect is filled with H up to a critical pressure (6.5 H atoms per W site), following the analysis done in [11] based on the jog-punching mechanism. Then, the H release rate from the defect is calculated as a function of increasing temperature. The goal of

such calculations is to define the position of the release peak, depending on the size of the defect and concentration of H inside.

3. Results and discussion

Following the above formulated equations, we analyse the TDS spectra obtained in [13]. In figure 2, a comparison of three normalized TDS spectra with the release rate according to the calculations is represented. Normalization of the TDS spectra was done by dividing each one by the maximum release rate value, since here we are interested in correspondence of the peak positions, but not the absolute values of H release. As can be seen from figure 2, TDS spectra for the low flux (figure (b)) and high flux high temperature exposure (figure (a)) reveals similar single peak as in the spectrum measured after ~ 870 K exposure. Temperature position of the peak corresponds to the release from 5 to 10 nm bubbles, following our calculations. TDS spectrum for high flux low temperature exposure (blue triangles) shows two peaks at lower temperature, whose positions can be well fit by imposing the release rate from 1.5 and 0.5 nm defects (blue and green lines in figure 2(a)).

The difference in shape and peak position of the TDS spectra can be related to a size of releasing defects, and in turn interlinked with the trapping mechanism, governing H retention depending on exposure conditions. In [11], the prediction of experimental flux–temperature combination for the dislocation-driven H trapping leading to the formation of super-critical H clusters (contributing to the TDS release at high temperature) was made. The flux–temperature combination favouring the nucleation of super-critical H bubbles is represented by a grey area in figure 3. As one can see, only high flux low temperature exposure is within the range of the dislocation-mediated retention. At the same time, all three other dots are outside the defined area. This is consistent with the fact that only the TDS spectrum after high flux low temperature exposure exhibits two peaks (low temperature peak can be attributed to 1 nm size defects). Whereas, all other spectra show only one peak corresponding to bubbles of 5–10 nm size. Small (1 nm scale) defects can be seen as traces of bubble nucleation on dislocation and their subsequent growth. While, if only large defects contribute to the TDS spectra, it is very likely that other mechanisms (such as triple junctions, natural porosity, etc) but dislocation-driven trapping govern H retention and bubble formation.

4. Conclusive remarks

The proposed modification for H release rate from nanometric pressurized bubbles allows one to relate positions of TDS peaks and explain a shift of high-temperature peak up to 200 K under exposure conditions favoring the growth of bubbles. The occurrence of a single-peak or multiple-peak in TDS spectra can be related to the mechanism of H bubble formation, depending on plasma flux and surface temperature.

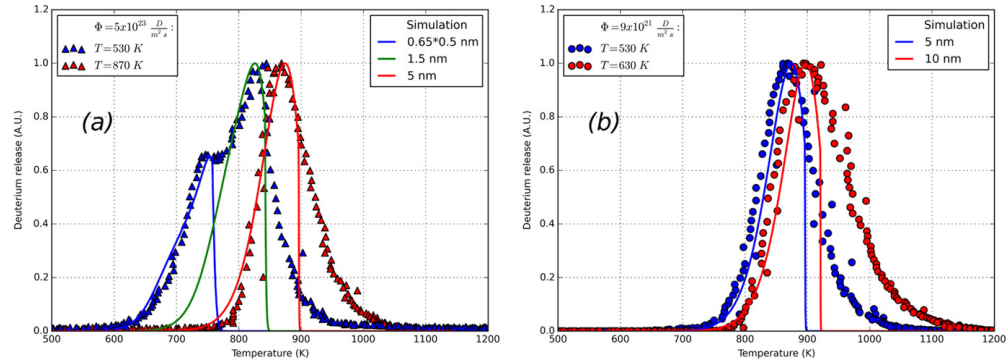


Figure 2. Comparison of normalized TDS spectra from work [13] with results of simulation for high flux ($5 \times 10^{23} \text{ D m}^{-2} \text{ s}^{-1}$ at 530 and 870 K) (a) and low flux ($9 \times 10^{21} \text{ D m}^{-2} \text{ s}^{-1}$ at 530 and 630 K) (b) exposures.

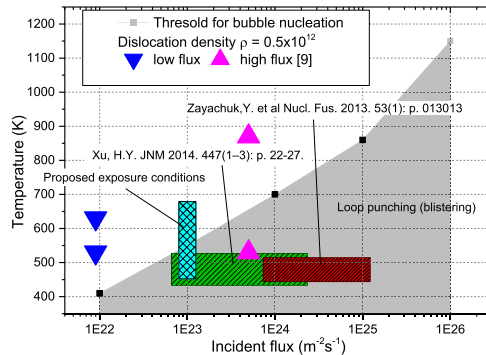


Figure 3. Comparison of experimental conditions from work [13] with prediction of the model for conditions for dislocation mediated retention.

The proposed here computational analysis was applied to experimental data from [13]. According to it, only a combination of high flux and low temperature exposure (530 K– $5 \times 10^{23} \text{ D m}^{-2}$) promotes the nucleation and growth of H bubbles on dislocations, as proposed earlier by jog punching mechanism [11]. In these exposure conditions, the TDS spectra exhibit two well defined peaks attributed to 1 nm size H clusters (presumably, H is trapped in jogs on dislocation lines) and H bubbles (resulting in the high temperature release peak). The three other TDS spectra exhibit only one peak (at high temperature) to be attributed to H bubbles with a size of 5–10 nm, nucleated at other ‘natural’ traps such as random grain boundaries and their junctions. Validation of the dislocation-driven mechanism and proposed here H release model can be realized by performing dedicated exposures in 450–600 K temperature range at flux of $10^{23} \text{ D m}^{-2} \text{ s}^{-1}$, which should result in the dislocation-driven trapping below ~ 500 K to be seen in TDS spectrum as

a peak conventionally attributed to vacancy-like defects (i.e. positioned around 600–700 K).

Acknowledgments

This work was supported by the European Commission and carried out within the framework of the Erasmus Mundus International Doctoral College in Fusion Science and Engineering (FUSION-DC). This work has been carried out within the framework of the EUROfusion Consortium and has received funding from the Euratom research and training programme 2014–2018 under grant agreement No 633053. The views and opinions expressed herein do not necessarily reflect those of the European Commission.

References

- [1] Federici G et al 2001 Plasma-material interactions in current tokamaks and their implications for next step fusion reactors *Nucl. Fusion* **41** 1967
- [2] Van Veen A et al 1988 Hydrogen exchange with voids in tungsten observed with TDS and PA *J. Nucl. Mater.* **155–7** (Part 2) 1113–7
- [3] Eleveld H and van Veen A 1992 Deuterium interaction with impurities in tungsten studied with TDS *J. Nucl. Mater.* **191–4** (Part A) 433–8
- [4] Eleveld H and van Veen A 1994 Void growth and thermal desorption of deuterium from voids in tungsten *J. Nucl. Mater.* **212–5** (Part B) 1421–5
- [5] Pintusuk G 2012 4.17—Tungsten as a plasma-facing material *Comprehensive Nucl. Mater.* **4** 551–81
- [6] ’t Hoen M H J et al 2012 Saturation of deuterium retention in self-damaged tungsten exposed to high-flux plasmas *Nucl. Fusion* **52** 023008
- [7] Schmid K, Rieger V and Manhard A 2012 Comparison of hydrogen retention in W and W/Ta alloys *J. Nucl. Mater.* **426** 247–53
- [8] Ogorodnikova O V, Roth J and Mayer M 2003 Deuterium retention in tungsten in dependence of the surface conditions *J. Nucl. Mater.* **313–6** 469–77

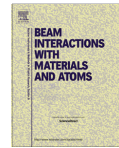
- [9] Terentyev D *et al* 2014 Dislocations mediate hydrogen retention in tungsten *Nucl. Fusion* **54** 042004
- [10] Terentyev D *et al* 2015 Effect of plastic deformation on deuterium retention and release in tungsten *J. Appl. Phys.* **117** 083302
- [11] Grigorev P *et al* 2015 Nucleation and growth of hydrogen bubbles on dislocations in tungsten under high flux low energy plasma exposure *Nucl. Instrum. Methods Phys. Res. B* **352** 96–9
- [12] Alimov V K *et al* 2012 Temperature dependence of surface morphology and deuterium retention in polycrystalline ITER-grade tungsten exposed to low-energy, high-flux D plasma *J. Nucl. Mater.* **420** 519–24
- [13] Buzi L *et al* 2014 Influence of particle flux density and temperature on surface modifications of tungsten and deuterium retention *J. Nucl. Mater.* **455** 316–9
- [14] Frauenfelder R 1969 Solution and diffusion of hydrogen in tungsten *J. Vac. Sci. Technol.* **6** 388–97
- [15] Johnson D F and Carter E A 2010 Hydrogen in tungsten: absorption, diffusion, vacancy trapping, and decohesion *J. Mater. Res.* **25** 315–27
- [16] Ogorodnikova O V *et al* 2011 The influence of radiation damage on the plasma-induced deuterium retention in self-implanted tungsten *J. Nucl. Mater.* **415** (Suppl. 1) S661–6
- [17] Jia Y Z *et al* 2015 Surface morphology and deuterium retention in tungsten exposed to high flux D plasma at high temperatures *J. Nucl. Mater.* **457** 213–9
- [18] Heinola K *et al* 2010 Hydrogen interaction with point defects in tungsten *Phys. Rev. B* **82** 094102
- [19] Sun L *et al* 2013 Hydrogen behaviors in molybdenum and tungsten and a generic vacancy trapping mechanism for H bubble formation *J. Nucl. Mater.* **434** 395–401

D

Nucleation and growth of hydrogen bubbles on dislocations in tungsten under high flux low energy plasma exposure

**P. Grigorev, D. Terentyev, V. Dubinko, G. Bonny, G. Van Oost,
J.-M. Noterdaeme, E. E. Zhurkin**

published in Nuclear Instruments and Methods in Physics Research B, 2015,
Vol. 352, pp. 96-99



Nucleation and growth of hydrogen bubbles on dislocations in tungsten under high flux low energy plasma exposure



Petr Grigorev ^{a,b,c,*}, Dmitry Terentyev ^a, Vladimir Dubinko ^d, Giovanni Bonny ^a, Guido Van Oost ^b, Jean-Marie Noterdaeme ^b, Evgeny E. Zhurkin ^c

^a SCK•CEN, Nuclear Materials Science Institute, Boeretang 200, Mol 2400, Belgium

^b Ghent University, Department of Applied Physics EA17 FUSION-DC, St. Pietersnieuwstraat, 41 B4, B-9000 Gent, Belgium

^c Department of Experimental Nuclear Physics K-89, Institute of Physics, Nanotechnology and Telecommunications, St. Petersburg State Polytechnical University,

29 Polytekhnicheskaya Str., 195251 St. Petersburg, Russia

^d National Science Center, Kharkov Institute of Physics and Technology, Kharkov 61108, Ukraine

ARTICLE INFO

Article history:

Received 10 July 2014

Received in revised form 10 October 2014

Accepted 29 November 2014

Available online 26 December 2014

Keywords:

Hydrogen retention
Tungsten
Bubble

ABSTRACT

A new mechanism for the nucleation and growth of hydrogen (H) bubbles on dislocations under plasma exposure of tungsten was recently proposed on the basis of direct *ab initio* calculations. Density functional theory calculations demonstrated that H atoms are strongly bound to a screw dislocation core and exhibit fast one-dimensional migration along its line. Once the number of hydrogen atoms trapped on a dislocation segment exceeds eight, the emission of a jog occurs thereby converting a pure H_N cluster into a H_{N+1} -jog configuration. On the basis of these results a kinetic model was formulated to evaluate the conditions (i.e., range of temperature and flux exposure) for the transformation of pure H clusters into supercritical hydrogen-vacancy clusters attached to the dislocation line. In this work, a parametric study employing the kinetic nucleation model was performed to derive the hydrogen bubble formation energy function that offers the best agreement with available experimental results. The obtained results allow one to rationalize the depth and temperature dependence of the experimentally observed hydrogen deposition after high flux low energy plasma exposure for ITER relevant conditions.

© 2014 Elsevier B.V. All rights reserved.

1. Introduction

Tungsten is the main candidate material for plasma facing components in future plasma devices. It was chosen as the divertor armor in ITER and is planned to be used in DEMO [1]. Plasma facing materials in fusion devices will be exposed to severe conditions in terms of heat loads and particle flux. Moreover, strict safety limitations are imposed on the amount of tritium accumulated in the reactor's chamber, because it is a toxic, radioactive and expensive material. For ITER the limit was set to be 700 g [2]. From this point of view understanding the mechanism of hydrogen isotopes (HI) retention is important in order to predict the tritium accumulation in the reactor and define its operational regimes.

There is a large amount of experimental studies on HI retention in tungsten (W) available in the literature and an extensive review can be found in [3,4]. Experiments involving plasma exposures at ITER relevant temperatures (400–800 K [1]) showed that after exposure below 600 K, HI sub-surface bubbles and surface blisters

are formed [5–9]. Such surface modifications can lead to the ejection of W atoms or flakes in case of a blister rupture, leading to plasma disruption and consequently to the reduction in the performance of the fusion device. Current models of bubble nucleation and growth [9,10] are based on the assumption that trapping of HI originates at vacancies created during implantation and followed by their subsequent growth by clustering HI and vacancies. Such approaches have shown a very good agreement with experiments involving ion beams exposure with an ion energy in the range 5–30 keV/ion [10]. The energy of such HI ions is above the threshold energy for the creation of displacement damage in W (threshold displacement energy for W is 45–90 eV [11]), and therefore it leads to the creation of stable Frenkel pairs, i.e., vacancy–interstitial defect pairs. More realistic conditions for the ITER environment are reached in experiments involving linear plasma generators where the energy of ions is around 50–100 eV [5–7]. This is significantly lower than the threshold energy for the generation of Frenkel pairs and such irradiation conditions will be referred to as “sub-thresholds conditions”. Thus, during the sub-threshold plasma exposure no vacancies are created directly by plasma ions due to atomic displacement and the vacancy-trapping

* Corresponding author at: SCK•CEN, Nuclear Materials Science Institute, Boeretang 200, Mol 2400, Belgium.

nucleation mechanism imposed in the current numerical models is not relevant. However, intensive blistering is also observed under sub-threshold plasma exposures, for which the mechanisms of bubble nucleation and growth are not properly understood yet. Homogeneous nucleation of hydrogen clusters is highly unlikely due to a very low binding energy between two hydrogen atoms in the bulk (~ 0.01 eV [12]), which does not allow reaching a cluster of critical size to punch out a self-interstitial atom and convert into a stable nucleus.

Recently, a new model of HI retention was proposed, based on the assumption that dislocation networks serve as nucleation sites for HI bubbles [13]. This assumption was confirmed by *ab initio* calculations addressing the interaction of hydrogen with a $\frac{1}{2}(111)$ screw dislocation, which showed that the dislocation can attract up to six H atoms and that the migration barrier of a H atom along the dislocation line (computed to be 0.15 eV) is significantly lower than in the bulk, i.e., 0.24–0.27 eV [14–16]. Moreover, the calculations suggested that the so-called jog-punching mechanism of bubble growth is initiated as soon as eight hydrogen atoms group on a screw dislocation segment. The jog-punching implies a nucleation of two anti-jogs, so that hydrogen atoms occupy a vacancy-type jog, while an interstitial-type jog migrates away along the dislocation line. A rate theory model based on these computational results has shown good agreement with the experimental trends regarding the saturation of HI retention with increasing implantation dose [5,6]. In this work we implement the previously formulated rate theory model to perform a numerical integration and to investigate the exposure conditions (i.e., flux and temperature) resulting in the bubble growth and blister formation.

2. Model description

A schematic picture of the system used in simulations is shown in Fig. 1(a). This is a one-dimensional system where material is divided into slabs of equal width λ_d . Each slab corresponds to a single nucleation site and is fed with H by a source term defined from the steady state solution for the bulk concentration of H atoms discussed in [13]:

$$S(x) = \omega Z \rho F \exp(-x\sqrt{Z\rho}), \quad (1)$$

with Z – geometrical factor ($Z=1$), ρ – dislocation density, ω – atomic volume, F – particle flux, R – particle range.

H atoms accumulate into H_N clusters at dislocation trapping sites following a binding energy function, and H atom can be dissolved from a H_N clusters at a rate defined by the equation:

$$R^-(i) = v C_T(i) \exp(-E_{bin}(N)/k_B T), \quad (2)$$

with v – the attempt frequency, $C_T(i)$ – the trap (or trapped cluster) concentration at slab number i , $E_{bin}(N)$ – the binding energy of a H

atom to the trapped H_N cluster, k_B – Boltzmann constant. The amount of H atoms that escapes from the traps is redistributed between neighboring slabs. Thus, the amount of trapped H at each nucleation site is defined by the balance of trapping, dissolution and exchange between neighboring slabs (Numbers $i-1$ and $i+1$):

$$\frac{\partial C_H(i)}{\partial t} = S(x) + 0.5[R^-(i-1) + R^-(i+1)] - R^-(i), \quad (3)$$

The size of H_N clusters growing during the exposure is determined by a simulation that follows the number of vacant sites generated by the jog-punching mechanism. To introduce the jog punching mechanism that allows a bubble to grow, we must introduce a threshold value for the number of trapped H atoms per vacancy (N_H/N_{vac}) beyond which the jog punching mechanism starts to operate. The main parameters of the model, which define the conditions for the bubble growth, is the binding energy of a H atom to a trapped H_N -VM complex, and the threshold size for a H_N cluster beyond which it is converted into H_{N+1} -jog configuration.

3. Parametrization of the model

To parameterize the model, let us first consider the binding energy of H_N to a screw dislocation and to a vacancy jog on the screw dislocation. Fig. 1(b) compares the binding energy of a H to a H_{N-1} cluster trapped at a vacancy [17–19] and trapped at the dislocation vacancy jog [13], obtained by *ab initio* calculations from the cited works. As can be seen, there is no significant difference between the evolution of the binding energy at a vacancy and at the dislocation jog. The red dashed line is a fit of these *ab initio* results, which are valid for small H_N clusters forming as nuclei for H bubbles. For the well-developed H bubbles, one cannot apply the *ab initio* fitted function. As a limiting case we used the formula obtained within the so-called liquid tear drop (LTD) model, parameterized using a recently developed W-H-He potential in [20], and based on the balance of volume and surface energy, shown in Fig. 1(b).

To define the jog punching threshold parameter (N_H/N_{vac}), let us consider the loop punching mechanism. Pressure is exerted on the bubble surface and the critical one needed to create a dislocation loop is defined as [21]:

$$P_{lp} = 2\gamma/R_b + \mu b/R_b \quad (4)$$

where $\gamma = 2.65$ N/m is the surface tension, $G = 158.6$ GPa is the shear modulus, $b = 2.7$ Å is the Burgers vector of the $\frac{1}{2}(111)$ loop, and R_b is the bubble radius. The values for the surface tension (γ) and shear modulus (G) were taken from [22,23]. The variation of the critical pressure as a function of bubble size (expressed as a number of vacant sites) is plotted in Fig. 2(a) on the right-hand side Y axis. To estimate the critical concentration of hydrogen contained in

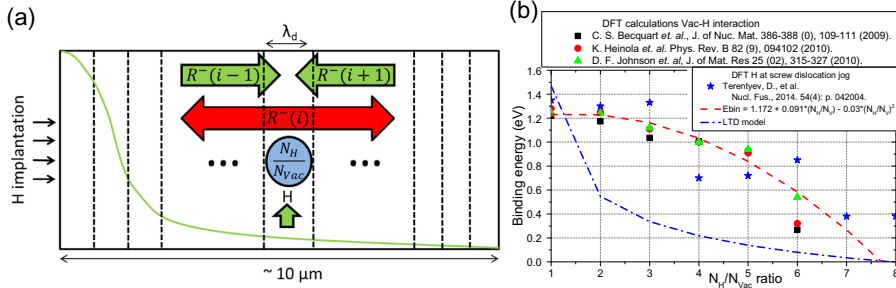


Fig. 1. (a) Schematic description of the model; (b) bubble-H binding energy data and approximations.

the bubble to induce the dislocation loop emission, we used the equation of state [24]:

$$N_b = \frac{4\pi R_b^3 N_a}{3v(p, T)} \quad (5)$$

where R_b is the bubble radius, N_a is the Avogadro constant, and $v(p, T)$ is the molar volume from the equation of state.

The resulting N_H/N_{vac} ratio corresponding to the loop punching pressure is shown in Fig. 2(a) on the left Y axis. As one can see, the ratio obtained using elasticity theory and equation of state goes from 6 to 4 with increasing bubble size up to ~ 4 nm (1000 vacancies). On the other hand, the critical ratio obtained from *ab initio* calculations is 8. Here, we shall explore the sensitivity of the results by varying the N_H/N_{vac} ratio within these two limits.

4. Fitting the model to experimental data

Firstly, we addressed the influence of the choice of the binding energy function on the nucleation of a H bubble, which initiates by the punching of the first jog. As said in the previous section, there is an uncertainty associated with the critical pressure and N_H/N_{vac} ratio for the jog punching. The uncertainty comes from the two models for the binding energy function, namely: LTD model and the fit to *ab initio* results, shown in Fig. 1(b). We applied these two models to investigate the evolution of the growth of H_N clusters and see whether the condition for the jog-punching was met. To define the simulation system, we stuck to the experimental conditions, where the intensive blistering (presumably originating as a result of loop punching) was reported [6], namely, exposure at 450 K with an ion flux of $10^{24} \text{ m}^{-2} \text{ s}^{-1}$. We found that using the LTD model the average size reached by the clusters is 3.6 H atoms per trapping site, while using the *ab initio* fit it is 7. Clearly, the LTD model does not satisfy the condition for the jog-punching in the nucleation regime when H clusters are still very small. That was expected because the extrapolation of the linear elasticity theory to describe atomic-size bubbles is inappropriate. The *ab initio* parameterized model allows for the jog punching mechanism to take place. However, the *ab initio* data are available only for the punching of the first jog, while the further growth of the H_N -jog cluster has not yet been studied by atomistic calculations. Obviously, the information about the binding energy function for the transition from atomic-scale bubbles to classical bubbles should be filled using empirical interatomic potentials.

To provide a physical choice for the critical pressure, we performed a parametric study varying N_H/N_{vac} from 5.0 to 7.0 and computed the distribution of the depth of H deposition for the experimental conditions applied in [6], where the H distribution profile was measured by nuclear reaction analysis (NRA). In particular, we modeled the plasma exposure of 50 eV ions at 450 K with a flux of $10^{24} \text{ m}^{-2} \text{ s}^{-1}$. In these calculations, the critical nucleation depth was the primary result of interest. Experimental profiles practically ceased at a depth around 4–5 μm . Three different profiles for threshold N_H/N_{vac} values of 5.0, 6.5, and 7.0 are shown on the Fig. 2(b). In case of a low value of the threshold (5.0), the evaporation of H atoms from the trap at 450 K is too low to influence the growth of the bubble and the threshold value for jog-punching is reached easily (this also explains the fact that there is almost no fluctuations in this depth profile). The calculations are performed for the system with a depth up to 5 μm , but we can state that in case of $N_H/N_{vac} = 5.0$, the growth of the bubble continues at a depth deeper than several tens of μm , which is not in line with the NRA measurements. In case of a high value of the threshold (7.0), nucleation of bubbles ceased at a depth around 2.5 μm meaning that beyond this level dislocations do not serve anymore as nucleation sites for bubbles and act as migration networks for HI diffusion. The best fit for the experimental profile is obtained for $N_H/N_{vac} = 6.5$, at which the nucleation stops at a depth around 4.5 μm . Therefore, this threshold will be used for the calculations addressing the effect of temperature and flux on the nucleation of stable bubbles.

5. Exposure conditions for the bubble growth

To study the conditions for the bubble formation and growth, we have performed a parametric study employing the above formulated kinetic model and here derived binding energy function. The incident flux and ambient temperature were varied to cover the ranges relevant for ITER conditions. The value of the critical temperature was defined for every value of the flux. At a temperature higher than critical value, no bubble formation at dislocation networks by the jog- and then later by loop-punching is foreseen. As a result of the calculations, we provide boundaries corresponding to the conditions in which the loop punching is expected to operate and in which HI clusters do not convert into stable bubbles. The boundaries obtained for W with dislocation density of $0.5 \times 10^{12} \text{ m}^{-2}$, which is typical for a stress-relieved BCC metal, is shown in Fig. 3.

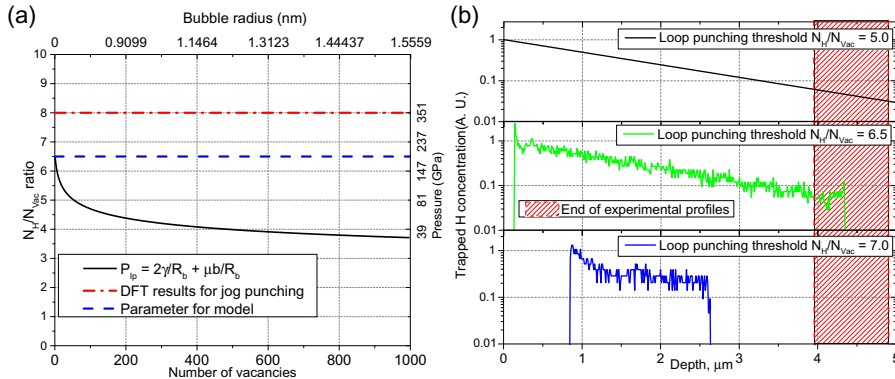


Fig. 2. (a) Estimation of the threshold value for the loop punching mechanism; (b) sensitivity of the system to the loop punching parameters.

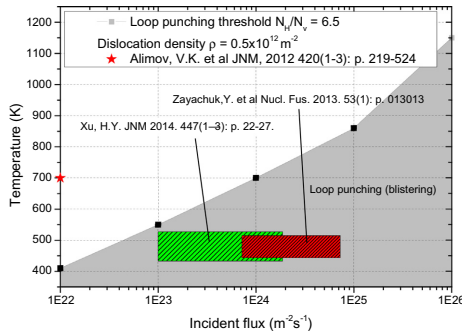


Fig. 3. Exposure temperature vs. flux required for the bubble growth.

Several experimental works addressing the effect of a low energy ion beam or plasma on the surface of tungsten reported blistering [4,5,7,8]. The range of doses and temperatures in which blisters were reported is shown in Fig. 3 by dashed rectangles. In general, the observation of blisters is registered below 700 K for fluxes up to $10^{24} \text{ m}^{-2} \text{s}^{-1}$, which is in line with the prediction of our model. The major exception is the observation of the blisters by Alimov et al. under low flux ion beam exposure ($10^{22} \text{ m}^{-2} \text{s}^{-1}$) at 580–670 K. Their work reported a bimodal size/shape distribution of blisters: large low-dome and small cone-shaped blisters. The authors mentioned that around 400–500 K the small blisters disappear, while the large blisters with a size of few tens of microns become evident. Most likely, the small ones are the signature of the loop punching of bubbles nucleated on dislocations, while the large ones appear as the result of the coalescence of the bubbles nucleated at grain boundary interfaces.

6. Summary

A parametric study employing a model for the bubble nucleation and growth at dislocation networks was performed. Based on the presented results and their discussion we can outline the following:

- The conditions for the transformation of a H_n cluster into H_{n+1} -jog configuration strongly depend on the underlying cohesive model and binding energy function. The comparison with the experiment performed at 450 K employing a high flux plasma confirms that only the *ab initio* parameterization can provide the necessary binding to initiate the bubble nucleation by the jog-punching mechanism.
- Following the comparison of the critical nucleation depth, the computational model provides the best agreement with the experimental results by taking 6.5 as a critical H-to-vacancy ratio to initiate the jog-punching.
- The parameterized model was used to predict the exposure conditions for the nucleation of stable bubbles, their growth and subsequent blister formation.

As a whole, this work aims at revealing a range of fusion relevant exposure conditions in which intensive subsurface degradation is expected. This degradation is expressed in the formation of bubbles that reduce the ductility and crack resistance of the W subsurface. Further improvements of the model and its parameterization are still necessary. For instance, it is essential to refine the binding energy function in the transition range of sizes to link *ab initio* data and the LTD model. Once the bubbles reach a significant size (exceeding nano-meters), the growth of the bubbles by continuous loop punching should take into account matrix hardening induced by already emitted dislocation loops. At the same time, the punched out dislocation loops will also serve as additional traps for the incoming hydrogen. The importance of this secondary dislocation family is still unclear. Nevertheless, the presented here computational model already allows one to rationalize the depth and temperature dependence of the experimentally observed hydrogen deposition after high flux low energy plasma exposure within a dose up to 10^{26} m^{-2} , as was demonstrated by the comparison with the experimental data.

Acknowledgements

This work was supported by the European Commission and carried out within the framework of the Erasmus Mundus International Doctoral College in Fusion Science and Engineering (FUSION-DC). The work was partially supported by the EUROfusion consortium.

References

- [1] 4.17 – Tungsten as a Plasma-Facing Material, Comprehensive Nuclear Materials, Elsevier, Oxford, 2012.
- [2] R. Joachim, T. Emmanuelle, L. Thierry, P. Volker, B. Sebastian, L. Alberto, et al., Plasma Phys. Control. Fusion 50 (2008) 103001.
- [3] R.A. Causey, T.J. Venhaus, Phys. Scr. 2001 (2001) 9.
- [4] J. Roth, K. Schmid, Phys. Scr. 2011 (2011) 014031.
- [5] Y. Zayachuk, M.H.Jt. Hoen, P.A.Z.v. Emmichoven, D. Terentyev, I. Uytdenhouwen, G.v. Oost, Nucl. Fusion 53 (2013) 013013.
- [6] Y. Zayachuk, M.H.Jt. Hoen, P.A.Z.v. Emmichoven, I. Uytdenhouwen, G.v. Oost, Nucl. Fusion 52 (2012) 103021.
- [7] V.K. Alimov, B.Tybarska-Puschel, S. Lindig, Y. Hatano, M. Balden, J. Roth, et al., J. Nucl. Mater. 420 (2012) 519.
- [8] H.Y. Xu, G.N. Luo, H. Schut, Y. Yuan, B.Q. Fu, A. Godfrey, et al., J. Nucl. Mater. 447 (2014) 22.
- [9] O.V. Ogorodnikova, J. Roth, M. Mayer, J. Nucl. Mater. 313–316 (2003) 469.
- [10] T. Ahlgren, K. Heinola, K. Vörtsler, J. Keinonen, J. Nucl. Mater. 427 (2012) 152.
- [11] G.S. Was, Fundamentals of Radiation Materials Science: Metals and Alloys, Springer Verlag, New York, 2007.
- [12] K.O. Henriksson, K. Nordlund, A. Krasheninnikov, J. Keinonen, Fusion Sci. Technol. 50 (2006) 43.
- [13] D. Terentyev, V. Dubinko, A. Bakaev, Y. Zayachuk, W.V. Renterghem, P. Grigorev, Nucl. Fusion 54 (2014) 042004.
- [14] R. Frauenfelder, J. Vac. Sci. Technol. 6 (1969) 388.
- [15] V. Nemanic, B. Zajec, D. Dellasega, M. Passoni, J. Nucl. Mater. 429 (2012) 92.
- [16] K. Heinola, T. Ahlgren, Phys. Rev. B 81 (2010) 073409.
- [17] C.S. Beccuart, C. Domain, J. Nucl. Mater. 386–388 (2009) 109.
- [18] K. Heinola, T. Ahlgren, K. Nordlund, J. Keinonen, Phys. Rev. B 82 (2010) 094102.
- [19] D.F. Johnson, E.A. Carter, J. Mater. Res. 25 (2010) 315.
- [20] G. Bonny, P. Grigorev, D. Terentyev, J. Phys.: Condens. Matter. (2014).
- [21] G.W. Greenwood, A.J.E. Foreman, D.E. Rimmer, J. Nucl. Mater. 1 (1959) 305.
- [22] K.O. Henriksson, K. Nordlund, J. Keinonen, Nucl. Instr. Meth. Phys. Res. B 244 (2006) 377.
- [23] R.D. Kolasinski, D.F. Cowgill, R.A. Causey, J. Nucl. Mater. 415 (2011) S676.
- [24] M. Tkacz, A. Litwiniuk, J. Alloys Compd. 330–332 (2002) 89.

E

Interaction of hydrogen with dislocations in tungsten: An atomistic study

P. Grigorev, D. Terentyev, G. Bonny, E. E. Zhurkin, G. Van Oost, J.-M. Noterdaeme

published in Journal of Nuclear Materials, 2015, Vol. 495, pp. 364-372



Interaction of hydrogen with dislocations in tungsten: An atomistic study



Petr Grigorev ^{a, b,*}, Dmitry Terentyev ^a, Giovanni Bonny ^a, Evgeny E. Zhurkin ^c, Guido Van Oost ^b, Jean-Marie Noterdaeme ^b

^a SCK•CEN, Nuclear Materials Science Institute, Boeretang 200, Mol, 2400, Belgium

^b Ghent University, Department of Applied Physics EA17 FUSION-DC, St.Pietersnieuwstraat, 41 B4 B-9000, Gent, Belgium

^c Department of Experimental Nuclear Physics K-89, Institute of Physics, Nanotechnology and Telecommunications, St.Petersburg State Polytechnical University, 29 Polytekhnicheskaya str., 195251, St.Petersburg, Russia

ARTICLE INFO

Article history:

Received 29 September 2014

Received in revised form

5 June 2015

Accepted 6 June 2015

Available online 12 June 2015

ABSTRACT

The interaction of interstitial hydrogen with a dislocation and point defects in tungsten is studied by means of atomistic simulations. Two different types of interatomic potentials were tested by comparing their results with available *ab initio* data. The recently developed embedded atom method potential showed a better agreement with *ab initio* results than the bond order potential. Static calculations involving screw and edge dislocations showed that hydrogen is attracted to the dislocation core in both cases. It is also found that hydrogen atoms prefer to arrange themselves as elongated clusters on dislocation lines. Molecular dynamics simulations of hydrogen migration along the edge dislocation core confirmed the results of the static calculations and demonstrated a strong attraction to the dislocation core and one-dimensional migration along it.

© 2015 Elsevier B.V. All rights reserved.

1. Introduction

Tungsten (W) is one of the currently considered in-vessel plasma-facing materials for ITER [1]. During ITER's exploitation, cyclic thermal stresses coupled with radiation damage and trapping of plasma components (retention) impose a serious uncertainty regarding the lifespan of the components made of W. Hydrogen (H) retention is a specific problem, since it has a dual impact defining the degradation of W-based components. On the one hand, the maximum retention is limited by the safety limits, and on the other hand, the storage of hydrogen provokes further embrittlement to be added to the detrimental effect of neutron irradiation and thermal fatigue.

Despite significant efforts done in past investigations to explore the main mechanisms of H retention in W [2–6], a complete physical model capable of describing a broad set of experimental data does not yet exist. In our recent works [7,8], we have drawn attention to the role played by dislocations in the trapping, transport and nucleation of hydrogen bubbles. Based on the *ab initio*

calculations we have proposed the so-called 'jog-punching' process as the mechanism to explain the transformation of a meta-stable hydrogen cluster into a stable hydrogen-vacancy cluster – nucleus for a future hydrogen bubble [7].

The idea of the jog-punching mechanism and the obtained *ab initio* data was then implemented in a new theoretical model for the H retention based on H trapping at dislocations and transport to the surface via the dislocation network [8]. Such a model was used to explain the experimentally observed saturation of H retention with dose in different W grades under high flux plasma implantation conditions. One of the principal conditions of this model was the assumption about transport of hydrogen atoms along a dislocation network. Although the *ab initio* calculations have demonstrated that the migration barrier for H to move along the core of a $\langle 111 \rangle$ screw dislocation is smaller than the bulk migration energy, no direct dynamic simulations have so far been performed to demonstrate the preferential diffusion of H in the dislocation core. Moreover, *ab initio* techniques are not suitable for considering defects that produce large stress fields such as edge dislocations and therefore classical molecular dynamics (MD) and molecular statics (MS) studies are still needed to close the gap.

In this work we perform an MD study to characterize the interaction of H with screw and edge dislocations at zero Kelvin and

* Corresponding author. SCK•CEN, Nuclear Materials Science Institute, Boeretang 200, Mol, 2400, Belgium.

E-mail address: petr.grigorev@sckcen.be (P. Grigorev).

finite temperature. The study is performed using two interatomic potentials, namely: the bond order type potential (BOP) developed by Li et al. [9,10], and the recently derived embedded atom method (EAM) potential [11]. The results are compared with available *ab initio* data. By comparing the performance of the two potentials regarding the description of H-vacancy and H-dislocation interaction, we reveal an uncertainty range of the results obtained by different atomistic techniques. Based on the preliminary MD data obtained here, we conclude that H exhibits strong attractive interaction with the core of the $\frac{1}{2}\langle 111 \rangle\{110}$ edge dislocation and at finite temperature performs enhanced one-dimensional migration as compared to the bulk diffusivity.

2. Computational details

As mentioned before, we used two different types of the interatomic potentials, namely: BOP and EAM. There were two different versions of the EAM potential, referred to as “EAM1” and “EAM2” in Ref. [11]. The BOP potential, developed in Refs. [9,10], was fitted to the H interaction with point defects in W. It reproduces very well H–W molecules and geometry of H-vacancy system (i.e. off-centered position of H displaced along $\langle 100 \rangle$ direction), however the resulting H-vacancy binding energy slightly differs from the *ab initio* result. Both EAM potentials were based on the interatomic potential for bcc W named “EAM2” from work [12]. The choice was made after critical review of 19 different EAM potentials given in Ref. [13]. For the EAM1 potential, emphasis was put on a quantitative reproduction of *ab initio* data for the binding between H–H, He–He and H–He pairs [11]. The off-center position of an H atom in a vacancy as predicted by Density Functional Theory (DFT) [14] was not considered, and therefore both H and He are described by pair potentials only. For the EAM2 potential, the focus was made on the stabilizing H in an off-center position in the vacancy and therefore an embedding function was added for H. Both types of the potentials predict the tetrahedral position for an H atom as the most favorable in bulk W, which is important for this work as we focus on the calculation of the binding between H atoms and defects.

MS and MD calculations were performed using the LAMMPS simulation package [15], where the above-mentioned interatomic potentials were implemented. Simulations were performed in bcc W. All MD simulations were performed using a classical MD algorithm in the microcanonical NVE ensemble with a timestep of 1 fs. All MS calculations were performed using a conjugate gradient algorithm embedded in the LAMMPS package with an energy change tolerance of 10^{-10} eV/atom.

The size of the crystallite used in simulations containing point defects (interstitial H, vacancies and their combinations) was $10 \times 10 \times 10 a_0^3$ (a_0 is the lattice constant predicted by the potential: 3.14 Å for EAM potentials and 3.165 Å for BOP), thus it contained 2000 atoms before any point defect or cluster was introduced. Periodic boundary conditions were applied in all three directions. For calculations involving a $\frac{1}{2}\langle 111 \rangle$ screw dislocation box size was $152.9 \times 78.1 \times 32.6$ Å (25,920 atoms) with axis orientations [1–10], [11–2], [111], respectively for X,Y,Z principal axes. Free surfaces along the X and Y were introduced, while periodic boundary conditions were applied along the Z direction, coinciding with the orientation of the dislocation line and dislocation Burgers vector. For the calculations involving a $\frac{1}{2}\langle 111 \rangle\{110}$ edge dislocation, the box size was $80.9 \times 38.8 \times 111.7$ Å (22,155 atoms). The X,Y,Z axes orientations were [111], [11–2], [–110] with periodic conditions imposed along the X and Y directions and free surfaces perpendicular to the Z direction. The dislocation line was oriented along [11–2] direction.

Estimation of the binding energy for point defects (H–H pairs and H-vacancy clusters) as well as the binding energy for H_N

clusters with the dislocation core requires the calculation of the total energy of the atomic system containing these defects being placed together and isolated. The corresponding binding energy of H with different types of lattice defects was defined as:

$$E_{HD}^B = E_H + E_D - E_{HD} - N_{at}E_{coh} \quad (1)$$

where E_{HD} is the total energy of the system when H is attached to the defect, E_H, E_D the total energy of the system containing only H or only a single considered lattice defect (i.e. a vacancy, another interstitial H atom or dislocation) correspondingly. $N_{at}E_{coh}$ is introduced to respect the particle number balance and to compensate for the different number of matrix W atoms present in the configurations corresponding to E_{HD}, E_H and E_D energies. Thus, N_{at} is the number of atoms, E_{coh} – is the energy per atom in pure W. In this notation, a positive value of the binding energy corresponds to attraction between the defects.

In order to estimate the diffusion parameters of H atoms and validate *ab initio* predictions regarding the preferential one dimensional H migration along the dislocation core, a number of MD calculations were performed at finite temperature, T . The main goal was to obtain the diffusion coefficient as a function of temperature, which would allow one to extract the pre-exponential factor D_0 and activation energy E_m using the Arrhenius type equation:

$$D = D_0 \exp\left(\frac{-E_m}{k_B T}\right) \quad (2)$$

In each MD run that lasted for a time τ , the trajectory of the H atom was followed and visualized to quantify the dimensionality of the H motion, which depends on the ambient temperature and type of defect present in the system. Then, the mean square displacement $\overline{R_n^2}$ of the position of the H atom was calculated to obtain the diffusion coefficient using the well-known Einstein equation:

$$D_n(T) = \frac{\overline{R_n^2}}{2n\tau}(T) \quad (3)$$

where n is dimensionality of the motion (i.e., $n = 1$ for one dimensional migration along a dislocation core, and $n = 3$ for three dimensional bulk diffusion), τ – simulation time.

3. Results and discussion

3.1. Benchmark calculations

Prior considering complex interactions of H_N clusters with dislocations we performed a set of benchmark calculations to compare the results with well established *ab initio* data. The benchmark calculations involved the characterization of the H–H and H-vacancy interaction as a function of distance, as schematically shown in Fig. 1. The corresponding binding energy as a function of distance, determined by the atomic positions after complete relaxation, is given in Figs. 2 and 3 for the H–H and H-vacancy interaction, respectively.

Let us first consider the results for H–H interaction presented in Fig. 2. Although all the presented curves provide the same trend as the *ab initio* method, we can see that the repulsive interaction in the first nearest neighbor position is significantly overestimated by the BOP. For the configurations corresponding to the interaction distance of $0.62 a_0$ and $0.7 a_0$, the BOP potential does not return stable configuration and the H atoms displace either to the $0.55 a_0$ or $0.8 a_0$ configurations, unlike the case of both the EAM potentials predicting metastable states. Furthermore according to the BOP, the

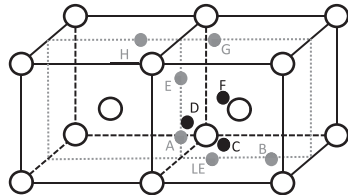


Fig. 1. Schematic picture showing the initial positions used to compute the H–H interaction. Eight pairs of atoms in tetrahedral positions are studied: H atom marked LE and eight atoms marked in alphabetical order with increasing distance between atoms. Black atoms (D, C, F) lie in the vertical plane facing the picture, gray atoms (LE, A, B, E, H, G) lie in vertical midplane marked by gray dashed lines. Tungsten atoms are presented as empty black circles and form bcc structure.

repulsive interaction does not vanish with increasing distance in contrast to the *ab initio* data. The EAM2 potential also predicts remarkable deviation from the *ab initio* data regarding the binding energy in the range of the interaction distance 0.7–1.1 a_0 . The EAM1 version provides very accurate agreement with the *ab initio* data not only with respect to the binding energy but also regarding the positions of the H atoms after the relaxation.

The binding energy of an interstitial hydrogen to a H_N -vacancy cluster is given in Fig. 3. We see that the BOP significantly overestimates the attractive interaction for the first, second and third H atom attached to a single vacancy. In addition, there is a non-monotonic reduction of the binding energy for the fourth and fifth H atom. The two EAM potentials provide accurate agreement for the binding of H_1 -vacancy and H_2 -vacancy complexes and systematically underestimate the bidding energy for the larger clusters

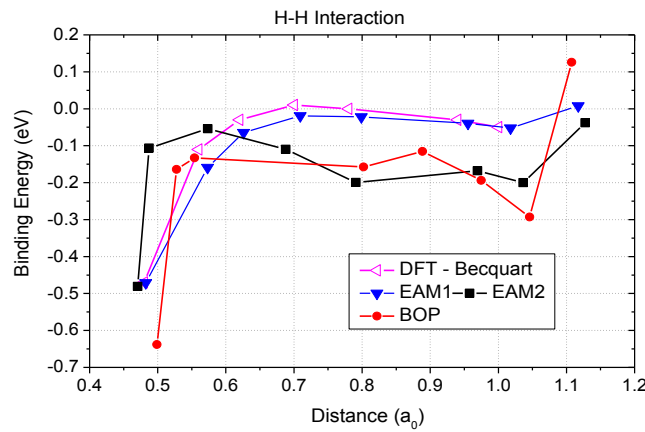


Fig. 2. The binding energy for the H–H interaction as a function of distance. 'DFT' refers to the ab-initio data taken from [16].

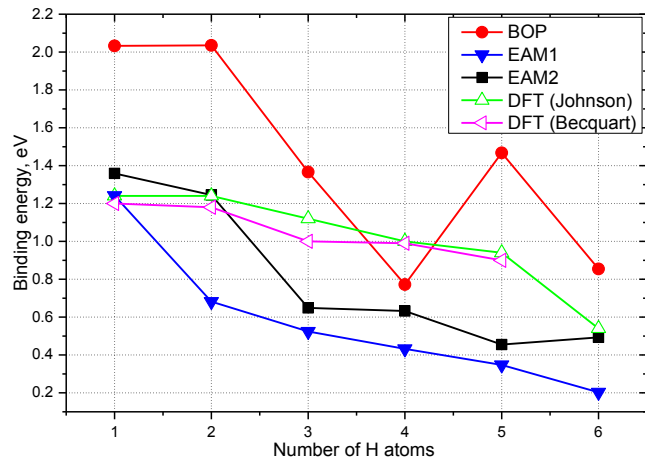


Fig. 3. The binding energy for the H-vacancy interaction as a function of number of H atoms. 'DFT' refers to the ab-initio data taken from [16,17].

by about 0.4 eV.

3.2. Interaction of hydrogen with a screw dislocation

Our second set of benchmark calculations consists of the characterization of the interaction of H with a $\frac{1}{2}\langle 111 \rangle$ screw dislocation (SD). In our preceding work, we have computed the distribution and corresponding binding energy of H around the core of the SD. The binding energy map revealed two types of energy minimum configurations for the H atom: inside the core (three equivalent sites, referred to as 'A' type) and adjacent to the core (six equivalent positions, referred to as 'B' type), as is shown in the original work in Fig. 1a [7]. Here, we provide a schematic representation of the location of these positions superposed on the differential displacement maps, calculated using the BOP and EAM potentials, which show the dislocation core structure (see caption of Fig. 4 for a detailed explanation). Note that the BOP potential predicts the three-fold split structure for the dislocation core, which contradicts the *ab initio* result [13,18–21]. Both versions of the EAM potential return the isotropic non-degenerate core structure, which complies with the *ab initio* data.

The identified positions for an H atom near the SD core coincide with tetrahedral interstitial sites, which are preferentially occupied by H atom in bcc W bulk as well. According to the *ab initio* results, the binding energy in the two configurations amounts to 0.55 eV and 0.54 eV, i.e., practically being the same. Nor the BOP, neither the EAM potentials could reproduce the *ab initio* data in full agreement, see Table 1. While the BOP model predicts reasonable agreement for the binding energy in position A, it overestimates the binding energy by a factor of two in position B. Both versions of the EAM potential do not predict the binding in position A, instead the interaction is practically neutral. The binding energy in the position B is calculated to be 0.42 eV and 0.66 eV for the two versions of the EAM potential, which bounds the *ab initio* result.

3.3. Interaction of H with an edge dislocation

A description of the edge dislocations using *ab initio* calculations is computationally heavy and that is probably why there is no *ab initio* data regarding the interaction of H with an edge dislocation in bcc W available so far in open source literature. Moreover, we could not find even the *ab initio* data regarding the interaction of H with edge dislocations in bcc W.

We have constructed a $\frac{1}{2}\langle 111 \rangle\{110\}$ edge dislocation (ED), as described in Section 2, and relaxed the crystal using the three

Table 1
Binding energy of H-SD core as predicted according the EAM, BOP and ab-initio method.

Position type	Binding energy, eV			
	EAM1	EAM2	BOP	Ab initio [7]
A	0.0	0.0	0.41	0.55
B	0.42	0.66	1.03	0.54

interatomic potentials. The core structure of the ED was found to be symmetric and extended in the {110} glide plane. It was similar with all the applied potentials, see the comparison between the BOP and EAM1 potentials presented in Fig. 5.

The interaction of H with the core of the ED was studied in all non-equivalent tetra- and octahedral positions above and below the dislocation glide plane. An example of the distribution of the interaction energy is provided in Fig. 6, which was obtained using the EAM2 potential. The binding energy maps calculated using the other potentials were essentially similar. From Fig. 6 it follows that the maximum binding energy is realized if H is placed in between the two planes forming the imaginary dislocation glide plane. The attractive interaction sharply vanishes as the H atom is moved above or below the glide plane. While inside the glide plane, the range of the strong interaction is spread over ~10 Å, which can be expected given the rather extended structure of the dislocation core (see Fig. 5). The maximum binding energy is found to be 0.63 eV, 0.89 eV and 1.64 eV for the EAM1, EAM2 and BOP, respectively. As in the case of the interaction with the SD (in position B) and H-vacancy, the BOP predicts a binding energy of a factor two higher than the EAM potentials. Even though we do not have reference *ab initio* data, we tend to consider that the BOP model overestimates the binding energy following the previous comparisons (see Section 3.1 and 3.2).

3.4. Interaction of H_N clusters with edge dislocation and screw dislocations

Our next step is to characterize the formation of H_N clusters on dislocations and deduce the incremental binding energy as a function of cluster size depending on the character of the dislocation. First, we present the result for the SD as this was also studied by *ab initio* calculations providing us important reference data to judge on the quality of the interatomic potentials.

The incremental binding energy of H_b to H_{N-1} -SD complex, i.e. binding of an interstitial H added from the bulk to the H_{N-1} cluster

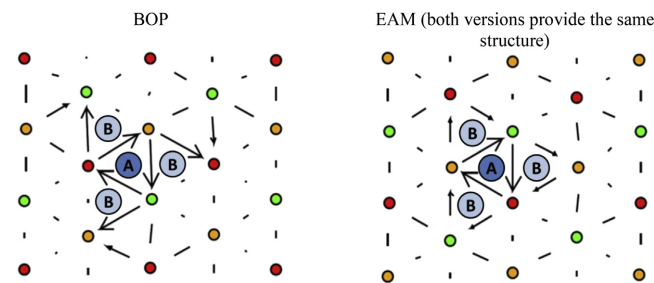


Fig. 4. The schematics of the core atoms in a $\frac{1}{2}\langle 111 \rangle$ screw dislocation in projection onto the (111) plane. The black arrows indicate the difference between displacements of neighboring $\langle 111 \rangle$ columns forming the dislocation core. The length of the arrow is proportional to the magnitude of displacement difference, and the direction of the arrow indicates the sign of the displacement difference. Among the three atoms that surround the centre of the dislocation, the arrows form a closed circuit – this is the dislocation core. Note that while the arrows reveal a displacement component in the (111) plane for convenience of visualization, the displacement component they represent is strictly out of the plane. Ground state positions in and next to the dislocation core are schematically shown by light- and dark-blue balls, respectively. (For interpretation of the references to color in this figure legend, the reader is referred to the web version of this article.)

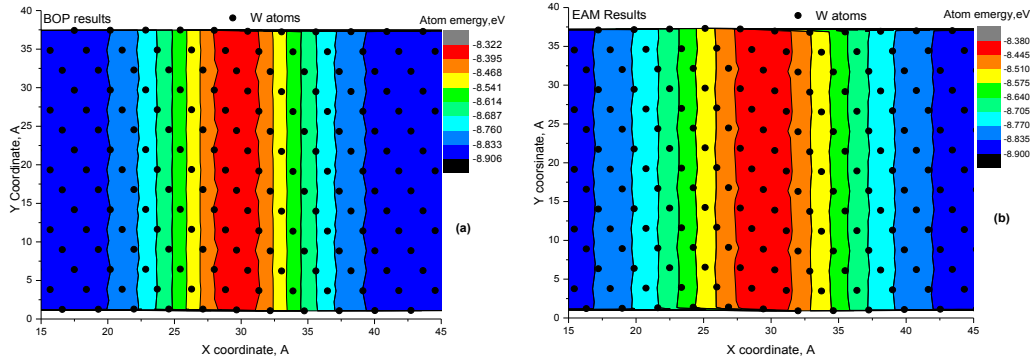


Fig. 5. The edge dislocation core structure obtained by the (a) BOP and (b) EAM2 potentials, and shown as the distribution of cohesive energy of the atoms forming the first extra-half {110} plane above the imaginary dislocation plane.

placed on the SD, is presented in Fig. 7a. According to the *ab initio* data, adding the second, third, fourth and fifth H atom to the cluster progressively reduces the partial binding energy down to 0.35 eV. A sudden drop takes place if the seventh H atom is added, and the recovery for the ninth atom originates from the jog-punching mechanism.

The BOP potential predicts much stronger binding for the second H atom, while the binding energy for the larger cluster is adequately described up to size $N = 6$. The EAM1 also provides a reasonable description but does not capture the reduction of the binding energy at $N > 6$. The EAM2 predicts a flat curve for the binding energy function, as is the case of the EAM1, but overestimates the result by about 0.1–0.2 eV as compared to the DFT data.

The incremental binding energy of a H_{SD} to a H_{N-1} -SD complex,

i.e. binding of an interstitial H attached to the SD core with the H_{N-1} cluster placed on the SD, is presented in Fig. 7b. *Ab initio* data suggest that only two H atoms may form a stable compact complex. Adding more H atoms should result in the formation of the H_N clusters 'stretched' along the dislocation line. Both BOP and EAM potentials correctly predict this trend, however, the strength of the interaction differs. The BOP potential provides much larger values for the binding energy, in absolute terms, as compared to the both EAM potentials. We can conclude that both types of the potentials predict correctly qualitative trends obtained from the *ab initio* calculations, while none of the potentials grasp a good quantitative agreement.

The incremental binding energy of H_b to a H_{N-1} -ED complex is presented in Fig. 8. It can be seen that all the potentials predict strong attractive interaction of H_b to the H_N cluster up to size $N = 5$.

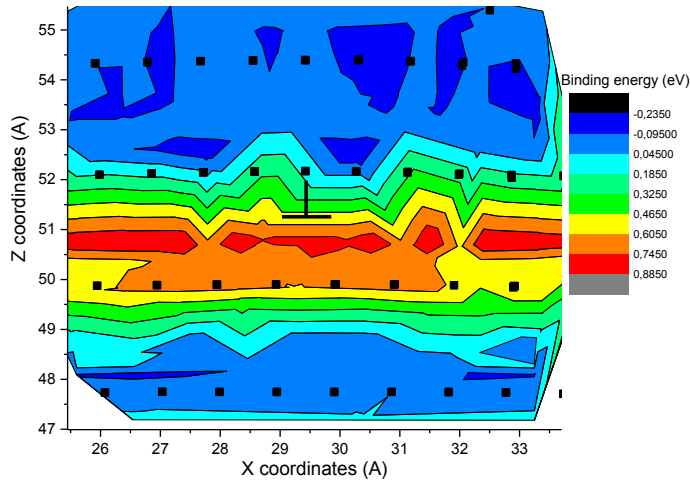


Fig. 6. Distribution of the binding energy of H with the core of the edge dislocation obtained using the EAM2 potential. The geometric center of the dislocation core is shown by the symbol '⊥'.

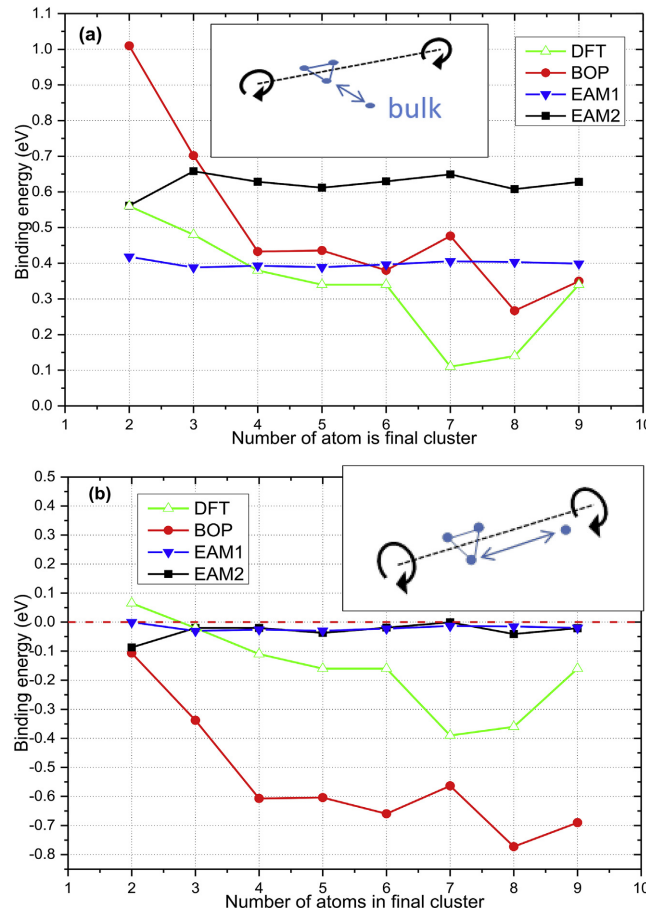


Fig. 7. (a) The incremental binding energy of H_b to a H_{N-1} cluster placed on the SD core. (b) The incremental binding energy of H_{SD} to a H_{N-1} cluster placed on the SD core. Inset figures schematically demonstrate the partition of $H_{b/SD}$ and H_{N-1} .

The incremental binding energy is of the order of the H-ED binding energy, which implies that H atoms inside the H_N cluster can accommodate inside the ED core practically not disturbing each other. This was not the case of the screw dislocation, for which the reduction of the attractive interaction of H_b to the H_{N-1} -SD was seen already starting from $N = 2$. This result reflects that the space available for the formation of the energetically stable H_N cluster is essentially larger in the core of the ED as compared to that in the SD core.

The incremental binding energy of a H_{ED} to a H_{N-1} -ED complex is also given in Fig. 8. The data suggest the absence of attractive interaction between H atoms moving along the ED core. Just as in the case of the screw dislocation, H_N clusters are expected to grow preferentially forming configurations 'stretched' along the dislocation line. All three interatomic models predict the same trend, but according to the EAM1 the interaction of a H_{ED} with a H_{N-1} -ED cluster is practically neutral.

3.5. Diffusion of H in the dislocation core

MD simulations to study the diffusion of H in a crystal containing an ED were done only using the EAM2 potential. Since these calculations were computationally heavy (due to large crystal and a relatively long MD run necessary to achieve satisfactory statistic), we have excluded the BOP potential because of larger computational demand comparing to EAM potentials and also due to the poor performance regarding the properties of dislocations as studied earlier [13].

Following and visualizing movement of H atom we found that it exhibits one dimensional migration along the dislocation core moving by jumping between the planes bounding the imaginary dislocation glide plane. At temperatures below 1300 K, H was attached to ED core for the whole time span of the MD run. This behavior is consistent with the strong attractive interaction of an H to an ED ($E_b = 0.63/0.89$ eV). Above 1300 K, we could regularly

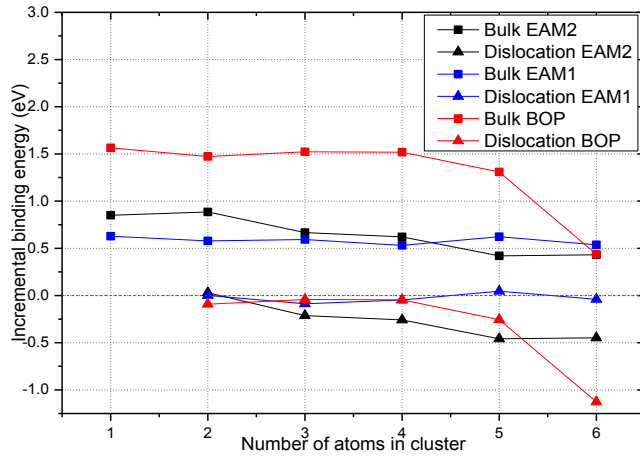


Fig. 8. Incremental binding energy of $H_b - H_{N-1}$ -ED ('Bulk') and $H_{ED} - H_{N-1}$ -ED ('Dislocation') obtained by the BOP and EAM potentials.

register detachment of the H atom. The trajectory of the H atom whilst migrating along the dislocation core was therefore reconstructed to obtain the diffusion coefficient from high temperature MD simulations. The example of H atom trajectory near edge the dislocation and in defect free crystal is available in the Appendix of the paper. The resulting diffusion coefficient for 1D-migration along the ED core is drawn in Fig. 9 as a function of temperature. The extracted D_0 and E_m are, respectively, $8.1 \times 10^{-9} \text{ m}^2/\text{s}$ and 0.17 eV. Note that this value is significantly smaller than the migration energy of an H in W bulk, estimated experimentally to be 0.4 eV [22] and obtained by MD: 0.23 eV. The experimentally measured [22] and calculated here with the same potential 3D bulk diffusion coefficient is also drawn in Fig. 9 for comparison.

Due to the scale of the graph on Fig. 9, the error bars are not seen, however, the relative error is in range of 5–10 % of the absolute values. The calculated value of E_m is 0.23 eV and is lower than the experimentally obtained value, but is consistent with the values of the migration barrier between tetrahedral positions, which is 0.21 eV as predicted by the potential [11], and 0.2 eV as obtained by *ab initio* in Ref. [16]. Clearly, the diffusivity of H attached to the dislocation line is much higher than the bulk diffusivity, especially at low temperatures as can be seen in Fig. 9.

It is interesting to compare this results with the results reported by H. Kimizuka and S. Ogata in Ref. [23]. In this work H-diffusion around a $a_0/2 <111>$ screw dislocation in α -Fe was investigated by means of path-integral molecular dynamics modelling. Despite the

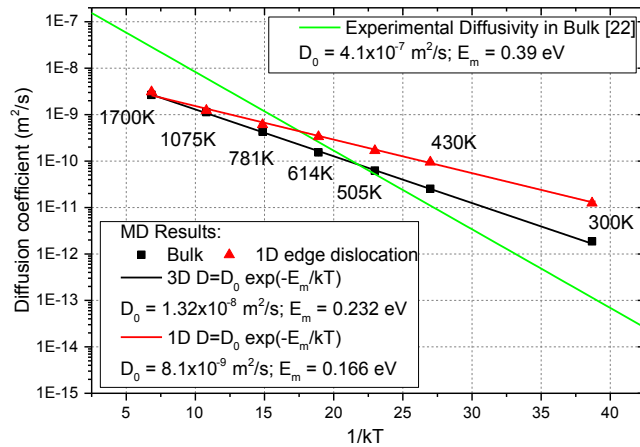


Fig. 9. 1-D diffusion coefficient of H in the core of the edge dislocation and 3D bulk diffusion coefficient as calculated using the EAM2 potential and drawn according to the experimental measurements [22].

fact that W and Fe do not necessarily possess the same properties, we believe that qualitative comparison of the results is possible. There were two migration paths along the dislocation core considered: inside the core of the screw dislocation and parallel to the dislocation core. This can be seen as diffusion along the A and B positions shown in Fig. 4. The barrier inside the dislocation core was 0.022 eV at 300 K and parallel to dislocation core was 0.43 eV. Compared to a bulk diffusion barrier of 0.088 eV, the diffusion barrier inside the core (A position) is significantly lower than the bulk and parallel to the core (B position) is higher than the bulk diffusion. Based on the fact that in Fe H does not bond to the position inside the core (A position), the conclusion about slow H diffusion along dislocation core was made, which is in contrast to our results. As was demonstrated by recent *ab initio* calculations in [7], H atom has a strong attraction to the A position inside the screw dislocation core in W. Thus, it appears that there is a principal difference in the interaction of H with a $a_0/2 <111>$ screw dislocation in BCC Fe and W. While in BCC Fe screw dislocations are not expected to influence the migration of H, in BCC W they should act as means for accelerated H diffusion, at least according the *ab initio* calculations performed in Ref. [7]. In addition, in the present work, we studied migration along an edge dislocation as that type of dislocation can not be accurately treated in the *ab initio* framework due to the obvious limitations. The results for edge dislocations are in the Appendix of the paper [23] and almost no details are given about these calculations.

4. Conclusions

To summarize, we have performed static and finite temperature simulations to characterize the interaction of H and hydrogen clusters with different types of dislocations in BCC W. Two types of interatomic potentials were used, namely: the bond order type developed by Li et al. [9,10], and recently derived embedded atom method potentials by Bonny et al. [11]. On the basis of the obtained results we can draw the following conclusions:

- a. By comparing the performance of the two types of potentials with *ab initio* results regarding the description of H-vacancy and H-dislocation interaction, we reveal an uncertainty range of the results obtained by different atomistic techniques. The BOP model reveals a strong contrast to *ab initio* calculations regarding the H–H interaction embedded in bcc W bulk, which was important for the present study. While the EAM1 potential provides very good agreement with ab-initio data. The H_N -vacancy interaction is well described by the EAM potential for $N = 1, 2$, however, the strength of the binding is systematically underestimated. At the same time, the BOP potential agrees very well with *ab initio* regarding the off centered position of H in vacancy, which the EAM potentials do not reproduce. The BOP overestimates the binding by more than 0.5 eV for $N = 1, 2$ and provides non-monotonic reduction of the binding energy for $N = 4, 5$ deviating from the trend obtained using *ab initio* techniques while the EAM potentials systematically underestimate the value of the binding energy.
- b. The results for the interaction of H with a screw dislocation core reveal that both types of potentials exhibit some disagreements being compared to the *ab initio* data. The BOP overestimates the interaction in the positions adjacent to the SD core, while the EAM potentials underestimate the interaction in the positions inside the dislocation core. In addition, the BOP fails to reproduce the equilibrium structure of the SD core, and predicts a dissociated three-fold structure in contrast to the *ab initio* result. The EAM potentials do not have this caveat.

- c. The interaction of the H with the edge dislocation core was not studied by means of *ab initio* data so far, and therefore we do not have reference data to compare the results obtained with the potentials. However, a qualitative result – strong and localized attraction of H to the core of the edge dislocation – is independent of the applied potential. Quantitatively, the BOP predicts the binding energy approximately twice as high as compared to both applied EAM potentials. This is overall consistent with the deviation of the results obtained using the BOP and EAM potentials in calculations involving a vacancy and screw dislocation.
- d. The analysis of the interaction of H_N clusters with the edge dislocation reveals a strong tendency to form compact H_N clusters without losing the binding strength up to five H atoms. Thus, the core of the edge dislocation can accept twice as much H atoms as compared to the screw dislocation. This reflects the fact that the space available for the H_N cluster is essentially larger in the core of the edge dislocation, as one should expect.
- e. Based on the MD data obtained here using the EAM2 model, we conclude that H exhibits strong attractive interaction to the core of the $\frac{1}{2}<111>\{110\}$ edge dislocation, consistent with MS results, and performs one-dimensional migration, which is remarkably faster as compared to the bulk diffusivity.

The last conclusion implies that not only a single H but also multiple energetically stable H_N clusters may exhibit significant diffusivity along the dislocation core. Investigation of the dynamical behavior of H_N clusters and possible mechanisms leading to the ‘jog-punching’ on the edge dislocation is currently ongoing.

Acknowledgments

This work was supported by the European Commission and carried out within the framework of the Erasmus Mundus International Doctoral College in Fusion Science and Engineering (FUSION-DC). The work is partially supported by EUROfusion program.

Appendix A. Supplementary data

Supplementary data related to this article can be found at <http://dx.doi.org/10.1016/j.jnucmat.2015.06.013>.

Appendix

The figure below demonstrates time dependence of an H atom position during an MD run in defect-free (a) and edge dislocation-containing (b) W crystals. These types of trajectories were used to calculate the diffusion coefficient. One clearly sees that in the case of an ideal crystal the diffusion is 3 directional as the displacement of an H atom along all three coordinates follows a similar time dependence. In the case of diffusion in a dislocation-containing crystal (with dislocation line along Y direction), the position of H on the Z coordinate practically stays constant. Along the X direction an H atom moves within 5 Å away from the center of the dislocation core, which demonstrates some flexibility of the migration of H in the dislocation core extended in the direction of the Burgers vector as is also shown in Fig. 5. The mean square displacement along the X direction gives only 11.3% of the total atom displacement. The rest, 88.7% of the displacement is along the Y direction, which confirms our observation of 1-dimensional migration along the edge dislocation core. A video illustration of 1-dimensional migration of H atom along the core obtained with MD simulation at 430 K is available as Supplementary Material.

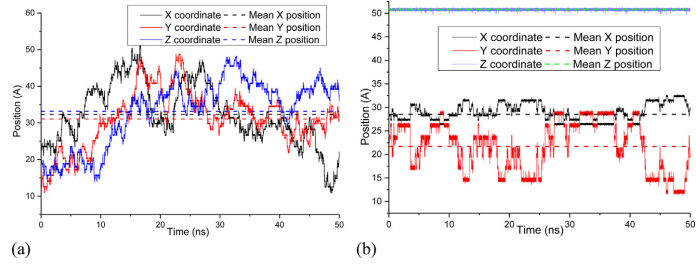


Fig. A1. Time dependence of the position of H atom in case of diffusion in the bulk (a) and diffusion along edge dislocation core (b) at 430 K

References

- [1] R.E. Clark, D. Reiter, *Nuclear Fusion Research: Understanding Plasma-surface Interactions*, Springer, 2005.
- [2] Y. Zayachuk, M.H.J.t. Hoen, P.A.Z.v. Emmichoven, I. Uytdehouwen, G.v. Oost, *Nucl. Fusion* 52 (2012) 103021.
- [3] O.V. Ogorodnikova, J. Roth, M. Mayer, *J. Nucl. Mater.* 313–316 (2003) 469–477.
- [4] V.K. Alimov, B. Tyburska-Püschel, S. Lindig, Y. Hatano, M. Balden, J. Roth, K. Isobe, M. Matsuyama, T. Yamanishi, *J. Nucl. Mater.* 420 (2012) 519–524.
- [5] T. Ahlgren, K. Heinola, K. Vörtsler, J. Keinonen, *J. Nucl. Mater.* 427 (2012) 152–161.
- [6] A.A. Haasz, J.W. Davis, M. Poon, R.G. Macaulay-Newcombe, *J. Nucl. Mater.* 258–263 (Part 1) (1998) 889–895.
- [7] D. Terentyev, V. Dubinko, A. Bakaev, Y. Zayachuk, W.V. Renterghem, P. Grigorev, *Nucl. Fusion* 54 (2014) 042004.
- [8] V.I. Dubinko, P. Grigorev, A. Bakaev, D. Terentyev, G. van Oost, F. Gao, D. Van Neck, E.E. Zhurkin, *J. Phys. Condens. Matter* 26 (2014) 395001.
- [9] X.-C. Li, X. Shu, Y.-N. Liu, Y. Yu, F. Gao, G.-H. Lu, *J. Nucl. Mater.* 426 (2012) 31–37.
- [10] X.-C. Li, X. Shu, Y.-N. Liu, F. Gao, G.-H. Lu, *J. Nucl. Mater.* 408 (2011) 12–17.
- [11] G. Bonny, P. Grigorev, D. Terentyev, *J. Phys. Condens. Matter* 26 (2014) 485001.
- [12] M.-C. Marinica, L. Ventelon, M.R. Gilbert, L. Provile, S.L. Dudarev, J. Marian, G. Bencetoux, F. Willaime, *J. Phys. Condens. Matter* 25 (2013) 395502.
- [13] G. Bonny, D. Terentyev, A. Bakaev, P. Grigorev, D.V. Neck, *Model. Simul. Mater. Sci. Eng.* 22 (2014) 053001.
- [14] K. Heinola, T. Ahlgren, K. Nordlund, J. Keinonen, *Phys. Rev. B* 82 (2010) 094102.
- [15] S. Plimpton, *J. Comput. Phys.* 117 (1995) 1–19.
- [16] C.S. Bequaert, C. Domain, *J. Nucl. Mater.* 386–388 (2009) 109–111.
- [17] D.F. Johnson, E.A. Carter, *J. Mater. Res.* 25 (2010) 315–327.
- [18] L. Romaner, C. Ambrosch-Draxl, R. Pippan, *Phys. Rev. Lett.* 104 (2010) 195503.
- [19] H. Li, S. Würster, C. Motz, L. Romaner, C. Ambrosch-Draxl, R. Pippan, *Acta Mater.* 60 (2012) 748–758.
- [20] G.D. Samolyuk, Y.N. Osetsky, R.E. Stoller, *J. Phys. Condens. Matter* 25 (2013) 025403.
- [21] S.L. Frederiksen, K.W. Jacobsen, *Philos. Mag.* 83 (2003) 365–375.
- [22] R. Frauenfelder, *J. Vac. Sci. Technol.* 6 (1969) 388–397.
- [23] H. Kimizuka, S. Ogata, *Phys. Rev. B* 84 (2011) 024116.

F

On the binding of nanometric
hydrogen-helium clusters in tungsten

G. Bonny, P. Grigorev and D. Terentyev

published in Journal of Physics: Condensed Matter, 2014, Vol. 26, p. 485001
(8 pp.)

On the binding of nanometric hydrogen–helium clusters in tungsten

G Bonny¹, P Grigorev^{1,2,3} and D Terentyev¹

¹ SCK•CEN, Nuclear Materials Science Institute, Boeretang 200, B-2400 Mol, Belgium

² FUSION-DC, Department of Applied Physics EA17, Ghent University, Sint-Pietersnieuwstraat 41 B4, B-9000 Gent, Belgium

³ St. Petersburg State Polytechnical University, Department of Experimental Nuclear Physics K-89, Faculty of Physics and Mechanics, 29 Polytekhnicheskaya str., 195251 St. Petersburg, Russia

E-mail: gbonny@sckcen.be

Received 3 April 2014, revised 28 August 2014

Accepted for publication 18 September 2014

Published 17 October 2014

Abstract

In this work we developed an embedded atom method potential for large scale atomistic simulations in the ternary tungsten–hydrogen–helium (W–H–He) system, focusing on applications in the fusion research domain. Following available *ab initio* data, the potential reproduces key interactions between H, He and point defects in W and utilizes the most recent potential for matrix W. The potential is applied to assess the thermal stability of various H–He complexes of sizes too large for *ab initio* techniques. The results show that the dissociation of H–He clusters stabilized by vacancies will occur primarily by emission of hydrogen atoms and then by break-up of V–He complexes, indicating that H–He interaction does influence the release of hydrogen.

Keywords: tungsten, bubbles, interatomic potential

(Some figures may appear in colour only in the online journal)

1. Introduction

Tungsten (W) and tungsten based alloys are the primary candidate materials for plasma facing components (PFCs) in fusion reactors. In the DEMO and future commercial reactors PFCs will be exposed to unprecedented and unexplored irradiation conditions. The exposure to high-energy radiation, consisting of neutron damage, helium (He) and hydrogen (H) high temperature/flux plasma, severely damage the microstructure of the materials by violently displacing atoms from their lattice and thereby creating vacancy clusters, dislocation loops, voids and even microscopic bubbles and cracks. All the above mentioned radiation-induced processes cause profound macroscopic property changes that severely degrade the performance and lifespan limits of PFC materials [1, 2].

One of the issues in the development of PFCs is the retention of H isotopes (namely tritium) [3], originating from the trapping of plasma components on pre-existing (i.e. natural) and radiation-induced lattice defects. Without neutron irradiation, experiments involving mixed ion beam and plasma

accelerators have shown that under mixed H–He exposures the interplay between H isotopes and He might have a significant effect on the enhancement of H retention [4–8]. Moreover, continuous production of displacement damage by neutron scattering will generate lattice defects serving as traps for H and He, and acting as obstacles to dislocation motion thereby further reducing the ductility of tungsten [2]. Trapping of H and He at natural and radiation-induced defects as well as irradiation embrittlement takes its origin at the nano-scale and therefore a good understanding of these phenomena should correspondingly be achieved at the atomic level. This is why the development and application of atomistic tools for W-based systems have recently received essential attention, for example in [9–13].

Theoretical attempts to study the synergy between H and He is so far limited to density functional theory (DFT) studies regarding the stability of vacancy-hydrogen–helium (VH_lHe_m) clusters [14–16]. Due to the computational limitations of DFT calculations only elementary clusters containing a single vacancy were considered. However, there is the essential desire to extend our knowledge to the

stability and mobility of larger $V_kH_lHe_m$ clusters (i.e. for $k, l, m \gg 1$) as their formation certainly occurs under high flux plasma exposure, which typically leads to the formation of well-resolved bubbles and blisters. Also, the study of H and He accumulation near extended lattice defects, such as dislocation lines, dislocation loops and grain boundaries and their effect on dislocation movement are outside the scope of DFT calculations. Therefore, all such studies require large scale atomistic simulations employing semi-empirical interatomic potentials that are known to offer an acceptable compromise between computational efficiency and physical reliability. For the development of such potentials, DFT data serves as a guide.

In this work we develop an embedded atom method (EAM) potential for the ternary W–H–He system. The potential is benchmarked against available DFT data from the literature and its performance is compared with the only ternary WHHe potential available so far: the bond order potential (BOP) by Li *et al* [9]. As a first step, we apply the developed potential to extend the information about the thermal stability of $V_kH_lHe_m$ clusters beyond the scale accessible to DFT calculations. For convenience and further use in kinetic mean field theory or object kinetic Monte Carlo models, the results are formatted within a frame of a simple yet accurate liquid tear drop (LTD) model.

The paper is organized as follows. In section 2 we explain the fitting strategy followed to fit the potentials and the procedures applied to obtain the binding energy of any $V_kH_lHe_m$ cluster. In section 3 we validate the potential by making one-to-one comparisons with both BOP and DFT data. In section 4 we present and discuss the results concerning the stability of $V_kH_lHe_m$ clusters. The paper is finalized by conclusions.

2. Methodology

In the literature, many EAM type interatomic potentials for bcc W are available, see e.g. [10–12, 17–30]. A critical review assessing their strengths and weaknesses is given in [13]. For this work, we selected the one, which gives the best ‘global performance’, i.e. ‘EAM2’ from the work of Marinica *et al* [11]. As key features, this potential provides elastic constants, point-defect, edge and screw dislocation properties as well as grain boundary energies consistent with DFT calculations or experiments (see [13] for more details).

In the literature three semi-empirical potentials exist for WHe [10, 31, 32] and two for WH [33, 34]. From those potentials, the ones by Wilson *et al* [31] and Henriksson *et al* [32] predict opposite stability for He in an octahedral and tetrahedral position. The one by Juslin and Wirth [10] provides a He migration barrier of 0.21 eV, which overestimates the DFT value (0.06 eV) by more than a factor three. The WH potential by Juslin *et al* [33], on the other hand, predicts the $<1\bar{1}0>$ dumbbell self interstitial be more stable than the $<111>$ one in bcc W, which is in contradiction with DFT data (see [13] and references therein). The one by Li *et al* [34] is part of the ternary WHHe BOP that is used as a benchmark throughout this work. At this point we also note that none of the potentials

for pure W used in the above works reproduce the key features as good as ‘EAM2’ by Marinica *et al* [11]. In addition, a $1/2 <1\bar{1}1>$ screw dislocation in bcc W relaxed by BOP provides a threefold degenerate core structure, which is contradictory to DFT results [35] and ‘EAM2’ by Marinica *et al* [11].

The H–H interaction in bulk W is essentially different from its description in vacuum. In vacuum, two H atoms form the strongly bonded H_2 molecule ($E_b = 4.75$ eV) [33]. In bulk W, on the other hand, two H atoms exhibit repulsion or weak binding [14] as they cannot form the strongly bonded H_2 molecule due to interactions with the surrounding W atoms. The modulation of such behaviour within the EAM framework is difficult to achieve. Therefore, we chose to focus on the effective interaction of H (and He) in bulk W. As a consequence, the here derived potentials for H and He should not be used in vacuum.

We have fitted two sets of WHHe potentials, namely, EAM1 and EAM2. Both potentials were fitted to reproduce the relative stability between tetrahedral (T) and octahedral (O) sites as well as between tetrahedral and $<1\bar{1}0>$ dumbbell position, with the latter serving as saddle for T–T migration. In addition, the binding between H–H, He–He and H–He pairs in bulk W and the binding between vacancy–H and vacancy–He pairs were fitted. For EAM1, emphasis was put on a quantitative reproduction of DFT data of the binding between H–H, He–He and H–He pairs. The off-centre position of a H atom in a vacancy as predicted by DFT [36] was not considered, and therefore both H and He are described by pair potentials only. For EAM2 we focussed on stabilizing H in an off-centre position in the vacancy and therefore an embedding function was added for H. For both H and He no density function is defined, i.e. only W adds to the electron density at a given site and there is no contribution to it by H or He. The optimized parameters for both EAM1 and EAM2 are reported in appendix A.

The total binding energy of a $V_kH_lHe_m$ cluster, E_b^{tot} , was calculated as,

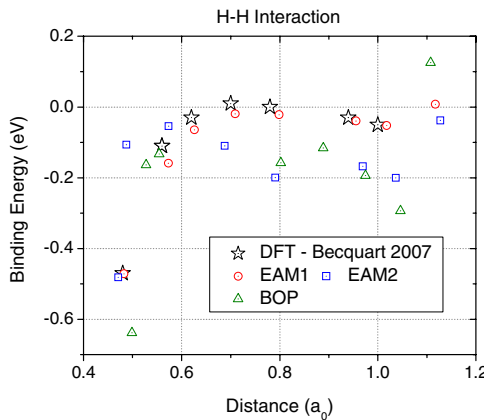
$$E_b^{\text{tot}}(V_kH_lHe_m) = k E(V) + l E(H) + m E(He) - E(V_kH_lHe_m) - (k + l + m - 1) E(W) \quad (1)$$

Here $E(W)$ is the total energy of the perfect bcc W crystal, $E(V)$, $E(H)$ and $E(He)$ are the total energy of the bcc W crystal containing one V, H and He atom, respectively, with H and He in the tetrahedral position. With this definition, positive values of E_b^{tot} indicate attraction.

In our study, we have considered $V_kH_lHe_m$ clusters containing up to 12 vacancies (in the most compact configuration) with a H to V ratio, x_H , and He to V ratio, x_{He} , in the range 0.1–6. For the selected maximum number of V, x_H and x_{He} , the sequential binding energy of a V, H and He to a $V_kH_lHe_m$ cluster saturates, respectively, so no larger clusters need to be addressed. In total, 2087 different $V_kH_lHe_m$ clusters were considered. In each cluster the H and He were introduced at random (with a maximum of 6H/He per vacancy) and the configuration was relaxed ten times using a quench method with a molecular dynamics (MD) run at 300 K for 1 ps in between each quench down to 0 K. The latter procedure allows the system to evolve out of local minima and

Table 1. Point defect properties of H and He in bcc W calculated by DFT and the potentials.

Property	Hydrogen				Helium			
	DFT	EAM1	EAM2	BOP	DFT	EAM1	EAM2	BOP
$\Delta E(\text{Octa-Tetra})$ (eV)	0.38	0.35	0.38	0.32	0.22	0.19	0.23	0.17
$\Delta E(<110>\text{-Tetra})$ (eV)	0.39	0.35	0.38	0.32	0.23	0.19	0.23	0.17
$\Delta E(<111>\text{-Tetra})$ (eV)	0.21	0.22	0.21	0.22	0.07	0.09	0.06	0.02
ΔE (eV)	1.51	2.10	2.70	2.29	0.51	1.40	0.98	0.75
$E_b(X\text{-Vac})$ (eV)	1.19	1.24	1.33	2.03	4.55	4.55	4.54	5.04
$E_m(X)$ (eV)	0.20	0.22	0.21	0.22	0.06	0.09	0.06	0.02

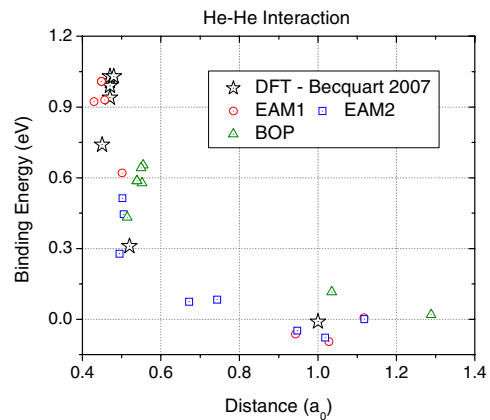
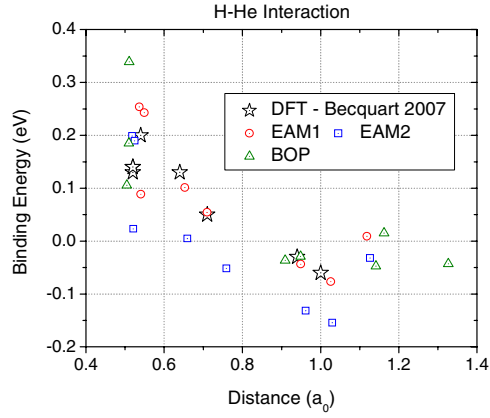
**Figure 1.** Comparison of the H–H binding energy as a function of distance as calculated by DFT and the potentials.

was tested to provide an absolute minimum in the case of the single vacancy. For each configuration, the lowest of the 10 values for the total energy was retained. For all runs, a cubic bcc W crystal was used containing 2000 atoms with periodic boundaries in all directions.

3. Validation of the potentials

In table 1 the point defect properties of H and He in bcc W calculated with our potentials are compared to DFT [14] and BOP [9]. Clearly, DFT predicts the tetrahedral position to be the most favourable for both H and He, which is reproduced by all potentials. In addition, all potentials predict the correct ordering in interstitial formation energies, although EAM1 and EAM2 show the best quantitative agreement with DFT. With respect to the binding energy between a H or He to a vacancy, both EAM1 and EAM2 closely reproduce the DFT values, while BOP underestimates and overestimates the binding for H and He, respectively. The migration energy for H is well reproduced by all potentials, but the one for He is only reproduced by EAM1 and EAM2, and underestimated by BOP by a factor three.

In figures 1–3 the binding energy between H–H, He–He and H–He pairs as a function of separation distance is plotted as calculated by DFT and the potentials. The

**Figure 2.** Comparison of the He–He binding energy as a function of distance as calculated by DFT and the potentials.**Figure 3.** Comparison of the H–He binding energy as a function of distance as calculated by DFT and the potentials.

considered configurations are taken from [14] and only the final distance between the pairs is considered. As with both DFT and the potentials the distance between H and He pairs changes considerably during atomic relaxation, a comparison of binding energy with distance is more sensible than a

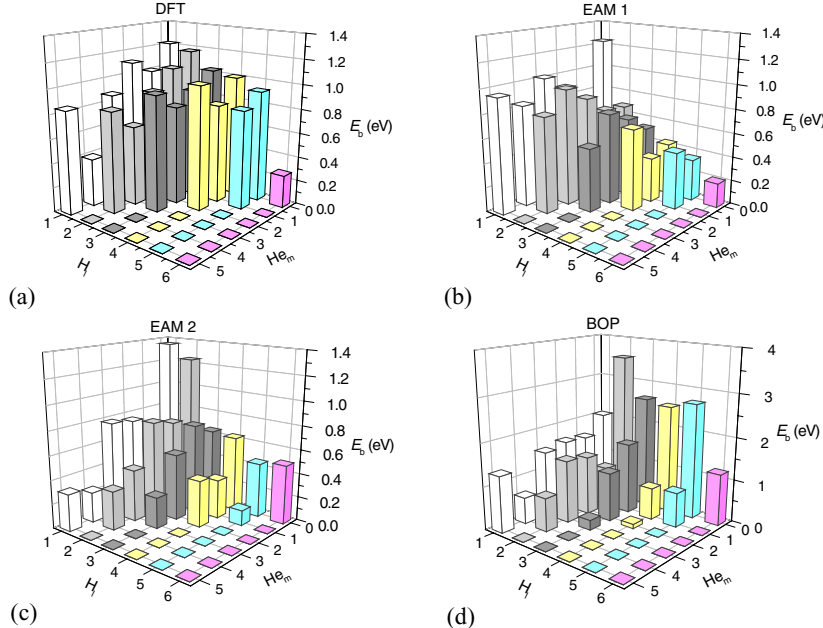


Figure 4. Binding energy of a H in a VH_lHe_m cluster as calculated by (a) DFT, (b) EAM1, (c) EAM2 and (d) BOP.

one-to-one comparison between the specific configurations. Taking DFT as the reference, He–He and He–H attract with maximum values of 1.03 eV and 0.20 eV, respectively, while H–H pairs repel with a maximum of –0.47 eV. This behaviour is qualitatively reproduced by all potentials and also quantitatively by EAM1. Both BOP and EAM2 have a too long interaction range for H–H pairs, underestimate the He–He attraction and overestimate (BOP) the H–He binding or underestimate (EAM2) the H–He interaction range.

In figures 4 and 5 the binding energy of a H and He atom to VH_lHe_m clusters calculated by the potentials and DFT [14] is compared. The DFT results show that He is bound stronger than H to the same VH_lHe_m cluster by roughly a factor four. For both H and He, the binding energy slightly decreases with increasing cluster size. For EAM1, the values for the binding energy are within the DFT range, but with increasing He content, the binding of He to the cluster does not decrease. For EAM2, the values for the binding energy are also within the DFT range, and qualitatively, also the binding energy decreases with cluster size. For BOP, the binding energy for H is overestimated by about a factor two, but for He, on the other hand, the values lay within the DFT range. Qualitatively, BOP reproduces the decrease in binding energy with cluster size.

4. Binding energy of VH_lHe_m clusters

From the results presented in section 3 with respect to VH_lHe_m clusters, EAM2 seems the most suitable to extend

the calculations to VH_lHe_m clusters. In figure 6, the data as calculated by molecular dynamics (MD) is presented as scatter for clusters containing 2, 4 and 6 vacancies. For both inter- and extra-polation purposes, we have fitted a 3D hyper surface based on a LTD model to represent the data, as detailed in appendix B. From this function, all sequential binding energies can easily be derived. Projections for clusters containing 2, 4 and 6 vacancies are superposed in figure 6. The average deviation between raw data and fitted surface is ~10%, which is acceptable for a simple LTD model.

As an additional validation of the model, we show the binding energy of a He atom to a VHe_m cluster (figure 7(a)) and of a H atom to a VH_l and $VHeH_l$ cluster (figure 7(b)) computed with the LTD model, DFT and EAM2. For VHe_m , the LTD model slightly overestimates the DFT and EAM2 results, but agreement is nevertheless satisfactory. For $VHeH_l$ and VH_l , the difference between the DFT data sets (and EAM2 data sets) is negligible. This trend is followed by the LTD model, although the values are somewhat underestimated. Considering all approximations, we find the LTD model satisfactory and this enables to extrapolate to larger $V_kH_lHe_m$ clusters.

In figure 8 we present the dissociation energy of a V, H and He in a $VHHe$ cluster as a function of x_{VH} and x_{He} for the limiting cases of clusters containing two (figure 8(a)) and 12 (figure 8(b)) vacancies. The dissociation energy was obtained in the standard way as the sum of the sequential binding energy of a V/H/He atom to the cluster and its migration energy. For a vacancy the sequential binding energy is obtained as,

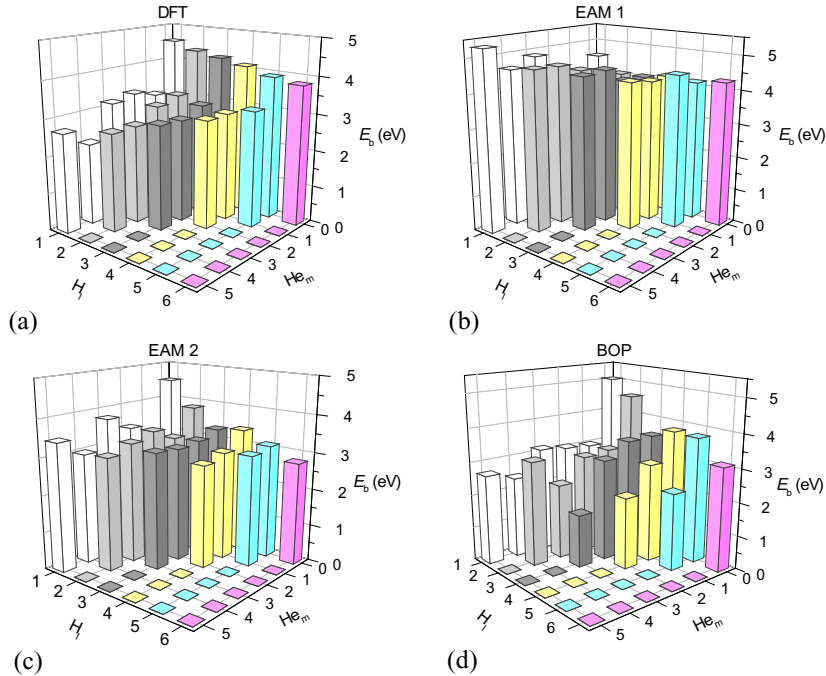


Figure 5. Binding energy of a He in a VH_iHe_m cluster as calculated by (a) DFT, (b) EAM1, (c) EAM2 and (d) BOP.

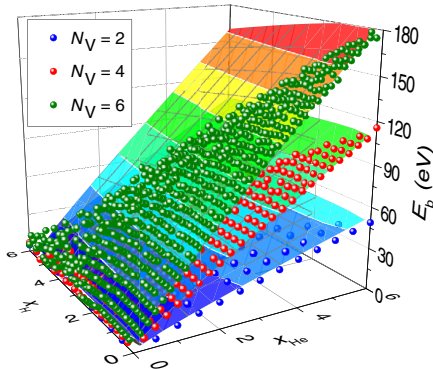


Figure 6. Total binding energy of VHHe clusters as a function of hydrogen- and helium-vacancy ratio (x_H , x_{He}) for clusters containing two, four and six vacancies.

$E_b^{\text{tot}}(V_k H_i He_m) - E_b^{\text{tot}}(V_{k-1} H_l He_m)$, with similar expressions for H and He. As values for the migration energy we used the ones provided by the potential ($E_m(V) = 1.85$ eV) [13], which is within the range of experiments and DFT calculations [13].

We observe that for both limiting cases the binding energy of H is lower than that of a V or He for all x_H and x_{He}

combinations, consistent with the single vacancy case (see figures 4 and 5). This implies that any VHHe cluster formed in W will first release all H before releasing a He or V. For VHe clusters, an optimum x_{He} exists above which He dissociates from the clusters and below which a V dissociates from the cluster. This optimum, indicated by the dashed line in figures 8(a) and (b), depends slightly on x_H and the number of vacancies in the clusters. The optimum point slightly increases with increasing x_H and saturates from ~ 2 for two vacancies to ~ 1 for six vacancies and more. In addition, the sequential binding of H to a cluster decreases with increasing number of vacancies while the sequential binding of He to the cluster increases with the number of vacancies. For the sequential binding energy of a vacancy the slope of the surface gets steeper with increasing number of vacancies.

5. Conclusions

We have developed two versions of a EAM potential for large scale atomistic simulations in the ternary W–H–He system. Both potentials reproduce key interactions between H, He and point defects calculated by DFT. We applied the potentials to compute the dissociation energy of various VHHe clusters of nano-metric size and parameterize a simple liquid-tear drop model applicable to up-scale mean field or kinetic Monte Carlo simulations. The obtained results show that the dissociation of mixed VHHe clusters primarily takes place by emission

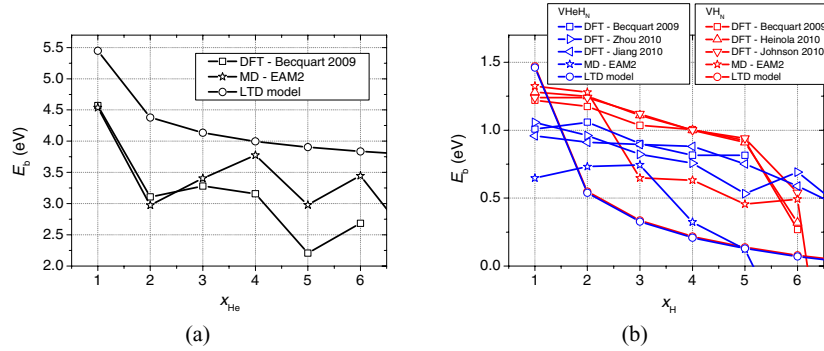


Figure 7. Binding energy of (a) He and (b) H to (a) VHe and (b) VHeH clusters, respectively.

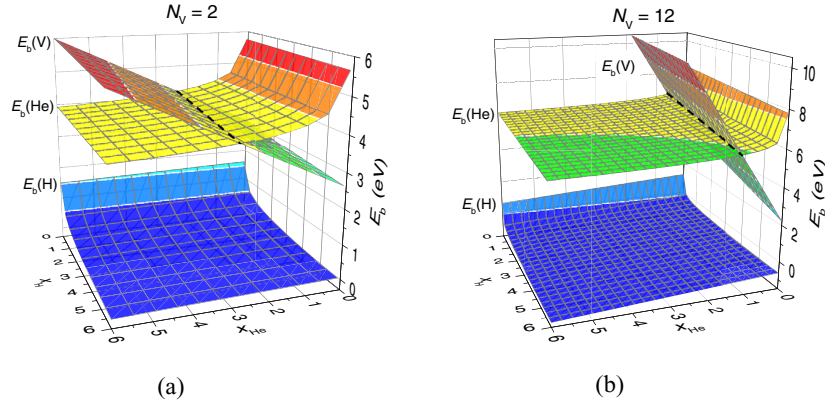


Figure 8. Dissociation energy for a V, H and He from VHHe clusters as function of hydrogen- and helium ratio (x_H , x_{He}) for a cluster containing (a) two and (b) twelve vacancies.

of H, whose trapping energy is not essentially changed by the presence He in the clusters. Hence, the H-He interaction does not affect the thermal stability of H in the vacancy-stabilized H-He clusters. Therefore we conclude that the origin of the H-He synergy expressed by the enhanced H uptake should be investigated at the stage of the nucleation of H-He defects.

Acknowledgments

This work, supported by the European Commission under the Contract of Association between EURATOM/SCK•CEN, was carried out within the framework of the European Fusion Development Agreement. We thank Professor C S Becquart for providing us with raw data of her DFT calculations. We also thank Professor R C Pasianot for his critical remarks during the preparation of this paper.

Appendix A. Parameterization interatomic potential

The atomic interactions are described using the EAM [37]. In addition to pair interactions, V , this approach includes an

embedding energy, F , dependent on the local electron density, ρ . The latter term approximates the many-body contribution of all nearby atoms. The total energy within EAM is given as,

$$E = \frac{1}{2} \sum_{i,j=1}^N V_{t_i t_j}(r_{ij}) + \sum_{i=1}^N F_{t_i}(\rho_i). \quad (\text{A1})$$

Here N represents the total number of atoms in the system, r_{ij} is the distance between atoms i and j , and t_i denotes chemical species. The local electron density around atom i ,

Table A1. Spline coefficients for the modified embedding function, F^{mod} .

Spline coefficient
$A_0 = -5.524855802\text{E} + 00$
$A_1 = 2.317313103\text{E} - 01$
$A_2 = -3.665345949\text{E} - 02$
$A_3 = 8.989367404\text{E} - 03$

Table A2. The optimized fitting parameters for the WHeH potentials.

k	EAM1		EAM2	
	r_k (Å)	a_k (eV Å $^{-3}$)	r_k (Å)	a_k (eV Å $^{-3}$)
V_{HeHe}				
1	2.000000000E + 00	2.106615791E + 00	1.800000000E + 00	2.000000000E + 01
2	3.000000000E + 00	-2.217639348E - 01	2.000000000E + 00	1.051327582E + 00
3			2.100000000E + 00	-4.000000000E + 00
4			3.000000000E + 00	3.203322671E - 02
V_{HH}				
1	2.000000000E + 00	4.862785907E - 01	1.600000000E + 00	4.000000000E + 01
2	3.000000000E + 00	1.018797872E - 01	2.000000000E + 00	2.315124670E - 01
3			2.200000000E + 00	-2.000000000E - 01
4			3.000000000E + 00	5.180584543E - 02
V_{HHe}				
1	1.800000000E + 00	1.500000000E + 01	2.000000000E + 00	3.256370012E + 00
2	2.000000000E + 00	2.563700119E - 01	2.500000000E + 00	-4.000000000E - 01
3	3.000000000E + 00	-4.489510592E - 02	3.000000000E + 00	-4.489510592E - 02
V_{WHe}				
1	1.900000000E + 00	2.100000000E + 01	1.900000000E + 00	0.000000000E + 00
2	2.200000000E + 00	8.565323293E - 01	2.000000000E + 00	1.400000000E + 01
3	3.500000000E + 00	2.750099819E - 01	2.200000000E + 00	-3.712116187E + 00
4			3.500000000E + 00	3.105031456E - 01
V_{WH}				
1	2.000000000E + 00	1.375733214E + 01	2.000000000E + 00	4.424459079E + 01
2	3.000000000E + 00	1.296071475E - 01	2.647500000E + 00	-4.993477782E + 00
3			3.295000000E + 00	1.461712984E + 00

contributed from its neighbours is given as,

$$\rho_i = \sum_{\substack{j=1 \\ j \neq i}}^N \varphi_{ij}(r_{ij}), \quad (\text{A2})$$

where φ denotes the electron density function of the considered element.

For pure W, ‘EAM2’ developed by Marinica *et al* [11] was used. However, we apply some minor modifications that do not modify the potential’s properties but exclude possible future problems when W is alloyed (with e.g. Ta, Re, …). Firstly, we transform the potential into its effective gauge [17, 38], characterized by an equilibrium density $\rho_0 = 1$ and $F^{\text{eff}}'(1) = 0$. The gauge transformation is given as,

$$\begin{cases} V^{\text{eff}}(r) = V(r) - 2C\varphi(r) \\ \varphi^{\text{eff}}(r) = S\varphi(r) \\ F^{\text{eff}}(\rho) = F\left(\frac{\rho}{S}\right) + \frac{C}{S}\rho \end{cases}, \quad (\text{A3})$$

with $C = 1.848055990E + 00$ and $S = 2.232322602E - 01$. After this transformation, the embedding function, F^{eff} , was modified beyond the inflection point to provide a positive curvature for all densities. The modified embedding function, F^{mod} , is then defined as,

$$F^{\text{mod}}(\rho) = \begin{cases} F^{\text{eff}}(\rho), \rho \leqslant \rho_i \\ A_0 + A_1\rho + A_2\rho^2 + A_3\rho^3, \rho > \rho_i \end{cases}, \quad (\text{A4})$$

with $\rho_i = 1.359141225E + 00$ the inflexion point and $\{A_i\}$ spline coefficients (see table A1) fitted to be continuous at ρ_i up to second derivative with F^{eff} . This modification does not

change the equilibrium properties of the potential, such as, elastic constants, lattice stabilities, formation energy of point defects and dislocation core structure.

The pair potentials fitted here are parameterized by the cubic spline expansion,

$$V(r) = \sum_{k=1}^N a_k (r_k - r)^3 H(r_k - r), \quad (\text{A5})$$

where N denotes the total number of knots, r_k the knots, a_k the fitting parameters and H the Heaviside unit step function. The embedding function for H (EAM2) is parameterized as,

$$F(\rho) = A\sqrt{\rho} + B\rho^2, \quad (\text{A6})$$

with $A = -2.610066441E + 01$ and $B = 4.688963869E - 01$. The optimized knots and fitting parameters for the pair potentials are given in table A2. We note that for both H and He no density function is defined, i.e. only W adds to the electron density at a given site and there is no contribution to it by H or He.

Appendix B. Parameterization of the total binding energy of $\text{V}_k\text{H}_l\text{He}_m$ clusters

The total binding energy of $\text{V}_k\text{H}_l\text{He}_m$ clusters was parameterized by a mixture of a LTD model and Redlich-Kister (RK) expansion. The LTD model consists of two terms: one proportional with volume, expressing the energy gain of the defects clustering together; and one proportional with interface area, expressing the energy loss due to the interface created between matrix and defect cluster. A RK expansion is

Table B1. Optimized parameters for the LTD model.

LTD model parameters			
$A_V = 4.524241E + 00$	$B_V = 5.985280E + 00$	$L_{VH}^0 = -3.727769E - 02$	
$A_H = -7.277276E - 01$	$B_H = -2.235115E + 00$	$L_{VHe}^0 = 2.659537E - 01$	
$A_{He} = 2.591062E + 00$	$B_{He} = -2.592230E + 00$	$L_{HHe}^0 = -9.119871E - 03$	

commonly used to parameterize free energy surfaces of solid solutions in thermodynamic modelling. It accounts for the interactions between the different defect types. In our model we included binary interactions only as the inclusion of ternary interactions did not improve the fit. Applying both models, the total binding energy of a $V_k H_l He_m$ clusters is given as,

$$E_b^{\text{tot}}(V_k H_l He_m) = A_V k - B_V k^{2/3} + A_H l - B_H l^{2/3} + A_{He} m - B_{He} m^{2/3} + L_{VH}^0 k l + L_{VHe}^0 k m + L_{HHe}^0 l m. \quad (\text{B1})$$

The optimized parameters for this expression are given in table B1.

References

- [1] Zinkle S J 2005 *Phys. Plasmas* **12** 058101
- [2] Pintus G 2012 *Comprehensive Nucl. Mater.* **4** 551
- [3] Roth J *et al* 2008 *Plasma Phys. Control. Fusion* **50** 103001
- [4] Hino T, Koyama K, Yamaguchi Y and Hirohata Y 1998 *Fusion Eng. Des.* **39–40** 227
- [5] Nagata S and Takahiro K 2001 *J. Nucl. Mater.* **290–293** 135
- [6] Iwakiri H, Morishita K and Yoshita N 2002 *J. Nucl. Mater.* **307–311** 135
- [7] Lee H T, Haasz A A, Davis J W and Macaulay-Newcombe R G 2007 *J. Nucl. Mater.* **360** 196
- [8] Lee H T, Haasz A A, Davis J W, Macaulay-Newcombe R G, Whyte D G and Wright G M 2007 *J. Nucl. Mater.* **363–365** 898
- [9] Li X-C, Shu X, Liu Y-N, Yu Y, Gao F and Lu G-H 2012 *J. Nucl. Mater.* **426** 31
- [10] Justin N and Wirth B D 2013 *J. Nucl. Mater.* **432** 61
- [11] Marinica M-C *et al* 2013 *J. Phys.: Condens. Matter.* **25** 395502
- [12] Wang J, Zhou Y L, Li M and Hou Q 2014 *Modelling Simul. Mater. Sci. Eng.* **22** 015004
- [13] Bonny G, Terentyev D, Bakaev A, Grigorev P and Van Neck D 2014 *Modelling Simul. Mater. Sci. Eng.* **22** 053001
- [14] Beccuart C S and Domain C 2009 *J. Nucl. Mater.* **386–388** 109
- [15] Jiang B, Wan F R and Geng W T 2010 *Phys. Rev. B* **81** 134112
- [16] Zhou H-B, Liu Y-L, Jin S, Zhang Y, Luo G-N and Lu G-H 2010 *Nucl. Fusion* **50** 115010
- [17] Finnis M W and Sinclair J E 1984 *Phil. Mag. A* **50** 45
- [18] Ackland G J and Thethford R 1987 *Phil. Mag. A* **56** 15
- [19] Johnson R A and Oh D J 1989 *J. Mater. Res.* **4** 1195
- [20] Foiles S M 1993 *Phys. Rev. B* **48** 4287
- [21] Wang Y R and Boercker D B 1995 *J. Appl. Phys.* **78** 122
- [22] Zhou X W *et al* 2001 *Acta Mater.* **49** 4005
- [23] Kong L T, Li X Y, Lai W S, Liu J B and Liu B X 2002 *Japan. J. Appl. Phys.* **41** 4503
- [24] Gong H R, Kong L T, Lai W S and Liu B X 2003 *Phys. Rev. B* **68** 144201
- [25] Zhang R F, Shen Y X, Gong H R, Kong L T and Liu B X 2004 *J. Phys. Soc. Japan* **73** 2023
- [26] Zhang R F, Kong L T, Gong H R and Liu B X 2004 *J. Phys.: Condens. Matter* **16** 5251
- [27] Zhang R F, Shen Y X, Yan H F and Liu B X 2005 *J. Phys. Chem. B* **109** 4391
- [28] Dai X D, Li J H and Kong Y 2007 *Phys. Rev. B* **75** 052102
- [29] Derlet P M, Nguyen-Manh D and Dudarev S L 2007 *Phys. Rev. B* **76** 054107
- [30] Björkås C, Nordlund K and Dudarev S 2009 *Nucl. Instrum. Meth. Phys. Res. B* **267** 3204
- [31] Björkås C, Nordlund K and Dudarev S 2010 *Nucl. Instrum. Meth. Phys. Res. B* **268** 1529 (erratum)
- [32] Wilson W D and Johnson R A 1972 *Interatomic Potentials and Simulation of Lattice Defects* ed P C Gehlen *et al* (New York: Plenum Press) p 375
- [33] Henriksson K O E, Nordlund K, Keinonen J, Sundholm D and Patzschke M 2004 *Phys. Scr.* **T108** 95
- [34] Justin N, Erhart P, Träskelin P, Nord J, Henriksson K O E, Nordlund K, Salonen E and Albe K 2005 *J. Appl. Phys.* **98** 123520
- [35] Li X-C, Shu X, Liu Y-N, Gao F and Lu G-H 2011 *J. Nucl. Mater.* **408** 12
- [36] Heinola K, Ahlgren T, Nordlund K and Keinonen J 2010 *Phys. Rev. B* **82** 094102
- [37] Samolyuk G D, Osetsky Y N and Stoller R E 2013 *J. Phys.: Condens. Matter* **25** 025403
- [38] Bonny G and Pasianot R C 2010 *Phil. Mag. Lett.* **90** 559

G

Many-body central force potentials for tungsten

G. Bonny, D. Terentyev, A. Bakaev, P. Grigorev and D. Van Neck

published in **Modelling and Simulation in Materials Science and Engineering**,
2014, Vol. 22, p. 053001

Topical Review**Many-body central force potentials for tungsten****G Bonny¹, D Terentyev¹, A Bakaev^{1,2,3}, P Grigorev^{1,4} and
D Van Neck²**¹ SCK-CEN, Nuclear Materials Science Institute, Boeretang 200, B-2400 Mol,
Belgium² Center for Molecular Modeling, Department of Physics and Astronomy,
Ghent University, Technologiepark 903, B-9052 Zwijnaarde, Belgium³ Faculty of Physics and Mechanics, Department of Experimental Nuclear
Physics K-89, St. Petersburg State Polytechnical University,
29 Polytekhnicheskaya str., 195251 St. Petersburg, Russia⁴ FUSION-DC Department of Applied Physics, Ghent University,
Sint-Pietersnieuwstraat 41 B4, B-9000 Gent, BelgiumE-mail: gbonny@sckcen.be

Received 31 January 2014, revised 14 April 2014

Accepted for publication 9 May 2014

Published 23 June 2014

Abstract

Tungsten and tungsten-based alloys are the primary candidate materials for plasma facing components in fusion reactors. The exposure to high-energy radiation, however, severely degrades the performance and lifetime limits of the in-vessel components. In an effort to better understand the mechanisms driving the materials' degradation at the atomic level, large-scale atomistic simulations are performed to complement experimental investigations. At the core of such simulations lies the interatomic potential, on which all subsequent results hinge. In this work we review 19 central force many-body potentials and benchmark their performance against experiments and density functional theory (DFT) calculations. As basic features we consider the relative lattice stability, elastic constants and point-defect properties. In addition, we also investigate extended lattice defects, namely: free surfaces, symmetric tilt grain boundaries, the $1/2\langle 111 \rangle\{110\}$ and $1/2\langle 111 \rangle\{112\}$ stacking fault energy profiles and the $1/2\langle 111 \rangle$ screw dislocation core. We also provide the Peierls stress for the $1/2\langle 111 \rangle$ edge and screw dislocations as well as the glide path of the latter at zero Kelvin. The presented results serve as an initial guide and reference list for both the modelling of atomically-driven phenomena in bcc tungsten, and the further development of its potentials.

Keywords: tungsten, interatomic potential, dislocation

(Some figures may appear in colour only in the online journal)

1. Introduction

Tungsten (W) and tungsten-based alloys are the primary candidate materials for plasma facing components in fusion reactors. In the demonstration power plant (DEMO) and commercial reactors these materials will be exposed to unprecedented and unexplored irradiation conditions. The exposure to high-energy radiation (neutron damage, helium and hydrogen high temperature/flux plasma) severely damages the microstructure of the materials by violently displacing atoms from their lattice and thereby creating vacancy clusters, dislocation loops, voids and even microscopic bubbles. All the above mentioned radiation-induced processes cause profound macroscopic property changes that severely degrade the performance and lifetime limits of the in-vessel components [1].

In an effort to better understand the mechanisms driving the microstructure and embrittlement, material modelling is applied to complement experimental investigations [2, 3]. Among different modelling tools, large-scale atomistic simulations such as molecular dynamics (MD) are employed to investigate the mechanisms of plasticity [4–6] and primary damage creation [7–10]. At the core of such simulations lies the interatomic potential, which enables computation of the forces between interacting atoms. Currently, for tungsten more than 30 different interatomic potentials are available in the literature in the form of pair potentials [11–14], many-body central force potentials [15–31] and its empirical modification [32], bond order potentials [33–36], modified embedded atom method potentials [37–39] and fourth moment tight binding potentials [18, 40, 41]. Each potential comes with its strengths and weaknesses. Since all results hinge on the quality of the interatomic potential, it is important that its properties are well understood. Given the vast number of available potentials, a review summarizing their basic properties is in order.

In this work we focus on the many-body central force formalism, which offers a good compromise between transferability/predictability and computational speed, especially when it comes to large-scale finite-temperature simulations. The many-body central force framework was developed independently under the forms: ‘embedded atom method’ (EAM) [42], ‘Finnis–Sinclair formalism [15]’ and ‘glue model [43, 44]’. We review the properties of 19 such potentials for W found in the literature [15–31]. As basic features we consider relative lattice stability, elastic constants and point-defect properties, which are all benchmarked against experimental data and density functional theory (DFT) calculations. In addition, we investigate extended lattice defects, namely: free surfaces, symmetric tilt grain boundaries, the $1/2\langle 111 \rangle$ $\{110\}$ and $1/2\langle 111 \rangle\langle 112 \rangle$ stacking fault energy profiles and the $1/2\langle 111 \rangle$ screw dislocation (SD) core. We also provide the Peierls stress for $1/2\langle 111 \rangle$ edge and SDs as well as the glide path of the latter at zero Kelvin.

2. Methods

A considerable amount of information on the properties of W is already available in the literature; however, we have used additional DFT calculations to extend the database for several defects not yet described in the open literature.

The DFT calculations were performed using the Vienna ab initio simulation package (VASP) [45, 46]. VASP is a plane-wave DFT code that implements the projector augmented wave (PAW) method [47, 48]. Standard PAW potentials supplied with VASP were used with the Vosko–Wilk–Nusair parameterization [49] for the local density approximation (LDA) combined with the Perdew–Wang [50] parameterization for the generalized gradient approximation (GGA) correction. A potential with six valence electrons was used and the plane wave cut-off was set to 450 eV. Brillouin zone sampling was performed using the

Table 1. Details of the calculation set-up for the different DFT and EAM calculations.

Configuration	DFT				EAM		
	Periodicity	N_{atoms}	Size (a_0^3)	k -points	Periodicity	N_{atoms}	Size (a_0^3)
Bulk	3D	128	$4.0 \times 4.0 \times 4.0$	$7 \times 7 \times 7$	3D	2000	$10.0 \times 10.0 \times 10.0$
Free surface	2D				2D		
{1 0 0}		252	$3.0 \times 3.0 \times 18.7$	$5 \times 5 \times 1$		2000	$10.0 \times 10.0 \times 10.0$
{1 1 0}		144	$21.7 \times 2.4 \times 1.7$	$1 \times 7 \times 9$		2016	$9.9 \times 9.8 \times 10.4$
{1 1 1}		288	$4.2 \times 4.9 \times 11.6$	$3 \times 1 \times 1$		2016	$9.9 \times 9.8 \times 10.4$
{1 1 2}		144	$2.8 \times 14.5 \times 2.6$	$5 \times 1 \times 6$		2016	$9.9 \times 9.8 \times 10.4$
γ -surface cut	2D				2D		
$1/2(1 1 1)$ {1 1 0}		60	$18.9 \times 2.4 \times 0.9$	$1 \times 7 \times 11$		6300	$21.2 \times 12.2 \times 12.1$
$1/2(1 1 1)$ {1 1 2}		90	$1.4 \times 41.5 \times 0.9$	$9 \times 1 \times 9$		3780	$12.7 \times 12.2 \times 12.1$
Grain boundary	3D				2D		
$\Sigma 3(1 1 0)$ {1 1 1}		72	$1.4 \times 2.4 \times 10.6$	$9 \times 5 \times 1$		2304	$5.6 \times 7.3 \times 27.8$
$\Sigma 3(1 1 0)$ {1 1 2}		96	$2.8 \times 1.7 \times 9.9$	$7 \times 9 \times 1$		1632	$5.6 \times 5.2 \times 28.0$
$\Sigma 5(1 0 0)$ {0 1 3}		120	$1.0 \times 3.2 \times 19.2$	$9 \times 5 \times 1$		3120	$9.0 \times 12.6 \times 22.1$
$\Sigma 11(1 1 0)$ {1 1 3}		112	$1.4 \times 6.6 \times 6.1$	$9 \times 1 \times 1$		4032	$5.6 \times 9.9 \times 28.0$
$\Sigma 9(1 1 0)$ {1 1 4}		192	$1.4 \times 8.5 \times 8.2$	$9 \times 1 \times 1$		3600	$5.6 \times 12.7 \times 28.1$
$\Sigma 9(1 1 0)$ {2 2 1}		160	$1.4 \times 6.0 \times 9.7$	$9 \times 1 \times 1$		2856	$5.6 \times 9.0 \times 28.2$
$\Sigma 19(1 1 0)$ {3 3 1}		308	$1.4 \times 8.7 \times 12.7$	$9 \times 1 \times 1$		5040	$5.6 \times 13.0 \times 28.2$
(1 1 1) atomic row	3D	36	$4.2 \times 4.9 \times 0.9$	$3 \times 2 \times 9$	3D	2160	$14.1 \times 14.7 \times 5.2$
displacement							
Dislocation screw	1D	108	$10.0 \times 8.8 \times 0.9$	$1 \times 1 \times 12$		18144	$49.5 \times 49.0 \times 5.2$
$1/2(1 1 1)$ edge		NA	NA	NA		22662	$49.5 \times 7.3 \times 86.6$

Monkhorst–Pack scheme, where the k -point meshes differ depending on the box size and are given in table 1. Finite-temperature smearing was obtained following the Methfessel–Paxton method with a smearing width of 0.3 eV. The ionic relaxation was performed using the conjugate gradient optimization scheme with a force convergence criterion of $0.03 \text{ eV } \text{\AA}^{-1}$.

The EAM calculations were performed using a standard MD code. The ionic relaxation was performed using the conjugate gradient optimization scheme, a quenching relaxation scheme or a combination of both, with an accuracy of 1 meV on the total energy.

The specifics of box size and boundary conditions depend on the calculated property and are summarized in table 1. The bulk properties and {1 0 0} free surface energy were calculated using a simulation box with principal axes oriented along the [1 0 0], [0 1 0] and [0 0 1] directions. For all other properties the principal axes of the simulation box were oriented along the [1 1 0], [$\bar{1}$ 1 2] and [1 $\bar{1}$ 1] direction, except for grain boundary (GB) calculations, which all have different orientations of the axes depending on the GB type (see below).

In the present work all values for the binding energy of a configuration containing the objects X_i is defined as,

$$E_b(X_1 \dots X_n) = \sum_i E(X_i) - \left[E\left(\sum_i X_i\right) + (n-1) E_{\text{ref}} \right], \quad (1)$$

where E_{ref} is the energy of the super cell without any objects (bcc W), $E(X_i)$ is the energy of the supercell containing the single object X_i , and $E(\sum_i X_i)$ is the energy of the super cell containing all interacting objects. Within this definition positive values of E_b denote attraction.

The surface energy for a (klm) free surface, $\gamma_{(klm)}$, is given as,

$$\gamma_{(klm)} = \frac{E_{(klm)} - N_{\text{atoms}} E_{\text{coh}}}{2 S}, \quad (2)$$

with $E_{(klm)}$ the total energy of the crystal with free surfaces, N_{atoms} the number of atoms in the box, E_{coh} the cohesive energy of the perfect crystal, and S the area of the free surface.

The stacking fault energy, γ_{SF} , in the γ -line profiles was calculated as,

$$\gamma_{\text{SF}} = \frac{E_{\text{SF}} - N_{\text{atoms}} E_{\text{coh}}}{S} - 2 \gamma_{\text{FS}}, \quad (3)$$

with E_{SF} the total energy of the crystal with stacking fault and γ_{FS} the free surface energy as calculated from equation (2).

The investigated GBs were prepared considering mirror symmetry for bi-crystals. The principal axes of the crystals x , y and z correspond to the tilt axis, GB axis and normal to GB plane, respectively. The initial separation between two layers belonging to different grains was set as equal to that inside the grains. In the DFT calculations 3D periodic super cells were used and the GB energy, γ_{GB} , was calculated following equation (2), where $E_{(klm)}$ was replaced by the total energy of the crystal containing the GB. In the EAM calculations 2D periodic super cells along the x and y directions were used. Free surfaces were applied perpendicular to the GB plane so the optimal spacing between the two grains was achieved automatically during the relaxation procedure. In this case, γ_{GB} was calculated following equation (3), where E_{SF} was replaced by the total energy of the crystal containing the GB.

For the study of dislocation properties, the principal axes x , y and z of the bcc crystal were oriented along the $[1\ 1\ 0]$, $[1\ 1\ 2]$ and $[1\ \bar{1}\ 1]$ directions, respectively. All studies were performed using ionic relaxation at zero Kelvin. The dislocation core structure was analysed using Vitek differential displacement maps [51]. In the DFT calculations a cylindrical crystal with periodic boundary condition along the dislocation line (created along the cylinder axis) was applied. The 40 atoms forming the outer surface of the cylinder were fixed to avoid the restoration to the perfect crystal upon relaxation. In the EAM calculations we employed the simulation model developed by Osetsky and Bacon [52]. The initial straight edge dislocation (ED) or SD with yz slip plane was created along the y or z direction with the Burgers vector $b = 1/2[1\ 1\ 1]$ parallel to z . Standard periodic boundary conditions were applied along the y and z directions for the ED, while modified periodic conditions (with $b/2$ shift along the y direction, as proposed by Rodney [53]) were applied for the SD. The simulation box was divided into three parts along x . The upper and lower parts consist of several atomic planes in which atoms were rigidly fixed in their original positions, whereas atoms in the ‘inner’ region were free to move during the ionic relaxation cycles. A glide force on the dislocation was generated by the relative displacement of the rigid blocks in the z direction, corresponding to a simple shear strain, ε_{xz} . The corresponding resolved shear stress induced by the applied deformation was calculated as $\tau = F_z/S_{yz}$, where F_z is the total force in the z direction on the lower outer block resulting from all atoms in the inner region, and S_{yz} is the area of the yz cross section of the box. The force, F_z , was computed after relaxation of the crystal so that the maximum force acting on any ‘inner’ atom in the system did not exceed $1 \text{ meV } \text{\AA}^{-1}$. It was verified that the chosen parameterisation, i.e., box size and relaxation criterion, provides full convergence of the results with a tolerance in the Peierls stress of $\sim 2 \text{ MPa}$. In addition to the numerical output, we have visualized the evolution of the dislocation core position and structure, using a combination of common neighbour analysis and potential energy [53].

Table 2. Nomenclature and remarks on the investigated many-body central force potentials.

Abbreviation	Reference	Remark
FS	Finnis and Sinclair, 1984 [15]	
AT	Ackland and Thetford, 1987 [16]	Minor upgrade in short range part FS
JO	Johnson and Oh, 1989 [17]	
FOI	Foiles, 1993 [18]	
WB	Wang and Boercker, 1995 [19]	Fcc more stable than bcc
ZWJ	Zhou <i>et al</i> 2001 [20]	
KLL	Kong <i>et al</i> 2002 [21]	
GKL	Gong <i>et al</i> 2003 [22]	Fcc more stable than bcc
ZSG	Zhang <i>et al</i> 2004 [23]	
ZKG	Zhang <i>et al</i> 2004 [24]	Identical to ZSG except for 0.02 Å in cut-off range
ZSY	Zhang <i>et al</i> 2005 [25]	Fcc more stable than bcc
DLK	Dai <i>et al</i> 2007 [26]	
DND	Derlet <i>et al</i> 2007 [27]	
BND	Björkas <i>et al</i> 2009 [28]	Stiffened version of DND
JW	Juslin and Wirth, 2013 [29]	Minor upgrade in short range part AT and stiffening
MVG1	'EAM-2' of Marinica <i>et al</i> 2013 [30]	
MVG2	'EAM-3' of Marinica <i>et al</i> 2013 [30]	
MVG3	'EAM-4' of Marinica <i>et al</i> 2013 [30]	
WZL	Wang <i>et al</i> 2014 [31]	

The latter allowed us to establish the mechanism of dislocation movement and to identify the glide plane under [1 1 1] (110) pure shear load.

3. Literature study

In this section we describe all many-body central force type potentials that are considered in the present work. We also correct some typographical errors found in the respective papers and report upon properties that we could not reproduce. For convenience, an overview of nomenclature of all considered potentials is given in table 2.

The first potential considered here is the one developed by Finnis and Sinclair (FS) [15] in 1984. The latter work in fact concerns the development of a new many-body central force potential formalism, namely, the so called 'Finnis–Sinclair' formalism. As an application, potentials for the bcc transition metals were fitted to the experimental lattice parameter, cohesive energy, elastic constants and vacancy formation energy.

In 1987 the same potential was modified in the short range region by Ackland and Thetford (AT) [16] to predict a more realistic pressure–volume relationship. Given the small changes induced by this modification, all properties obtained for FS are also valid for AT, unless explicitly stated otherwise.

In 1989 Johnson and Oh (JO) [17] developed an analytical parameterization and fitting methodology within the EAM for bcc transition metals. The potentials were fitted to the same experimental properties as FS. We note that although we find the reported

lattice parameter and cohesive energy, we could not reproduce the elastic constants (see table 3).

In 1993 Foiles (FOI) [18] developed ‘fourth moment’ Finnis–Sinclair type potentials and EAM ones for W and Mo. The latter were developed as a benchmark for the fourth moment ones. The EAM potentials were fitted to the same experimental properties as FS. In his paper we found a typographical error in the cut-off function that should read: $x^3(6x - 15x + 10)$. In addition, the cut-off distance was not defined for the pair potential, which we chose to be 3.5 Å. The latter distance is close to the zero cross-over of the pair potential function. As a peculiarity of the potential, we remark that at zero density the embedding function has a value of -5.16 eV, whereas this value is generally 0 eV.

In 1995 Wang and Borcker (WB) [19] provided EAM-like parameterizations for bcc transition metals with an emphasis on the reproduction of experimental phonon spectra. This was realized by the introduction of Friedel oscillations in the density function. To avoid the possibility of a negative density due to those oscillations, the total density is biased by an additive constant and therefore the latter is formally not of EAM-type. Nevertheless, we tested the reported parameterization and could reproduce the reported lattice parameter ($a_0 = 3.16259$ Å) and cohesive energy ($E_c = 8.6588$ eV) for the bcc lattice. However, we found the fcc lattice with lattice parameter ($a_0 = 4.06877$ Å) and cohesive energy ($E_c = 8.7276$ eV) to be more stable, in contrast to the claims in the paper. Therefore the latter potential was not considered any further in the present review.

In 2001 Zhou *et al* (ZWJ) [20] developed a set of interatomic potentials for 16 transition metals and their binary alloys. The potentials for the pure elements were fitted to the same properties as FS and the alloys were fitted to the heats of solution. Although the provided parameterizations are complete, we could not retrieve any references with respect to the target data used to fit the potentials.

In 2002 Kong *et al* (KLL) [21] developed a potential for the WCu system to study bcc/fcc interfacial reactions. The potential for W was fitted to the same experimental properties as FS. We remark on a typographical error in the reference to the experimental work reported in table I of the paper: reference “[14]” should read “[91]” instead. The latter reference refers to the work of Finnis and Sinclair [15], but we note that for the vacancy formation energy the calculated value from table 2 of the latter work was used as a fitting target instead of the experimental value. Finally, we note that although we can reproduce the reported lattice constant and cohesive energy, the elastic constants cannot be reproduced (see table 3).

In 2003 Gong *et al* (GKL) [22] also developed a potential for the WCu system to study glass formation. In the paper we found a typographical error in formula (7), which must read: $k_a = 4.5\{1 + 4/\left[\frac{2C_{44}}{(C_{11} - C_{12})} - 0.1 \right]\}$. We tested the corrected parameterization and could reproduce all reported values, i.e., lattice constant ($a_0 = 3.16475$ Å), cohesive energy ($E_c = 8.6600$ eV) and elastic constants ($C_{11} = 533$ GPa, $C_{12} = 205$ GPa and $C_{44} = 163$ GPa). However, we found the fcc lattice with lattice parameter ($a_0 = 4.07815$ Å) and cohesive energy ($E_c = 8.6719$ eV) to be more stable than the bcc one. Therefore the latter potential was not considered any further in the present review.

In 2004 two binary potentials were developed by Zhang *et al* [23, 24]. The first one (ZSG) [23] was developed in the framework of the study of metastable phases in the AgW system. The second one (ZKG) [24] focussed on glass formation in the CuW system. Both W potentials were fitted to the same experimental properties as FS and only differ by 0.02 Å in the cut-off distance. Despite this small difference, both potentials lead to equivalent results. Therefore all results reported for ZSG are also valid for ZKG unless explicitly stated. We remark that we could not retrieve the reported target values for cohesive and vacancy formation

Table 3. Comparison between experiments, DFT and potentials with respect to the lattice parameter and cohesive energy of close packed lattices, elastic constants, formation energy of different self-interstitial configurations, vacancy formation and migration energy and binding energy of di-vacancies. The target data to which the potentials were fitted are indicated by footnotes a..i.

Property	Exp.	DFT	FS	JO	FOI	ZWJ	KLL	ZSG	DLK	DND	MVG1	MVG2	MVG3	WZL
a_0 (bcc) (Å)	3.165 ^{2-a,f,i} [54, 68, 69]	3.19 [67]	3.16520	3.16475	3.16347	3.16519	3.16500	3.16500	3.18356	3.16520	3.14000	3.18738	3.14339	3.16519
	3.16475 ^{a,c} [70]													
	3.1648 ^b [71]													
	3.178 ^b													
a_0 (fcc) (Å)	4.05 ^b [67]	3.92700	4.11944	4.1193	4.12194	4.05534	4.11222	3.77264	3.98946	4.05340/ 3.79258	4.19954/ 3.82918	4.05339/ 3.79588		
	4.025 [72]													
	4.029 ^b													
E_c (bcc) (eV)	8.90 ^{c,d,f,h,i} [54, 71]	8.48 [72]	8.9000	8.6600	8.8598	8.7590	8.9000	8.6600	8.4003	8.9000	8.9000	8.8992	8.9000	8.8999
	8.66 ^{b,c} [57]	9.97 [73]												
	9.89 [68]													
E_c (fcc) (eV)	8.43 ^{b,m} [67]	8.7454	8.6045	8.8557	8.5969	8.8069	8.6067	7.9088	8.8476	8.4300/ 8.5272	8.4456/ 8.5362	8.4300/ 8.5161		
	8.37 ^m [74]													
	8.42 ^m [26]													
	8.41 ^m [72]													
E_c (hcp) (eV)	8.34 ^b [26]	8.7454	8.6045	8.8557	8.5969	8.8069	8.6067	7.8601	8.8476	8.5624	8.5445	8.5605	8.8080	
C_{11} (GPa)	522 ^{a,b,c,d,f} [56, 75]	488 [67]	523	503	543	524	679	533	531	524	523	474	523	523
	533 ^b [54]	517 [66]												
	523 ^{b,x} [54, 71, 76]	526 [79]												
	529 [77]	515 [64]												
	521 ^b [78]													
C_{12} (GPa)	204 ^{b,c} [56, 75]	200 [67]	205	185	215	205	361	205	188	205	203	192	202	205
	205 ^{a,d,f,i,l} [54, 76]	203 [66]												
	203 ^b [71]	194 [79]												
	209 [77]	197 [64]												
	202 ^b [78]													
C_{44} (GPa)	161 ^{a,b,c,d,f,x} [54, 56, 75, 76]	137 [67]	161	161	163	161	161	163	147	161	160	148	161	161
	163 ^b [54]	139 [66]												
	160 ^b [71, 78]	146 [64, 79]												
	162 [77]													
E_f (1 1 1) (eV)	9.55 ^{f,g,i} [80]	8.87 ^e , 9.52 ^e ,	8.05	8.48	10.55	16.21	12.22	9.32	9.48	10.40	10.15	10.40	9.48	
	10.53 ^b [67]	7.81												
	10.44 [67]													
	9.82 [81]													
	10.09 [79]													
	9.73 ^b													
E_f (1 1 0) (eV)	9.84 ^{f,g,i} [80]	9.62 ^e , 10.19 ^e ,	7.77	7.95	9.70	16.22	10.78	8.53	9.78	10.86	10.99	10.89	9.81	
	10.82 ^b [67]	8.45												
	10.79 [67]													
	10.10 [81]													
	10.55 [79]													
	10.04 ^b													
E_f (1 0 0) (eV)	11.49 ^{f,g,i} [80]	9.80 ^e , 10.30 ^e ,	9.35	9.58	12.20	16.00	14.85	9.05	11.34	12.93	11.32	12.81	11.41	
	12.87 ^b [67]	8.66												
	11.74 [81]													
	12.20 [79]													
	11.74 ^b													
E_f (Octa) (eV)	11.68 ^{f,g} [80]	9.98 ^e , 10.41 ^e ,	9.46	10.71	12.02	20.95	14.90	9.04	11.57	12.73	11.11	12.62	11.59	
	13.11 ^b [67]	8.87												

Table 3. (Continued.)

Property	Exp.	DFT	FS	JO	FOI	ZWJ	KLL	ZSG	DLK	DND	MVG1	MVG2	MVG3	WZL
E_f (Tetra) (eV)		11.05 ^{f,g,i} [80]	9.97 ^a , 10.47 ^p ,	8.78	9.22	11.52	14.28	13.77	9.12	10.92	12.01	11.39	11.95	10.86
		12.47 ^b [67]	8.82											
E_f (Vac) (eV)	3.15 ^{a,d} [82]	3.56 ^{d,g,i} [80]	3.63, 3.71 ^p	3.55	3.28	3.58	3.42	3.57	3.48	3.56	3.49	4.36	3.82	3.57
	3.95 ^{b,c} [58–60]	3.49 ^g [67]												
	3.5 [71]	3.25 [67]												
	4.1 [71]	3.23 [67]												
	3.67 ± 0.2 [83]	3.20 [21]												
	4.0 ± 0.3 [58]	3.34 [85]												
	3.76 ± 0.39 [84]	3.06 ^f												
E_m (Vac) (eV)	1.7 [71]	1.78 [67,80]	1.45	1.95	2.25	1.90	1.97	2.29	1.77	2.07	1.85	0.99	1.84	1.43
	2.0 [71]	1.66 [81]												
	1.78 ± 0.1 [83]	1.71 [85]												
		1.65 [21]												
		1.68 ^f												
E_b (V-V) 1nn (eV)	0.7 [86]	0.41 [27]	0.43, 0.01	0.31	0.27	0.37	0.36	0.31	0.37	0.57	0.49	0.46	0.52	0.44
		[79]	0.47 ^p											
		0.03 [79]												
		-0.09 [67]												
		-0.03 [67]												
		-0.04 [67]												
		-0.06 [81]												
		0.05 [87]												
		-0.18 ^f												
E_b (V-V) 2nn (eV)		0.19	0.40, [27]	0.47	0.43	0.46	0.38	0.45	0.37	0.37	0.38	0.61	0.45	0.39
			0.41 ^p											
		-0.19 [79]												
		-0.37 [79]												
		-0.41 [67]												
		-0.47 [67]												
		-0.44 [67]												
		-0.40 [81]												
		-0.27 [87]												
		-0.49 ^j												

^a Target data FS.^b Target data JO.^c Target data FOI.^d Target data KLL.^e Target data ZSG.^f Target data DND.^g Target data JW.^h Target data MVG1, MVG2 and MVG3.ⁱ Target data WZL.^j DFT data obtained in this work.^k Data obtained at 300 K [54].^l Extrapolated data to 0 K [54].^m Experimental value for bcc (8.90 eV) augmented by the DFT calculated energy difference between fcc and bcc.ⁿ Experimental value for bcc (8.90 eV) augmented by the DFT calculated energy difference between hcp and bcc.^o AT.^p JW.

energy from the quoted references, which are [54–56]. Instead, the reported target values are consistent with [57] and [58–60] for the cohesive energy and vacancy formation energy, respectively.

In 2005 Zhang *et al* (ZSY) [25] developed a potential for the ScW system to study the formation of amorphous alloys by ion beam mixing. We could not reproduce the reported

cohesive energy for the bcc lattice ($E_c = 8.42$ eV compared to a reported $E_c = 8.66$ eV). The optimum lattice parameter and elastic constants for the bcc lattice, on the other hand, could be reproduced. Moreover, we found that the fcc lattice with lattice parameter ($a_0 = 4.08256$ Å) and cohesive energy ($E_c = 8.4432$ eV) is more stable than the bcc one. Therefore the latter potential was not considered any further in the present review.

In 2007, independently of each other, two potentials were developed. Dai *et al* (DLK) [26] developed long-range Finnis–Sinclair type potentials for bcc transition metals to improve the prediction of the relative stability between competing close packed lattices. The potentials were fitted to the same experimental properties as FS. Derlet *et al* (DND) [27] developed potentials for bcc transition metals in the framework of a DFT and classical MD study with respect to the migration of interstitials. The potentials were fitted to the experimental lattice parameter, cohesive energy and elastic constants. In addition, it was fitted to the DFT calculated formation energy of the mono-vacancy and several self-interstitial configurations.

In 2009 the latter potential (and the one for molybdenum) (DND) was stiffened to the Ziegler–Biersack–Littmark (ZBL) [61] function by Björkas *et al* (BND) [28] to simulate collision cascades in W (and Mo). The stiffening does not affect the equilibrium properties of DND and therefore all obtained results for DND are also valid for BND, unless explicitly stated.

In 2013 AT was further modified and stiffened by Juslin and Wirth (JW) [29] to study He bubble formation in W. Besides the stiffening to the ZBL potential, the AT short range part was modified to better fit the DFT calculated formation energy of self-interstitial configurations. As most of the equilibrium properties remain unchanged compared to FS (and therefore also AT), all properties obtained for FS are also valid for JW, unless explicitly stated.

In the same year, 2013, three potentials were developed by Marinica *et al* (MVG1, MVG2 and MVG3) [30] to model radiation defects and dislocations in W. The potentials themselves represent refits of DND and are fitted to the same DFT data on lattice defects (as used for DND), as well as to new DFT calculated forces from liquid state configurations (see for example [62, 63]). In addition, the potentials were forced to provide a non-degenerate core structure for a 1/2(1 1 1) SD, as predicted by DFT [64–66]. We remark a typographical error in table 1 of paper [30], where reference [42] must be replaced by [67] in the present paper. We note that for MVG1 and MVG2 the reported elastic constants could not be reproduced (see table 3).

In 2014 an additional potential was developed by Wang *et al* (WZL) [31]. The potential is based on DFT calculations and focusses on self-interstitial defects and the thermal expansion of W. We note a typographical error in table 2 of the paper: the parameters with and without primes are switched.

4. Lattice stability, point-defects and elastic constants

In table 3 the lattice stability, elastic constants, interstitial and vacancy formation energy, vacancy migration and di-vacancy binding energy calculated by the above selected potentials is presented. In the same table, the obtained values are compared to DFT and experimental data (target data to which the potentials were fitted are indicated by ^a . . . ⁱ).

Focusing on the lattice stability first, all potentials were fitted to the experimental or DFT-obtained bcc lattice constants and cohesive energy, in particular, FS, KLL and DND were fitted to [54], JO, FOI and ZSG to [57, 70], MVG1, MVG2 and MVG3 to [71], and WZL to [54, 69]. For ZWJ and DLK, however, no references regarding the target data were given. In addition to the bcc data, MVG1, MVG2 and MVG3 were also fitted to the DFT-obtained fcc lattice constant

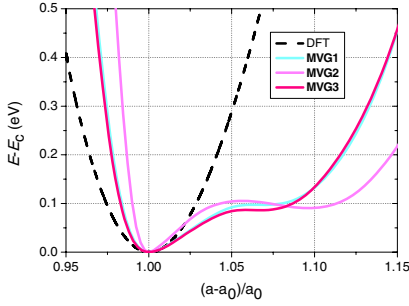


Figure 1. The cohesive energy difference for the fcc lattice as a function of relative lattice parameter variation calculated by both DFT and potentials.

and cohesive energy [30, 67]. We observe that all potentials and DFT data are in excellent or satisfactory (<10% deviation) agreement with the experimental bcc lattice constant and cohesive energy. Furthermore, for all potentials the bcc lattice is the ground state, compared to other close packed structures such as fcc (Strukturbericht A1) and hcp (Strukturbericht A3). We remark that the lattice constant and cohesive energy for the fcc lattice reported in [30] for MVG1, MVG2 and MVG3 corresponds to a local minimum in the energy landscape, with the global minimum about 0.1 eV lower. As shown in figure 1, the latter is an artefact of the potentials as DFT data shows a single minimum for the fcc lattice. We note that only the latter potentials exhibit this peculiarity.

With respect to the elastic constants, all potentials were fitted to experimental data, in particular, FS, KLL and DND were fitted to [75], JO, FOI and ZSG to [56], MVG1, MVG2 and MVG3 to [71], and WZL to [78]. Note that for ZWJ and DLK no references for the target data were provided. All potentials and DFT data, except for KLL, are in excellent or satisfactory (<10% deviation) agreement with the experimental data. For KLL the deviations for C_{11} and C_{12} reach 70%, while all reported DFT data are within 10% of the experimental results.

Regarding the formation energy of self-interstitial configurations, all reported DFT data suggest the (1 1 1) crowdion as the most stable configuration. This is respected by FS, AT, DND, JW, MVG1, MVG2, MVG3 and WZL, while JO, FOI, ZWJ, ZSG and DLK predict the (1 1 0) dumbbell and KLL the (1 0 0) dumbbell as the most stable self-interstitial configuration. We remark that only DND, JW, MVG1, MVG2, MVG3 and WZL were explicitly fitted to ensure the appropriate order in the formation energy of the interstitial configurations, namely, DND, JW and WZL to DFT data from [80] and MVG1, MVG2 and MVG3 to DFT data from [67].

All potentials were also fitted to the experimental or DFT calculated vacancy formation energy. In particular, FS and KLL were fitted to [82], JO, FOI and ZSG to [58–60], DND and WZL to [80], and MVG1, MVG2 and MVG3 to [67]. We note, that for ZWJ and DLK no references regarding the target data were given. All potentials and DFT data are in good agreement with experiments, providing results within the experimental range, i.e., 3.15–4.1 eV.

The vacancy migration barrier was not explicitly fitted for any of the potentials. Nevertheless, all the potentials and DFT data, except for FS, FOI, ZSG, MVG2 and WZL, are within 10% of the experimental range (1.7–2.0 eV). Besides the absolute value, the migration barrier curvature followed by a migrating atom exchanging its position with a vacancy is also

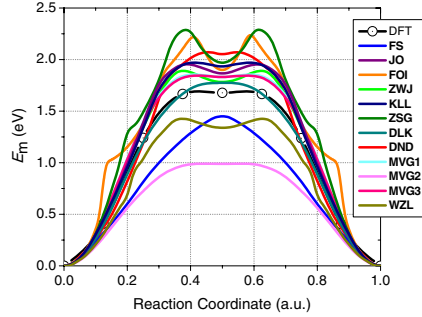


Figure 2. The vacancy migration energy path calculated by both DFT and the potentials.

of importance. In figure 2 we compare the vacancy migration energy path between DFT and the potentials. The DFT curve shows a plateau (or shallow minimum) around the saddle point. This specific shape is reproduced by JO, ZWJ, KLL, DND, MVG1, MVG2, MVG3 and WZL. However, more important than this specific shape is the overall smoothness of the curve. We note that in addition to the latter, FS and DLK exhibit a smooth curve, while FOI and ZSG reveal unphysical humps.

With respect to the binding energy of the di-vacancy, the combined field-ion microscopy and electrical resistivity experiments by Park *et al* [86] predict a strong binding (0.7 eV) and suggest that the first nn configuration is the ground state for the di-vacancy. While all DFT data indicate lower binding or stronger repulsion for the second nn di-vacancy complex compared to the first nn configuration, only the study by Derlet *et al* [27] reports significant binding (0.41 eV) for the first nn configuration. All other data suggests insignificant binding or repulsion. The origin of the vacancy–vacancy repulsion in the second nn configuration is explained in [30] in terms of the shape of the distribution of the local density of states near the Fermi level obtained by DFT calculations. The latter is a purely quantum mechanical effect that is not expected to be reproducible by empirical many-body central-force potentials. Indeed, DND, JW, MVG1 and MVG3 predict the first nn configuration of the di-vacancy to be significantly more stable than the second nn one. All other potentials, except for FS, AT, DLK and WZL that provide similar binding for the two configurations, underestimate the experimental binding energy.

5. Extended defects

5.1. Surface defects

In figure 3 we present the relative energy difference of several low index free surfaces, namely: {1 0 0}, {1 1 1} and {1 1 2}, taking {1 1 0} as baseline, which has the lowest formation energy. The presented DFT data sets give similar results, except for the {1 1 1} free surface that shows a discrepancy of about 200 mJ m⁻². As shown in the figure, all potentials predict the {1 1 0} surface to be the most stable, consistent with DFT. With respect to the DFT trends, only DND consistently predicts the highest formation energy for the {1 0 0} surface orientation. In fact, the resulting curve from DND is also in good quantitative agreement with the DFT

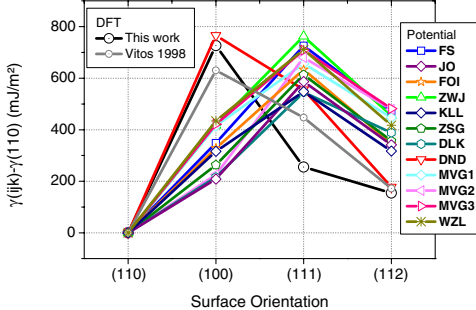


Figure 3. Free surface energy per unit area for various low index surface configurations.

Table 4. Reference value for the $\{110\}$ free surface energy obtained from experiment, DFT calculations and the potentials.

Property	Exp.	DFT	FS	JO	FOI	ZWJ	KLL	ZSG	DLK	DND	MVG1	MVG2	MVG3	WZL	
$\gamma_{(110)}$		3250 [89]	3197 ^a	2575	2600	2440	2566	2435	2629	2649	2402	2306	3096	2509	2402
(mJ m ⁻²)															
		3675		4005											
		[90]		[88]											

^a DFT data obtained in this work.

data from [88]. Other potentials predict that the $\{111\}$ surface requires the highest formation energy. In table 4 we report the absolute values for the $\{110\}$ surface as calculated by the potentials and DFT [88], as well as the experimental data [89, 90]. While the DFT values and results for MVG3 are within 10% of the experimental data range, the other potentials remarkably underestimate the formation energy of the $\{110\}$ surface.

In figures 4 and 5 we present the stacking fault energy for $1/2\langle 111 \rangle \{110\}$ and $1/2\langle 111 \rangle \{112\}$ shear, respectively, calculated by both DFT [91] and the potentials. The stacking fault energy profiles (henceforth referred to as γ -line) provide information about the energy landscape for the shear process of a perfect crystal in $\{110\}$ and $\{112\}$ atomic planes, and can be used to compute the dislocation core structure and Peierls stress [92, 93]. As shown in the figures, all DFT data predicts smooth curves with a single well-defined maximum. On the γ -lines obtained using FOI, ZSG and DND we identify unphysical humps, while other potentials provide a curvature in agreement with the DFT result. The saddle point in the γ -lines predicted by JO, KLL, ZWJ, MVG1 and MVG3 is within 10% of the DFT data, in the case of the $1/2\langle 111 \rangle \{110\}$ shear. In the $\{112\}$ plane, a good quantitative prediction (i.e. within 10%) is achieved only by MVG1 and MVG3.

Comparison of the GB energies is presented in figure 6. All the potentials accurately predict the energy of the $\Sigma_3\langle 111 \rangle \{112\}$ tilt boundary as compared to the DFT data. The deviation from the DFT results is especially significant in the case of GBs with $\langle 110 \rangle$ tilt axis. Indeed, these GBs reveal essential reconstruction of the atoms at the interface, which apparently cannot be easily reproduced by the potentials. Regarding quantitative accuracy, none of the potentials is capable of predicting the interface energy within 10% of all the DFT data. FOI and ZSG reveal the strongest deviation from the DFT prediction. The appropriate

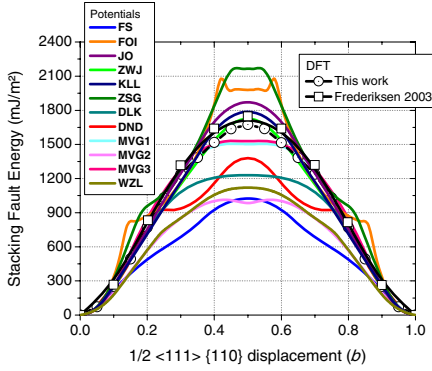


Figure 4. Comparison between DFT and the potentials of the $1/2\langle 111 \rangle \{110\}$ stacking fault energy profile.

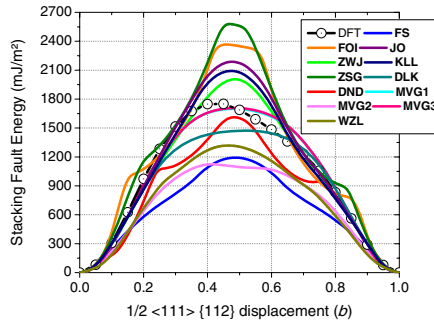


Figure 5. Comparison between DFT and the potentials of the $1/2\langle 111 \rangle \{112\}$ stacking fault energy profile.

trend with respect to the order by which the interface energy depends on interface orientation is adequately predicted only by MVG1, DND, FOI and ZWJ. This agreement, however, does not imply that the structure of the GBs is also correctly predicted by these four potentials.

5.2. Line defects

Figure 7 presents the $1/2\langle 111 \rangle$ atomic row displacement energy curves, also known as inter-row potential (IRP), calculated by both DFT and the interatomic potentials. The IRP provides information with respect to the SD core structure and can be used to model its movement (see, e.g., [94]). The DFT calculated IRP shows a wide plateau near the middle of the reaction path, which is only reproduced by MVG2. While the curves for FOI, ZSG and DND exhibit unphysical humps, the other curves show smooth behaviour with a well-defined

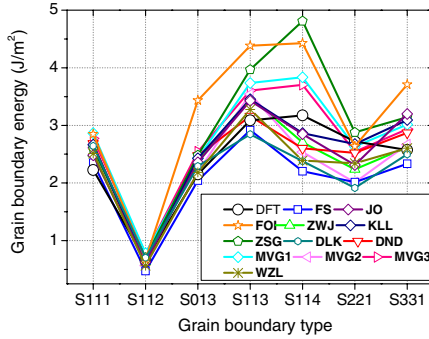


Figure 6. GB interface energy per unit area for various grain boundary configurations.

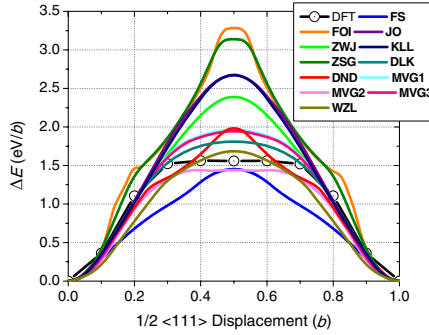


Figure 7. Comparison between DFT and the potentials for the energy difference during a $\langle 111 \rangle$ atomic row displacement.

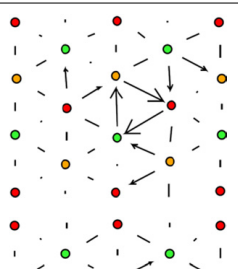
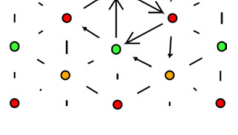
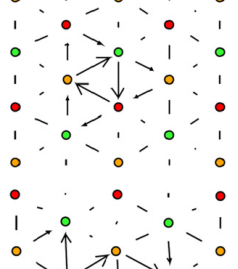
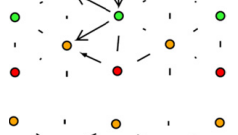
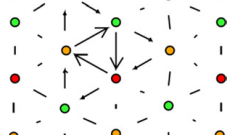
single maximum. From all the smooth curves, only FS, MVG2 and WZL provide results within 10% of the DFT data.

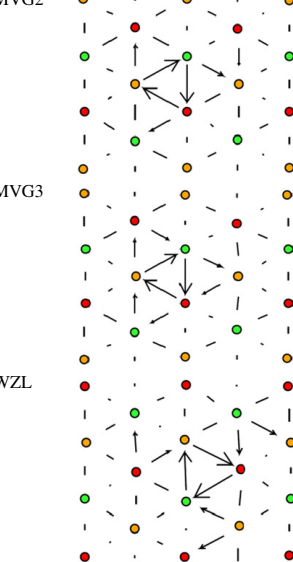
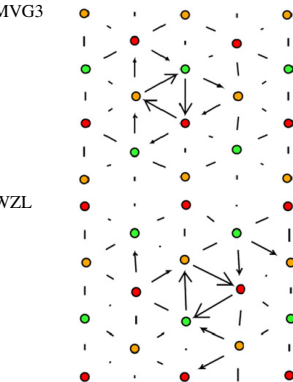
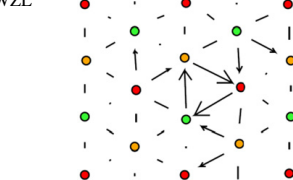
In table 5 we present the SD core structure, movement mechanism under the $\langle 111 \rangle\langle 110 \rangle$ shear load and the corresponding Peierls stress, calculated using the potentials. The Peierls stress for a $1/2\langle 111 \rangle\langle 110 \rangle$ ED is also presented in table 5. The dislocation core structure is visualized by means of differential displacement maps [51]. For all bcc transition metals, and W in particular, DFT predicts a compact isotropic core structure for a $1/2\langle 111 \rangle$ SD [64–66, 91, 95–98]. Consistent with DFT results, the compact core is reproduced by ZSG, DLK, MVG (all), FOI and ZWJ. The three fold core structure is predicted by FS, JO, KLL, DND and WZL. Note that FOI and ZSG fail to reproduce (even qualitatively) the DFT-predicted γ -lines and IRP profile, but adequately describe the SD core structure. Hence, there is no direct correlation between the shape of the IRP profile and SD core structure, although such correlation has been speculated in the literature [99]. We note that similar calculations for FS, ZWJ and MVG3 were performed in [100]. Except for ZWJ, which was found to exhibit a degenerate core in [100], our results are in agreement with [100].

Table 5. SD core structure, SD glide path and Peierls stress for ED and SD. The SD and ED were generated and loaded in crystals so that the maximum resolved shear stress (MRSS) was exerted in a {110} plane. EDs were always seen to glide in the MRSS plane, i.e., {110} plane.

Method	Core structure	Mechanism of SD movement	τ_p screw	τ_p edge
DFT		Glide in {110} [66]	1.71 GPa [66]	
FS		Split & glide in {110}	3.98 GPa	38 MPa
JO		Split & glide in {112}	4.4 GPa	85 MPa
FOI		Transformation into degenerate core and glide of 1/6 (111) partial in {112} with formation of fault	15 GPa	6 GPa
ZWJ		Glide in {112}	4.1 GPa	50 MPa

Table 5. (Continued.)

Method	Core structure	Mechanism of SD movement	τ_p screw	τ_p edge
KLL		Split & glide in {112}	4.2 GPa	85 MPa
ZSG		Transformation into degenerate core and glide of 1/6 (111) partial in {112} with formation of fault	8.2 GPa	4.2 GPa
DLK		Glide in {112}	2.9 GPa	10 MPa
DND		Transformation into degenerate core and glide of 1/6 (111) partial in {112} with formation of fault	5.5 GPa	1.4 GPa
MVG1		Glide in {112}	3.55 GPa	1 MPa

MVG2		Glide in {110}	0.98 GPa	3 MPa
MVG3		Glide in inclined {110}	4.43 GPa	3 MPa
WZL		Split & glide in {112}	1.9 GPa	180 MPa

The mechanism of dislocation movement under $\langle 111 \rangle \langle 110 \rangle$ shear load was also found to essentially depend on the applied potential. Overall, it is possible to distinguish three frequently observed mechanisms, namely: (i) glide of the compact core; (ii) split of the core into a planar structure and glide of the two dissociated dislocations; (iii) transformation of the core into a three fold degenerate structure and the emission of a gliding $1/6\langle 111 \rangle\langle 112 \rangle$ partial dislocation (gliding in a $\{112\}$ plane) with the formation of a planar fault. We remind that according to DFT, the dislocation overcomes the Peierls barrier without changing its compact structure [66]. Among the tested potentials, qualitatively, the movement mechanism was predicted correctly by ZWJ and MVG (all), but the expected $\{110\}$ glide plane is reproduced only by the MVG2 and MVG3 potentials. The latter two potentials predict the Peierls stress to be 0.98 and 4.43 GPa, which bound the DFT value of 1.7 GPa [66]. The values of the Peierls stress of the SD obtained with other potentials are not discussed as the movement mechanism is inconsistent with the DFT predictions. We note that for FS, ZWJ and MVG3 similar calculations were performed in [100]. While the same Peierls stress is obtained for ZWJ, the values reported in [100], i.e., 2.0 and 1.8 GPa for FS and MVG3, respectively, are about a factor two lower than the ones reported in table 5. The discrepancy might be related to the calculation method, from which the Peierls stress was obtained. In [100], the Peierls stress is derived from the energy barrier obtained using a nudged elastic band method (NEB) relaxation-activation method [101] in a manner proposed by Gröger and Vitek [102]; while in this work the Peierls stress follows from static loading of a crystal (see section 2), applied in small increments to achieve the displacement of the core.

With respect to the ED, in all cases its core structure was found to be planar non-split, being very similar to that studied previously in bcc Fe [103, 104]. Three potentials (FOI, ZSG, DND)

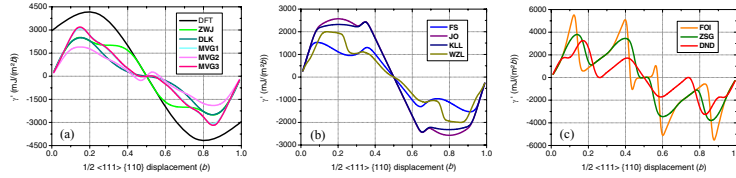


Figure 8. Derivative of the $1/2\langle 111 \rangle\langle 110 \rangle$ γ -line corresponding with DFT and potentials that exhibit, *a*) glide of the compact SD core, *b*) planar split and glide of the dissociated SD, and *c*) threefold degenerate split of the SD and glide of a partial.

have shown exceptional results: a split in the $\{110\}$ plane into two partials connected by a stacking fault. Note that exactly those three potentials were also found to predict an unphysical shape for the $\{110\}$ γ -line (see figure 4). As a result of the splitting, the dislocation moves by removal and generation of stacking faults in the $\{110\}$ glide plane, which requires a very high critical shear stress exceeding 1 GPa. All other potentials reveal a Peierls stress in the range of 1–180 MPa, which is consistent with the values obtained in bcc Fe using DFT-derived potentials [105]. Experimental data for the Peierls stress of EDs in bcc W is not available, to our knowledge.

Based on the results of this section, we conclude that the most appropriate potentials, i.e., describing properties of extended defects in line with DFT data (qualitatively or quantitatively), are MVG2 and MVG3.

To conclude this section, we attempt to correlate the γ -line (for $\{110\}$ planes, but the same holds for $\{112\}$ planes) corresponding to the different potentials with their observed dislocation behaviour. In figure 8 the derivative of the $\{110\}$ γ -lines from DFT and the potentials are summarized and classified into three categories. The derivative characterizes the force to be overcome by a dislocation in the $\{110\}$ plane. The first class (figure 8(a)) is consistent with DFT data, which predicts a single maximum and is consistent with the observed glide of the compact SD core (mechanism (i)). The second class (figure 8(b)) is characterized by a shallow maximum just beside the global maximum and is representative of the observed planar split and glide of a SD (mechanism (ii)). The third class exhibits two clearly distinct maxima of similar height and is representative of the observed transformation of a SD into a threefold degenerate core and glide of a partial (mechanism (iii)) or planar split and glide of an ED. Thus, figure 8 suggests a correlation between the stacking fault energy derivative and the path that the SD follows under shear of the crystal due to externally applied stress. The potentials predicting the barriers to be comparable to the DFT value result in stable SD glide in a $\{110\}$ or $\{112\}$ plane. However, the core of the SD apparently undergoes essential modification prior to the Peierls stress being reached in the case of the potentials grouped in figure 8(b). For that reason, the glide of the SD is realized along with the well-pronounced dislocation split. For the potentials grouped in figure 8(c), the resistance against shear is apparently so strong that the resolved shear stress is high enough to emit a partial dislocation in a $\{112\}$ plane, as we observed in the static simulations involving load. With these observations we conclude that adequate reproduction of the equilibrium core structure and γ -line curve is not enough to ensure a stable $\{110\}$ glide by the SD upon external load at 0 K. For instance, no clear reason was found for the difference in the SD glide plane for MVG1 and MVG3, given that they provide almost identical γ -lines and SD core structures. Apparently, competing mechanisms such as glide in an inclined $\{112\}$ plane or partial dislocation emission may come into play

Table 6. Schematic summary of the performance of the potentials for different physical properties.

Property	FS	JO	FOI	ZWJ	KLL	ZSG	DLK	DND	MVG1	MVG2	MVG3	WZL
Elastic constants	C	C	C	C	IC	C	C	C	C	C	C	C
E_f (Vac)	C	C	C	C	C	C	C	C	C	C	C	C
E_m (Vac)	UE	C	IC	C	C	IC	C	C	C	UE	C	UE
E_b (Di-Vac)	IC	IC	IC	IC	IC	IC	IC	UE	UE	IC	UE	UE
E_f (SIA)	UE ^a	IC	IC	IC	IC	IC	IC	C	C	C	C	C
(1 1 1) row potential	C	OE	IC	OE	OE	IC	OE	IC	OE	C	OE	C
Screw dislocation core	IC	IC	C	C	IC	C	C	IC	C	C	C	IC
Screw dislocation glide	IC	IC	IC	C	IC	IC	IC	IC	C	C	C	IC
Edge dislocation glide	C	C	IC	C	C	IC	C	IC	C	C	C	C
Free surface	UE	UE	UE	UE	UE	UE	UE	UE	C	UE	UE	
Grain boundary	UE	C	C	C	C	C	UE	C	UE	C	UE	
Gamma surface cuts	UE	C	IC	C	C	IC	UE	IC	C	UE	C	UE
R_{cut}	2nn	2nn	2nn	2nn	2nn	2nn	6nn	2nn	5nn	4nn	5nn	2nn

IC-Inconsistent with experimental or DFT data.

C-Consistent with experimental or DFT data.

OE-Overestimation compared to experimental or DFT data.

UE-Underestimation compared to experimental or DFT data.

^a Both AT and JW are consistent with the DFT data.

depending on the other properties of the potential, i.e., generalized stacking fault energy surface and polarizability of the SD core as a function of external load. As an indication as to what may be done towards further development of the potentials, we suggest verifying, or even including in the fitting, the core structure of the dislocation in the saddle point of the Peierls barrier, which could be obtained by *ab initio* calculations.

6. Summary

In this last section we summarize the performance of the tested potentials by identifying their strong and weak points. Table 6 presents a schematic summary of the potentials' performance, which is evaluated as 'consistent' (C) with experimental or DFT data if there is a qualitative (correct order or smooth curve) and quantitative (within 10% of the given range) agreement; 'inconsistent' (IC) if there is no qualitative agreement; 'underestimated' (UE) if there is qualitative agreement but the target value is underestimated by more than 10%; and 'overestimated' (OE) in the case of qualitative agreement but the target value is overestimated by more than 10%. Depending on the target application, a compromise between the performance and computational speed (R_{cut}) can be achieved by selecting an appropriate version of the potential. The results presented here can serve as an initial guide and reference list for both the modelling of atomically-driven phenomena in bcc tungsten, and the further development of its potentials.

Acknowledgments

This work, supported by the European Commission under the Contract of Association between EURATOM/SCK-CEN, was carried out within the framework of the European Fusion Development Agreement. Part of this work was carried out using the HELIOS supercomputer

system at Computational Simulation Centre of International Fusion Energy Research Centre (IFERC-CSC), Aomori, Japan, under the Broader Approach collaboration between Euratom and Japan, implemented by Fusion for Energy and JAEA. We thank Ms N Baetens for useful discussions.

References

- [1] Zinkle S J 2005 *Phys. Plasmas* **12** 058101
- [2] Rieth M *et al* 2011 *J. Nucl. Mater.* **417** 463
- [3] Rieth M *et al* 2013 *J. Nucl. Mater.* **432** 482
- [4] Gröger R, Bailey A G and Vitek V 2008 *Acta Mater.* **56** 5401
- [5] Mrovec M, Elsässer C and Gumbsch P 2009 *Phil. Mag.* **89** 3179
- [6] Srivastava K, Gröger R, Weygand D and Gumbsch P 2013 *Int. J. Plasticity* **47** 126
- [7] Juslin N, Jansson V and Nordlund K 2010 *Phil. Mag.* **90** 3581
- [8] Troev T, Nankov N and Yoshiie T 2011 *Nucl. Inst. Meth. Phys. Res. Sec. B* **269** 566
- [9] Fu B, Xu B, Lai W, Yuan Y, Xu H, Li C, Jia Y and Liu W 2013 *J. Nucl. Mater.* **441** 24
- [10] Sand A E, Dudarev S L and Nordlund K 2013 *Europhys. Lett.* **103** 46003
- [11] Johnson R A and Wilson W D 1972 *Interatomic Potentials and Simulation of Lattice Defects* ed P C Gehlen *et al* (New York: Plenum) p 301
This concerns the pair potential for tungsten.
- [12] Johnson R A and White P J 1978 *Phys. Rev. B* **18** 2940
- [13] Johnson R A 1983 *Phys. Rev. B* **27** 2014
- [14] Mundim K C, Malbouisson L A C, Dorfman S, Fuks D, Van Humbeeck J and Liubich V 2001 *J. Mol. Struct. (Theochem)* **539** 191
- [15] Finnis M W and Sinclair J E 1984 *Phil. Mag. A* **50** 45
- [16] Ackland G J and Thetford R 1987 *Phil. Mag. A* **56** 15
- [17] Johnson R A and Oh D J 1989 *J. Mater. Res.* **4** 1195
- [18] Foiles S M 1993 *Phys. Rev. B* **48** 4287
- [19] Wang Y R and Boernerker D B 1995 *J. Appl. Phys.* **78** 122
- [20] Zhou X W *et al* 2001 *Acta Mater.* **49** 2939
- [21] Kong L T, Li X Y, Lai W S, Liu J B and Liu B X 2002 *Japan. J. Appl. Phys.* **41** 4503
- [22] Gong H R, Kong L T, Lai W S and Liu B X 2003 *Phys. Rev. B* **68** 144201
- [23] Zhang R F, Shen Y X, Gong H R, Kong L T and Liu B X 2004 *J. Phys. Soc. Japan* **73** 2023
- [24] Zhang R F, Kong L T, Gong H R and Liu B X 2004 *J. Phys.: Condens. Matter* **16** 5251
- [25] Zhang R F, Shen Y X, Yan H F and Liu B X 2005 *J. Phys. Chem. B* **109** 4391
- [26] Dai X D, Li J H and Kong Y 2007 *Phys. Rev. B* **75** 052102
- [27] Derlet P M, Nguyen-Manh D and Dudarev S L 2007 *Phys. Rev. B* **76** 054107
- [28] Björkas C, Nordlund K and Dudarev S 2009 *Nucl. Instrum. Methods Phys. Res. B* **267** 3204
Björkas C, Nordlund K and Dudarev S 2010 *Nucl. Instrum. Methods Phys. Res. B* **268** 1529
(erratum)
- [29] Juslin N and Wirth B D 2013 *J. Nucl. Mater.* **432** 61
- [30] Marinica M-C *et al* 2013 *J. Phys. Condens. Matter* **25** 395502
- [31] Wang J, Zhou Y L, Li M and Hou Q 2014 *Modelling Simul. Mater. Sci. Eng.* **22** 015004
- [32] Hu W, Shu W and Zhang B 2002 *Comput. Mater. Sci.* **23** 175
- [33] Xie Q and Chen P 1997 *Phys. Rev. B* **56** 5235
- [34] Henriksson K O E, Nordlund K, Keinonen J, Sundholm D and Patzschke M 2004 *Phys. Scr.* **T108** 95
- [35] Juslin N, Erhart P, Träskelin P, Nord J, Enriksson K O, Nordlund K, Salonen E and Albe K 2005 *J. Appl. Phys.* **98** 123520
- [36] Mrovec M, Gröger R, Bailey A G, Nguyen-Manh D, Elsässer C and Vitek V 2007 *Phys. Rev. B* **75** 104119
- [37] Baskes M I 1992 *Phys. Rev. B* **46** 2727
- [38] Lee B J, Baskes M I, Kim H and Choo Y K 2001 *Phys. Rev. B* **64** 184102

- [39] Park H, Fellinger M R, Lenosky T J, Tritton W W, Trinkle D R, Rudin S P, Woodward C, Wilkins J W and Hennig R G 2012 *Phys. Rev. B* **85** 214121
- [40] Carlsson A E 1991 *Phys. Rev. B* **44** 6590
- [41] Xu W and Adams J B 1994 *Surf. Sci.* **301** 371
- [42] Daw M S and Baskes M I 1984 *Phys. Rev. B* **29** 6443
- [43] Ercolessi F 1983 Molecular dynamics studies of gold: bulk, defects, surfaces and clusters *PhD Thesis* University of Trieste
- [44] Ercolessi F, Tosatti E and Parrinello M 1986 *Phys. Rev. Lett.* **57** 719
- [45] Kresse G and Hafner J 1993 *Phys. Rev. B* **47** 558
- [46] Kresse G and Furthmüller J 1996 *Phys. Rev. B* **54** 11169
- [47] Blochl P E 1994 *Phys. Rev. B* **50** 17953
- [48] Kresse G and Joubert D 1999 *Phys. Rev. B* **59** 1758
- [49] Vosko S H, Wilk L and Nusair M 1980 *Can. J. Phys.* **58** 1200
- [50] Perdew J P, Chevary J A, Vosko S H, Jackson K A, Pederson M R, Singh D J and Fiolhais C 1992 *Phys. Rev. B* **46** 6671
- [51] Vitek V, Perrin R C and Bowen D K 1970 *Phil. Mag.* **21** 1049
- [52] Ossetsky Yu N and Bacon D J 2003 *Modelling Simul. Mater. Sci. Eng.* **11** 427
- [53] Rodney D 2004 *Acta Mater.* **52** 607
- [54] Kittel C 1976 *Introduction to Solid State Physics* 5th edn (Wiley: New York)
- [55] Brandes E A and Brook G B 1992 *Smithells Metals Reference Book* 7th edn (Oxford: Butterworth-Heinemann)
- [56] Simmons G and Wang H 1971 *Single Crystal Elastic Constants and Calculated Aggregate Properties: A Handbook* 2nd edn (Cambridge, MA: M.I.T. Press)
- [57] Kittel C 1971 *Introduction to Solid State Physics* 4th edn (New York: Wiley)
- [58] Maier K, Peo M, Saile B, Schaefer H E and Seeger A 1979 *Phil. Mag. A* **40** 701
- [59] Tietze M, Takaki S, Schwirlich I A and Schultz H 1982 *Point Defects and Defect Interactions in Metals* ed J-I Takamura *et al* (Amsterdam: North Holland) p 266
- [60] Ziegler R and Schaefer H E 1987 *Vacancies and Interstitials in Metals and Alloys* ed C Abromait and H Wollenberger (Switzerland: Trans Tech) p 145
- [61] Ziegler J F, Biersack J P and Littmark U 1985 *The Stopping and Range of Ions in Matter* (New York: Pergamon)
- [62] Ercolessi F and Adams J B 1994 *Europhys. Lett.* **26** 583
- [63] Mendelev M I, Han S, Srolovitz D J, Ackland G J, Sun D Y and Asta M 2003 *Phil. Mag.* **83** 3977
- [64] Romaner L, Ambrosch-Draxl C and Pippan R 2010 *Phys. Rev. Lett.* **104** 195503
- [65] Li H, Wurster S, Motz C, Romaner L, Ambrosch-Draxl C and Pippan R 2012 *Acta Mater.* **60** 748
- [66] Samolyuk G D, Ossetsky Y N and Stoller R E 2013 *J. Phys. Condens. Matter* **25** 025403
- [67] Ventelon L, Willaime F, Fu C-C, Heran M and Ginoux I 2012 *J. Nucl. Mater.* **425** 16
- [68] Lassner E and Schubert W D 1999 *Tungsten: Properties, Chemistry, Technology of the Element, Alloys, and Chemical Compounds* (New York: Kluwer Academic)
- [69] Lide D R 2004 *Handbook of Chemistry and Physics* 85th edn (Boca Raton, FL: CRC Press)
- [70] Gray D E 1957 *American Institute of Physics Handbook* (New York: McGraw-Hill)
- [71] Ehrhart P and Ullmaier H 1991 *Atomic Defects in Metals (Landolt-Börnstein New Series, Group III* vol 25) (Springer-Verlag, Berlin)
- [72] Heinola K and Ahlgren T 2010 *J. Appl. Phys.* **107** 113531
- [73] Ochs T, Beck O, Elsasser C and Meyer B 2000 *Phil. Mag. A* **80** 351
- [74] Skriver H L 1985 *Phys. Rev. B* **31** 1909
- [75] Bujard P 1982 *Thesis dissertation* University of Geneva
- [76] Featherstone F H and Neighbours J R 1963 *Phys. Rev.* **130** 1324
- [77] Ayres R A, Shanette G and Stein D 1975 *J. Appl. Phys.* **46** 1526
- [78] Bolef D I and Klerk J D 1962 *J. Appl. Phys.* **33** 2311
- [79] Muzyk M, Nguyen-Manh D, Kurzydłowski K J, Baluc N L and Dudarev S L 2011 *Phys. Rev. B* **84** 104115
- [80] Nguyen-Manh D, Horsfield A P and Dudarev S L 2006 *Phys. Rev. B* **73** 020101

- [81] Becquart C S and Domain C 2007 *Nucl. Instrum. Methods Phys. Res. B* **255** 23
- [82] Górecki T 1974 *Z. Metallk.* **65** 426
- [83] Rasch K-D, Siegel R W and Schultz H 1980 *Phil. Mag. A* **41** 91
- [84] Smedskjaer L C, Chason M K and Siegel R W 1983 *Bull. Am. Phys. Soc.* **28** 242
- [85] Heinola K, Ahlgren T, Nordlund K and Keinonen J 2010 *Phys. Rev. B* **82** 094102
- [86] Park J Y, Huang H C W, Siegel R W and Balluffi R W 1983 *Phil. Mag. A* **48** 397
- [87] Kato D, Iwakiri H and Morishita K 2011 *J. Nucl. Mater.* **417** 1115
- [88] Vitos L, Ruban A V, Skriver H L and Kollár J 1998 *Surf. Sci.* **411** 186
- [89] Tyson W R and Miller W A 1977 *Surf. Sci.* **62** 267
- [90] de Boer F R, Boom R, Mattens W C M, Miedema A R and Niessen A K 1988 *Cohesion in Metals* (Amsterdam: North-Holland)
- [91] Frederiksen S L and Jacobsen K W 2003 *Phil. Mag.* **83** 365
- [92] Peierls R E 1940 *Proc. Phys. Soc.* **52** 34
- [93] Nabarro F R N 1947 *Proc. Phys. Soc.* **59** 256
- [94] Chen Z, Kioussis N, Ghoniem N and Hasebe T 2008 *Phys. Rev. B* **77** 014103
- [95] Ismail-Beigi S and Arias T A 2000 *Phys. Rev. Lett.* **84** 1499
- [96] Ventelon L and Willaime F 2007 *J. Comput. Aided Mater. Des.* **14** (suppl. 1) 85
- [97] Kaburaki H, Shimizu F, Ogata S, Yamaguchi M, Kano T, Kimizuka H and Itakura M 2007 Annual Report on Earth Simulator Center
- [98] Shimizu F, Ogata S, Kano T, Li J and Kaburaki H 2007 *J. Earth Simulator* **7** 17
- [99] Chiesa S, Gilbert M R, Dudarev S L, Derlet P M and Van Swygenhoven H 2009 *Phil. Mag.* **89** 3235
- [100] Cereceda D, Stukowski A, Gilbert M R, Querryau S, Ventelon L, Marinica M-C, Perlado J M and Marian J 2013 *J. Phys. Condens. Matter* **25** 085702
- [101] Henkelman G, Johannesson G and Jonsson H 2000 *Progress on Theoretical Chemistry and Physics* (Dordrecht: Kluwer) p 269
- [102] Gröger R and Vittek V 2012 *Modelling Simul. Mater. Sci. Eng.* **20** 035019
- [103] Chen L, Wang C and Yu T 2006 *Comput. Mater. Sci.* **38** 39
- [104] Monnet G and Terentyev D 2009 *Acta Mater.* **57** 1416
- [105] Malerba L *et al* 2010 *J. Nucl. Mater.* **406** 19

H

Dislocations mediate hydrogen
retention in tungsten

**D. Terentyev, V. Dubinko, A. Bakaev, Y. Zayachuk, W. Van
Renterghem and P. Grigorev**

published in Nuclear Fusion, 2014, Vol. 54, p. 042004 (5 pp.)

Letter

Dislocations mediate hydrogen retention in tungsten

D. Terentyev¹, V. Dubinko², A. Bakaev^{1,3}, Y. Zayachuk¹,
W. Van Renterghem¹ and P. Grigorev^{1,4}

¹ SCK-CEN, Nuclear Materials Science Institute, Boeretang 200, Mol, 2400, Belgium

² National Science Center, Kharkov Institute of Physics and Technology, Kharkov 61108, Ukraine

³ Center for Molecular Modeling, Department of Physics and Astronomy, Ghent University, Technologiepark 903, 9052 Zwijnaarde, Belgium

⁴ Department of Applied Physics, Ghent University, St. Pietersnieuwstraat 41, 9000 Ghent, Belgium

Received 12 November 2013, revised 9 January 2014

Accepted for publication 26 February 2014

Published 21 March 2014

Abstract

In this letter, a comprehensive mechanism for the nucleation and growth of bubbles on dislocations under plasma exposure of tungsten is proposed. The mechanism reconciles long-standing experimental observations of hydrogen isotopes retention, essentially defined by material microstructure, and so far not fully explained. Hence, this work provides an important link to unify material's modelling with experimental assessment of W and W-based alloys as candidates for plasma facing components.

Keywords: dislocations, tungsten, retention, hydrogen

 Online supplementary data available from stacks.iop.org/NF/54/042004/mmedia

(Some figures may appear in colour only in the online journal)

Development of fusion technology for electrical power production is one of the biggest challenges faced in 21th century. Its realization must overcome a number of challenges, one of which is the selection of appropriate plasma facing materials (PFM). *High flux* plasma exposure degrades properties of materials and leads to permeation and trapping of plasma components including highly toxic tritium (phenomenon known as *retention*). Low erosion/sputtering, high melting point and controlled retention are typical prerequisites of PFM, among which *tungsten* (W) is the main candidate [1, 2].

The retention of hydrogen (H) isotopes is attributed to their trapping at lattice defects resulting in the formation of bubbles and their subsequent growth into sub-surfaces blisters. The conventional analysis of the retention under high energy ion implantation is based on the premise that vacancies, generated in collision cascades, are responsible for the nucleation of stable H-vacancy clusters [3–5]. In International Thermonuclear Experimental Reactor (ITER), the energy of impinging ions (<100 eV) is well below the displacement threshold, and the implantation range is limited to several nanometers. Nevertheless, samples exposed at linear plasma generators, demonstrate that the H permeation

extends up to several micrometers (μm) [6, 7]. At such depths, deep permeation of H cannot be assigned to the vacancy trapping as their equilibrium concentration is negligible at typical temperatures accessible to existing plasma generators, i.e. 300–800 K.

Grain boundaries were suggested as nucleation sites for bubbles [8], however, the retention also takes place in the recrystallized W [9] and even in single crystal W [10]. The self-trapping and nucleation of stable H clusters in W bulk is ruled out as a pair and triplet of H atoms exhibit negligible binding energy ($\sim 0.01 \text{ eV}$ [11]). Moreover, different impurity concentrations do not result in any significant difference in the H depth profiles. Hence, the mechanisms of H retention provoking intensive blistering and bubble formation under sub-threshold plasma exposure are still to be identified.

In this letter, we explore the interaction of H with screw dislocations (SDs), the main microstructural features of metals including W. Using density functional theory (DFT) calculations, we demonstrate that H atoms are strongly bound to the SD core and exhibit fast one-dimensional (1D) migration along the dislocation line. An elementary dislocation segment accepts up to six H atoms practically without losing the interaction strength. Once the cluster of eight H atoms

is formed, it spontaneously transforms into an immobile configuration by punching out a jog on a dislocation line. The DFT data are incorporated in continuum rate theory model to evaluate the nucleation rate of H bubbles on a dislocation network as a function of depth. A good agreement with the experimental profiles suggests that dislocation microstructure is primarily responsible for the trapping of H isotopes under high flux plasma exposure. The TEM analysis performed on the W samples, exposed to plasma in our previous work [12] in conditions not yet featuring the blisters, reveals the presence of numerous nanometric cavities decorating dislocations with a linear density matching the predictions of our calculations.

To assess H–SD interaction we used the Vienna Ab-Initio Simulation Package (VASP) [13]. The projected augmentation wave [14] and the generalized gradient approximation [15] were used for the pseudopotential and the exchange-correlation potential, respectively. The 1s state for H and 5d6s states for W are treated as valence states. The atomic relaxation is carried out using the conjugate-gradient algorithm with the force convergence criterion of $0.03 \text{ eV } \text{\AA}^{-1}$. The migration energy barrier is calculated using the nudged elastic-band (NEB) method with the quick-min algorithm [16], considering seven intermediate images with the same force convergence criterion of $0.03 \text{ eV } \text{\AA}^{-1}$.

The dislocation dipole approach [17] is applied to model a $1/2(1\bar{1}\bar{1})$ SD in a periodic crystal. Two SDs with antiparallel Burgers vectors are inserted into an ideal bcc W crystal, forming a dislocation quadruple [18]. A principal unit cell consists of three non-equivalent ($1\bar{1}\bar{1}$) atomic layers and has dimensions of $41.01 \times 38.82 \times 2.75 \text{ \AA}^3$ in the $\langle\bar{1}\bar{1}2\rangle$ (x), $\langle\bar{1}\bar{1}0\rangle$ (y) and $\langle1\bar{1}1\rangle$ (z) directions, which amounts to 135 W atoms in total. It is known to provide a reliable core structure and dislocation self-interaction brings negligible effect on the core properties [19]. This and twice larger (replicated in the $[1\bar{1}\bar{1}]$ direction) unit cells are used in this work. More details on VASP parametrization are provided in the online supplementary material (stacks.iop.org/NF/54/042004/mmedia).

Firstly, the site preference for an interstitial H near the SD core was determined. The H–SD binding energy for all tetra- and octahedral interstitial sites (henceforth TIS and OIS) was computed as $E_{\text{H-SD}}^b = (E_{\text{H+SD}} + E_{\text{Bulk}}) - (E_{\text{SD}} + E_{\text{H}})$. $E_{\text{H+SD}}$, E_{SD} , E_{H} are the total energy of the crystals containing, respectively, H and SD dipole simultaneously, only the SD dipole or H atom. E_{Bulk} is the total energy of the perfect W crystal with the same dimensions as used to model the SD dipole. Negative $E_{\text{H-SD}}^b$ implies that a system gains energy due to association of objects. Therefore, attractive interaction between two objects will correspond to the negative binding energy. The resulting 2D map zoomed near the SD core is given in figure 1(a). The SD core is composed of three ($1\bar{1}\bar{1}$) atomic rows connected by dashed black arrows in figure 1(a) (as it is conventionally represented by differential displacement analysis [20]). H atoms placed in OISs far from the core are unstable and relax to TISs. Few metastable OIS near the core are defined, but still occupation of TIS is more favorable. This corresponds to the fact that in W bulk, H also prefers to occupy TIS rather than OIS, with the energy difference of $\sim 0.4 \text{ eV}$ [21].

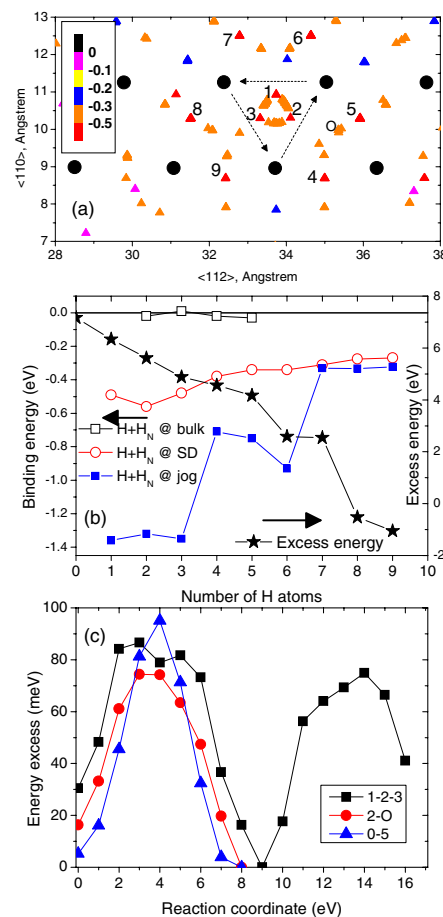


Figure 1. (a) H–SD binding energy map. Color code denotes the binding energy value in eV, note that H exhibits negative binding energy (i.e. attracted) in all positions near the dislocation core. Filled triangles display all metastable H positions, black circles display W atoms. Three dashed arrows show the ($1\bar{1}\bar{1}$) atomic rows forming the SD core. (b) Left axis—incremental binding energy of H to H_N cluster placed in W bulk, or on the perfect dislocation core, or on the jogged dislocation core. Right axis—the excess energy as a function of H_N size to punch out the jog. (c) Migration energy paths between the metastable positions indicated in (a).

The binding energy map reveals three deep (equivalent) energy minima states for H atom inside the core and six especially favorable (and again equivalent) positions adjacent to the core, enumerated from 1 to 9 in figure 1(a). These positions coincide with TISs, where H atom is bound to the core with the energy of $\sim 0.55 \text{ eV}$. Analysis of the charge distribution reveals that these positions coincide with the regions depleted by charge density (see the online supplementary material figure S.1(a) (stacks.iop.org/NF/54/042004/mmedia)), also interrelated with the distribution of local stress around the core.

The strong binding therefore originates from the compensation of local charge density (see the online supplementary figure S.1(b)(stacks.iop.org/NF/54/042004/mmedia)). Adding the second and the third H reduces the depleted region (see the online supplementary figures S.1(c) and (d)(stacks.iop.org/NF/54/042004/mmedia)) but does not cover it completely, pointing at a possibility of multiple trapping.

We therefore explored the binding energy and site preference for multiple H_N clusters adding them on a SD line in the nine revealed local minima i.e. forming a (1 1 1) platelet (henceforth H_N -SD cluster). For each relaxed H_N -SD configuration we computed the incremental binding energy for an extra H atom, presented in figure 1(b). A progressive removal of the depleted zone begins once $N > 3$. Addition of the fourth H atom results in a decrease of the absolute value of the binding energy. The most energetically favorable sequence to add H atoms is shown by numbers in figure 1(a). Starting from the seventh H atom, it is more favourable to continue growing the cluster along the dislocation line (i.e. place H in the next in-core position) rather than to build a (1 1 1) platelet. After adding the 8th H atom, we observed a considerable reconstruction of the H_N -SD cluster accompanied by a shift of W atoms forming the SD core. We attribute this to the formation of a pair of jogs, namely: a vacancy jog occupied by H_N cluster and an interstitial jog pushed aside. This process is analogous to the interstitial punching mechanism in the case of He self-trapping in bulk Fe [22].

To validate this hypothesis, we have computed the energy balance $E_{\text{EX}} = [E(H_N - \text{SD}) + E(\text{SD})] - [E(H_N - \text{JOG}_V) + E(\text{JOG}_I)]$. Here, $E(\text{SD})$ and $E(H_N - \text{SD})$ are the total energies of the crystals containing, respectively, SD dipole and H_N cluster attached to SD core, while, $E(H_N - \text{JOG}_V)$ and $E(\text{JOG}_I)$ are the energy of crystals with H_N cluster attached to a vacancy jog and SD dipole containing an interstitial jog. A positive value of E_{EX} implies that the jog-punching is not favorable, while a negative value points to an exothermic reaction expected to occur spontaneously.

The vacancy and interstitial jogs were constructed, respectively, by removing and adding one W atom from/to the core of the SD. The formation energies for JOG_I and JOG_V were computed to be 7.2 eV and 2.23 eV, respectively. Their sum is 3.8 eV lower than the Frenkel pair formation energy in W bulk, which is 9.73 + 3.5 eV being the formation energy for a vacancy and a self-interstitial atom, computed here in a 128 atomic supercell. As the creation of a pair of anti-jogs costs less energy than the Frenkel pair formation, a threshold for jog-punching on SD core may occur for a relatively low N still affordable for DFT techniques. E_{EX} as a function of N is shown in figure 1(b), which proves that the spontaneous jog-punching occurs once $N \geq 8$. In addition, we have calculated the binding energy of H to a H_N cluster on a vacancy jog. Note that the trapping of H at a pre-existing jog is much stronger, practically comparable to the binding energy for a single vacancy [5]. Therefore, jogs on dislocation lines, formed due to e.g. cyclic deformation under transient heat loads, will act as additional trapping sites for hydrogen and its isotopes.

Finally, we explored a possibility for H atom trapped on the SD core to exhibit 1D migration that is viewed as a mechanism by which H_N clusters may grow and reach the

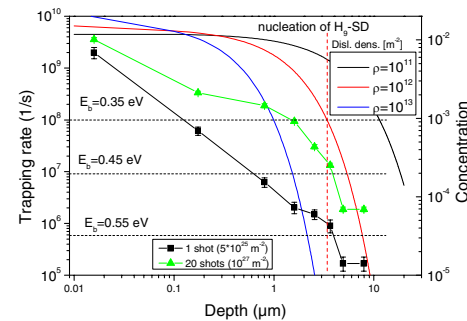


Figure 2. Left Y axis presents the reaction rates for H trapping by stable H_N -SD clusters versus depth calculated using equations (2a) and (2b)-(3) at 460 K, varying dislocation density in the range 10^{11} – 10^{13} (m^{-2}). Horizontal black dashed lines reveal dissociation rates, \bar{w}_n , of H from H_N -SD clusters with $N = 1$ – 3 ($E_b = 0.55$ eV), $N = 4$ – 6 ($E_b = 0.45$ eV), $N = 7$ – 9 ($E_b = 0.35$ eV) obtained using equation (3). A vertical red dashed line specifies the depth threshold until which the nucleation of supercritical H_9 -SD clusters takes place given the dislocation density and exposure temperature. Right Y axis displays the concentration of H isotope, deuterium, as a function of depth measured using nuclear reaction analysis techniques applied to the samples exposed to high flux plasma at 460 K as described in [23, 27]. The total fluence corresponding to the two exposures is given in figure on the inset.

critical size. Considering the site preference near the SD core, shown figure 1(a), we have explored two migration trajectories, namely: ‘in-core’ and ‘out-core’ paths. The former migration mode involves jumps between positions 1–2–3. The migration from the inner (shown by three arrows in figure 1(a)) to outer part of the core requires a jump from ‘2’ to ‘O’ (octahedral site) and from ‘O’ to ‘5’. By performing a sequence of ‘O–5–O’ jumps H atom may migrate along the dislocation line being adjacent to its core. The computed excess energy profiles are provided in figure 1(c). In all the cases, the migration barrier does not exceed 0.1 eV, proving a possibility for fast 1D migration of H along the SD line at room temperature and above. In addition, H is fully flexible to occupy any of the nine trapping TISs (see figure 1(a)), as the transition barriers are also extremely low.

The above presented DFTC results are applied to treat a series of recent experiments on H retention in W exposed to high flux plasma (see our previous work [23]). We used the kinetic rate theory method and couple 3D bulk and 1D dislocation diffusion modes (see e.g. [24, 25]). The duration of the plasma impulse was 70 s and the surface temperature was 460 K. A typical retention profile obtained by nuclear reaction analysis (NRA) in such experiments shows that the H concentration drops sharply after several μm (see right hand-side Y-axis in figure 2).

A free path of the H along a dislocation before its detrapping to the bulk is given by [24]

$$\lambda_d^0 = b \exp \left(\frac{E_m^b - E_m^d + E_b^1}{2k_B T} \right) \quad (1)$$

where $E_b^1 = -E_{H-\text{SD}}^b$ i.e. the absolute value of the H-SD binding energy, E_m^d and E_m^b is, respectively, the migration

energy of H along SD core and the migration energy in the bulk ($E_m^b = 0.4 \text{ eV}$ [26]); b is the dislocation Burgers vector $\sim 2.8 \text{ \AA}$. At 460 K, λ_d^0 exceeds $10 \mu\text{m}$ implying that trapped H atoms practically do not dissociate from the dislocation core prior to reaching a grain boundary interface or a free surface. While migrating along the core, H atoms will form H_N -SD clusters.

The rate of the formation of H_N -SD clusters on a dislocation segment of length λ_d located at a depth x , hereafter called $w_n^+(x)$ [s^{-1}], is given by the product of the H flux from bulk to the dislocation unit length, J_H^d [particles $\text{m}^{-1} \text{ s}^{-1}$], and λ_d :

$$w_n^+ = J_H^d \lambda_d, \quad (2a)$$

$$J_H^d = \frac{Z_d}{w} D_H^b C_H^b(x) \quad (2b)$$

where $Z_d \sim 1$ is the dimensionless dislocation capture efficiency for H atoms diffusing from the bulk [25] with the diffusion coefficient, D_H^b , and w is the atomic volume $\sim 15 \text{ \AA}^3$. λ_d therefore becomes the mean spacing of H_N -SD clusters forming on dislocation lines. $w_n^+(x)$ depends on the depth via the bulk H concentration, $C_H^b(x)$, given by a steady-state solution of the diffusion problem of H in the effective medium with homogeneously distributed sinks:

$$C_H^b(x) = \frac{\omega F_H x_H}{D_H^b} \exp(-x k_H), \quad k_H \approx (Z_d \rho_d)^{0.5} \quad (3)$$

where F_H is the H flux, x_H is the implantation straggling ($\sim 1 \text{ nm}$), and $k_H (\text{m}^{-1})$ is a measure of the sink strength for migrating H atoms to be absorbed by dislocations with density, $\rho_d [\text{m}^{-2}]$. Equation (3) is valid at a steady-state condition (i.e. for times longer than it takes for H to reach a depth x). Given the duration of plasma exposure (70 s), H migration energy (0.4 eV) and sample temperature (460 K), a steady-state profile of equation (3) is established at a longer time than H diffusion through the region of interest takes (i.e. H covers $10 \mu\text{m}$ per second). The depth of H penetration and the corresponding H clustering rate are therefore essentially determined by the dislocation density, as shown in figure 2.

The balance of trapping (equations 2(a)-(b)) and detrapping of H atoms to/from H_N -SD clusters will define the condition for the formation of critical H_N -SD clusters and the condition for the jog-punching. The detrapping rate, w_n^- , is independent of depth and is defined as

$$w_n^- = w_0 \exp\left(-\frac{E_b^n + E_m^d}{k_B T}\right) \quad (4)$$

where E_b^n is the incremental binding energy of H to H_N -SD cluster given in figure 1(b) and w_0 is the attempt frequency factor (taken as 10^{13} s^{-1}). The rates, w_n^- , obtained for the relevant exposure conditions [23] are plotted in figure 2. For the medium dislocation density (i.e. typical for annealed BCC metals) H permeation extends to a several μm thick layer, in which $w_n^+(x) > w_n^-$ and therefore the supercritical clusters are expected to form there, which is in a good agreement with the NRA profiles, also shown in figure 2.

As the clustering process starts, the actual linear number density of H_N -SD clusters ($N_C [\text{m}^{-1}]$) will define λ_d as soon as N_C will exceed $\rho_d \cdot \lambda_d^0$. Accordingly, the trapping rate will

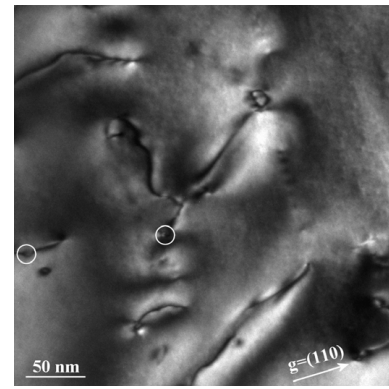


Figure 3. Dark field TEM image of screw dislocations decorated by H clusters. Two examples are indicated by the white circles.

decrease inversely proportional to N_C , which will limit the number density of H_N -SD clusters. Applying the DFT data on H_N -SD binding, we estimated $N_C^{\max} \approx 10^{19}-10^{20} \text{ m}^{-3}$, corresponding to the mean cluster spacing $\lambda_d \approx 100-10 \text{ nm}$.

Following the analytical assessment, the samples exposed in the above discussed experiment (i.e. with pre-defined depth profiles) have been inspected by transmission electron microscopy (TEM). To retain the plasma-induced damage, the samples were polished from the opposite site of the plasma exposure only. As an example, a typical dark field image showing SD lines decorated by cavities is given in figure 3. The dislocation density was roughly estimated to be in the range of $10^{12}-10^{13} \text{ m}^{-2}$, i.e. above the ‘medium’ value as expected since the exposed samples were double forged. The amount of visible hydrogen clusters is rather low for an accurate statistical determination, but based on the inspection of dozens of images, a mean linear spacing of $100 \pm 20 \text{ nm}$ was obtained, which is in the range estimated using the rate theory analysis.

We have therefore proposed and defended a comprehensive mechanism for the nucleation and growth of hydrogen bubbles on dislocation lines under high flux plasma exposure of tungsten. The mechanism comprises the following stages: interstitial H atom trapping at dislocation lines, its fast 1D migration, growth of multiple H_N clusters eventually resulting in the punching of a jog. DFT data points that the jog-punching operates spontaneously once the number of clustered H atoms exceeds eight. This information coupled with the continuum rate theory model provides an adequate description of the depth profile typically observed after high flux plasma exposure in W. The density of supercritical hydrogen bubbles, predicted by the proposed model, was also confirmed by the TEM study. Hence, the proposed mechanism reconciles long-standing experimental observations of hydrogen isotopes retention and debates about its dependence on W microstructure. Moreover, this work provides an example of how the microstructural features interfere non-equilibrium material properties becoming dominant in e.g. determination of susceptibility of W and its alloys to plasma exposure.

Additional information

Details on parametrization of DFTC and charge density maps explaining the origin of the ‘hydrogen compensation’ effect are provided as supplementary information and available online (stacks.iop.org/NF/54/042004/mmedia).

Competing financial interests

The authors declare no competing financial interests.

Acknowledgments

The work was supported by the European Fusion Programme. V. Dubinko acknowledges the support of the Erasmus Mundus Fusion EP fellowship.

References

- [1] Kaufmann M. and Neu R. 2007 *Fusion Eng. Des.* **82** 521
- [2] Zinkle S.J. 2005 *Phys. Plasmas* **12** 058101
- [3] Ahlgren T., Heinola K., Vörtsler K. and Keinonen J. 2012 *J. Nucl. Mater.* **427** 152
- [4] Roszell J.P., Haasz A.A. and Davis J.W. 2011 *J. Nucl. Mater.* **415** S641
- [5] Heinola K., Ahlgren T., Nordlund K. and Keinonen J. 2010 *Phys. Rev. B* **82** 094102
- [6] ‘t Hoen M.H.J., Tyburska-Püschel B., Ertl K., Mayer M., Rapp J., Kleyn A.W. and Zeijlmans van Emmichoven P.A. 2012 *Nucl. Fusion* **52** 023008
- [7] Schmid K., Rieger V. and Manhard A. 2012 *J. Nucl. Mater.* **426** 247
- [8] Zhou H.B., Liu Y.L., Jin S., Zhang Y., Luo G.N. and Lu G.H. 2010 *Nucl. Fusion* **50** 025016
- [9] Ogorodnikova O.V., Roth J. and Mayer M. 2008 *J. Nucl. Mater.* **373** 254
- [10] Haasz A.A., Poos M., Macaulay-Newcombe R.G. and Davis J.W. 2001 *J. Nucl. Mater.* **290**–**293** 85
- [11] Johnson D.F. and Carter E.A. 2010 *J. Mater. Res.* **25** 315
- [12] Zayachuk Y., ‘t Hoen M.H.J., van Emmichoven P.A.Z., Terentyev D., Uytendhouwen I., van Oost G. 2013 *Nucl. Fusion* **53** 013013
- [13] Kresse G. and Hafner J. 1993 *Phys. Rev. B* **47** 558
- [14] Blochl P.E. 1994 *Phys. Rev. B* **50** 17593
- [15] Perdew J., Wang Y. and Engel E. 1991 *Phys. Rev. Lett.* **66** 508
- [16] Henkelman G. and Jonsson H. 2000 *J. Chem. Phys.* **113** 9978
- [17] Cai W., Bulatov V.V., Chang J.P., Li J. and Yip S. 2003 *Phil. Mag.* **83** 539
- [18] Ventelon L. and Willaime F. 2007 *J. Comput.-Aided Mater. Des.* **14** 85
- [19] Li H., Wurster S., Motz C., Romaner L., Ambrosch-Draxl C. and Pippard R. 2012 *Acta Mater.* **60** 748
- [20] Vittek V. 1974 *Cryst. Lattice Defects* **5** 1
- [21] Heinola K. and Ahlgren T. 2010 *J. Appl. Phys.* **107** 113531
- [22] Fu C.C. and Willaime F. 2007 *J. Nucl. Mater.* **367** 244
- [23] Zayachuk Y., ‘t Hoen M.H.J., van Emmichoven P.A.Z., Uytendhouwen I. and van Oost G. 2012 *Nucl. Fusion* **52** 103021
- [24] Ryazanov A.I., Arutyunova G.A., Manichev V.M., Sokursky Y.N. and Chuev V.I. 1985 *J. Nucl. Mater.* **135** 232
- [25] Dubinko V.I., Hu S., Li Y., Henager C.H. and Kurtz R.J. 2012 *Phil. Mag.* **92** 4113
- [26] Frauenfelder R. 1968 *J. Vac. Sci. Technol.* **6** 388
- [27] Zayachuk Y. 2013 Deuterium retention in tungsten and tungsten–tantalum alloys under high-flux plasma exposure *PhD Thesis* Faculty of Engineering, Ghent University (ISBN: 9789 0857 8635 1)

I

Dislocation mechanism of deuterium retention in tungsten under plasma implantation

**V. Dubinko, P. Grigorev, A. Bakaev, D. Terentyev, G. van Oost,
F. Gao, D. Van Neck 6 and E. E. Zhurkin**

published in Journal of Physics: Condensed Matter, 2014, Vol. 26, p. 395001
(10 pp.)

Dislocation mechanism of deuterium retention in tungsten under plasma implantation

V I Dubinko¹, P Grigorev^{2,3}, A Bakaev^{2,5}, D Terentyev², G van Oost⁴, F Gao⁵,
D Van Neck⁶ and E E Zhurkin⁷

¹ National Science Center ‘Kharkov Institute of Physics and Technology’, Kharkov 61108, Ukraine

² SCK•CEN, Boeretang 200, 2400 Mol, Belgium

³ Ghent University, Applied Physics EA17 FUSION-DC, St. Pietersnieuwstraat 41 B4, B-9000 Ghent, Belgium

⁴ Department of Applied Physics, Ghent University, 9000 Ghent, Belgium

⁵ Pacific Northwest National Laboratory, Richland, WA 99352, USA

⁶ Center for Molecular Modeling, Department of Physics and Astronomy, Ghent University, Technologiepark 903, 9052 Zwijnaarde, Belgium

⁷ Department of Experimental Nuclear Physics, Institute of Physics, Nanotechnologies and Telecommunications, St. Petersburg State Polytechnical University, 29 Polytekhnicheskaya street, 195251, St. Petersburg, Russia

E-mail: dterenty@sckcen.be

Received 31 March 2014, revised 28 June 2014

Accepted for publication 4 July 2014

Published 20 August 2014

Abstract

We have developed a new theoretical model for deuterium (D) retention in tungsten-based alloys on the basis of its being trapped at dislocations and transported to the surface via the dislocation network with parameters determined by *ab initio* calculations. The model is used to explain experimentally observed trends of D retention under sub-threshold implantation, which does not produce stable lattice defects to act as traps for D in conventional models. Saturation of D retention with implantation dose and effects due to alloying of tungsten with, e.g. tantalum, are evaluated, and comparison of the model predictions with experimental observations under high-flux plasma implantation conditions is presented.

Keywords: tungsten, retention, plasma

(Some figures may appear in colour only in the online journal)

1. Introduction

The current choice of materials to be used in ITER plasma-facing components includes tungsten (W) and beryllium [1]. The sputtering yield of tungsten is much lower than that of beryllium, while its melting point is significantly higher. However, the practical use of W is hindered by its high ductile-to-brittle transition temperature, and therefore risk of brittleness between plasma pulses in the course of operation. In order to improve the mechanical properties, tungsten alloys are considered. One of the issues still to be clarified is the retention of hydrogen (H) isotopes (including deuterium and radioactive tritium) in tungsten alloys, as the

plasma-facing components are supposed to sustain high-flux plasma.

As hydrogen isotope ions are neutralized and thermalized following the implantation, further evolution depends on hydrogen solubility in W – i.e. the energy of H solution in W, which is positive. According to the phase diagram of a W-H system, in the temperature region of 300–1,000 K, relevant for ITER conditions, an equilibrium concentration of H dissolved in α -W ranges from 10^{-18} to 10^{-6} at.% [2]. Above this solubility limit (e.g. under plasma exposure that implants H ions into material), H does not form hydrides with W, but precipitates in the bubbles filled with H_2 molecules [2]. However, the thermodynamic diagram does not indicate the ways of the

bubble formation, which occurs via diffusion, trapping, nucleation and growth. The critical issue here is to determine the mechanisms of trapping and nucleation of H bubbles, which basically define the retention of hydrogen in material.

Recently a significant amount of works have been dedicated to both computational assessment of hydrogen permeation in W (see e.g. [3–6]) and experimental characterization of this phenomenon (see e.g. [7–12]). Experimental investigations of trapping and release of D in pure tungsten (W) and tungsten-tantalum (W-Ta) alloys [6–8] show that there is a considerable amount of trapped D in the bulk within a depth of several microns, which is similar to the case of He trapping in W. However, the essential difference between hydrogen and helium agglomeration in tungsten is that the binding energy between two hydrogen atoms is an order of magnitude lower than that for helium. It means that, in a marked contrast to He, a homogeneous nucleation of D clusters is highly improbable. Accordingly, nucleation of hydrogen clusters requires binding sites. In current models dealing with deuterium (D) retention in tungsten [2], it is argued that the nucleation of D-complexes is determined crucially by the concentration of radiation-produced vacancies, which act as traps for fast-migrating D atoms. One vacancy has been argued to trap up to 5–6 hydrogen atoms [3–5]. At sufficiently low temperatures considered in ref. [2], vacancies are immobile while self-interstitial atoms (SIAs) diffuse and become trapped with impurity atoms (mainly carbon, C) or are absorbed by dislocations. Thus, the result strongly depends on the dislocation density and C-SIA trapping energy, which have to be high enough to trap SIAs so that the remaining vacancies can trap D atoms and act as nucleation sites for D-clusters. This model was developed to describe ion implantation with energies of 5–30 keV, but cannot be applied (even qualitatively) to nucleation of D-clusters at *sub-threshold* implantation conditions, i.e. when the ion energy is too low to produce stable vacancy-SIA pairs in the crystal bulk, and the operating temperature range is too low (<500 K) to induce any significant concentration of thermal vacancies. The sub-threshold implantation conditions are important, however, since they correspond to the plasma-wall interaction regime expected to occur in the ITER and experiments involving high-flux, high-temperature deuterium plasmas with ion energies of up to several tens of eV [6, 7]. Hence, the description of the trapping of D at these irradiation conditions requires alternative mechanisms to those considered in the current models.

In this work, we analyze the trapping of hydrogen on typical microstructural features such as dislocations and compare the efficiency of this mechanism with the homogenous self-trapping mechanism (conventionally considered for helium retention). Based on the available *ab initio* results, we construct a theoretical model to evaluate the retention of D on dislocation lines. The model is then applied to describe thermal desorption spectroscopy (TDS) results, which are used to verify activation energies of deuterium detrapping.

2. Homogeneous self-trapping of deuterium in the bulk

Ab initio calculations [5] show that two hydrogen atoms trap each other weakly with a binding energy $E_b \sim 0.01$ eV, (as

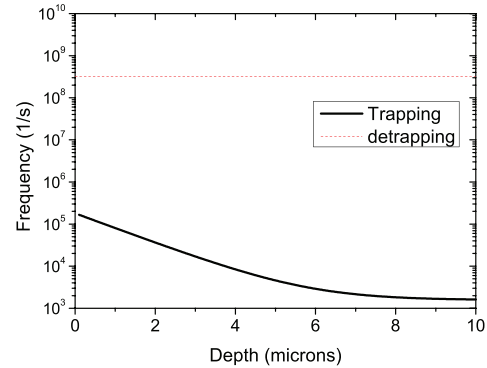


Figure 1. Trapping and detrapping frequency for D-D pairs in W bulk as a function of depth. Implantation conditions correspond to those applied in [6, 7], i.e. D flux $F_D = 10^{20} \text{ m}^{-2}\text{s}^{-1}$ and temperature $T = 460 \text{ K}$.

compared, e.g. with helium forming strong pairs with a binding energy of $E_b \sim 1 \text{ eV}$). Figure 1 shows detrapping frequency, w_{de} , for D-D pairs based on these estimates, as compared to trapping frequency, w_{DD} , i.e. the frequency of collisions of one D atom with others having concentrations of C_D^b in the crystal bulk, given by the following expressions:

$$w_{DD} = \alpha_{DD} C_D^b, \quad \alpha_{DD} = \frac{4\pi}{\omega} \left(\frac{3\omega}{4\pi} \right)^{1/3} D_D^b, \quad (1)$$

$$D_D^b \approx b^2 w_0 \exp\left(-\frac{E_m^b}{k_B T}\right), \quad (2)$$

$$w_{de} = w_0 \exp\left(-\frac{E_b + E_m^b}{k_B T}\right), \quad w_0 = 10^{13} \text{ s}^{-1}, \quad (3)$$

where $\omega \approx 0.5b^3$ is the atomic volume, b is the lattice spacing, D_D^b is the bulk diffusion of D atoms, w_0 is the attempt-frequency prefactor, E_m^b is the bulk migration energy and $k_B T$ has the usual meaning.

One can see that the trapping frequency decreases with distance (depth) from the surface due to decreasing C_D^b (see the next section), and it is several orders of magnitude lower than that of detrapping. So a homogeneous nucleation of D (or H) clusters is indeed questionable in such implantation conditions, and one needs an alternative trapping mechanism for D atoms at some intrinsic defects to provide the nucleation sites for the D clustering. Grain boundaries were suggested as nucleation sites for bubbles [9]; however, the retention also takes place in the recrystallized W [10], and even in single crystal W [11]. What is more, the presence of different impurities does not result in any significant difference in the D depth profiles, either [6, 7].

In the next section we consider a model of D retention mediated by dislocations, which are proven to act not only as trapping sites, but also as pathways for preferential D diffusion through bulk. This complex trapping-detrapping D diffusion along dislocation lines results in the removal of D to the exposure surface and in-bulk penetration.

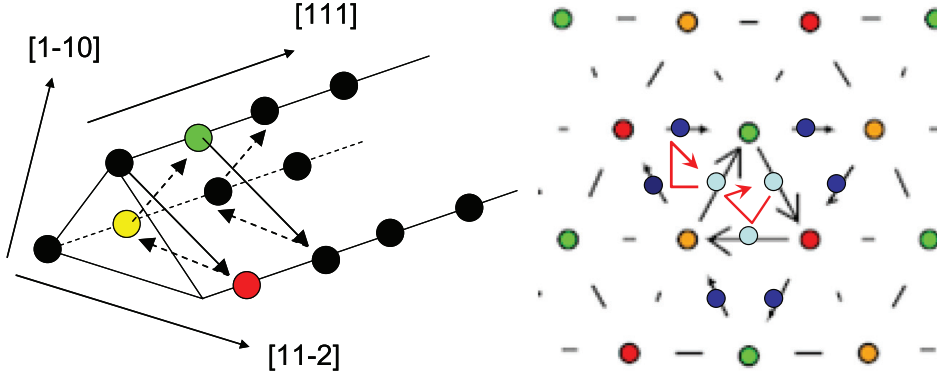


Figure 2. The schematics of core atoms in a $\frac{1}{2}<111>$ screw dislocation in 3D (left figure) and projection onto the (111) plane (right figure). The black arrows indicate the difference between displacements of neighboring $<111>$ columns forming the dislocation core. The length of the arrow is proportional to the magnitude of displacement difference, and the direction of the arrow indicates the sign of the displacement difference (i.e. the column that the arrow points to has a larger displacement than the column on the other end of the arrow). Among the three atoms that surround the centre of the dislocation, the arrows form a closed circuit. Note that while the arrows reveal a displacement component in the (111) plane for convenience of visualization, the displacement component they represent is strictly out of the plane. The three ground state positions in, and six ground state positions next to, the dislocation core are schematically shown in the right figure by light- and dark-blue balls, respectively. The red arrow connecting three light-blue balls reveals the migration path for H inside the SD core. The red arrow connecting one light-blue with two dark-blue balls represents the migration path along the dislocation core.

3. Trapping of hydrogen isotopes mediated by dislocations

3.1. Ab initio calculations

The microstructure of tungsten below $0.1 T_m$ (melting temperature) is characterized by long $a_0/2 < 111 >$ screw dislocation lines [13], as is usual for BCC metals, where a_0 is the lattice constant. Density functional theory (DFT) calculations have been applied to compute the interaction of D with the screw dislocation (SD) core in our previous work [14]. Here we extend these calculations further to assess H_N-SD interaction for different configurations of hydrogen clusters. We used the Vienna *Ab-Initio* Simulation Package (VASP [15]). The projected augmentation wave [16] and the generalized gradient approximation (GGA [17]) were used for the pseudopotential and the exchange-correlation potential, respectively. The 1s state for H and 5d6s states for W are treated as valence states in the calculations. The atomic relaxation is carried out using the conjugate-gradient algorithm with the force convergence criterion of $0.03 \text{ eV}\text{\AA}^{-1}$.

It has been shown that there are at least three positions for D inside the core, in which D is trapped with the binding energy $E_b^l = 0.6 \text{ eV}$. In addition, there are six positions for D adjacent to the dislocation core, in which the binding energy is only slightly lower (i.e. being 0.55 eV). The schematic picture showing the core structure of $a_0/2 < 111 >$ screw dislocation and location of D atoms is presented in figure 2. The calculations of the migration barrier between in-core positions provide the migration barrier for the H diffusion along the dislocation line. The two migration paths (inside and adjacent to the SD core, as shown in figure 2) were analyzed, and the resulting migration barrier, E_m^d , was computed to be $\sim 0.1 \text{ eV}$.

The in-core migration energy is essentially lower than the bulk migration energy, $E_m^b = 0.4 \text{ eV}$ [2], which means the travel path of H diffusing along the dislocation line before detrapping, L_d^0 , is expected to be significant. The latter can be estimated as follows [18]:

$$L_d^0 = b \exp\left(\frac{E_m^b - E_m^d + E_b^l}{2k_B T}\right), \quad (4)$$

At $T < 460 \text{ K}$, L_d^0 exceeds $10 \mu\text{m}$ (typical size of subgrains in polycrystalline W), implying that D atoms trapped at dislocations will remain until they reach another microstructural feature (e.g. a free surface, dislocation junction or grain boundary). Condensation of migrating D atoms on dislocation lines will result in the formation of D₂ clusters also attached to dislocations, as DFT calculations suggest the presence of the attractive interaction not only for an isolated D, but for small clusters as well [14]. The growth of a D_N cluster starting from D₂ will occur by its extension along the dislocation line. A comparison of the interaction energy of D to a D_{N-1} cluster in different configurations is presented in figure 3. The interaction energies were computed following the standard definition – i.e. as the difference of the total energy corresponding to the states of an atomic system that contains two relevant defects together and apart. Following this definition a negative value of the interaction energy corresponds to the attractive interaction. The expressions for the interaction energy of a D atom with a D_{N-1} cluster located in bulk, or placed on a dislocation or dislocation jog are the following:

$$E(D^D + D_{N-1}^D) = E_N^D + E^D - E_{N-1}^D - E_l^D, \quad (5)$$

$$E(D^B + D_{N-1}^D) = E_N^D + E^B - E_{N-1}^D - E_l^B, \quad (6)$$

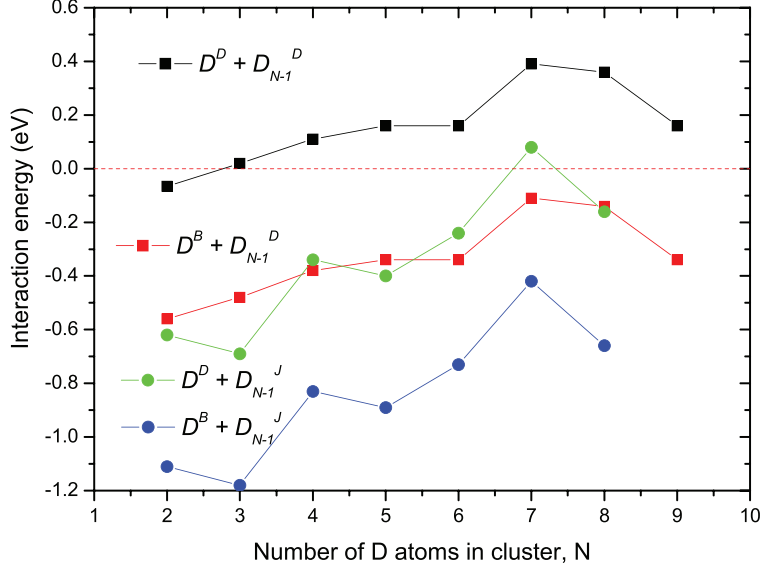


Figure 3. The interaction energy of $D^X - D_{N-1}^Y$, where symbols X and Y imply the location of interstitial D and D_{N-1} clusters. This correspondingly could be B=bulk, D=dislocation, J=jog on dislocation. The interaction energy is measured as the difference of the total energy of configurations, including two objects together and apart. With this notation, the negative value of the interaction energy implies attractive interaction (i.e. positive binding energy). Positive values (for $D^B + D_{N-1}^D$) favour dissolution of D_N (for $N > 2$) into smaller ones without leaving the dislocation core, while the formation of D_N on a dislocation jog is an energetically favourable process.

$$E(D^D + D_{N-1}^J) = E_N^J + E^D - E_{N-1}^J - E_l^D, \quad (7)$$

$$E(D^B + D_{N-1}^J) = E_N^J + E^B - E_{N-1}^J - E_l^B, \quad (8)$$

where E^D is the total energy of the crystal containing the screw dislocation (containing m W atoms), and E^B is the total energy of the perfect crystal with the same dimensions and number of W atoms as were used to create the screw dislocation. Cohesive energy of a single W atom, defined as $E_{coh} = E^B/m$; E_l^B , is the total energy of the crystal containing a single interstitial (tetrahedral) hydrogen atom relaxed in a perfect crystal; E_l^D and E_N^D are the total energy of a crystal containing a single interstitial hydrogen atom or a cluster of N hydrogen atoms placed at the most favourable position(s) on the screw dislocation line and relaxed; E_N^J is the total energy of the crystal containing a cluster of N hydrogen atoms placed in the jog on the screw dislocation.

Results in figure 3 show that on a perfect dislocation line, the accumulation of D clusters into a compact 3D structure is not a favourable process, and D atoms would prefer to form chains decorating the dislocation core. (Note that D chains also remain trapped by the dislocation). It means that the formation and growth of compact larger D_N clusters will require the presence of nucleation sites, such as jogs or dislocation intersections, in which D atoms will also become immobilized. To validate this hypothesis, we generated a vacancy jog on a screw dislocation line and assessed the interaction of H_N clusters with that jog. The interaction energy of D with a D_{N-1} cluster located on the jog is also given in figure 3 and table 1.

Table 1. The interaction energy of $D^X - D_{N-1}^Y$, where symbols X and Y imply the location of interstitial D and D_{N-1} cluster.

Number of D atoms in cluster	$D^B - D_{N-1}^B$	$D^B - D_{N-1}^D$	$D^B - D_{N-1}^J$	$D^D - D_{N-1}^J$
2	-0.0652	-0.56	-1.11	-0.62
3	0.02	-0.48	-1.18	-0.69
4	0.11	-0.38	-0.83	-0.34
5	0.16	-0.34	-0.89	-0.4
6	0.16	-0.34	-0.73	-0.24
7	0.39	-0.11	-0.42	0.08
8	0.36	-0.14	-0.66	-0.16
9	0.16	-0.34	—	—

The figure shows that a compact cluster can grow (being fed by D coming from both bulk and dislocation core) and accommodate at least eight D atoms.

The D_N clusters formed on jogs can grow and eventually reach a supercritical size, at which they transform into a bubble by emission of secondary jogs that release necessary volume for the cluster, as more D atoms will approach the nucleus. The energetic analysis of this process was performed in [14], where it is suggested that a ‘jog-punching’ mechanism operates once the cluster size exceeds D_s . (See the relaxed configuration of a D_8 cluster placed on a dislocation jog in figure 4). Once the supercritical size is reached, the cluster will grow as a macroscopic bubble by the classical loop punching mechanism [19]. The dissolution of D bubbles attached to the screw dislocation line may, however, occur by

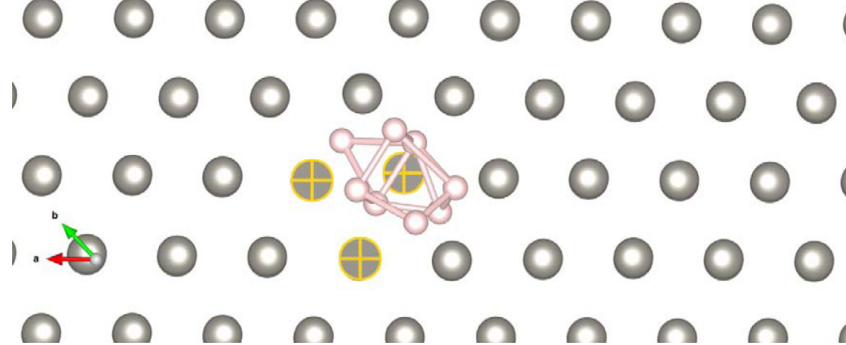


Figure 4. Relaxed configuration of an H_8 cluster formed on a jog in a core of a $1/2 < 111 >$ screw dislocation. The dislocation line is oriented normal to the paper, and the three W atoms marked with crosses form the SD core. See the atomic core structure in figure 2.

two channels: (i) emission of D into bulk or (ii) emission of D on a dislocation line. The former is the classical process, and its activation energy can be roughly estimated as the permeation energy (which varies in the range 1.25–2.0 eV following DFT calculations for H in W [5]). Experimentally, the activation energy for this process is deduced to be ~1.5–1.7 eV. (See the section 4). Emission from bubble to dislocation requires a lower energy barrier, since the emitted D would be bound to the dislocation core and the corresponding activation energy is lower by $E_b^l = 0.6$ eV. Taking the permeation energy from the experimental assessment (~1.6 eV), we shall consider that the activation energy for the D emission from a bubble to the dislocation line is ~1 eV. Even though there will be a significant difference in the activation energy for the two emission channels, they will compete with each other as temperature rises (especially at high heating rates typical of TDS measurements, which will be discussed further in section 4). The reason for the competition originates from the essential discrepancy of the effective emission surface, which is higher by a factor of $4\pi R^2/2a_0^2$ for the bulk emission as compared to the emission directly on the dislocation line. Hence, the first emission channel will also operate especially for large bubbles and at high temperature.

Based on the above-presented DFT results, a model for D trapping, transport by dislocation network (accounting for D clustering along the dislocation lines) and detrapping at typical TDS conditions is described in the following.

3.2. Rate theory of D trapping and transport

The model of D-cluster nucleation and growth at dislocation junctions is sketched in figure 5. The upper figure shows W samples exposed to high-flux D plasma [7, 8] being inspected by transmission electron microscopy (TEM [13]). A typical dark field image shows screw dislocation lines decorated by cavities (presumably D bubbles, as such features were not detected in the pre-exposed samples). The amount of visible hydrogen clusters is rather low for an accurate statistical determination, but based on the inspection of a considerable number of images, a mean linear spacing of 100 ± 20 nm

was obtained. The lower picture illustrates a mechanism of D-transport via the dislocation network, in which junctions act as nucleation sites for D-clusters. The exposure surface is on the left-hand side.

The trapping rate of an N_{th} atom by a D_{N-1} cluster $w_n^+(x)$ formed at such a nucleation site at the depth x can be estimated as the product of the D flux from the bulk to the unit length of the dislocation J_d^D , and the length along the dislocation, from which each cluster is fed with migrating D-atoms, L_d :

$$w_n^+(x, t) = J_d^D L_d, \quad J_d^D = \frac{Z_d}{\omega} D_b^b [C_D^b(x, t) - C_d^{th}], \\ C_d^{th} = \exp\left(-\frac{E_b^l}{k_B T}\right), \quad (9)$$

where $Z_d \sim 1$ is the dislocation capture efficiency for D-atoms from the bulk [20], $C_D^b(x)$ is the mean bulk D-concentration determined by trapping at dislocations, and C_d^{th} is the thermal equilibrium concentration determined by detrapping from dislocations. The maximum value of L_d is determined by equation 4 (figure 3), but in reality it should be limited by the mean distance between the clusters.

The bulk D-concentration $C_D^b(x, t)$ depends on the distance from the implanted surface, and can be evaluated by solving diffusion problems in the effective medium (see e.g. [20]), in which dislocations are the dominant sinks for D atoms implanted at the surface ($x = 0$):

$$\frac{\partial C_D^b}{\partial t} = D_b^b \frac{d^2 C_D^b(x, t)}{dx^2} - k_b^2 D_b^b [C_D^b(x, t) - C_d^{th}], \quad (10)$$

$$k_D \approx (Z_d \rho_d)^{0.5},$$

$$C_D^b(0, t) = \frac{\omega F_D X_D}{D_b^b} \equiv C_D^b(0), \quad C_D^b(\infty, t) = C_d^{th}, \quad (11)$$

where ρ_d is the dislocation density. D concentration at the surface $C_D^b(0, t)$ is determined by the implantation flux F_D , straggling X_D , and D-atom mobility, while deep in the bulk it is assumed to be in thermal equilibrium with respect to detrapping from dislocations.

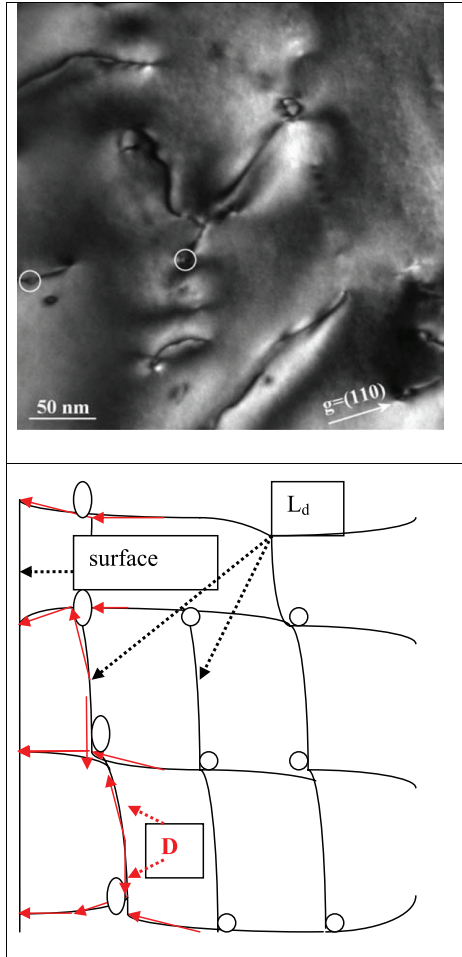


Figure 5. Dark field TEM image of screw dislocations decorated by D clusters (two examples are indicated by the white circles [14]), and schematic illustration of D-transport via the dislocation network with D-clusters separated by dislocation segments L_d .

At times larger than diffusion times through the region of interest (~ 1 s for 10 micron depth at an implantation temperature of 460 K), a steady-state profile of $C_D^b(x)$ is established, which is given by:

$$C_D^b(x) - C_d^{th} = [C_D^b(0) - C_d^{th}] \exp(-xk_D). \quad (12)$$

The concentration profile is shown in figure 6(a) for different dislocation densities ranging from annealed to cold worked state. It is significantly lower than the profile of the D retention measured experimentally [7–9] (figure 6(b)), which implies that the transport of D atoms along dislocations to the surface should be lower than the transport in the bulk. This could be accomplished via formation of traps – stable

D-clusters attached to dislocations, in the vicinity of which the activation energy for D migration is significantly enhanced compared to that in a ‘bare’ dislocation core.

Let us evaluate a steady-state profile of the concentration of D atoms attached to dislocation, which is determined by the balance between D absorption from the bulk and migration along the core:

$$\frac{\partial C_D^b(x)}{\partial t} = \left(\frac{dC_D^b(x)}{dt} \right)_b - D_D^b \frac{d^2 C_D^b(x)}{dx^2} = 0, \quad (13)$$

$$C_D^d(0) = C_D^b(0) \frac{D_D^b}{D_D^d}, \quad C_D^b(\infty) = C_d^{th}, \quad (14)$$

$$\left(\frac{dC_D^d(x)}{dt} \right)_b = Z_d \rho_d D_D^b [C_D^b(x) - C_d^{th}]. \quad (15)$$

The solution of equation (13) with boundary conditions (14) is given simply by:

$$C_D^d(x) - C_d^{th} = \frac{D_D^b}{D_D^d} [C_D^b(0) - C_d^{th}] \exp(-xk_D) \quad (16)$$

which differs from the bulk concentration (12) only by the ratio of the bulk-to-dislocation diffusion coefficients D_D^b/D_D^d . Let us estimate D_D^d by the following expression:

$$D_D^d = \frac{L_d^2}{\tau_d}$$

which assumes that migration along the dislocation occurs by quick ‘jumps’ (i.e. fast diffusion) between the D-clusters attached to the core at spacing L_d , from which D atoms can escape with an effective activation energy E_m^{eff} . Figure 6 shows the resulting profiles for the bulk concentration and retention of D at dislocations, taking $E_m^{\text{eff}}=1$ eV and different cluster spacing ranging from 250 to 80 nm. Decreasing L_d may be attributed to the increasing concentration of D-clusters with implantation time rising from 70 to 1,400 s. The choice of E_m^{eff} is motivated by the discussion provided in the previous section and the estimation of the activation energy for the D emission from a bubble attached to a dislocation line. (See also the discussion in section 3).

Now let us estimate the mean cluster radius corresponding to the D retention at dislocations, which is given by the deuterium balance equation and shown in figure 7:

$$R_C(x) = \left(\frac{3L_d C_D^d(x)}{4\pi\rho_d n_{Dv}} \right)^{1/3}, \quad (18)$$

where $n_{Dv} \approx 5$ is the number of D atoms per vacancy in the cluster, which is estimated from DFT calculations showing that a vacancy can trap up to 5–6 hydrogen atoms [4–6].

Now the total D retention can be evaluated by integrating $C_D^d(x)$ over the depth, x , up to the depth L , from which deuterium can reach the surface during TDS: $R_{\text{D}}^d = \int_0^L C_D^d(x) dx$.

If one assumes the following decrease of spacing L_d with implantation time due to nucleation of new clusters, which saturates at 80 nm (figure 8) in accordance with TEM observations (figure 5), then the retention first increases and subsequently saturates, as shown in figure 9.

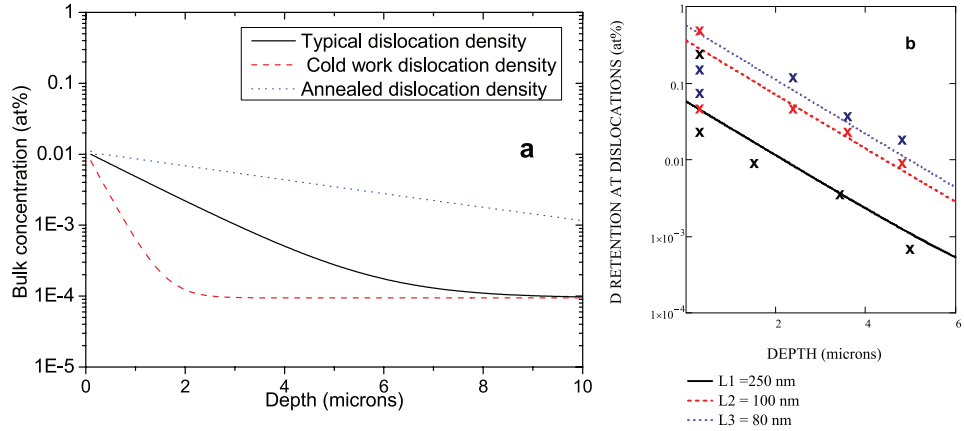


Figure 6. (a) Steady-state profile of the concentration of D atoms in the bulk, determined by trapping at dislocations with the following densities: annealed $\rho_l = 0.5 \times 10^{11} \text{ m}^{-2}$, typical $\rho_l = 0.5 \times 10^{12} \text{ m}^{-2}$, cold worked $\rho_l = 0.5 \times 10^{13} \text{ m}^{-2}$. (b) D retention at dislocations at $\rho_l = 0.5 \times 10^{12} \text{ m}^{-2}$. Implantation conditions [7, 8]: $F_D = 10^{20} \text{ m}^{-2} \text{s}^{-1}$, $X_D = b$, $T = 460 \text{ K}$. Experimental data is shown for different implantation times ranging from 70 s (black); 490 s (red) 1,400 s (blue).

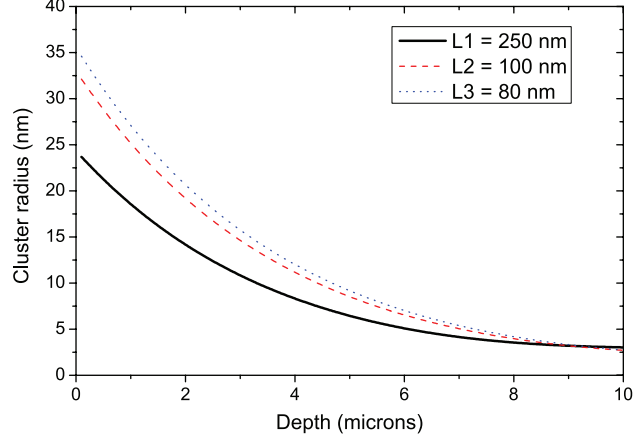


Figure 7. Mean cluster radius corresponding to the D retention at dislocations presented in figure 6(b).

The comparison with experimental data shows that the present model can account for the observed saturation of the D retention with implantation time that adjusts itself adiabatically to changing cluster structure. Alloying W with Ta has been shown to increase dislocation density [12], which can explain the observed decrease in the total retention in the W-Ta alloys compared to pure W.

4. Analysis of TDS results

In order to verify activation energies used in the present model, let us consider results of thermal desorption spectroscopy (TDS [7]) shown in figure 10(a). The rate of deuterium release

was measured as the sample temperature was increased at a constant rate 0.5 K/s , which defined characteristic time of the temperature change as $\tau_T \approx 2 \text{ s}$. During this time, deuterium can be transported to the surface via dislocation network from a depth $x = \sqrt{D_D \tau_T}$, which allows one to estimate the dependence of the desorption temperature on the depth and desorption activation energy E_m^{eff} as follows:

$$T_{de}(x) = \frac{E_m^{\text{eff}}}{\ln(w_0 \tau_T L_d^2 / x^2)}. \quad (20)$$

Figure 10(b) shows that desorption temperature ranges from 450 to 700 K , with depth increasing from 1 nm to 1 micron , taking $E_m^{\text{eff}} = 1 \text{ eV}$. The profile of retained deuterium

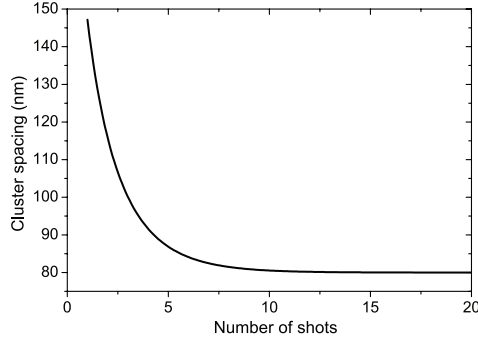


Figure 8. Cluster spacing fitted to describe saturation of the total D retention with implantation ‘shots’ (1 shot = 70 s) given by fit $L_d(N) = 80 \text{ nm} \cdot \exp\{\exp[-0.5(N - 0.1)]\}$.

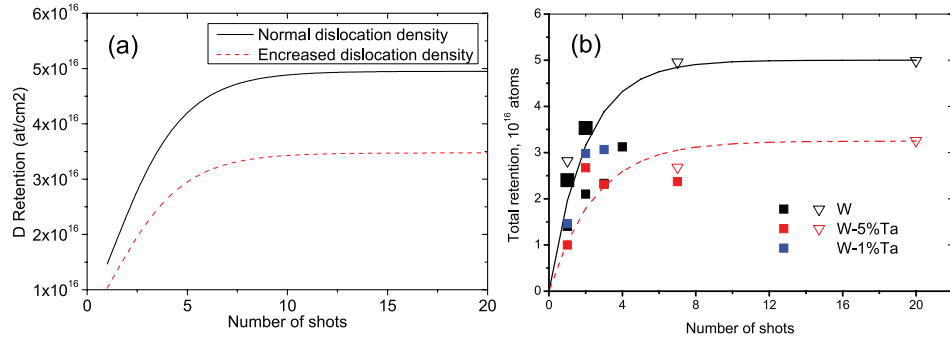


Figure 9. Total D retention versus the number of shots at different dislocation densities: (a) normal $\rho_d = 0.5 \times 10^{12} \text{ m}^{-2}$, increased $\rho_d = 10^{12} \text{ m}^{-2}$ versus (b) experimental data [8] for W, W-1%Ta and W-5%Ta. Hollow symbols correspond to accumulating exposures, filled symbols – to the exposures where TDS measurements were performed after each shot. The lines are to guide the eye.

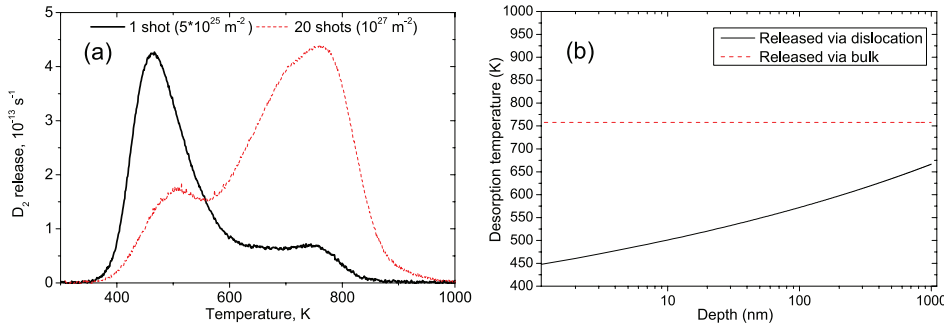


Figure 10. (a) TDS spectra of the W sample after exposures to 1 plasma shot (70 s) and 20 shots at high deuterium flux $F_D = 10^{20} \text{ m}^{-2} \text{ s}^{-1}$ [7]. (b) Calculated dependence of the temperature of desorption via dislocations on the depth, assuming $E_m^{\text{eff}} = 1 \text{ eV}$, versus the temperature of desorption via bulk, assuming the activation energy of 2 eV.

steeply decreases with depth, so the maximum of released deuterium comes from subsurface layers, which explains the position of the first TDS peak near 460 K. The second peak lies near 750 K, which corresponds to the release of deuterium from clusters via bulk diffusion. Activation energy for this

process is given by the sum of detrapping and bulk migration energies, and is equal to 2 eV in order to fit the second peak at 750 K (figure 10(b)). It does not depend on the depth since the limiting process in this case is detrapping deuterium from clusters rather than facilitating its diffusion to the surface. So,

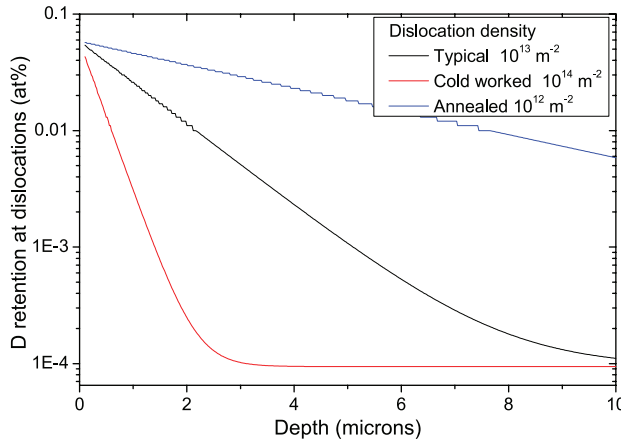


Figure 11. The prediction of the D retention on the dislocation network as a function depth for the same implantation conditions as in figure 6.

taking the D migration energy in bulk $E_m^b = 0.4 \text{ eV}$, the detrappping activation energy is estimated as 1.6 eV . This value corresponds well to the H absorption barrier (from vacuum to W bulk) found by DFT to be 1.7 and 2.0 eV for the (100) and (110) surface [5].

Note that the second peak increases with rising implantation time, which implies that large bubbles formed at high fluence cannot be emptied by deuterium release via dislocation channels at the imposed heating rate. Apparently the second mechanism (i.e. emission directly to bulk) comes into play at sufficiently high temperature and competes with the emission via dislocation lines.

5. Conclusions and outlook

We developed a model for D retention in W-based alloys under sub-threshold plasma implantation conditions, assuming the trapping of D at dislocation network. The latter serves not only as the source of trapping, but also as a means for D transport deeper in the bulk. The formulation of the present model was realized with the aid of *ab initio* calculations and experimental estimates deduced from TDS measurements. The model explains the observed saturation of D retention with implantation dose and effects due to alloying of tungsten by tantalum (which essentially changes grain size distribution). Hence, this work provides a link between the kinetics of D retention and microstructural features of the exposed W samples. Further experimental tests may include verification of a strong dependence of the D-penetration depth on the dislocation density. The prediction of the presently developed model for the effect of cold work/deformation on the dislocation-mediated retention is presented in figure 11. The validation of the prediction can be realized by exposure and subsequent nuclear reaction analysis (NRA) measurements, which offers excellent resolution up to a depth of several microns.

As an outlook regarding further development of the microstructure-mediated retention models, we consider that mobility and ‘loop-punching’ processes on edge dislocations, dislocation junctions and grain boundaries are the primary issues to be assessed. This information will provide a much more accurate description of the nucleation and growth kinetics of D-clusters in a wide range of exposure conditions.

Acknowledgments

V Dubinko acknowledges financial support from Erasmus Mundus (FUSION-EP_0). The work is partially supported by the EUROfusion programme. P Grigorev acknowledges the support from the Erasmus Mundus International Doctoral College in Fusion Science and Engineering (FUSION-DC).

References

- [1] Clark R and Reiter D 2005 *Nucl. Fusion Research* (Berlin: Springer)
- [2] Frauenfelder R 1968 *J. Vac. Sci. Technol.* **6** 388 Condon J B and Schober T 1993 *Nucl. Fusion* 207 1
- [3] Ahlgren T, Heinola K, Vörtsler K and Keinonen J 2012 *J. Nucl. Mater.* **427** 152
- [4] Heinola K, Ahlgren T, Nordlund K and Keinonen J 2010 *Phys. Rev. B* **82**
- [5] Johnson D F and Carter E A 2010 *J. Mater. Res.* **25** 315
- [6] Henriksson K O E, Nordlund K, Krasheninnikov A and Keinonen J 2006 *Fusion Sci. Technol.* **50** 163113
- [7] Zayachuk Y, 't Hoen M H J, Zeijlmans van Emmichoven P A, Uytdehouwen I, and van Oost G 2012 *Nucl. Fusion* **52** 103021
- [8] Zayachuk Y, 't Hoen M H J, Zeijlmans van Emmichoven P A, Terentyev D, Uytdehouwen I and van Oost G 2013 *Nucl. Fusion* **53** 1
- [9] Schmid K, Rieger V and Manhard A 2012 *J. Nucl. Mater.* **426** 247
- [10] Zhou H B, Liu Y L, Jin S, Zhang Y, Luo G N and Lu G H 2010 *Nucl. Fusion* **50** 025016

- [11] Ogorodnikova O V, Roth J and Mayer M 2008 *J. Nucl. Mater.* **373** 254
- [12] Haasz A A, Poon M, Macaulay-Newcombe R G and Davis J W 2001 *J. Nucl. Mater.* **290–293** 85
- [13] Stephens J 1970 *Metall. Trans.* **1** 1292
- [14] Terentyev D, Dubinko V, Bakaev A, Zayachuk Y, Van Renterghem W and Grigorev P 2014 *Nucl. Fus. Lett.* **54** 042004
- [15] Kresse G and Hafner J 1993 *Phys. Rev. B* **47** 558
- [16] Blochl P E 1994 *Phys. Rev. B* **50** 17593
- [17] Perdew J, Wang Y and Engel E 1991 *Phys. Rev. Lett.* **66** 508
- [18] Ryazanov A I, Arutyunova G A, Borodin V A, Sikursky Yu N and Chuev V I 1982 *J. Nucl. Mater.* **110** 62
- [19] Greenwood G W, Foreman A J E and Rimmer D E 1959 *J. Nucl. Mat.* **4** 505
- [20] Dubinko V I, Hu S, Li Y, Henager C H Jr and Kurtz R J 2012 *Phil. Mag.* **92** 4113

